UNIVERSITÄT SIEGEN

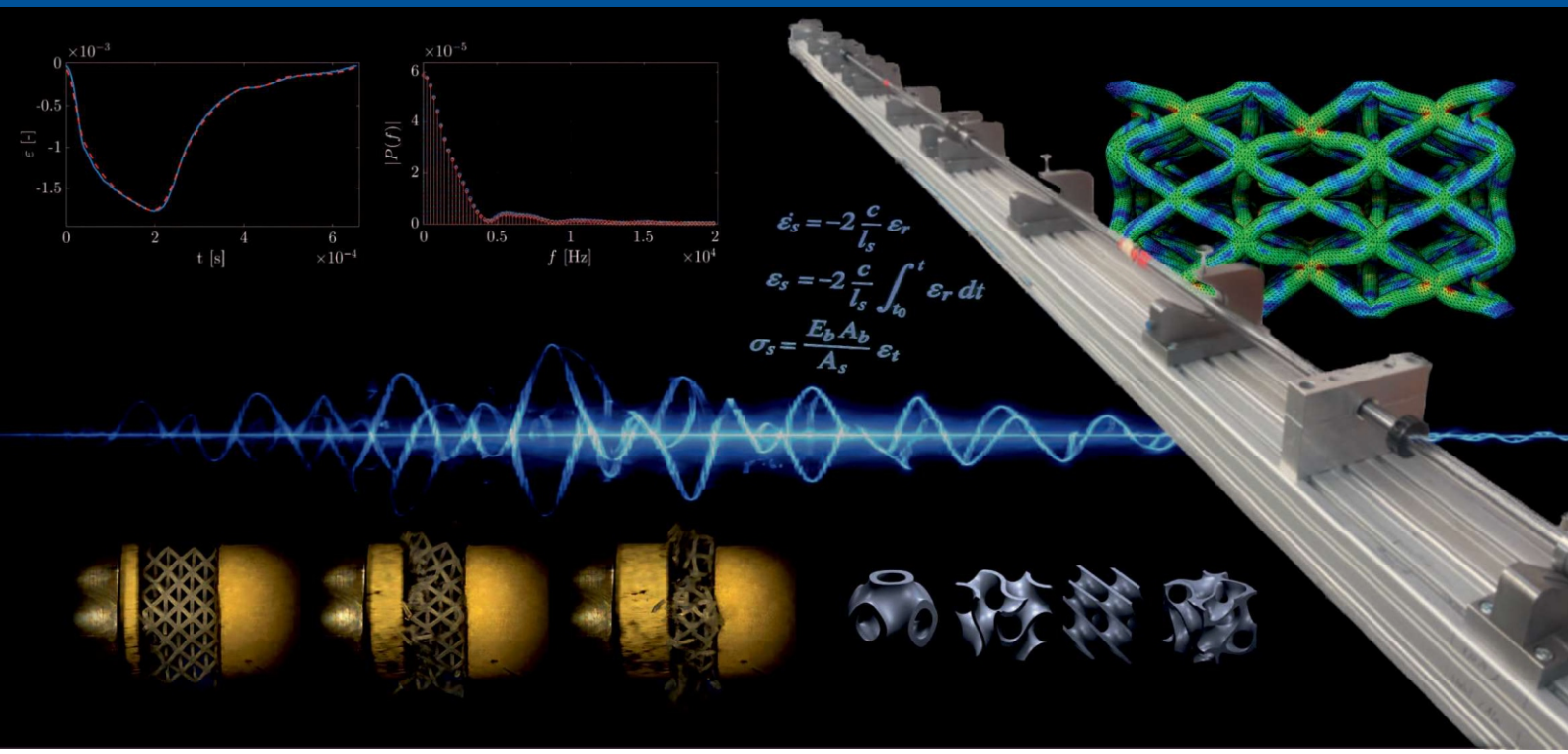

Sören Bieler

On the Response of Additively Manufactured Micro-Structured Materials to Static and Dynamic Loading

Dissertationsschrift

Festkörpermechanik

Impressum

Prof. Dr.-Ing. Kerstin Weinberg
Lehrstuhl für Festkörpermechanik
Universität Siegen
57068 Siegen
ISSN 2193-5629
URN urn:nbn:de:hbz:467-104129
DOI 10.25819/ubsi/11037
Zugl.: Siegen, Univ., Diss., 2026

On the Response of Additively Manufactured Micro-Structured Materials to Static and Dynamic Loading

DISSERTATION

zur Erlangung des Grades eines Doktors
der Ingenieurwissenschaften

vorgelegt von
M.Sc. Sören Bieler
geb. am 16.04.1986 in Siegen

eingereicht bei der Naturwissenschaftlich-Technischen Fakultät
der Universität Siegen
Siegen 2026

Betreuerin und erste Gutachterin
Prof. Dr.-Ing. Kerstin Weinberg
Universität Siegen

Zweiter Gutachter
Prof. Dr.-Ing. Detlef Kuhl
Universität Kassel

Tag der mündlichen Prüfung
09.07.2026

Acknowledgments

This thesis was written as part of my work as a research assistant at the Chair of Solid Mechanics at the University of Siegen.

First, I would like to thank Prof. Dr.-Ing. Kerstin Weinberg, who made it possible for me to write this thesis in the form it is presented here. She was always open to new ideas, many of which found their way into this work under her supervision. I would also like to thank Prof. Dr.-Ing. Detlef Kuhl for accepting as the second assessor of the thesis. Furthermore, I would like to thank Prof. Dr.-Ing. Peter Kraemer for being the chairman of the examination committee and Prof. Dr. Ulf Lorenz as a further examiner.

Many thanks to all the members of the group for Solid Mechanics who have supported me or have been in touch with this thesis and other publications. I would like to thank Dr.-Ing. Ralf Nötzel for the laboratory assistance during my time as a member of the group. Special thanks belong to my former colleague, Dr.-Ing. Marek Werner. I am also grateful to him for offering the basic structure of this LaTeX template. The many discussions often resulted in new perspectives and ideas, which finally contributed to the work in its current form. The same applies to my colleagues, M.Sc. Stefan Buchen and Dr.-Ing. Thomas Reppel. I am grateful for the interesting discussions on various scientific topics and the great time we spent together as office mates. I would also like to thank the student assistants and students who contributed to this work as part of their employment or through their bachelor or master theses.

Without the support of my family, it would not have been possible to write this thesis. For this reason, I would like to thank my partner Anna and our children Ida and Leni, who have always given me the strength to continue working on this dissertation, even in difficult phases. In this way, my family has made a considerable contribution to the realization of this thesis. I love you!

Siegen, December, 2025 Sören Bieler

Abstract

The study of material behavior is a fundamental aspect of research in science and engineering, as it directly influences the design, performance, and reliability of components across a wide range of applications. For most applications, static tests are performed by relevant standards to determine material data. Since technical constructions like buildings, bridges etc. are considered not to move with time, quasi-static materials parameter are sufficiant to calculate stability of such construction. Under varying loading conditions, especially under dynamic or high-strain-rate impacts, materials can exhibit significantly different mechanical responses compared to those observed under quasi-static conditions. This discrepancy poses challenges for accurate modeling and prediction of material performance in some scenarios, such as in automotive crashes, ballistic impacts, or aerospace applications. As a result, a deeper understanding of the mechanical behavior of materials under dynamic loading is essential for developing more robust and efficient structures. In this context, experimental methods and numerical simulations play a critical role in characterizing and predicting material response under such extreme conditions. The split Hopkinson pressure bar test is a key experimental device in determining material behavior under high strain rates.

Additive manufacturing has developed steadily over the years and is now used not only for prototyping but also in series production. There are nearly no limits to the complexity of structures and components that can be achieved with additive manufacturing, as it allows for structures that would be difficult or impossible to achieve with conventional manufacturing processes. In this work, different additive manufactured materials are examined in terms of their behavior under static and dynamic loading.

Energy absorption plays an important role, particularly in the case of impact forces acting on the body. Materials that enable good energy absorption through deformation are particularly suitable for this purpose. Lattice structures can exhibit damping properties with relatively low material costs, which, with the appropriate choice of materials, are also designed for multiple loads and thus represent sustainable energy-absorbing structures. Therefore, this study examines 3D-printed structures made of a TPU-like material subjected to multiple impact loads. The same types of structures are used to examine their energy-absorbing properties under quasi-static loads, but in this scenario, by structures made of hard, acrylic-like materials. For both types of loading, eight structural types are compared for their specific energy absorption properties. Various structural parameters are considered, including the number of struts or the structure's surface areas. By designing the individual structure types in this way, the same relative densities

can be achieved across all structures, enabling a fair comparison.

This work aims to determine the significant differences between static and dynamic loads for additively manufactured specimens made of different materials. Based on the results obtained, initial simulations for such test conditions can be created and compared with the experiments. Furthermore, the experiments are intended to investigate and compare the energy absorption behavior of different structures with the same relative density.

Keywords: split Hopkinson pressure bar; additive manufacturing; impact loading; wave propagation; glass fiber reinforced plastics; lattice structures; triply periodic minimal surfaces; energy absorption

Zusammenfassung

Die Untersuchung des Materialverhaltens ist ein grundlegender Aspekt der Forschung in Wissenschaft und Technik, da sie direkten Einfluss auf die Konstruktion, Leistung und Zuverlässigkeit von Bauteilen in einer Vielzahl von Anwendungen hat. Für die meisten Anwendungen werden quasi-statische Tests gemäß den einschlägigen Normen durchgeführt, um Materialdaten zu ermitteln. Da technische Konstruktionen wie Gebäude, Brücken usw. als zeitlich unveränderlich gelten, reichen statische Materialparameter aus, um die Stabilität solcher Konstruktionen zu berechnen. Unter wechselnden Belastungsbedingungen, insbesondere unter dynamischen Belastungen mit hohen Dehnungsraten, können Materialien im Vergleich zu denen, die unter quasi-statischen Bedingungen beobachtet werden, ein deutlich unterschiedliches mechanische Materialverhalten aufzeigen. Diese Diskrepanz stellt eine Herausforderung für die genaue Modellierung und Vorhersage von Bauteilen in bestimmten Szenarien dar, wie z. B. bei Autounfällen, ballistischen Einschlägen oder Anwendungen in der Luft- und Raumfahrt. Daher ist ein tieferes Verständnis des mechanischen Verhaltens von Materialien unter dynamischer Belastung für die Entwicklung robusterer und effizienterer Strukturen unerlässlich. In diesem Zusammenhang spielen experimentelle Methoden und numerische Simulationen eine entscheidende Rolle bei der Charakterisierung und Vorhersage des Materialverhaltens unter solchen extremen Bedingungen. Der Split Hopkinson Pressure Bar ist eine wichtige Versuchsapparatur zur Bestimmung des Materialverhaltens unter hohen Dehnungsraten.

Die Additive Fertigung hat sich mit den Jahren stetig weiterentwickelt und wird heute nicht mehr nur zur Prototypenerstellung sondern auch bereits in Serienproduktionen eingesetzt. Der Komplexität von Strukturen und Bauteilen sind mit der additiven Fertigung kaum Grenzen gesetzt – sie erlaubt Konstruktionen, die mit herkömmlichen Fertigungsverfahren nur schwer oder gar nicht realisierbar wäre. Innerhalb dieser Arbeit werden unterschiedliche additiv gefertigte Materialien bzgl. ihres Verhaltens unter statischer und dynamischer Belastung untersucht.

Besonders in Hinsicht auf ein schlagartiges Einwirken von Kräften auf Körper, spielt die Energieabsorption eine wichtige Rolle. Hierzu eigenen sich unter Anderem Materialien, die durch Verformung eine gute Energieabsorption ermöglichen. Gitterstrukturen können bei verhältnismäßig geringem Materialaufwand dämpfende Eigenschaften aufweisen, die bei geeigneter Materialwahl auch für mehrfache Belastungen ausgelegt sind und somit nachhaltige energieabsorbierende Strukturen darstellen. Entsprechend untersucht die vorliegende Arbeit hierzu 3D-gedruckte Strukturen, die aus einem TPU-ähnlichem Material gefertigt sind und mehrfacher schlagartiger Belastung ausgesetzt sind. Für die Betrachtung energieabsorbierender Strukturen

aufgrund von quasi-statischer Belastung werden die gleichen Strukturen eingesetzt, jedoch in diesem Belastungsszenario aus härterem acryl-ähnlichem Material gefertigt. Für beide Belastungsarten werden acht verschiedene Typen von Strukturen hinsichtlich ihrer spezifischen Energieabsorptionseigenschaften verglichen. Dabei werden verschiedene Parameter der Strukturen berücksichtigt, wie beispielsweise die Anzahl der Streben innerhalb der Struktur oder deren Oberflächenwerte. Durch die Auslegung der einzelnen Strukturtypen lassen sich so gleiche relative Dichten für alle Strukturen realisieren, um einen geeigneten Vergleich zwischen den einzelnen Strukturtypen zuzulassen.

Ziel der Arbeit ist es, die starken Unterschiede von statischer und dynamischer Belastung für additiv gefertigte Proben aus unterschiedlichen Materialien zu ermitteln. Anhand der gewonnenen Resultate können erste Simulationen für solche Testbedingen erstellt werden und mit den Experimenten verglichen werden. Weiterhin soll durch die Experimente das Energieabsorptionsverhalten unterschiedlicher Strukturen mit gleicher relativer Dichte untersucht und miteinander verglichen werden.

Schlagwörter: Split Hopkinson Pressure Bar; Additive Fertigung; schlagartige Belastungen; Wellenausbreitung; glasfaserverstärkte Kunststoffe; Gitterstrukturen; dreifach periodische Minimalflächen; Energieabsorption

Nomenclature

Greek symbols

α	reflection coefficient
$\hat{\alpha}$	attenuation factor
β	transmission coefficient
ε	strain
$\dot{\varepsilon}$	strain rate
ε_D	densification strain
η	viscosity
ν	Poisson number
ρ	density
$\bar{\rho}$	relative density
σ	stress
σ_{var}	standard derivation
σ^2_{var}	variance
τ_i	relaxation times
Φ	phase
ω	frequency
Ω	ohmic resistance

Latin symbols

A	cross-section area
A_{ext}	external cross-section
c	wave propagation velocity
c_{D}	factor for densification strain
d	diameter
d_{s}	diameter of a specimen
E_{stat}	modulus of elasticity (static)
E_{dyn}	modulus of elasticity (dynamic)
E_{∞}	equilibrium (elastic) modulus
E_0	instantaneous (elastic) modulus
E_i	Prony coefficient (moduli)
$E(t)$	relaxation function
E_{kin}	kinetic energy
E_{int}	internal energy
F	force
f	frequency
f_{F}	volume fraction fiber
f_{M}	volume fraction matrix
$\mathcal{F}$	Fourier transform operator
g_i	normalized Prony coefficient
$g(t)$	Prony series
G	shear modulus
G_0	instantaneous shear modulus
G_i	Prony coefficient (shear modulus)
H	mean curvature
I	current
$J(t)$	creep funcion
k	k-factor
$\hat{k}$	wave number
l	length
l_{s}	length of a specimen
l_{u}	edge length of a unit cell
L_{el}	element length (ABAQUS)
m	mass
M	Maxwell number
P	probability

$P(f)$	frequency amplitude
r_{u}	strut radius of structures
R	stress equilibrium ratio & electrical resistance
t	time
t_{w}	wall thickness
Δt_{crit}	critical stable time step (ABAQUS)
u	displacement
$\dot{u}$	particle velocity
$u(t)$	time signal of a pulse
U	voltage
$U(\omega)$	frequency spectrum of a pulse
v	velocity
v_{st}	striker velocity
V	volume
V_{ref}	reference volume
W	energy
x	distance
x_m	position of the measured signal
x_{cp}	position of the predicted signal
Z	mechanical impedance

Abbreviations

ABS	acrylonitrile-butadiene-styrene
AM	additive manufacturing
BCC	body-centered cubic
BFCC	body-face-centered cubic
DFT	Discrete Fourier Transformation
DLP	digital light processing
EA	ernergy absorption (total)
EBM	electron beam melting
FDM	fused deposition modeling
FEA	finite element analysis
FFT	Fast Fourier Transformation
FIR	finite impulse response filter
FCC	face-centered cubic
GFRP	glass fiber reinforced plastic
LENS	laminated engineered net shaping
LOM	laminated object manufacturing
MMA	methyl methacrylate
OCTET	octet truss
PMMA	polymethyl methacrylate
RHOMOCTA	rhombicuboctahedron
SEA	specific energy absorption
SHPB	split Hopkinson pressure bar
SLA	stereolithography
SLS	selective laser sintering
TPMS	Triply Periodic Minimal Surfaces
TPU	thermoplastic polyurethane
TRUNOCTA	truncated octahedron

Contents

Nomenclature vii

Contents xi

List of Figures xv

List of Tables xxi

1 Introduction 1
- 1.1 Energy absorption . . . 4
- 1.2 Objective of the work . . . 6
- 1.3 Organization of the Work . . . 7

2 Additive manufacturing 11
- 2.1 Origins of additive manufacturing . . . 12
- 2.2 Classification in manufacturing technology . . . 12
- 2.3 Different additive manufacturing processes . . . 13
- 2.4 Polymerization-based printing process . . . 15
  - 2.4.1 Stereolithography . . . 15
  - 2.4.2 Digital Light Processing . . . 16
- 2.5 Investigated materials . . . 17

3 Materials under static loading 21
- 3.1 Viscoelastictity . . . 21
  - 3.1.1 Creep test . . . 22
  - 3.1.2 Relaxation test . . . 22
- 3.2 Rheology . . . 24
  - 3.2.1 Maxwell model . . . 24
  - 3.2.2 Kelvin-Voigt model . . . 26
  - 3.2.3 Linear standard body . . . 27
  - 3.2.4 Maxwell group . . . 28
- 3.3 Specimen design and printing orientation . . . 29
- 3.4 Experiments . . . 31
  - 3.4.1 Statistical evaluation of the experiments . . . 31
  - 3.4.2 Uniaxial tensile test . . . 33
  - 3.4.3 Relaxation test . . . 37
  - 3.4.4 Viscoelastic material model . . . 38

4 Materials under dynamic loading 45
- 4.1 High strain rate testing . . . 46

4.1.1 Historical review of the split Hopkinson pressure bar . . . 47
4.1.2 Principle of the split Hopkinson pressure bar . . . 47
4.2 Theoretical background . . . 50
4.2.1 Wave propergation in long bars . . . 50
4.2.2 Solution of the one-dimensional wave equation . . . 51
4.2.3 Stresses and strains within the specimen . . . 55
4.2.4 Transmission of longitudinal waves between different media . . . 56
4.3 Experimental setup and operation . . . 59
4.3.1 Bearing system . . . 59
4.3.2 Measuring system . . . 60
4.3.3 Stress equilibrium . . . 65
4.4 Hard 3D-printed polymere under high strain rates . . . 67
4.4.1 Wave propagation velocity and impedance mismatch of polymers . . . 68
4.4.2 Experimental results at different strain rates . . . 69
4.4.3 Comparison of mechanical response at different strain rates in hard polymers . . . 72
4.5 Soft 3D-printed polymere under high strain rates . . . 73
4.5.1 Signal correction by exponential fitting . . . 74
4.5.2 Signal correction by spectral analysis . . . 76
4.5.3 Experimental results at different strain rates . . . 80
4.5.4 Comparison of mechanical response at different strain rates in soft polymers . . . 84

5 Dynamic behavior of glass fiber reinforced plastics 87
5.1 Specimen preperation and properties . . . 88
5.2 Fiber volume fraction of the GFRP material . . . 89
5.3 Experimental setup . . . 90
5.4 Experimental results . . . 92
5.5 Comparison of results with previous studies . . . 93

6 Energy absorption of open-cell structures under static loading conditions 97
6.1 Classification . . . 98
6.2 Investigated structures . . . 100
6.2.1 Beam based lattice structures . . . 101
6.2.2 Shell based structures . . . 105
6.2.3 Printing process . . . 107
6.3 Experimental investigation of hard polymer structures under static loading . . . 109
6.3.1 Experimental setup . . . 111
6.3.2 Results of static compression of lattice structures . . . 113
6.3.3 Results of static compression of TPMS structures . . . 115
6.3.4 Energy absorption . . . 117
6.3.5 Energy absorption according to Gibson & Ashby . . . 120
6.4 Numerical simulation . . . 125

7 Energy absorption of open-cell structures under dynamic loading conditions 133
7.1 Modified split Hopkinson pressure bar setup . . . 134
7.2 Experimental investigation of soft polymer structures under dynamic loading . . . 136

7.2.1 Attenuation of the pulses . . . 137
7.2.2 Energy absorption . . . 143
7.2.3 Comparison of frequency spectrum . . . 144
7.3 Numerical Simulation . . . 145

8 Summary of Achievements **151**
8.1 Outlook . . . 155

References **157**

Appendices **171**
A.1 Technical drawings of the newly developed bearing system and acceleration tube of the Split-Hopkinson pressure bar . . . 171
A.2 Derivations of the stress-strain curves for determining the starting point of the respective plateau . . . 181
A.3 Response signals of investigated structures under repeated loading . . . 183
A.4 Spectra of the pulses attenuated by investigated structures at different relative densities . . . 191

List of Figures

1.1 Crash test of a head-on collision involving two vehicles 2
1.2 Head-on collision between two NFL players 5
1.3 Brain-structures cross-sections 6

2.1 Global revenue for products and services in the additve manufacturing segment . 11
2.2 Main groups of manufacturing processes according to DIN 8580 13
2.3 Groups and subgroups of primary moding according to DIN 8580 14
2.4 Overview of different additive manufacturing processes 15
2.5 3D printer Form 2 and the working principle of a typical SLA system. 16
2.6 Voxels in 3D printing processes 17
2.7 Digital Light Processing working setup. 18

3.1 Force application F_0 for the creep test and the resulting creep function $J(t)$ 23
3.2 Strain history in the relaxation test and the resulting relaxation function $E(t)$ . . . 23
3.3 Different models of rheology: Kelvin-Voigt model and Maxwell model 24
3.4 Parallel connection of Maxwell body and Hooke's body: linear standard body. . . 27
3.5 Maxwell group with n elements. 28
3.6 Dog-bone specimen (type: 5A), DIN EN ISO 527/2. 29
3.7 Printing angles with respect to loading direction 30
3.8 Universal testing machine Inspekt Duo 5 from Hegewald & Peschke 32
3.9 Tension test measurement according to DIN EN ISO 527/2 for Anycubic Tough 2.0 for different printing orientations. 34
3.10 Comparison of the mean curves of specimen made of Anycubic Tough 2.0 with different printing orientations 34
3.11 Tension test measurement according to DIN EN ISO 527/2 for 3D-Materials SuperFlex for different printing orientations. 36
3.12 Comparison of the mean curves of specimen made of 3D-Materials SuperFlex with different printing orientations 37
3.13 Relaxation test measurement of Anycubic Tough 2.0 for different print orientations at an applied strain of 5% 39
3.14 Relaxation test measurement of 3D-Materials SuperFlex for different print orientations at an applied strain of 10% 40

4.1 Strain rate regime and experimental techniques for characterization 46
4.2 Original apparatus of Bertram Hopkinson 47
4.3 Schematic of the SHPB apparatus. 48
4.4 Illustration of a longitudinal and transversal wave. 51
4.5 Stress at an infinitesimal small element of a long bar. 52
4.6 Wave reflection and transmission at interfaces of bars and specimen. 57
4.7 Experimental setup of the custom-built split Hopkinson pressure bar at the laboratory of the chair for solid mechanics of the university Siegen. 59
4.8 3D CAD model of the newly developed bearing system. 60
4.9 Measuring system from HBM GEN7t 61
4.10 Wheatstone bridge 63
4.11 Deformation of foam recorded by a high-speed camera Photron Nova S16. . . . 66
4.12 Wave propagation velocity with and without a specimen 69
4.13 Time shifted pulses, applied forces, stress equilibrium and stress-strain curve of Anycubic Tough 2.0 at a strain rate $\dot{\varepsilon} = 300\text{s}^{-1}$. 70
4.14 Time shifted pulses, applied forces, stress equilibrium and stress-strain curve of Anycubic Tough 2.0 at a strain rate $\dot{\varepsilon} = 500\text{s}^{-1}$. 71
4.15 Time shifted pulses, applied forces, stress equilibrium and stress-strain curve of Anycubic Tough 2.0 at a strain rate $\dot{\varepsilon} = 700\text{s}^{-1}$. 71
4.16 Comparison of the stress-strain curves of Anycubic Tough 2.0 at different strain rates and the elastic modulus calculated by the slope of the elastic region of the stress-strain diagram 73
4.17 Illustration of wave attenuation and dispersion in PMMA bars 74
4.18 Signal measurement to generate a curve fit for the amplitude reduction 74
4.19 Curve fit of an exponential function through the amplitudes of the measured signal and application of the determined correction factors to the output signal in the center of the bars 75
4.20 Illustration of a signal (green) with its individual frequency components with their corresponding amplitudes 76
4.21 Location of the strain gauges with their corresponding signal placed on the incident bar and transmission bar 79
4.22 Predicted incident and transmission pulses and their corresponding amplitude spectra 80
4.23 Measured and predicted signals from the three strain gauges applied to the incident and the transmission bar and the bar/specimen interface 81
4.24 Time shifted pulses, applied forces, stress equilibrium and stress-strain curve of 3D Materials SuperFlex at a strain rate $\dot{\varepsilon} = 300\text{s}^{-1}$. 82
4.25 Time shifted pulses, applied forces, stress equilibrium and stress-strain curve of 3D Materials SuperFlex at a strain rate $\dot{\varepsilon} = 500\text{s}^{-1}$. 82

4.26 Time shifted pulses, applied forces, stress equilibrium and stress-strain curve of 3D Materials SuperFlex at a strain rate $\dot{\varepsilon} = 700\text{s}^{-1}$. 83
4.27 Comparison of the stress-strain curves of 3D-Materials SuperFlex at different strain rates and the elastic modulus calculated by the slope of the elastic region of the stress-strain diagram 84

5.1 Two different types of GFRP specimens, with fibers aligned parallel and perpendicular to the force applied 89
5.2 Voight-Reus rule of mixture for the investgated GFRP. 90
5.3 GRFP specimen clamped between steel bars. 91
5.4 Pulse shaper mounted to the surface of the incident bar and the resulting signal . . 92
5.5 Forces on the front and back side of the specimen as well as the stress equilibrium factor R 92
5.6 Stress-strain diagramms for GFRP $\parallel$ and GFRP $\perp$ at different strain rates 93

6.1 Various cellular structures from nature and technology 98
6.2 Cellular structure classification 99
6.3 Different types of lattice structures in 2D and 3D 100
6.4 Node positions in a unit cell, Octet structure and final specimen design ($3 \times 3 \times 3$ unit cells) 101
6.5 Unit cells of the investigated lattice types. 102
6.6 Composition of the BCC and FCC structure. 103
6.7 Relative density $\bar{\rho}$ and surface area A for different strut radii and a constant edge length of $l_u = 4.5$ mm per unit cell 104
6.8 TPMS design with Matlab: the two-dimensional surface of the unit cell is provided with a wall thickness. 107
6.9 Relative density $\bar{\rho}$ and surface area A for different wall thicknesses and a constant edge length of $l_u = 4.5$ mm per unit cell 108
6.10 Printed lattice structure specimens made of Anycubic Tough 2.0 and SuperFlex consisting of $3 \times 3 \times 3$ unit cells 109
6.11 Printed TPMS structure specimens made of Anycubic Tough 2.0 and SuperFlex consisting of $3 \times 3 \times 3$ unit cells 109
6.12 Typical force-displacement diagram for cellular structures under quasi-static compression. 110
6.13 Tension machine from the companyHegewald & Peschke equipped with compression plates. 112
6.14 Investigated lattice structures with a relative density of $\bar{\rho} = 0.2$ under 0 %, 25 % and 50 % of compression. 113
6.15 Investigated lattice structures with a relative density of $\bar{\rho} = 0.3$ under 0 %, 25 % and 50 % of compression. 113

6.16 Investigated lattice structures with a relative density of $\bar{\rho} = 0.4$ under 0 %, 25 % and 50 % of compression. . . . 114
6.17 Recorded force-displacement curve for the lattice structures under quasi-static compression . . . 115
6.18 Investigated TPMS structures with a relative density of $\bar{\rho} = 0.2$ under 0 %, 25 % and 50 % of compression. . . . 116
6.19 Investigated TPMS structures with a relative density of $\bar{\rho} = 0.3$ under 0 %, 25 % and 50 % of compression. . . . 117
6.20 Investigated TPMS structures with a relative density of $\bar{\rho} = 0.4$ under 0 %, 25 % and 50 % of compression. . . . 117
6.21 Recorded force-displacement curve for the TPMS structures under quasi-static compression . . . 118
6.22 Energy absorption at different states of deformation during compression test for the investigated beam-based lattice structures with $\bar{\rho} = 0.2.....0.4$ and the specific energy absorption by compression of $\varepsilon = 0.5$. . . . 120
6.23 Energy absorption at different states of deformation during compression test for the investigated TPMS structures with $\bar{\rho} = 0.2.....0.4$ and the specific energy absorption by compression of $\varepsilon = 0.5$. . . . 121
6.24 Densification strain ε_D for different factors c_D. . . . 122
6.25 Stress-strain curves of the investigated structures and the corresponding energy absorption within the plateau phase . . . 124
6.26 Specific energy absorption of the plateau part of the stress-strain curve. . . . 125
6.27 FEA mesh density for the Octet structure. . . . 126
6.28 Assembly in ABAQUS of the quasi-static compression test with a Octet structure. 127
6.29 Simulation of the compression test of the investigated lattice structures with a relative density of $\bar{\rho} = 0.2$ at different stages of deformation . . . 129
6.30 Simulation of the compression test of the investigated lattice structures with a relative density of $\bar{\rho} = 0.3$ at different stages of deformation . . . 130
6.31 Simulation of the compression test of the investigated lattice structures with a relative density of $\bar{\rho} = 0.4$ at different stages of deformation . . . 131
6.32 Numerical simulation of the force-displacement curve for the lattice structures under quasi-static compression . . . 131

7.1 Evolution of football helmets . . . 134
7.2 Modified SHPB setup. . . . 135
7.3 Different states of deformation during the experiment with the BFCC structure with a relative density of $\bar{\rho} = 0.2$. . . . 137
7.4 Different states of deformation during the experiment with the Octet structure with a relative density of $\bar{\rho} = 0.2$. . . . 138

7.5 Different states of deformation during the experiment with the RhomOcta structure with a relative density of $\bar{\rho} = 0.2$. 139
7.6 Different states of deformation during the experiment with the TrunOcta structure with a relative density of $\bar{\rho} = 0.2$. 140
7.7 Measured pulses signals and the cumulative impulse of the different lattice types. 141
7.8 Measured pulses signals and the cumulative impulse of the different TPMS types. 142
7.9 Octet $\bar{\rho} = 0.2$ pulses measured during repeated loading and the resulting cumulative pulses 143
7.10 Absolute energy absorption and specific energy absoption for each lattice typ at different $\bar{\rho}$ 145
7.11 Spectra of the investigated lattices and TPMS structures at a relative density of $\bar{\rho} = 0.3$. 146
7.12 Finite element mesh for the simulation of the impact test. 147
7.13 Snapshots of the FEA of the SHB experiment with an Octet-lattice structure ($\bar{\rho} = 0.2$) 148
7.14 Stresses during dynamic deforamtion of the Octet structure ($\bar{\rho} = 0.2$) at different time steps. 149
7.15 Comparison of pulse signals in the experiment and in the simulation for Octet $\bar{\rho} = 0.2$ 150

A.1 Derivations of the stress-strain curves for the investigated lattice structures with a relative density $\bar{\rho} = 0.4$. 181
A.2 Derivations of the stress-strain curves for the investigated TPMS structures with a relative density $\bar{\rho} = 0.4$. 182
A.3 Pulses (left) of BFCC for different relative densities: a) $\bar{\rho} = 0.2$, b) $\bar{\rho} = 0.3$, c) $\bar{\rho} = 0.4$, under repeated loading to examine the structural sustainability, together with the resulting cumulative impulse (right). 183
A.4 Pulses (left) of Octet for different relative densities: a) $\bar{\rho} = 0.2$, b) $\bar{\rho} = 0.3$, c) $\bar{\rho} = 0.4$, under repeated loading to examine the structural sustainability, together with the resulting cumulative impulse (right). 184
A.5 Pulses (left) of RhomOcta for different relative densities: a) $\bar{\rho} = 0.2$, b) $\bar{\rho} = 0.3$, c) $\bar{\rho} = 0.4$, under repeated loading to examine the structural sustainability, together with the resulting cumulative impulse (right). 185
A.6 Pulses (left) of TrunOcta for different relative densities: a) $\bar{\rho} = 0.2$, b) $\bar{\rho} = 0.3$, c) $\bar{\rho} = 0.4$, under repeated loading to examine the structural sustainability, together with the resulting cumulative impulse (right). 186
A.7 Pulses (left) of SchwarzP for different relative densities: a) $\bar{\rho} = 0.2$, b) $\bar{\rho} = 0.3$, c) $\bar{\rho} = 0.4$, under repeated loading to examine the structural sustainability, together with the resulting cumulative impulse (right). 187

A.8 Pulses (left) of Gyroid for different relative densities: a) $\bar{\rho} = 0.2$, b) $\bar{\rho} = 0.3$, c) $\bar{\rho} = 0.4$, under repeated loading to examine the structural sustainability, together with the resulting cumulative impulse (right). 188
A.9 Pulses (left) of SchwarzD for different relative densities: a) $\bar{\rho} = 0.2$, b) $\bar{\rho} = 0.3$, c) $\bar{\rho} = 0.4$, under repeated loading to examine the structural sustainability, together with the resulting cumulative impulse (right). 189
A.10 Pulses (left) of SplitP for different relative densities: a) $\bar{\rho} = 0.2$, b) $\bar{\rho} = 0.3$, c) $\bar{\rho} = 0.4$, under repeated loading to examine the structural sustainability, together with the resulting cumulative impulse (right). 190
A.11 Spectra for BFCC for different relative densities $\bar{\rho}$. 191
A.12 Spectra for Octet for different relative densities $\bar{\rho}$. 192
A.13 Spectra for RhomOcta for different relative densities $\bar{\rho}$. 192
A.14 Spectra for TrunOcta for different relative densities $\bar{\rho}$. 193
A.15 Spectra for SchwarzP for different relative densities $\bar{\rho}$. 193
A.16 Spectra for Gyroid for different relative densities $\bar{\rho}$. 194
A.17 Spectra for SchwarzD for different relative densities $\bar{\rho}$. 194
A.18 Spectra for SplitP for different relative densities $\bar{\rho}$. 195

List of Tables

2.1 Material properties of the used specimens 19
2.2 Dimensions of the conventional SHPB setup equipped with aluminium bars. . . . 19

3.1 Dimensions of the specimen type: 5A, DIN EN ISO 527/2 29
3.2 Modulus of elasticity for specimen with different printing orientations. 37
3.3 Prony coefficients for Anycubic Tough 2.0 for different print orientations. 42
3.4 Prony coefficients for 3D-Materials SuperFlex for different print orientations. . 43

4.1 Wave propagation velocity in different media 53
4.2 Dimensions of the conventional SHPB setup equipped with aluminium bars. . . . 67
4.3 Static modulus of elasticity and dynamic moduli of elasticity of Anycubic Tough 2.0 for different strain rates, the corresponding striker velocity v_{st} and the geometry of the puls shaper. 73
4.4 Dimensions of the SHPB setup for testing soft materials. 83
4.5 Static modulus of elasticity and dynamic moduli of elasticity of 3D-Materials SuperFlex for different strain rates, the corresponding striker velocity v_{st}. 85

5.1 Dimensions of the conventional SHPB setup equipped with steel bars. 91
5.2 Static modulus of elasticity and dynamic moduli of unidirectional GFRP $\parallel$ with a fiber volume of 58% for different strain rates. 93
5.3 Static modulus of elasticity and dynamic moduli of unidirectional GFRP $\perp$ with a fiber volume of 58% for different strain rates. 94
5.4 Comparison of static and dynamic elastic moduli experimental results determined by SHPB tests 95

6.1 Number of struts and nodes at different positions of the lattice unit cells. 102
6.2 Required strut radius r for a given relative density $\bar{\rho}$ as well as the resulting surface area A of the unit cells (l = 4.5 mm). 104
6.3 Required wall thickness t_w for a given relative density $\bar{\rho}$ as well as the resulting surface area A of the unit cells (l_u = 4.5 mm). 108
6.4 Total energy absorption at $\varepsilon = 0.5$ and the percentage increase in energy absorption when the relative density $\bar{\rho}$ increases. 121

6.5 Percentage proportion of energy absorption in the three phases for a compression of 50% for the investigated structures with a relative density $\bar{\rho} = 0.4$. 125
6.6 Number of elements for the FEA of the investigated specimen. 128
6.7 Comparison of forces required for compression of 50%: experiments vs. simulation. 132

7.1 Dimensions of the SHPB-setup for lattice structure experiments. 136

CHAPTER 1

INTRODUCTION

As Einstein once said, *nothing happens until something moves*. In the context of this thesis, this statement highlights that many physical phenomena are fundamentally governed by motion and, in particular, by the rate at which deformation occurs.

The determination of material data is of great importance in technology and science, as they constitute an essential basis for the design and dimensioning of machines and structural components. Material properties are typically obtained from static tests, such as the well-known tensile test. However, the mechanical behavior of materials and structures is sensitive to both the type of loading and the applied strain rate. Numerous standards are available for determining material parameters. These standards define the test conditions, including specimen geometry and loading configurations. A common characteristic of most standardized procedures is that testing is generally performed under quasi-static conditions. This approach offers several advantages, particularly with regard to achieving and maintaining a constant strain rate for a given specimen geometry. In contrast, controlling or maintaining a constant strain rate under impact or high-loading scenarios is considerably more challenging.

However, numerous engineering applications subject components and structures to dynamic or impact loading conditions. The material response under quasi-static loading differs markedly from that observed at high strain rates; accordingly, appropriate material models and assumptions must be selected for the respective loading conditions. In the worst case, incorrect assumptions regarding material parameters may lead to strucutural failure through flawed design concepts. Testing under high strain rate conditions is considerably more complex and demanding, requiring dedicated experimental facilities and advanced measurement techniques. Nevertheless, such investigations are essential for characterizing material behavior under dynamic loading and for ensuring reliable and robust component design.

A car crash, as illustrated in Fig. 1.1, represents a classic scenario in which vehicles are subjected to high strain rates, particularly in the front region where deformation is most pronounced. Accordingly, the strain rate sensitivity of materials is a critical factor in understanding its mechanincal performance under dynamic loading. Exposure to high strain rates can significantly alter the deformation behavior, strength, and failure mechanisms of materials compared to the materials response under static or quasi-static loading.

Fig. 1.1 – Crash test of a head-on collision involving two vehicles, [Lunawat 2022].

Metals that are increasingly used in additive manufacturing, such as titanium alloys, stainless steels, and aluminum alloys, exhibit mechanical behavior that is influencd by several interacting mechanisms. In general, metals exhibit an increase in strength due to strain rate-dependent hardening. Higher strain rates limit dislocation mobility, resulting in an increase in yield stress. However, at very high strain rates, adiabatic heating may occur due to the limited time available for heat dissipation. This localized temperature rise can lead to thermal softening, which counteracts the strain hardening effect. The overall materials response therefore depends on the competition between strain rate hardening and thermal softening. Fatigue behavior becomes increasingly critical under high strain rate loading conditions. Rapid loading and unloading cycles may accelerate crack initiation and propagation, thereby reducing the fatigue life of the material.

Polymers are often used in additive manufacturing due to their versatility, excellent processing properties, and relatively low costs. However, in applications with high strain rates, such as crash simulations in automotive and aerospace engineering or protection systems, the performance of polymers can vary considerably. The mechanical behavior of polymers under dynamic or impact loading is critical to understanding their potential for high-performance applications. Polymers can exhibit ductile, viscoelastic, or hyperelastic properties depending on their composition and molecular structure. Their mechanical response is therefore governed

by both elastic (recoverable) and viscous (time-dependent) deformation mechanisms. Under high strain rates, the behavior of polymers differs significantly from that observed under quasi-static or low loading rates. The viscoelastic material response of polymers often does not fully develop under high strain-rate conditions due to the short loading duration. As a consequence, polymers that exhibit viscoelastic behavior under quasi-static loading may display a more stiff or even brittle material response at elevated strain rates.

At high strain rates, the molecular mobility of polymer chains is significantly reduced, resulting in an apparent increase in stiffness accompanied by a decrease in deformability. When the rate of molecular rearrangement is lower than the applied strain rate at which the material can respond, the material exhibits a stiffer mechanical response. Consequently, increasing strain rate generally leads to higher modulus values due to restricted chain mobility. Although the material appears „harder“ as it resists deformation more strongly, its ability to undergo plastic deformation is reduced, which may promote premature failure under impact loading. With increasing strain rate, polymers progressively lose their capacity to sustain significant elastic or plastic deformation prior to fracture. As a result, their energy absorption capability decreases, and failure may occur in a brittle manner even at relatively small strains. This ductile or even brittle transition is particularly relevant for impact-resistant applications in which toughness is a critical design parameter. Furthermore, post-processing of additively manufactured structures must be performed carefully and uniformly to ensure reproducible mechanical properties. For example, residual stresses can be reduced through controlled curing at appropriate temperatures.

The layer-by-layer fabrication process inherent to additive manufacturing can significantly influence the mechanical properties of polymer components, depending on the printing resolution and overall process quality. These effects are reflected in both the static and dynamic material behavior. In particular, the orientation of the printed layers relative to the loading direction, as well as the interlayer bonding quality, play a decisive role. In comparatively coarse additive manufacturing processes such as Fused Deposition Modeling (FDM), insufficient interlayer adhesion can lead to premature structural failure at the layer interfaces, even under quasi-static loading conditions. Beyond the fabrication of simple geometries, additive manufacturing enables the design and realization of highly complex structures. Such structures can be tailored to allow controlled, reversible deformation under dynamic or impact loading, thereby dissipating large amounts of energy without permanent damage.

Composite materials, particularly fiber-reinforced polymers (FRP) such as glass fiber-reinforced polymers (GFRP), exhibit complex strain rate-dependent behavior due to the interaction between the polymer matrix and the reinforcing fibers. Under quasi-static loadings, composites generally demonstrate higher stiffness and strength than its individual components (matrix and fibers) considered seperately, owing to synergistic load transfer mechanisms. At high strain rates, the mechanical response is often initially governed by the matrix material, as it controls stress redistribution and damage initiation. For instance, epoxy-based composites may exhibit increased strength but also enhanced brittleness at high strain rates, whereas

thermoplastic matrix composites may retain a certain degree of ductility. Another important factor is the orientation of the fibers relative to the loading direction, as well as the fiber volume fraction. Even under quasi-static testing conditions, fiber alignment at a constant fiber volume fraction significantly influences stiffness, strength, and failure mechanisms, thereby strongly affecting the overall material behavior.

1.1 Energy absorption

„Energy absorption“ is important in many technical and scientific fields, particular in development of systems or materials designed to withstand or mitigate shocks, vibrations, or loads. Even under quasi-static conditions, the energy absorption capabilies of such structures play a significant role in their performance across a wide range of applications.

Energy can be absorbed elastically or plastically through the deformation of components. The energy-absorbing components do not need to be excessively stiff or heavy. Cellular structures are more suitable for such applications, as they can deform under relatively low loads if designed appropriately, and such structures can be engineered to withstand multiple loading cycles for certain load cases. The aspect of sustainability provides several advantages, including cost reduction, since properly designed components do not necessarily require replacement after each load application. In this work, different cellular structures with varying relative densities $\bar{\rho}$ were compared, and their absorption properties were evaluated under both static and impact loading conditions.

The application in which energy-absorbing properties play a critical role are highly diverse. In biomedical engineering, such structures are designed to mimic bone [El-Gizawy et al. 2024] and, depending on the specific function of the implant, must posses tailored energy-absorbing properties, that enable reversible elastic deformations.

In the automotive industry and transportation sectors, the primary focus is on occupant protection. Elements such as crumple zones or bumpers are designed to absorb the kinetic energy through elastic or plastic deformation in an event of impact [Boursier Niutta et al. 2022; Hou et al. 2023; Ming et al. 2019]. Crash boxes often filled with internal structures, such as honeycomb architectures [Balaji and Annamalai 2019] or engineered geometries, including re-entrant structures [Aktaş et al. 2023], to enhance energy absorption. Beyond automotive applications, lattice structures play an important role in aerospace engineering [Liu et al. 2022] and military applications [Reddy et al. 2024].

The energy-absorbing properties of materials and structures are particularly important in scenarios under dynamic impact loads that involve humans. The statement attributed to Einstein *nothing happens until something moves* introduced at the beginning of this chapter becomes especially relevant when the participating objects are exposed to collisions. In scenarios involving humans, potential injuries are mitigated in advance through protective measures such as seat belts, airbags, helmets, and other devices.

Helmets, in particular, are worn as protective devices in road traffic, occupational settings, military operations, and sports. In sports, a distinction is made between disposable and reusable helmets, e.g., a bicycle helmet is typically replaced after a single crash, whereas a National Football League (NFL) player's helmet (see Fig. 1.2) is designed to provide protection throughout an entire game. The design of these helmets aims to protect the wearer from direct impacts while simultaneously attenuating the transmission of shock waves caused by falls or collisions through internal damping.

This sporting example serves as a practical and tangible illustration of the critical role of energy-absorbing strucutures and provides a concrete context for the investigations presented in this work. By examining helmets, which must reliably protect the humen head from high-strain-rate impacts while balancing reusability and weight, the study highlights the challenges of designing structures that effectively absorb and dissipate energy under dynamic loading conditions. The principles observed in these everyday protective systems are directly applicable to the lattice and cellular structures analyzed in Chapter 7, making the sporting example an ideal starting point for understanding the mechanisms, performance criteria, and design strategies that will be explored in the subsequent investigations.

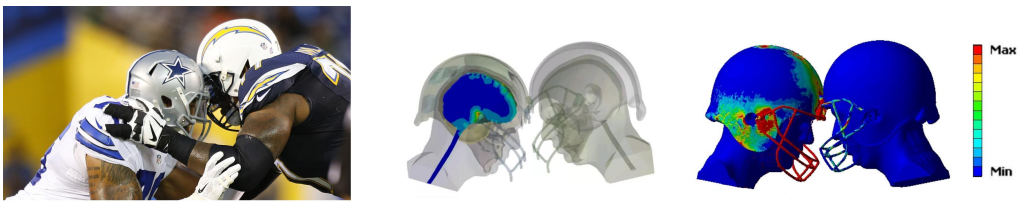

(a) (b) (c)

Fig. 1.2 – Head-on collision between two NFL players a) photography during game [West 2018], b) heads' stress distribution, and c) helmets' stress distribution, [Gerber 2016].

The frontal collision of two NFL players can be studied regarding bio-mechanical questions what is happening at the player's brain region or pure non-organic mechanical questions regarding the optimal helmet structure. Severe collisions may lead to concussion and have been associated with long-term diseases such as Alzheimer's, chronic traumatic encephalopathy (CTE), depression, and dementia, [Strain et al. 2013]. These diseases manifest a decade or more after the end of a player's career, and concussion have been linked to a doubling of the suicide rate, [Hüll 2019]. The different brain functions affected by CTE are shown in Fig. 1.3.

In addition, at least one player died immediately during a game every year between 1930 and 1990, [Kucera et al. 2014]. Consequently the development of an improved helmet design is a matter of great interest and an urgent necessity.

On average, players suffer 6.3 impacts per training session and 14.3 impacts during a game [Cournoyer et al. 2016]. In total, the average football player therefore suffers 1400 impacts over the course of a season [Crisco et al. 2010]. A study by the [Schnebel et al. 2007] demonstrates that the magnitude of impacts depends on the player's position. In this study, a total of 54,154

impacts were recorded at the University of Oklahoma. The work of [Mihalik et al. 2007] examines the magnitude of impacts to the heads of college football players. Both studies empleyed the Head Impact Telemetry System technology (HITS), embedded within the helmet, to quantify the impacts.

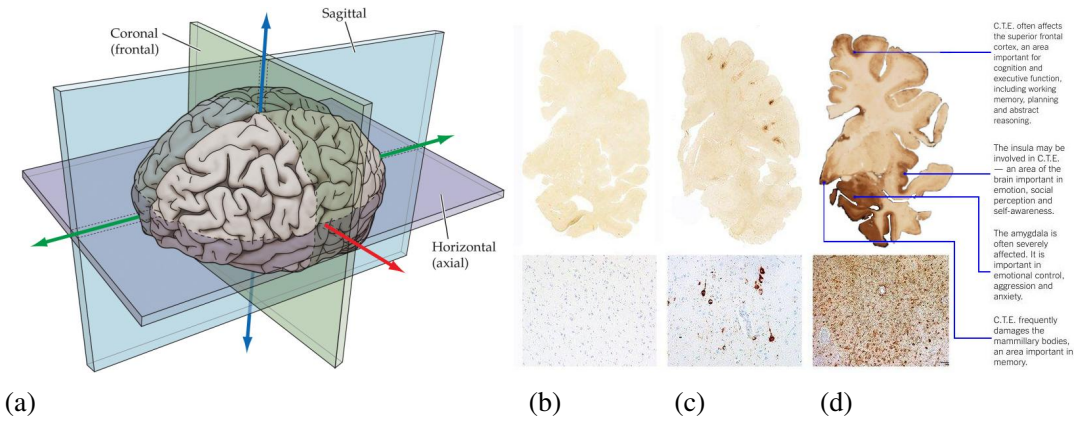

Fig. 1.3 – Brain-structures cross-sections a) planes' terminology [Song and Bruce 2019], and degenerative brain disease CTE: b) normal, c) middle, and d) serve [Mckee et al. 2018; Ward et al. 2017].

Both cases, the car accident and the impact to NFL helmets, have something in common: objectives have to be protected by a suitable energy-absorbing structure. In both cases - the car accident and impacts to NFL helmets - there is a common principle: vulnerable entities must be protected by appropriately designed energy-absorbing structures. In each scenario, the goal is to minimize damage and reduce the risk of injury by controlling how kinetic energy is absorbed and dissipated through structural deformation, whether in a vehicle's crumple zones or in the internal architecture of a helmet.

1.2 Objective of the work

This work aims to examine different materials under various loads, with a particular focus on the strain rate to which the materials are subjected. In many practical application scenarios, it is essential to understand how materials respond to specific loads. Determining material properties under high strain rates, i.e., impact loading, requires complex experimental setups and specialized equipment. The split Hopkinson pressure bar experiment serves as the central method for these investigations. The interpretation and evaluation of the resulting data demand significantly higher effort than with conventional static tests, which may explain why many materials are still primarily characterized under quasi-static conditions.

The moduli of elasticity for different materials (additively manufactured polymers and glass fiber-reinforced plastics) are examined in this work according to the load/strain rate, in order to enable their more targeted use in potential applications.

Various additional structures are investigated with respect to their energy absorption properties utilizing the design possibilities offered by additive manufacturing. Both static and impact loads are investigated. The focus is on the reusability of the structure, meaning that they should withstand multiple loads before failing under an applied load. Relatively stiff and ductile polymers are suitable for quasi-static loading, as they recover their original shape after deformation. Softer polymers are preferred for impact loading, since they maintain their ductility and resist brittle failure under high strain rate loading. For improved comparability, all structures are designed with the same relative density, and three different relative densities are examined in total.

1.3 Organization of the Work

Unless explicitly stated otherwise, all experiments were conducted in-house using the available machines and equipment. The evaluation of the measurement data was performed using the MATLAB software environment. Numerical simulations were performed with the commercial FEA sofware ABAQUS and the CAD software SOLIDWORKS was used for the design and modeling of the investigated structures. This work is divided into eight chapters as follows:

Chapter 2

This chapter introduces additive manufacturing as a relatively recent technology that has gained increasing attention in both research and industry due to its versatility and capability for producing complex geometries. A brief overview of the various additive manufacturing processes is provided, highlighting their respective advantages and disadvantages, including factors such as accuracy, build speed, material compatibility, and post-processing requirements. Particular attention is given to the stereolithography (SLA) printing process and its technological variations, which offer high resolution and superior surface quality compared to other techniques. Furthermore, the fundamental systematics of the SLA process, including the layer-by-layer building principle, the interaction of light with photopolymer resins, and key process parameters, are explained to provide a comprehensive understanding of the technology and its potential applications.

Chapter 3

Viscoelastic material behavior is crucial in quasi-static tests for the materials investigated in this thesis. This chapter shows the basics of viscoelastic theory and the experimental determination of corresponding parameters to describe this behavior. Furthermore, the orientation of the layers during the printing process of additively manufactured specimens is discussed in detail. Experimental investigations using standardized dog-bone specimens, including tensile and relaxation tests, are performed for different printing orientations. The results demonstrate

a pronounced orientation-dependent viscoelastic response of the materials under quasi-static loading conditions.

Chapter 4

The split Hopkinson pressure bar experiment is used for the dynamic tests under high strain rates. This chapter describes the basic setup, modifications, and the necessary measurement technology. In addition, the conditions under which a correct measurement is obtained are discussed in more detail. Furthermore, the basic assumptions, such as wave propagation in solids and the required stress equilibrium during the tests, are explained. The investigations deal with additively manufactured polymer specimens, whereby both hard and soft materials are tested. The behavior of the materials under investigation is examined at different strain rates, and the corresponding dynamic modulus of elasticity is determined.

Chapter 5

The SHPB experiment is employed to investigate the behavior of glass fiber reinforced plastics under high strain rates. Necessary adaptations of the SHPB setup are described and implemented for two fiber orientations, parallel and perpendicular relative to the loading direction. Analagous to Chapter 4, the dynamic moduli of elasticity are determined for different strain rates. The obtained resuls are subsequently compared with findings from similar studies and discussed.

Chapter 6

In this chapter additively manufactured structures produced by an SLA printer are discussed. Different lattice structures regarding to their energy absorption capabilities under quasi-static compression are examined here. First, a brief introduction to the investigated cellular structures and the concept of a unit cells is provided. The examined structures include both beam-based lattices and shell-based triply periodic minimal surface (TPMS) architectures. The energy absorption properties under quasi-static loading is investigated using a classical tension-compression machine. The structures are compared based on their energy absorption capacities. In addition, numerical simulations of beam-based structures in ABAQUS are presented and compared with the experimental results.

Chapter 7

Similar to Chapter 6, this chapter examines the energy absorption behavior of the structures introduced. However, in this case, the structures are not quasi-statically loaded but are subjected to impact loading. This dynamic loading scenarios are achived by using a modified SHPB test setup. The energy-absorbing capabilities of the investigated beam-based and shell-based structures are compared to identify the most efficient structural configuration. A numerical

simulation was perfomerd for a better understanding of the deformation mechanisms under high impact loading conditions.

Chapter 8

This chapter summarizes the findings of the present work and provides a structured overview of the experimental investigations and numerical simulations. The results are discussed in the context of the defined research objectives. In addition, the limitations of the current work are outlined, and suggestions for further research are provided. Finally, an outlook on potential future research opportunities is presented, including the extension of the findings to additional structures and loading scenarios.

CHAPTER 2

ADDITIVE MANUFACTURING

The application of AM has steadily increased over the years, both in industrial production and research institutions, with an optimistic growth forecast for this market, see Fig. 2.1. This manufacturing technology is no longer limited to producing prototypes, but is also increasingly being adopted for mass production, [Hashemi et al. 2020].

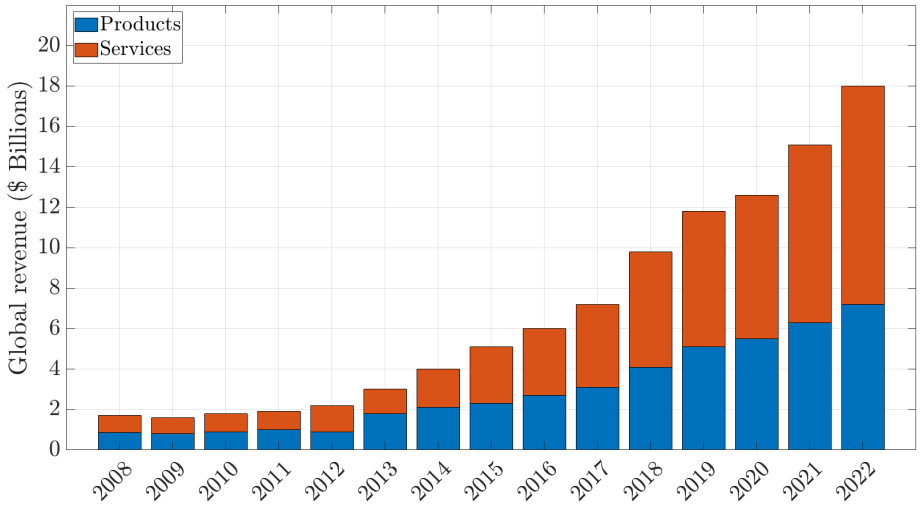

FIG. 2.1 – Global revenue for products and services in the additve manufacturing segment [Suva and Rahman 2025].

The technologies of the 3D printing process enable the fabrication of structures that could only be produced under difficult conditions, with reduced quality or not at all using conventional manufacturing technologies (turning, milling, welding, casting, etc.), cf. [Gibson et al. 2021].

2.1 Origins of additive manufacturing

As early as 1981, Chuck Hull [Hull 1984] developed the manufacturing process of stereolithography (SLA), laying the foundation for other 3D printing processes that were to follow. The patent for the SLA process was filed in 1984 and granted in 1986. Just one year later, Carl Deckard [Deckard 1988] published the technology of Selective Laser Sintering (SLS) at the University of Texas. As a doctoral student, he developed this technology under supervision of Joe Beaman, a professor at the University of Texas. He was a co-founder of Desk Top Manufacturing (DTM) Corp.. The technology of Fused Deposition Modeling (FDM), which is widely used today, goes back to S. Scott Crump. A patent application for the technology was filed in 1989 and granted in 1992, after which he and his wife, Lisa Crump founded the company Stratasys.

Current AM processes are based on photo-activated or thermo-activated reactions. A further development or another method is based on pressure processes using sound waves, [Habibi et al. 2022]. However, this process is still at a relatively early stage of development and is not yet used commercially.

For further information on the development of additive manufacturing, the reader is refered to the numerous books and papers available, only a few of which are mentioned here [Bandyopadhyay and Bose 2019; Gross et al. 2014; Lachmayer and Lippert 2017, 2020; Richard et al. 2017].

2.2 Classification in manufacturing technology

Traditional manufacturing processes such as drilling, sawing, etc., are classified as subtractive manufacturing processes, cf. [Winkelmann et al. 2021]. In these processes, a component is produced by removing the starting material available in different forms. In AM, the component is produced by adding material. The component is created in a so-called layered structure. The accuracy of the component produced depends on the resolution (x-y plane) and the printer's layer thickness in build direction (z-direction). For the different printing processes, the layer thicknesses can vary between 25 μm and 250 μm. Depending on the manufacturing process, an additively manufactured component undergoes a more or less complex post-processing process, see [VDI-3405 2007]. This can include washing processes, drying and curing times, or removing support structures required during fabrication.

The areas of application in which AM is used are broad. These include the automotive industry [de Mattos Nascimento et al. 2022; Yin et al. 2018], the aerospace sector [Magerramova et al. 2018; Totaro and Gürdal 2009; Vasiliev et al. 2012; Zhu et al. 2016], medicine [Al-Tamimi et al. 2020; Javaid and Haleem 2018], the electrical engineering industry [Hoerber et al. 2014] and the nanotechnology sector [Velu et al. 2019; Wang et al. 2018]. Since 2020, AM has been one of the primary moding manufacturing processes, including the casting and sintering

processes, see Fig. 2.2.

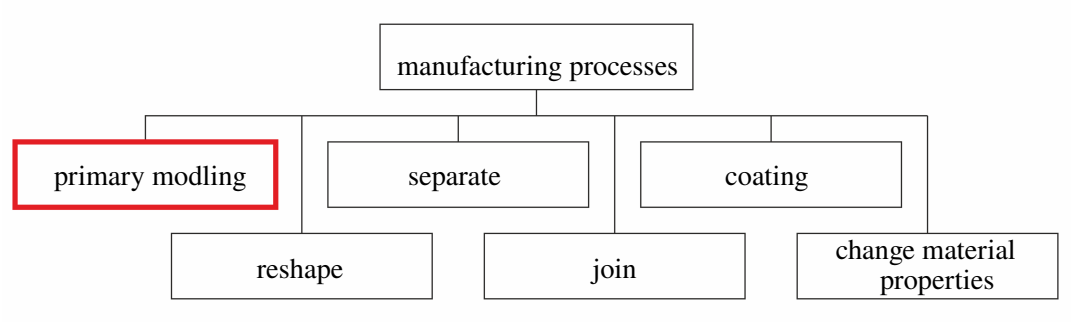

Fig. 2.2 – Main groups of manufacturing processes according to DIN 8580 [Norm 2022] (translated to English).

The production technology of primary molding is further divided into ten groups, each containing subgroups. Group 1.10 includes additive manufacturing, subgroup 1.10.7 describes the process of bath-based photopolymerization, which describes the SLA process (stereolithography) used for this work, see Fig. 2.3

2.3 Different additive manufacturing processes

3D printing technology is not only becoming increasingly popular in companies, but is finding its way more and more into private households. This is lagely due to the increasingly compact design of printers. The slicer software for subsequent printing, which is responsible for layering the component to be printed, can usually be used on any PC without any special knowledge. Inexpensive printers based on the fused deposition modeling process (FDM) or the stereolithography process are available for private individuals from various manufacturers (Anycubic, Creality, Elegoo, Nova3D) with excellent resolution. In general, it can be said that for home use, higher surface qualities and finer structures with more detail can be printed with SLA technology. Owing to their substantially higher acquisition and operating costs, metal printers are more suited to the professional sector of industry and research institutions.

The technology of 3D printing is playing an increasingly important role in the industry, especially in the area of product development. The relatively cost-effective production of prototypes means that products can be manufactured in a very short production times. The AM process offers the advantage of extensive design freedom in terms of the complexity of the components. This gives product development a maximum degree of flexibility. Today, many different AM processes are available, which differ depending on the choice of material and/or process technology. Generally, manufacturing processes are divided into three groups (liquid-based, solid-based, and powder-based), see Fig. 2.4.

Further subcategories of these three main branches show many different manufacturing processes, each with advantages and disadvantages. A detailed description of the individual

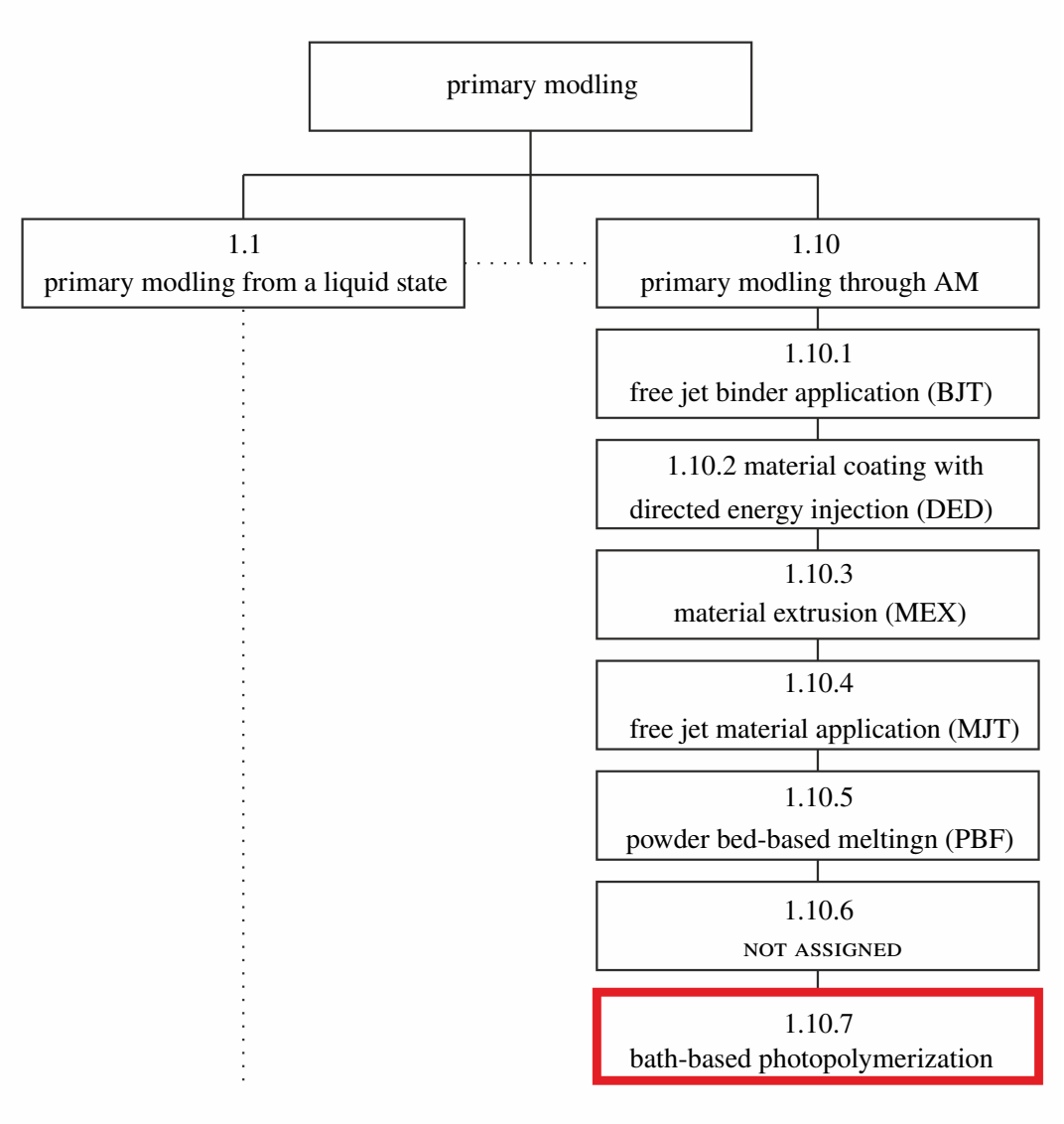

Fig. 2.3 – Groups and subgroups of primary moding according to DIN 8580 [Norm 2022] (translated to English).

processes, which are listed in Fig. 2.4, can be found in [Gardan 2016; Gibson et al. 2021]. The selection of printable materials has increased significantly in recent years; AM is no longer limited to plastics and resins; components can also be manufactured from metals or ceramics, cf. [Bourell et al. 2017; Deckers et al. 2014]. Owing to the continuously improving resolution of AM processes and the associated increase in quality, even very delicate structures, such as lattice structures, can now be produced at small scales.

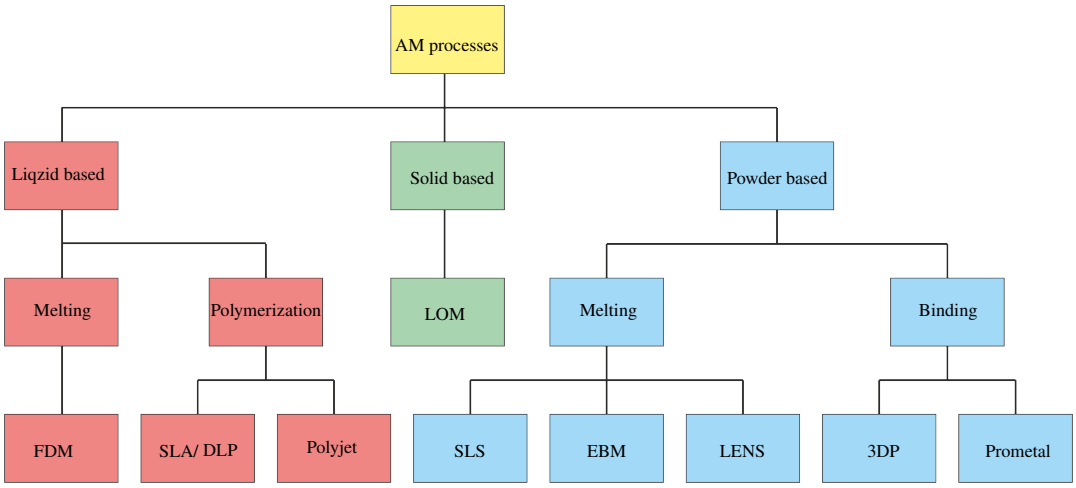

Fig. 2.4 – Overview of different additive manufacturing processes, [Kruth 1991; Wong and Hernandez 2012].

2.4 Polymerization-based printing process

Two 3D printers were available for the samples and structures created in this work, both based on the polymerization process. The printer Form 2 from the company Formlabs works according to the principle of classical stereolithography and cures liquid resin point by point by a laser. The printer Mars 3 Pro from the company Elegoo works according to the same principle of polymerization and is therefore counted among the SLA processes. However, an entire layer is cured at once by a projector underneath the resin basin.

2.4.1 Stereolithography

In the SLA process, resin in liquid form is cured by selective curing using a UV laser light. The liquid resin is a so-called photopolymer (e.g., acrylic or vinyl ester resin) that polymerizes when hit by the laser light. A build platform is required to create the component, which serves as a carrier plate for the structure. The structure is immersed in a basin filled with the liquid resin allowing the laser to selectively cure the resin on the build platform point by point. Once all points in one layer have cured, the platform is lifted out of the basin by a spindle drive, and excess liquid resin can drip into the basin. The process is repeated for each subsequent layer, so the workpiece is created layer by layer while hanging from the build platform, see Fig. 2.5. The SLA process is one of the oldest rapid prototyping technologies, patented by Chuck Hull in 1986.

Since the resin does not fully cure during printing, appropriate support structures are added to the component to ensure its stability. These support structures are particularly necessary for very delicate structures to prevent collapse due to a lack of material rigidity. Furthermore, for components with multiple cavities, it is important to ensure that the support structures are

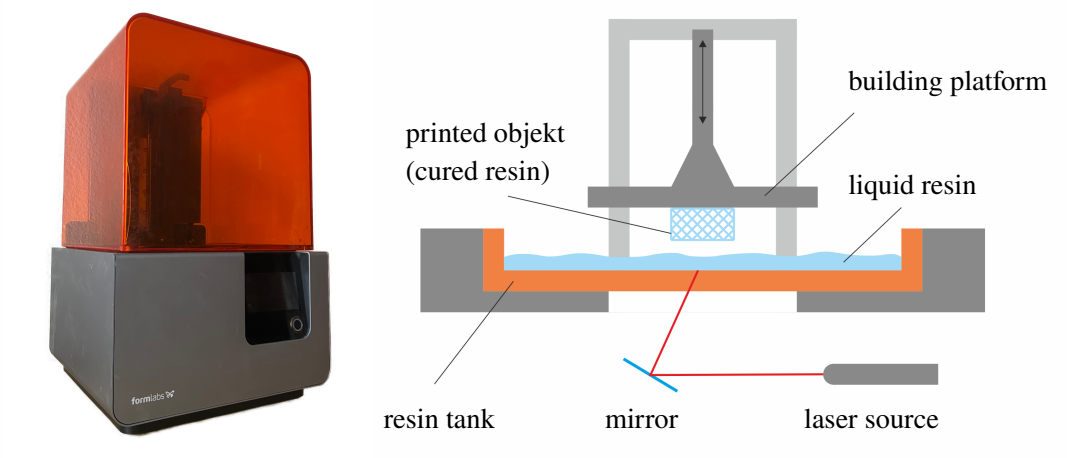

Fig. 2.5 – 3D printer Form 2 and the working principle of a typical SLA system.

attached in a way that the structure can be removed later. This is important for the lattice structures discussed later, since support structures in the „body interior“ are complicated to remove. Accordingly, only the outer surfaces of the actual lattice body need to be provided with appropriate support structures.

After the printing process is complete, the component and its support structures are freed of any adhering liquid resin using several baths of isopropanol. The isopropanol bath is necessary to prevent these residues from becoming permanently fused to the actual component during the subsequent curing process. Before the support structures can be removed from the printed part, the workpiece must be cured under material-specific parameters (temperature and UV light). Through this curing process, the material achieves its final rigidity, rendering the support structures obsolete.

2.4.2 Digital Light Processing

In contrast to the SLA process, Digital Light Processing (DLP) does not use a laser but rather a projector located beneath the transparent resin tank. The process works the same as the SLA process. A build platform is immersed in the resin tank, and a layer is cured using UV light. The build platform is raised in the next step, and the next layer can be exposed. However, the entire layer in the x-y plane is directly exposed with the DLP process. Like a digital screen, an entire layer is projected onto the platform to be cured. The projector has a specific resolution, similar to a commercial screen. So the projector consists of the x-y plane of many small rectangles (pixels). Analogous to the word „pixel“, the smallest printed units created by the printing process are called voxels (volumes; see Fig. 2.6 a). The disadvantage of this process is the occurrence of the so-called voxel effect. Because the DLP process renders planes using rectangular voxels, a closer look reveals a stepped pattern, the vertical voxel rows (see Fig. 2.6 b) and Fig. 2.6 c). With the classic SLA process, the laser can cure a continuous line,

resulting in finer gradations in the z-direction. With today's printers, generating resolutions of 16K or even higher is easily possible. Depending on the projector size and the optical system, resolutions of 25 μm are possible. The DLP process also uses support structures for overhangs and critical edges to maintain the shape of the actual part.

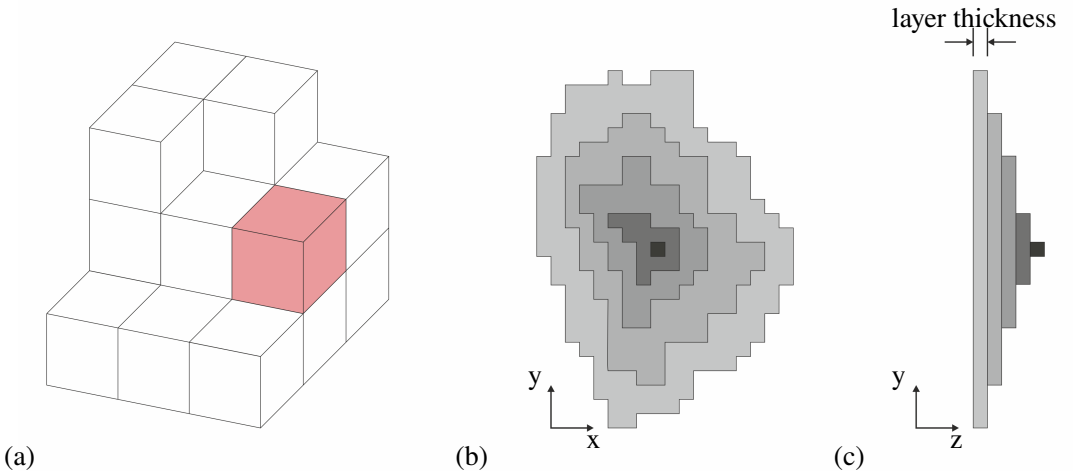

Fig. 2.6 – Voxels: a) stacked voxels with one highlighted voxel, b) voxel effect in xy-plane, and c) voxel effect in yz-plane.

Both SLA-printing technologies have their advantages and disadvantages, but are equally suitable for creating tensile specimens and more delicate structures. Due to the high resolution of DLP printers, the stair-step or voxel effect is only visible at very high magnification. However, it cannot be completely eliminated. Because the DLP process cures an entire layer simultaneously, shorter print times for identical objects are needed. The Mars 3 Pro from the company Elegoo is used for the printed specimens in this work due to its higher resolution and broader selection of print materials. Furthermore, the Chitubox software environment can be used, which offers the user far more freedom than the mandatory PreForm software from Formlabs. The Chitubox software allows exposure times, lifting speeds, and many other printing parameters to be adjusted in order to achieve optimal print results. To remove resin residues and post-cure the parts after printing, the wahsing and curing equipment provided by Elegoo is used, see Fig. 2.7.

2.5 Investigated materials

Within this work, specimens and structures are printed using two different materials. Both materials are available as liquid resins and can be processed accordingly using SLA printers or DLP printers. The investigated materials are:

- Anycubic Tough 2.0
- 3D Materials SuperFlex

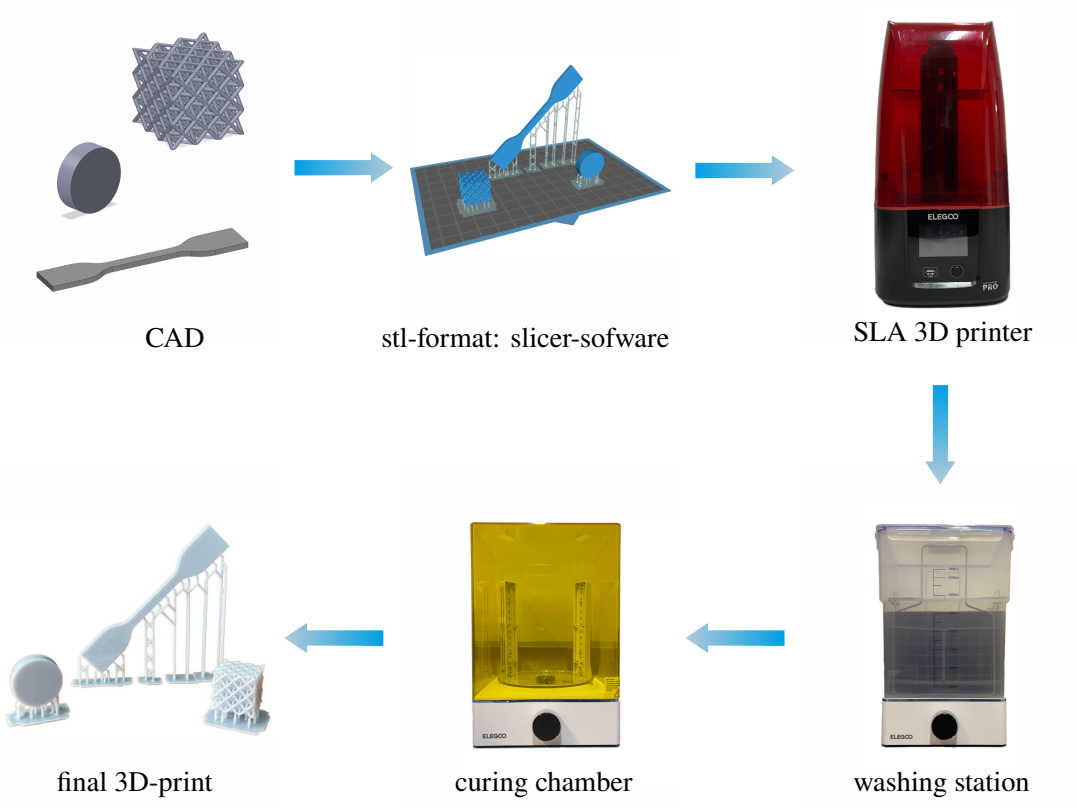

Fig. 2.7 – Digital Light Processing working setup.

The first resin tested is Anycubic Tough 2.0. The acrylic (acrylonitrile-butadiene styrene) resin belongs to the group of styrene polymers and is an amorphous thermoplastic. By mixing different proportions of styrene ($H_2C = CH - C_6H_5$), butadiene ($H_2 = C = CH - HC = CH_2$) and acrylonitrile ($H_2C = CH - C \equiv N$), the acrylic plastic can be adapted to the respective application. Increasing the butadiene content can make the material more ductile, for example, to increase the impact strength. The styrene in ABS plastic is characterized by its hard but brittle properties. The tested resin Anycubic Tough 2.0 shows a good ductility and high breaking strength, [Anycubic 2025]. Therefore, acrylic-like materials distinguish the material from very brittle thermoplastics, mainly consisting of methyl methacrylate (MMA). The so-called Standard Resin from Formlabs is an example of such a material behavior.

The second material examined is significantly softer and more flexible than the Anycubic Tough 2.0. The 3D Materials SuperFlex is a rubber-like material which is comparable with caoutchouc or elastomeres. It simulates thermoplastic polyurethane (TPU) which is an elastomer (synthetic plastic). TPU is characterized by its high flexibility and resistance during further processing and combines the properties of thermoplastics and elastomers, cf. [3D-Materials 2025]. Table 2.1 shows some of the material parameters determined by the manufacturers. However, these values are only a rough estimate of the actual values, as the test conditions, such as print orientation and laboratory conditions, are not specified in more detail.

For the sake of completeness, however, some of the parameters published by the manufacturer are listed here.

Table 2.1 – Material properties of the used specimens (provided by manufacturer).

	manufacturer	polymer base	tensile strength	hardness
Tough 2.0	Anycubic	acrylic-like	30-42 MPa	Shore 82-84D
SuperFlex	3D-Materials	TPU-like	5.5 MPa	Shore 80A

The information about the material properties provided by manufacturers on different parameters is only comparable to a certain extent, as different manufacturers use varying standards, such as DIN ISO or the American ASTM. Particularly with 3D printing materials, especially with liquid resins, the values determined depend heavily on the printing parameters, such as the wavelength of the light, exposure time, post-curing conditions, and washing times. Although many manufacturers provide recommended processing parameters in this regard, these are highly depend on the laboratory conditions and the 3D printer used.

For this reason, some of the parameters used to print the specimens in this work are listed in Table 2.2. The printing materials were stored in a sideboard at a temperature of 20°C. After printing, all specimens were washed with isopropanol and post-cured according to the times specified in Table 2.2. After the subsequent curing process, the specimens were stored in a cabinet without a light source for one week before the tests were carried out.

Table 2.2 – Dimensions of the conventional SHPB setup equipped with aluminium bars.

	Anycubic Tough 2.0	3D-Materials SuperFlex
exposure time [s]	6.5	7.0
lifting speed of the platform [mm/s]	20.0	20.0
rest period after layer printing [s]	0.5	0.5
isopropanol bath [min]	10.0	2.0
curing chamber [min]	3.0	10.0

In contrast to metallic materials, polymers exhibit a pronounced time dependent behavior. Appropriate material characterization studies are conducted to describe better the deformation of the materials used in this work. Accordingly, the fundamentals of viscoelasticity are necessary and are described in the following chapter.

Chapter 3

Materials under static loading

Typically, materials are tested under quasi-static conditions to determine their mechanical behavior and characteristic parameters. These essential parameters serve as the basis for numerous technical and scientific applications. This chapter presents the design of specimen geometries using 3D printing and the experimental viscoelastic investigations under quasi-static loading. The tensile tests allow the materials' properties to be derived, thus creating a model for simulations. The viscoelastic behavior of the specimens under investigation is examined using relaxation tests.

The current thesis employs tension and relaxation tests for material characterization. These analysis were performed on a universal tensile machine of the company Hegewald & Peschke, which will be discussed in more detail in the experimental part of this section.

3.1 Viscoelastictity

The materials investigated in this work exhibit more or less viscoelastic behavior. For this reason, this aspect is examined in more detail here. Linear viscoelasticity refers to the properties of materials that show viscous (flow-like: $\sigma = \eta\,\dot{\varepsilon}$) and elastic (spring-like: $\sigma = E\,\varepsilon$) behavior when subjected to stress or deformation [Wrana 2014]; the combination of both properties is called viscoelasticity. When a viscoelastic material is subjected to a constant force or deformation, it initially deforms like an elastic solid, but over time, it exhibits a steady flow or creep. This behavior is due to the material's internal molecular structure and interactions. Viscoelastic materials can expose time-dependent responses, such as stress relaxation (gradual decrease in stress over time at a constant strain) or creep (gradual increase in deformation over time at constant stress). These properties are essential in various fields, including materials science, engineering, and biomechanics, as they affect the performance and behavior of materials under

different loading conditions. Understanding the viscoelastic behavior of materials is crucial for designing and predicting the performance of products and structures, such as in the automotive, aerospace, and medical industries.

3.1.1 Creep test

There are two complementary classical experiments for determining viscoelastic material behavior: the creep test and the relaxation test. Both tests are carried out using conventional tensile specimens on a tensile machine. In the creep test, the specimen is loaded with a constant stress. The specimen's displacement $u(t)$ is then recorded over time. The stress σ_0 is calculated based on the initial cross-section of the specimen web A_0 and the constant force F_0 according to Eq. (3.1):

$$\sigma_0 = \frac{F_0}{A_0} \tag{3.1}$$

The force F_0 is applied abruptly over a very short initial time. This abrupt application of the force or other quantity can be mathematically described using the Heaviside function, cf. Eq. (3.2).

$$H(t) = \begin{cases} 0, & t < 0 \\ 1, & t \geq 0 \end{cases} \tag{3.2}$$

In reality, such an infinitely short period of time is impossible to achieve. The time interval must be chosen as short as technically feasible. This time interval is labeled t_0 in Fig. 3.1 and Fig. 3.2. At this point, the specified force or strain is reached. Events before this point in time are disregarded. The technical strain is determined from the time-dependent displacement and the original length of the specimen:

$$\varepsilon(t) = \frac{u(t)}{L_0} \tag{3.3}$$

The creep function or retardation function $J(t)$ is obtained from the Eqs. (3.1) and (3.3).

$$J(t) = \frac{\varepsilon(t)}{\sigma_0} \tag{3.4}$$

The function J_0 describes the instantaneous compliance and J_∞ the equilibrium compliance. This equilibrium compliance corresponds to the $J(t)$ limit for $t \Rightarrow \infty$, cf. Fig. 3.1.

3.1.2 Relaxation test

In contrast to the creep test, the force is not held at a constant value in the relaxation test, but rather the strain ε_0. Accordingly, this strain results from the given displacement u_0 and the

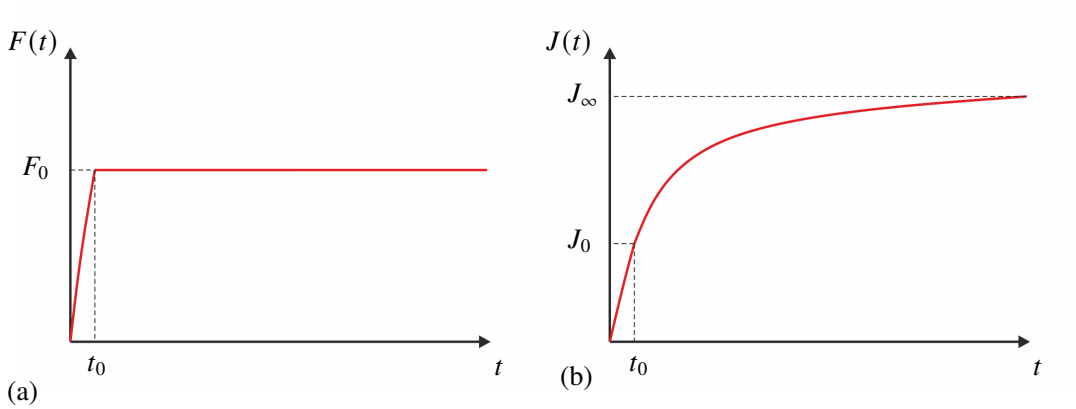

Fig. 3.1 – a) Force application F_0 for the creep test and b) the resulting creep function $J(t)$.

initial length L_0. Analogous to the creep function, the strain jump is applied abruptly over a very short time interval and is described by the Heaviside function from Eq. (3.2).

$$\varepsilon_0 = \frac{u_0}{L_0} \tag{3.5}$$

In the relaxation test a appruptly strain jump is applied to a specimen (usually a dog-bone specimen) and held constant. The measured force decreases over time during the test. This decrease in force is caused by the internal cross-links in polymers „unknot“.

$$\sigma(t) = \frac{F(t)}{A_0} \tag{3.6}$$

The corresponding function is the relaxation function $E(t)$, cf. Eq. (3.7) and Fig. 3.2.

$$E(t) = \frac{\sigma(t)}{\varepsilon_0} \tag{3.7}$$

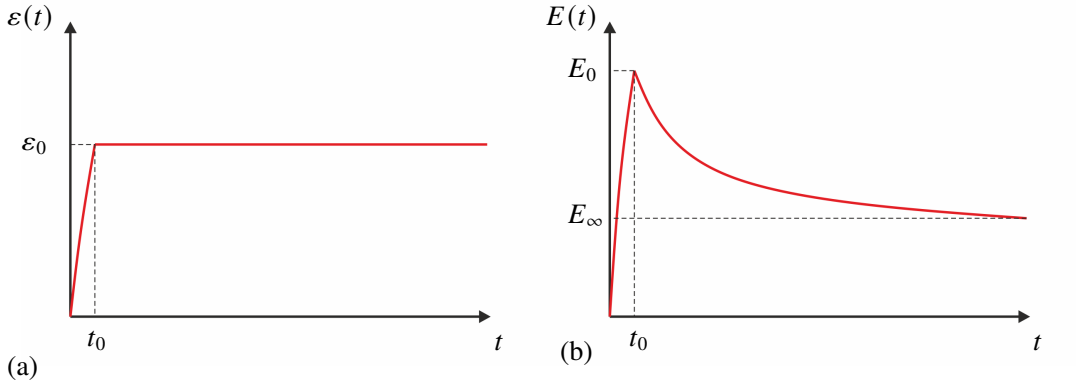

Fig. 3.2 – a) Prescribed strain ε_0 in the relaxation test and b) the resulting relaxation function $E(t)$.

3.2 Rheology

Rheology studies the flow and deformation of materials under applied forces or stresses [Tanner and Walters 1998]. It is a branch of physics that focuses on understanding how materials respond to external forces and how their internal structure and properties affect their deformation behavior. The term rheology originated in 1920 and was established by Professor Eugene C. Bingham and Markus Reiner, who worked at Lafayette College [Gross et al. 2002]. The derivations of this chapter are essentially based on these works and can be read in more detail there.

To model viscoelastic behavior in rheology, one needs the elastic component represented by a spring. This element represents a Hookean body, which undergoes elastic deformation under load and returns to its original shape upon unloading, cf. Eq. (3.8). Viscoelastic materials, however, exhibit a time-dependent recovery upon unloading. This behavior is described by a damper (Newtonian body), cf. Eq. (3.9). By itself, a damper mimics the behavior of a fluid. The damper is represented by a moving piston containing a fluid with a dynamic viscosity η.

$$\sigma_H = E\,\varepsilon \tag{3.8}$$

$$\sigma_N = \eta\,\dot{\varepsilon} \tag{3.9}$$

Here the index „H“ stands for the Hooke element and the index „N“ for the Newtonian element. The properties of both elements are combined to describe viscoelastic material behavior. The two elements can be combined either in series (Maxwell model) or in parallel (Kelvin-Voigt model), see Fig. 3.3

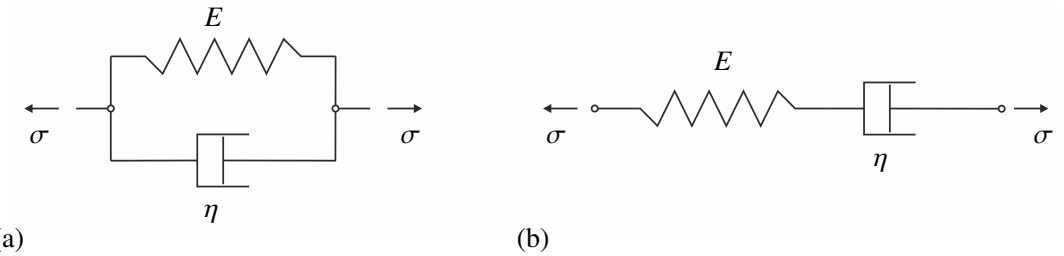

(a) (b)

Fig. 3.3 – Different models of rheology: a) Kelvin-Voigt model and b) Maxwell model.

3.2.1 Maxwell model

In the Maxwell model, the stress applied to both elements is equal. The strain is distributed between the two elements (cf. Eq. (3.10), Eq. (3.11) and Fig. 3.3 b):

$$\sigma = \sigma_H = \sigma_N \tag{3.10}$$

$$\varepsilon = \varepsilon_H + \varepsilon_N \tag{3.11}$$

Differentiating Eq. (3.11) with respect to time, one obtains:

$$\dot{\varepsilon} = \dot{\varepsilon}_H + \dot{\varepsilon}_N \tag{3.12}$$

Turning Eq. (3.8) to ε, differentiate it with respect to time, and insert this form as well as Eq. (3.9) into Eq. (3.12) we get:

$$\dot{\varepsilon} = \frac{\dot{\sigma}}{E} + \frac{\sigma}{\eta} \tag{3.13}$$

Introducing the relaxation time τ, Eq. (3.13) can be written as follows:

$$\sigma + \tau\,\dot{\sigma} = \eta\,\dot{\varepsilon} \qquad \text{with} \qquad \tau = \frac{\eta}{E} \tag{3.14}$$

Inserting the Heavyside function $\sigma(t) = \sigma_0\,H(t)$ into Eq. 3.14, we get for $\dot{\sigma}(t \geq 0) = 0$:

$$\dot{\varepsilon} = \frac{\sigma_0}{\eta} \tag{3.15}$$

By integrating Eq. (3.15) we get:

$$\varepsilon(t) = \frac{\sigma_0}{\eta}\,t + C \tag{3.16}$$

Using the initial condition $\varepsilon(0) = \sigma_0/E = C$ we get:

$$\varepsilon(t) = \sigma_0 \left(\frac{1}{E} + \frac{t}{\eta}\right) \tag{3.17}$$

With $J(t) = \varepsilon(t)/\sigma_0$ the creep function for the Maxwell model is:

$$J(t) = \frac{1}{E}\left(1 + \frac{t}{\tau}\right) \tag{3.18}$$

If a constant strain jump $\varepsilon = \varepsilon_0\,H(t)$ is specified, the relaxation function $E(t)$ can be determined. Inserted into Eq. (3.14), the derivative $\dot{\varepsilon} = 0$ results from the constant strain $\varepsilon = const.$:

$$\sigma + \tau\,\dot{\sigma} = 0 \tag{3.19}$$

The exponential approach for the homogeneous differential equation from Eq. (3.19) yields:

$$\sigma(t) = C\ \exp(\lambda\, t) \qquad \text{with} \qquad \lambda = -\frac{1}{\tau} \tag{3.20}$$

The initial condition $\sigma(0) = E\,\varepsilon_0 = C$ yields:

$$\sigma(t) = \varepsilon_0\, E\ \exp\left(-\frac{t}{\tau}\right) \tag{3.21}$$

$E(t) = \sigma(t)/\varepsilon_0$ represents the relaxation function for the Maxwell model:

$$E(t) = E\ \exp\left(-\frac{t}{\tau}\right) \tag{3.22}$$

3.2.2 Kelvin-Voigt model

The spring and damper elements are connected in parallel in the Kelvin-Voigt body, see Fig. 3.3 a). Accordingly, the applied stress is distributed to both elements, cf. Eq. (3.23). In contrast, the strain of both elements is always the same, Eq. (3.24).

$$\sigma = \sigma_H + \sigma_N \tag{3.23}$$

$$\varepsilon = \varepsilon_H = \varepsilon_N \tag{3.24}$$

The derivative of Eq. (3.24) with respect to time yields:

$$\sigma = E\,\varepsilon_H + \eta\,\dot{\varepsilon}_N \tag{3.25}$$

The stress jump is represented by the Heaviside function:

$$\sigma = \sigma_0\, H(t) \tag{3.26}$$

For $t > 0$, the material law from Eq. (3.25):

$$\varepsilon + \tau\,\dot{\varepsilon} = \frac{\sigma_0}{E} \tag{3.27}$$

Here, the exponential approach to solving the differential equation is used again. However, in the Kelvin-Voigt model, the overall solution consists of a homogeneous and a particular solution.

$$\varepsilon = \underbrace{C\ \exp(-\frac{t}{\tau})}_{\varepsilon_{\text{hom}}} + \underbrace{\frac{\sigma_0}{E}}_{\varepsilon_{\text{part}}} \tag{3.28}$$

By inserting the initial condition $\varepsilon(0) = 0$ we get $C = -\sigma_0/E$ as homogeneous solution:

$$\varepsilon(t) = \frac{\sigma_0}{E}\left(1 - \exp\left(-\frac{t}{\tau}\right)\right) \tag{3.29}$$

$$\dot{\varepsilon}(t) = \frac{\sigma_0}{\eta}\exp\left(-\frac{t}{\tau}\right) \tag{3.30}$$

Thus, $J(t) = \varepsilon(t)/\sigma_0$ represents the creep function for the Kelvin-Voigt model:

$$J(t) = \frac{1}{E}\left(1 - \exp\left(-\frac{t}{\tau}\right)\right) \tag{3.31}$$

The Kelvin-Voigt model cannot realize a relaxation function, so it plays only a minor role in this work.

3.2.3 Linear standard body

Linear standard bodies are combinations of the two basic models presented above. These can be arranged in series or parallel. By combining the models, viscoelastic behavior can be described. Here, the linear standard body, in the form of a parallel connection of a Hookean body and a Maxwell body (index M), will be examined in more detail.

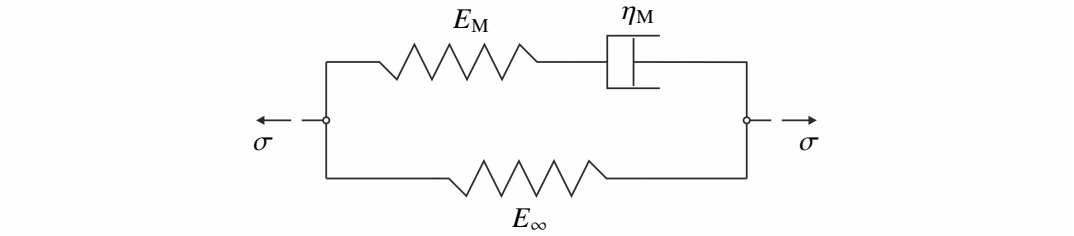

Fig. 3.4 – Parallel connection of Maxwell body and Hooke's body: linear standard body.

This linear standard body in Fig. 3.4 is named by the English physicists John Henry Poynting and Joseph John Thomson (Poynting-Thomson model). In this model, the differential equation can be written as follows ($\sigma = \sigma_H + \sigma_M$):

$$\frac{1}{\eta_M}\sigma + \frac{1}{E_M}\dot{\sigma} = \frac{E_\infty}{\eta_M}\varepsilon + \frac{E_M + E_\infty}{E_M}\dot{\varepsilon} \tag{3.32}$$

By superposing the stresses of both bodies, we obtain the relaxation function $E(t)$ for the Poynting-Thomson model:

$$E(t) = E_\infty + E_M \exp\left(-\frac{t}{\tau}\right) \tag{3.33}$$

The Hookean body specifies the stiffness for $t \to \infty$. Therefore, E_∞ is also called the equilibrium modulus. For $t = 0$, the instantaneous modulus of elasticity results, which decreases over time due to the damping element in the Maxwell body and approaches the equilibrium modulus, see Eqs. (3.34) and (3.35).

$$E(t \to \infty) = E_\infty \tag{3.34}$$

$$E(t = 0) = E_\infty + E_\mathrm{M} \tag{3.35}$$

All models discussed in this section assume incremental strain changes. As a result, they describe material behavior within the framework of linear viscoelasticity, assuming small deformations and a linear relationship between stresses and strains. This enables analytically manageable modeling but, at the same time, limits the models' scope of application to load scenarios in which nonlinear effects can be neglected.

3.2.4 Maxwell group

The Maxwell group, or generalized Maxwell model, is a parallel connection of n Maxwell elements. By adding a Hookean element in parallel, this circuit models a solid. A parallel Newtonian element is included in such circuits in many representations of the generalized Maxwell model. However, this would simulate an infinitely high stiffness when applying a strain jump, which is why it is omitted in many cases, as is the case here (see Fig. 3.5).

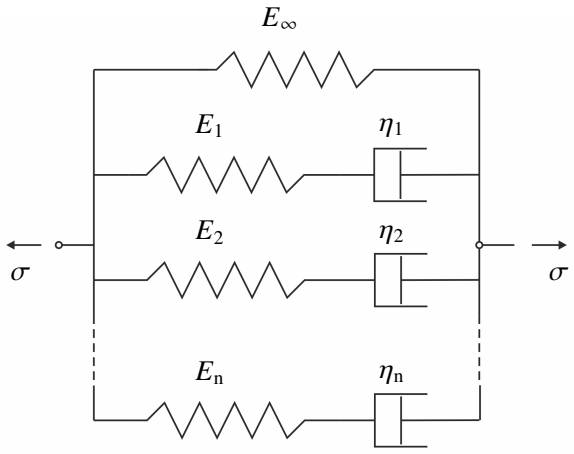

Fig. 3.5 – Maxwell group with n elements.

The relaxation times of molecular chains differ depending on their length. This means that polymers do not have a single relaxation time but a spectrum of relaxation times, cf. [Roylance 2001]. These relaxation times can be accounted for by the Maxwell group model. Eq. (3.36) is called the Prony series. It contains $2n + 1$ parameters corresponding to the number of Maxwell elements.

$$E(t) = E_\infty + \sum_{i=1}^{n} E_i \exp(-\frac{t}{\tau_i}) \qquad \text{with} \qquad \tau_i = \frac{\eta_i}{E_i} \tag{3.36}$$

3.3 Specimen design and printing orientation

DIN EN ISO 527/2 [DIN 1996] is used for the specimen design in this work. This standard specifies the speeds for the tensile test. Due to the printer's build space, specimen type 5A is used, see Fig. 3.6 and Table 3.1.

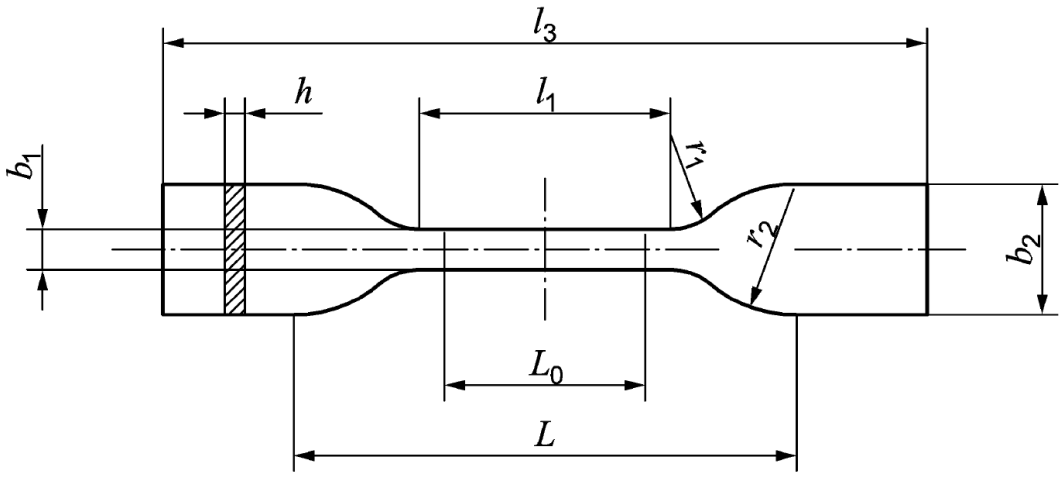

Fig. 3.6 – Dog-bone specimen (type: 5A), DIN EN ISO 527/2.

Table 3.1 – Dimensions of the specimen type: 5A, DIN EN ISO 527/2 (translated to English).

		specimen type 5A [mm]
l_3	overall length	≥ 75.0
b_2	width at the ends	12.5 ± 1.0
l_1	length of the tight parallel part	25.0 ± 1.0
b_1	width of the tight part	4.0 ± 0.1
r_1	small radius	8.0 ± 0.5
r_2	large radius	12.5 ± 1.0
L	initial distance between clamps	50.0 ± 2.0
L_0	measuring length	20.0 ± 0.5
h	thickness	2.0 ± 0.2

To determine the Young's modulus, according to DIN EN ISO 527/2, a test speed must be set corresponding to a strain rate of 1% min^{-1}. The strain rate corresponds to the ratio of the test speed and the distance L_0 between the clamps of the tensile machine when the specimen is clamped:

$$\frac{v_{\text{test}}}{L_0} = \dot{\varepsilon} \tag{3.37}$$

For the Type 5A specimen, this results in a test speed of v_{test} = 0.5 mm/min. The tensile tests are carried out until the specimen fails.

Printing orientation

Since 3D-printed specimens exhibit orientation, it is reasonable to assume that there is no isotopic behavior. The orientation is clearly the case for additively manufactured materials using FDM processes due to the very coarse layers. There are different reports regarding the SLA process. Some sources assume that SLA-printed and DLP-printed samples are considered isotropic and homogeneous with sufficient post-processing [Naik and Kiran 2018]. Other publications document that the print orientation plays a significant role in the mechanical properties [Saini et al. 2020] and that the material is therefore not homogeneous. For this reason, the effect of the print orientation on the mechanical behavior of the samples will be investigated for the materials used in this work. Depending on the positioning of the specimen on the printing platform, an angle results between the layer direction and the subsequent tensile load. Seven different layer angles were investigated in this work (0° to 90° in 15° subdivisions). Since in both the SLA and DLP processes the layer is always created at the bottom of the tank, the specimens for the printing process are arranged differently in the build space in order to realize different angles of the layer generation, see Fig. 3.7.

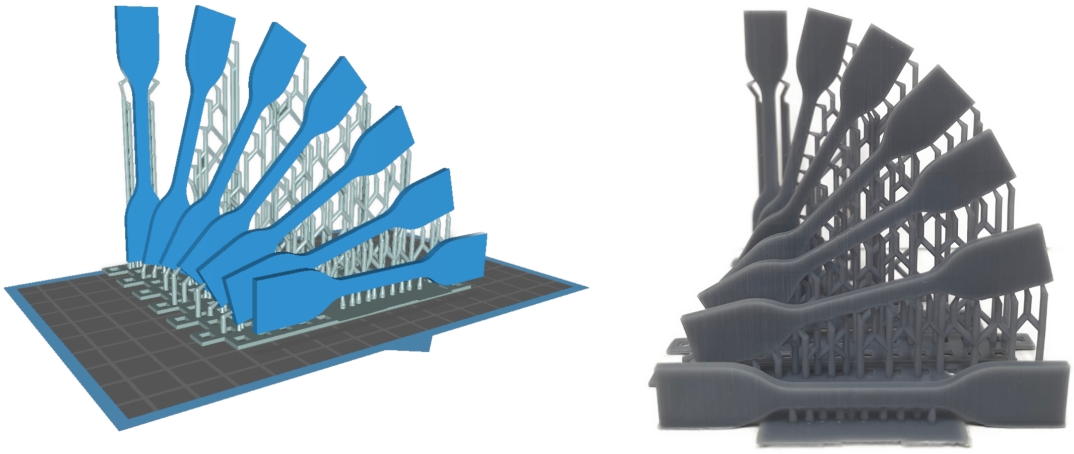

Fig. 3.7 – Printing angles with respect to loading direction: from front to back: 0°, 15° 30°, 45°, 60°, 75°, 90°.

In Fig. 3.7, the support structures mentioned in Chapter 2 are shown. These serve to support the actual specimen structures during the actual printing process. After the print is finished, the specimens are cleaned by an isopropanol bath. The washing station from ELEGOO has a rotating paddle wheel on the floor. The rotation of the paddle wheel creates a vortex in the isopropanol bath, which separates the samples particularly well from liquid resin residues. The

specimens are then cured under appropriate UV light with a wavelength of 405 nm. After removing the support structures, any remaining residue has to be removed with sandpaper.

3.4 Experiments

The universal testing machine Inspekt Duo 5 from Hegewald & Peschke is used for the tensile tests. It is equipped with a load cell with a capacity of up to 2 kN. The machine allows test speeds from 0.8 μm/min up to 1200 mm/min and a crosshead speed resolution of $< 0.025\,\mu$m. Fig. 3.8 shows the machine's setup in the laboratory of the chair for solid mechanics at the University of Siegen. Screw clamps with pyramid-shaped surfaces securely hold the specimens in place. The installed load cell is suitable for loads of up to 2 kN, which is sufficient for the quasi-static tensile tests. In all tests, time, stress, strain, force, position, and displacement are recorded at a sampling rate of 50 Hz by default. Based on the previously implemented specimen geometry, the stresses are calculated in the LabMaster software. The technical strain is calculated using the measuring length L_0 and the corresponding crosshead displacement of the machine:

$$\varepsilon = \frac{\Delta l}{L_0} \tag{3.38}$$

The system creates a test report as a .txt file and can then be further processed with Matlab.

3.4.1 Statistical evaluation of the experiments

For the investigations in this work, five tests were conducted for each printing orientation to obtain a statistically reliable evaluation. The constant test speed was 0.5 mm/min and continued until the specimen failed. The test speed thus complies with the specifications of DIN EN ISO 527-2, which specifies a strain rate of 1%/min. The sudden drop in force stops the machine and ends the measurement.

First, the arithmetic mean of all calculated values from all tests in each group of the same printing orientation is determined. Here n represents the number of specimens.

$$\bar{x} = \frac{1}{n} \sum_{i=1}^{n} x_i \tag{3.39}$$

Furthermore, the variance σ_{var}^2 and the standard deviation σ_{var} are calculated.

$$\sigma_{\text{var}}^2 = \frac{1}{n-1} \sum_{i=1}^{n} (x_i - \bar{x})^2 \tag{3.40}$$

$$\sigma_{\text{var}} = \sqrt{\frac{1}{n-1} \sum_{i=1}^{n} (x_i - \bar{x})^2} \tag{3.41}$$

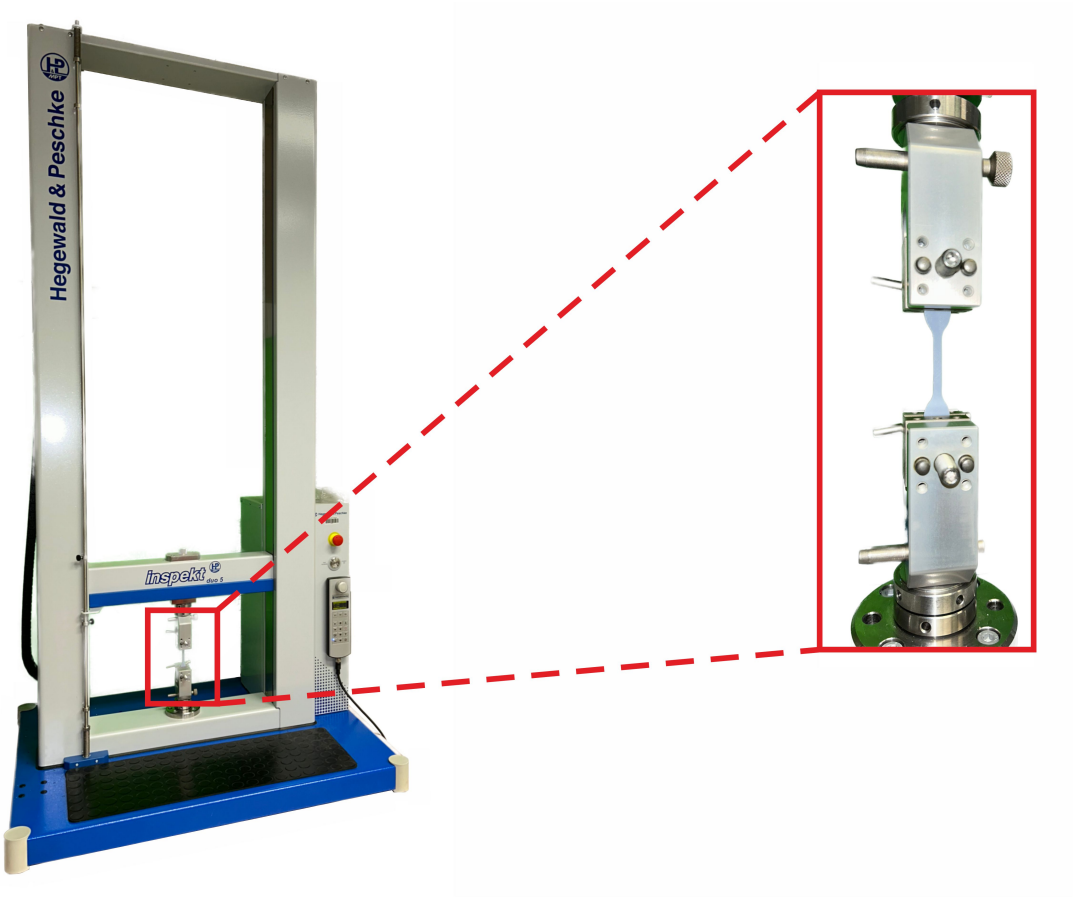

Fig. 3.8 – Universal testing machine Inspekt Duo 5 from Hegewald & Peschke with a close-up of the screw clamps with a dog bone specimen made of 3D Materials SuperFlex.

The Student's t-distribution, or t-distribution, is a probability distribution frequently used in statistics. This distribution is primarily used when the number of specimens is relatively small (typically $n < 30$) and the population standard deviation is unknown. It is bell-shaped and symmetric about the origin, similar to the normal distribution. However, it has larger tails, so the values are further from the mean than the standard normal distribution. The shape of the t-distribution is influenced by the degrees of freedom, which usually relate to the number of specimens. For n specimens, the t-distribution has $n - 1$ degrees of freedom. As the degrees of freedom increase, the t-distribution approaches the standard normal distribution. A confidence level of 95% is used for the measurements to determine the statistical error. Using n specimens, a number of $n - 1$ degrees of freedom, and the 97.5% quantile $t_{0.975}$, t can be calculated or read from the t-distribution table. This value can be used to determine the limits of the confidence interval.

$$I = \left[\bar{x} - t_{0.975} \frac{\sigma_{\text{var}}}{\sqrt{n}} \quad ; \quad \bar{x} + t_{0.975} \frac{\sigma_{\text{var}}}{\sqrt{n}} \right] \tag{3.42}$$

The probability P that the expectancy value μ is part of the corresponding interval is 95%.

$$P\left(\bar{x} - t_{0.975}\frac{\sigma_{\text{var}}}{\sqrt{n}} \quad < \quad \mu \quad < \quad \bar{x} + t_{0.975}\frac{\sigma_{\text{var}}}{\sqrt{n}}\right) = 0.95 \tag{3.43}$$

3.4.2 Uniaxial tensile test

Two investigated materials, printed at seven different print orientations, each orientation five times resulted in a test setup of 70 tests.

Fig. 3.9 shows the measured curves for the different printing orientations mad of Anycubic Tough 2.0. The thin error band indicates a good and uniform print quality and has a significance level of 95%.

To allow a better comparison of the different print orientations and the stress-strain behavior, Fig. 3.10 a) only the mean values of the respective specimens without error band are plotted. The curves indicate that the printing orientation has a significant influence on material behavior.

Three different groups of stress-strain curves can be roughly identified from the seven printing orientations investigated. The specimens with printing orientations of 60°, 75°, and 90° can be summarized very nicely. The investigations show that all three curves agree very well, with hardly any differences detectable between the different printing orientations. The initial increase in stress is lowest in these specimens and thus yields the lowest measured modulus of elasticity. On the other hand, these specimens exhibit the highest strain of all tested orientations before the specimens fail. Failure only occurs between strains of 31% and 35%.

The second group consists of specimens with printing orientations of 15° and 30°. Here too, the two averaged curves show a very high degree of agreement in the stress-strain behavior. The curves show a stronger increase at the start of the test, but already fail at a strain of approximately 20%.

The third group consists of specimens with the print orientations 0° and 45°. Both show a strong increase in the initial slope, but differ in terms of their failure strain and maximum stress. In contrast to the other orientations, a plateau follows the initial increase in stress in the specimens. However, this plateau is only maintained for a slight further elongation by the specimen with a printing orientation of 0° before the specimen fails. Thus, although this structure exhibits a strong increase and high stress in contrast to the other specimens, it can only withstand low strains. So, the specimen with a printing orientation of 0° has the lowest failure strain of approximately 11%. The specimens with printing orientations of 45° show a pronounced plateau phase, followed by a further increase in stress. However, this increase in stress leads to failure at an elongation of approximately 25% and a stress of $\sigma = 20$ MPa.

The calculated moduli of elasticity were determined from the mean curves and are shown in Fig. 3.10 b). The elastic moduli show correspondingly different values, whereby the specimens with the same print orientations can be summarized here due to the similar initial behavior, see

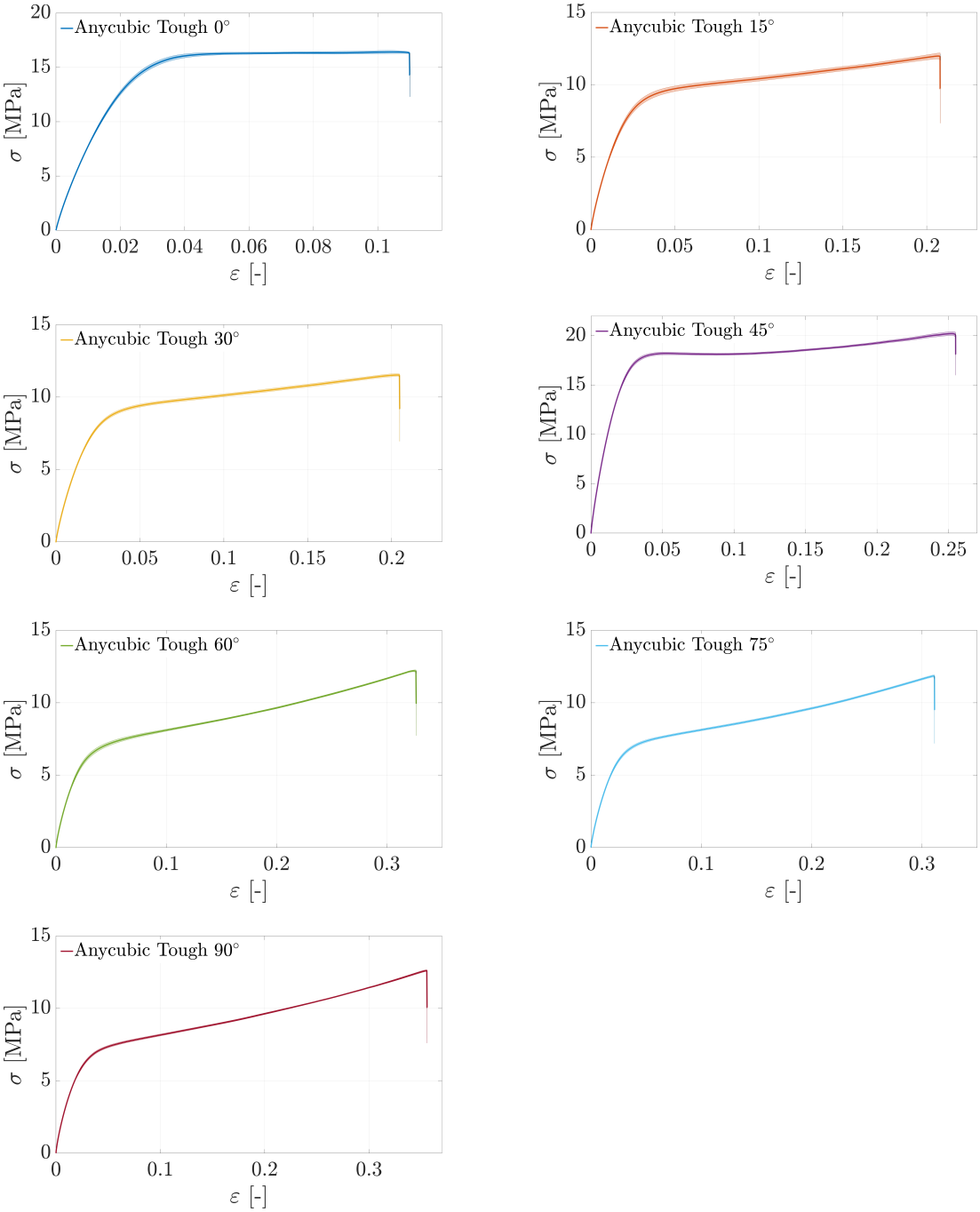

Fig. 3.9 – Tension test measurement according to DIN EN ISO 527/2 for Anycubic Tough 2.0 for different printing orientations.

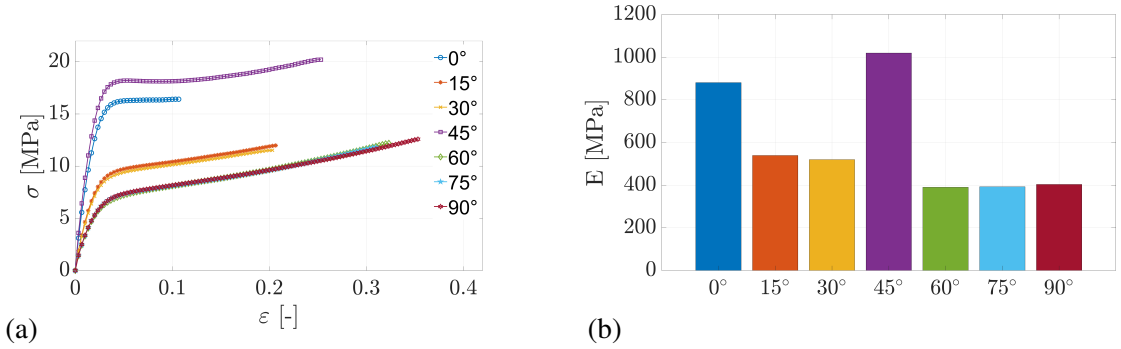

Fig. 3.10 – Comparison of the mean curves of specimen made of Anycubic Tough 2.0 with different printing orientations: a) stress-strain behavior and b) the determined modulus of elasticity.

Table 3.2. The determined modulus of elasticity depends significantly on the print orientation with respect to the direction of loading. The moduli of elasticity determined here were measured in the first slope of the stress-strain curves up to a strain of 0.5%. The values specified by the manufacturer for the modulus of elasticity of $E = 800 - 1200$ MPa are achieved with a print orientation of 45°, but differ considerably from those of the manufacturer in the other printing orientations.

The material 3D-Materials SuperFlex shows a much less strong dependence on the printing orientation than the material Anycubic Tough 2.0, see Fig. 3.11. The stress-strain behavior shows an almost linear behavior until failure. Although the material is a very soft TPU-like material, its stress-strain behavior exhibits a rather unexpected linear progression. The exposure time or intensity and the post-curing process significantly influence the degree of cross-linking. By adjusting these parameters, it is possible to produce a less cross-linked material with non-linear stress-strain behavior. The parameters in this work were selected according to Table 2.2 in order to print stable, complex structures from the materials, which were not possible to print with shorter exposure times and led to misprints.

Fig. 3.11 shows that only slight fluctuations occur within the groups of equal printing orientations. For all specimens strains between 25% and 30% were achieved. Independently of the printing orientation, all specimens exhibit a similar linear stress-strain curve.

Fig. 3.12 a) shows all mean value curves of the different 3D-Materials SuperFlex specimens without the corresponding error bands. Here it becomes very clear that the printing orientation is a much smaller influencing factor on the stress-strain behavior than with the material Anycubic Tough 2.0. The scatter of the results is very low, especially in the initial slope. Accordingly, the modulus of elasticity shows less fluctuations, cf. Fig. 3.12 b).

Due to the linear stress-strain curve, the modulus of elasticity for the material 3D-Materials SuperFlex could be determined more easily in the configuration printed in this work than in the case of a strongly non-linear curve. Table 3.2 shows the determined moduli of elasticity as numerical values.

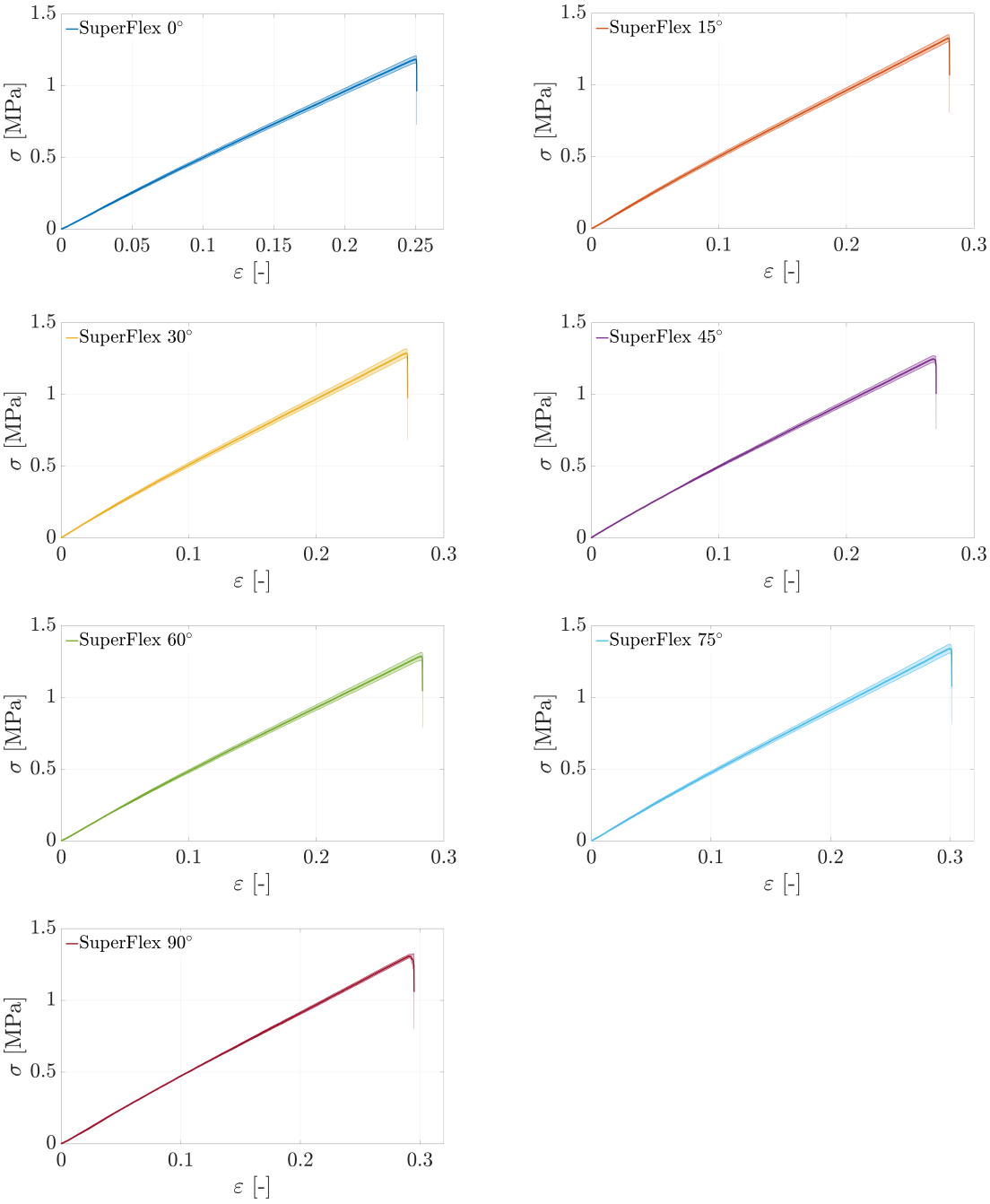

Fig. 3.11 – Tension test measurement according to DIN EN ISO 527/2 for 3D-Materials SuperFlex for different printing orientations.

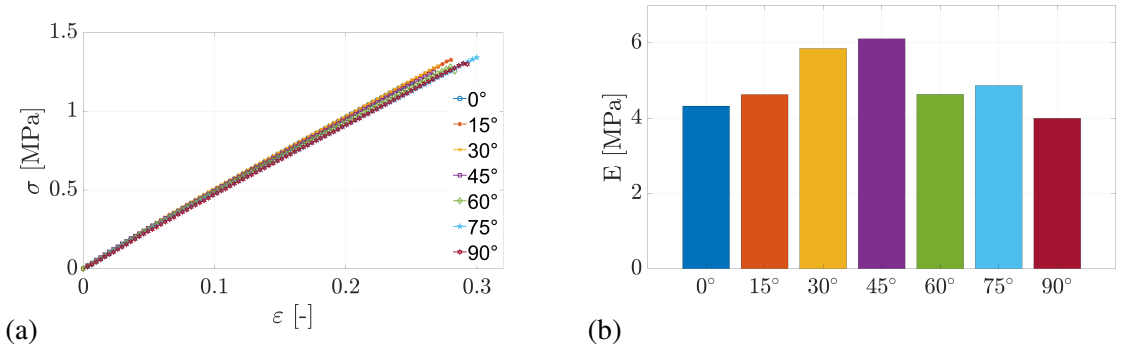

Fig. 3.12 – Comparison of the mean curves of specimen made of 3D-Materials SuperFlex with different printing orientations: a) stress-strain behavior and b) the determined modulus of elasticity.

For the materials tested, the highest stiffness is observed at a print orientation of 45°. The reasons for this are the mixed type of load applied to the specimen. When the load is applied parallel to the print orientation, delamination of the layers occurs. This delamination leads to rapid failure of the specimens. Although a print orientation orthogonal to the load direction exhibits a higher modulus of elasticity than other print directions; a print orientation of 45° seems to be the most stable print orientation. With this configuration, there is no load dominance due to delamination or shearing of the individual layers in the specimen.

Table 3.2 – Modulus of elasticity for specimen with different printing orientations.

printing orientation	Anycubic Tough 2.0 E [MPa]	3D-Materials SuperFlex E [MPa]
0°	880.7	4.3
15°	539.2	4.6
30°	519.8	5.8
45°	1019.3	6.1
60°	390.2	4.6
75°	392.7	4.8
90°	403.5	4.0

3.4.3 Relaxation test

In addition to the uniaxial tensile tests, relaxation tests were conducted on the investigated materials. The spindle drive of the tensile machine used makes it advantageous from a control point of view to apply and then maintain a predetermined strain. For this reason, the relaxation test is chosen to determine the viscoelastic parameters in our test setup. Since there is no valid

standard for the relaxation test, the test was carried out using the same specimen geometry as the classic tensile test.

Because of the different materials, different values are applied for the rapid strain. Due to its TPU-like material properties, 3D Materials SuperFlex can withstand higher strains than the acrylic-like Anycubic Tough 2.0 by applying rapid strains. Accordingly, different strain jumps were defined for both materials in the relaxation test; a strain jump of 5% was applied to Anycubic Tough 2.0, while a strain jump of 10% was applied to 3D-materials SuperFlex. Due to the low strains of 5% and 10%, respectively, linear viscoelastic material behavior can be assumed. In this strain range, the relationship between stress and strain is approximately linear, allowing the time-dependent material response to be described by a Prony series. The Prony series is examined in more detail in Section 3.4.4.

After clamping the specimen and starting the test program, the crosshead is moved up at a low speed of 3 mm/min until the set preload of 0.01 N is reached. The suddenly applied strain of 5%, respectively 10%, is applied by moving the crosshead up at a high velocity of 300 mm/min. The strain is then held for 600 seconds. At the constant strain, the internal stress decreases over time due to viscoelastic relaxation, corresponding to a decrease of the relaxation modulus toward the equilibrium modulus E_∞.

The specimens were tested with different print orientations in the relaxation experiment to identify any orientation-dependent effects. To ensure statistical validity, five specimens per print orientation were tested and analyzed following the same procedure as in the tensile tests.

The relaxation curves of Anycubic Tough 2.0 in Fig. 3.13 show a very thin error band with correspondingly low error dispersion of the measurement results of each group of printing orientation. This slim error band indicates high precision, accuracy, and reproducibility of the determined measurement results. The curves show a very similar progression across all print orientations. Only the specimens with a print orientation of 0° showed a lower equilibrium value E_∞. The beginning of the relaxation curve shows a steeper decrease, which explains this lower final equilibrium value.

Deviations in relaxation tests with 3D-Materials SuperFlex within a measurement series for the same print orientation show a slightly wider error band than those with Anycubic Tough 2.0. Across all print directions for 3D-Materials SuperFlex, differences in relaxation behavior are minimal. This is supported by the similar Prony coefficients in Table 3.4. Thus, the viscoelastic behavior of 3D-Materials SuperFlex can be considered largely independent of print orientation.

3.4.4 Viscoelastic material model

As descibed before a common method for representing linear viscoelastic behavior is the Prony series, which approximates the relaxation modulus as the sum of exponential decay functions, see Eq. (3.7). This mathematical formulation is particularly useful for implementation in finite

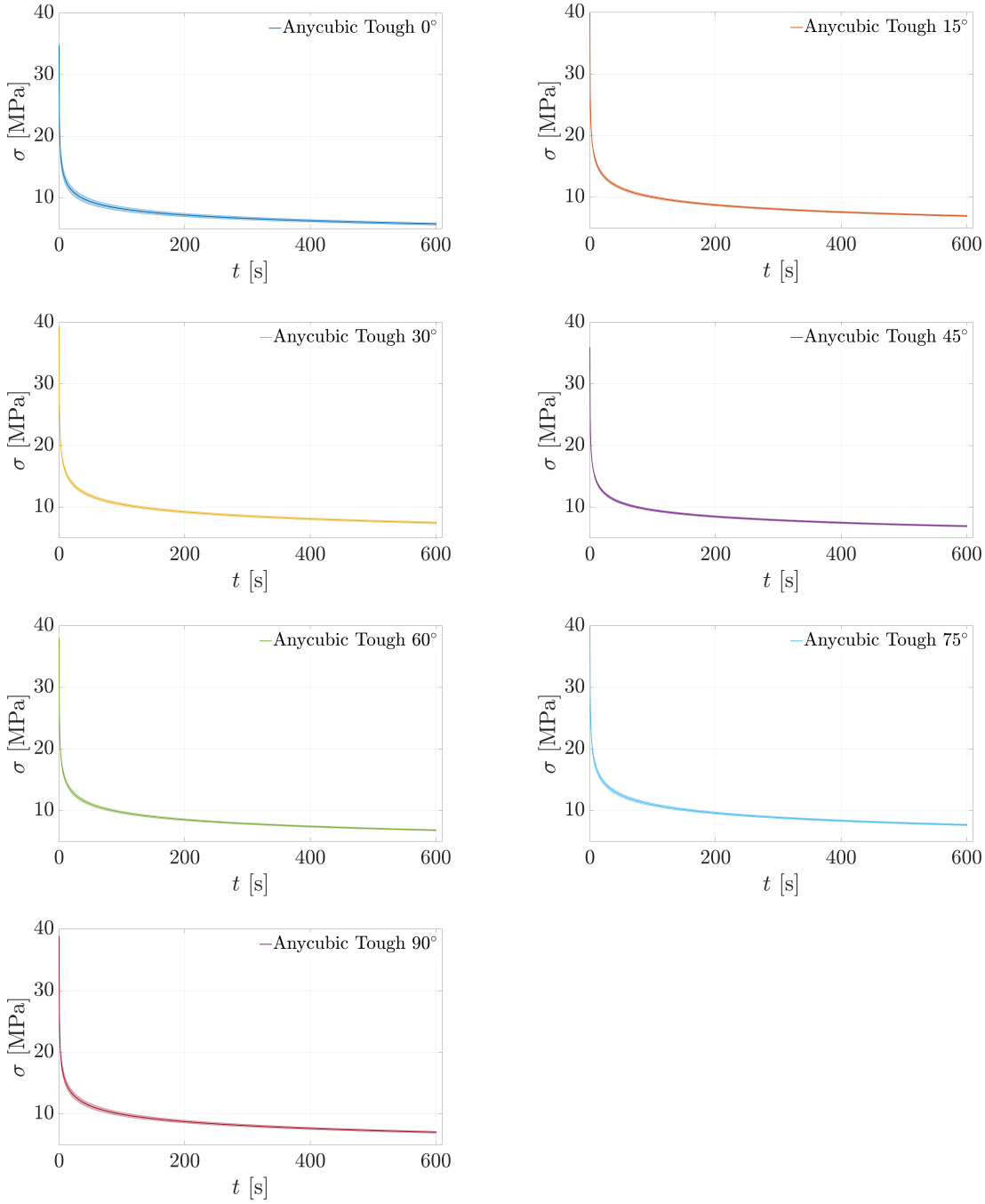

Fig. 3.13 – Relaxation test measurement of Anycubic Tough 2.0 for different print orientations at an applied strain of 5%

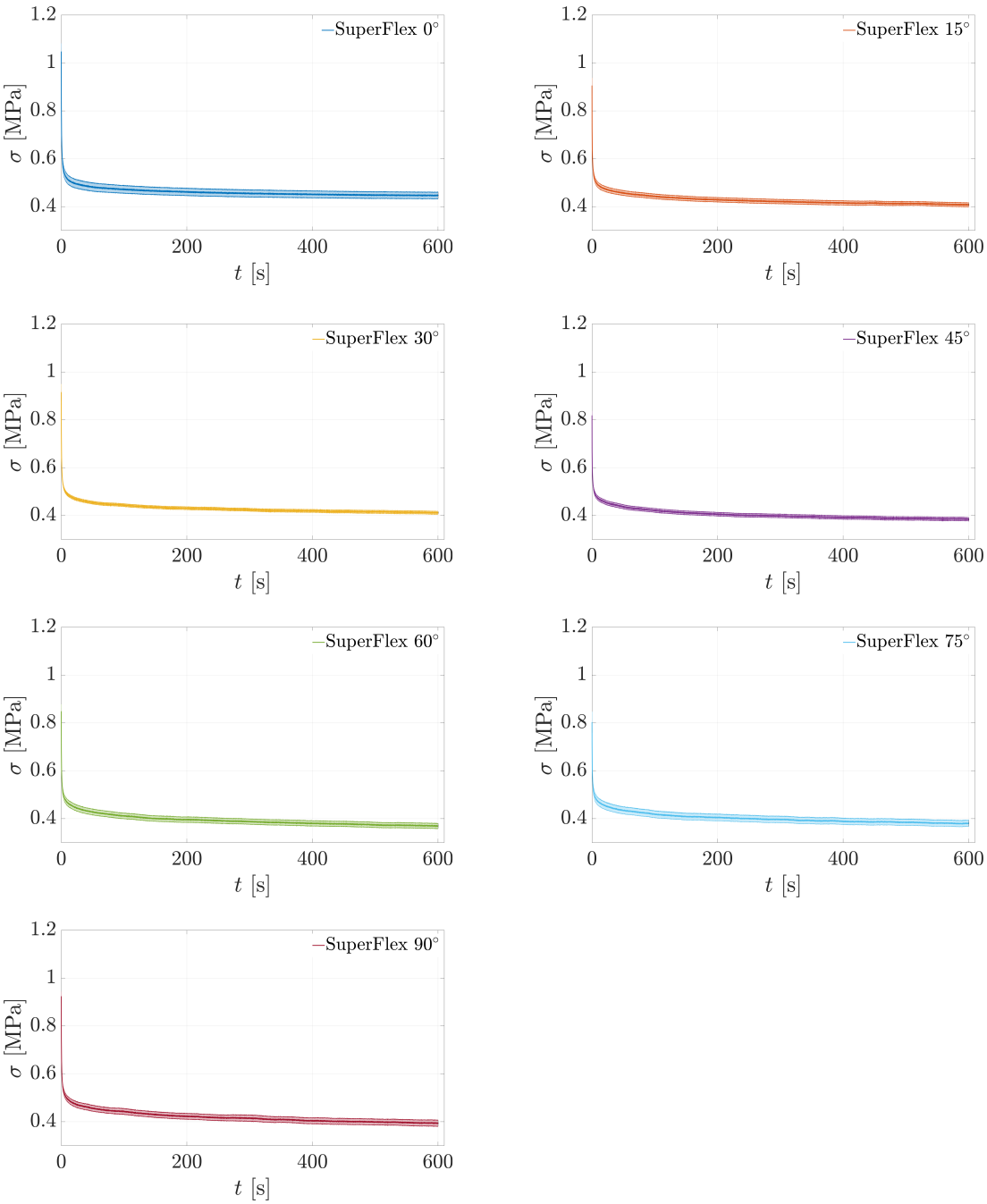

Fig. 3.14 – Relaxation test measurement of 3D-Materials SuperFlex for different print orientations at an applied strain of 10%

element simulations, as it enables precise prediction of material behavior under various loading conditions. In this study, relaxation experiments are performed and fitted using a Prony series representation to determine the time-dependent behavior of the investigated materials. Four prony elements are sufficient to describe the relaxation process with adequate accuracy.

As already mentioned, the viscoelastic behavior of the two structures examined is largely independent of print orientation. In ABAQUS, viscoelastic behavior is described by the shear modulus. Accordingly, the Prony coefficients must be adjusted. The linear relationship between the elastic modulus and the shear modulus for isotropic material is generally described by the following relationship:

$$G = \frac{E}{2(1+\nu)}. \tag{3.44}$$

Due to the independence of the print orientation of the materials examined and the assumed isotropic behavior with regard to linear viscoelasticity, the formulation of the normalized Prony coefficients required by ABAQUS can be carried out as follows:

$$g_i = \frac{G_i}{G_0} = \frac{\frac{E_i}{2(1+\nu)}}{\frac{E_0}{2(1+\nu)}} = \frac{E_i}{E_0} \tag{3.45}$$

The Prony series is represented by the Maxwell group from Section 3.2.4 added by a parallel spring element (E_∞) and Eq. (3.36), see Eq. (3.46).

$$g(t) = \frac{E_\infty}{E_0} + \sum_{i=1}^{n} g_i \exp(-\frac{t}{\tau_i}) \qquad \text{with} \qquad E_0 = E(t=0) \tag{3.46}$$

The Tables 3.3 and 3.4 show the Prony coefficients G_i and τ_i. For the implementation in in ABAQUS the G_i needs to be modified by Eq. (3.45). Additional the instantanous relaxation modulus and the equilibrium modulus are listet here.

Table 3.3 – Prony coefficients for Anycubic Tough 2.0 for different print orientations.

			i=1	i=2	i=3	i=4
Tough 2.0 (0°)	E_0	34.6965				
	E_∞	5.3504				
	E_i		4.5444	13.3069	7.6071	3.8876
	g_i		0.1549	0.4534	0.2592	0.1325
	τ_i		28.5750	0.3167	3.6082	275.9587
Tough 2.0 (15°)	E_0	40.7738				
	E_∞	6.4718				
	E_i		5.3115	15.7586	8.4218	4.8101
	g_i		0.1548	0.4594	0.2455	0.1402
	τ_i		29.5965	0.3164	3.7230	267.2557
Tough 2.0 (30°)	E_0	39.4963				
	E_∞	6.9654				
	E_i		5.1389	14.5661	8.1253	4.7006
	g_i		0.1580	0.4478	0.2498	0.1445
	τ_i		29.5460	0.3145	3.7066	274.0782
Tough 2.0 (45°)	E_0	35.5942				
	E_∞	6.4638				
	E_i		4.7101	12.7628	7.5046	4.1529
	g_i		0.1617	0.4381	0.2576	0.1426
	τ_i		27.5928	0.3045	3.5115	277.4795
Tough 2.0 (60°)	E_0	38.0797				
	E_∞	6.3487				
	E_i		5.0237	14.1968	7.9336	4.5769
	g_i		0.1583	0.4474	0.2500	0.1442
	τ_i		29.0733	0.3157	3.6876	272.0284
Tough 2.0 (75°)	E_0	42.1801				
	E_∞	7.1600				
	E_i		5.6192	15.5513	8.6607	5.1889
	g_i		0.1605	0.4441	0.2473	0.1482
	τ_i		29.4119	0.3126	3.6837	267.8200
Tough 2.0 (90°)	E_0	38.8702				
	E_∞	6.5549				
	E_i		5.1035	14.4514	8.1630	4.5974
	g_i		0.1579	0.4472	0.2526	0.1423
	τ_i		29.0269	0.3119	3.6561	273.7691

Table 3.4 – Prony coefficients for 3D-Materials SuperFlex for different print orientations.

			i=1	i=2	i=3	i=4
SuperFlex (0°)	E_0	1.0316				
	E_∞	0.4442				
	E_i		0.0558	0.3021	0.1847	0.0448
	g_i		0.0949	0.5143	0.3145	0.0763
	τ_i		14.7221	0.1338	1.5720	206.5511
SuperFlex (15°)	E_0	0.8772				
	E_∞	0.4045				
	E_i		0.1345	0.2431	0.0415	0.0536
	g_i		0.2845	0.5143	0.0877	0.1134
	τ_i		2.2904	0.1917	31.0352	250.9731
SuperFlex (30°)	E_0	0.9176				
	E_∞	0.4077				
	E_i		0.2596	0.1485	0.0520	0.0497
	g_i		0.5091	0.2913	0.1021	0.0975
	τ_i		0.1503	1.6745	20.9807	263.3590
SuperFlex (45°)	E_0	0.7853				
	E_∞	0.3779				
	E_i		0.0485	0.1941	0.1097	0.0551
	g_i		0.1190	0.4765	0.2694	0.1351
	τ_i		37.5194	0.2025	2.3602	293.6906
SuperFlex (60°)	E_0	0.8091				
	E_∞	0.3402				
	E_i		0.0588	0.2220	0.1120	0.0761
	g_i		0.1254	0.4735	0.2388	0.1622
	τ_i		41.9510	0.2183	2.6973	628.1908
SuperFlex (75°)	E_0	0.7843				
	E_∞	0.3619				
	E_i		0.0509	0.2125	0.0945	0.0644
	g_i		0.1206	0.5032	0.2237	0.1525
	τ_i		41.6206	0.3286	3.1859	468.9996
SuperFlex (90°)	E_0	0.8987				
	E_∞	0.3837				
	E_i		0.0482	0.2566	0.1333	0.0768
	g_i		0.0936	0.4983	0.2589	0.1491
	τ_i		26.2812	0.1882	2.3052	306.0738

CHAPTER 4

MATERIALS UNDER DYNAMIC LOADING

This chapter addresses the material behavior under high strain rate loading, which can differ significantly from the material response observed under quasi-static loading conditions. The split Hopkinson pressure bar (SHPB) experiment constitutes a central aspect of this chapter, as it enables the determination of material properties at high strain rates.

Material properties are usually determined under quasi-static conditions. The conventional tensile test is the common standard test method for determining a stress-strain relationship in materials. Various material parameters can be derived by this test, such as the modulus of elasticity E, the tensile strength R_m, or the yield strength R_e. The required condition to the tensile machine and the specimen geometry are specified mainly in DIN regulations (e.g., DIN ISO 527 for plastics) and can therefore be easily reproduced. The quasi-static nature of tensile testing allows for a precise control of the loading process. Therefore, loading the specimen at a (low) constant strain rate is possible.

The dynamic properties of materials and structures are often of interest in field where material is affected by impact loads. Popular examples include crash tests for cars and human protection systems such as helmets and similar devices. For this reason, products that are exposed to impact loads must be tested under appropriate loading conditions, which require complex test setups such as the SHPB test mentioned above. However, the determination of dynamic parameters is associated with a much higher experimental effort than the static parameter identification under conventional material testing machines. Appropriate standards for conducting such dynamic tests to identify material parameters are sparse. There are many industries like the automotive [Uenishi et al. 2003] and the aerospace instries [Gurusideswar et al. 2022] for which it is essential to know how metals or plastics behave under high strain rates. The development of a wide variety of plastics and composite materials, such as glass fiber reinforced plastics (GFRP), is progressing steadily, and increasingly replacing metals in many

applications. Consequently, knowledge of their dynamic properties is becoming increasingly important in modern mechanical engineering [Kerns 2016].

4.1 High strain rate testing

The strain rate plays a key role in the behavior of materials. Various experimental approaches and test setups are available for investigating materials under high strain rate loadings. Depending on the targeted strain rate regime, different experimental apparatuses are employed, see Fig. 4.1. High strain rates up to $\dot{\varepsilon} = 10^5\,\mathrm{s}^{-1}$ can be achieved using two relatively well-established methods: the rapid rupture method and the split Hopkinson bar (SHB) experiment, cf. [Keuerleber 2006]. For even higher strain rates, flyer-plate impact tests are commonly used. The SHB experiment exists in various configurations, influenced by past and current research. The most common variant is the pressure bar version SHPB. This setup is used for the experiments in this work.

One of the topics of this thesis is the change in the modulus of elasticity and the extend to which it increases with increasing strain rate. This phenomenon is attributed to several physical mechanisms. The inertia of the material mass plays a role in the case of impact loading, which can be neglected under quasi-static conditions. Heat conduction is not possible in the same way as it is at slow deformation. Due to the short time span, part of the deformation energy is converted into heat (adiabatic heating). Time-dependent behavior, such as viscoelasticity or hyperelasticity, becomes significant under certain loading conditions. This is especially true for polymeric materials, where the molecular chains do not have sufficient time to relax. Their restricted mobility leads to an increase in stiffness and an overall stiffening response of the material. Accordingly, polymers or elastomers exhibit significant differences in the modulus of elasticity when considering quasi-static loading and high strain rate loading.

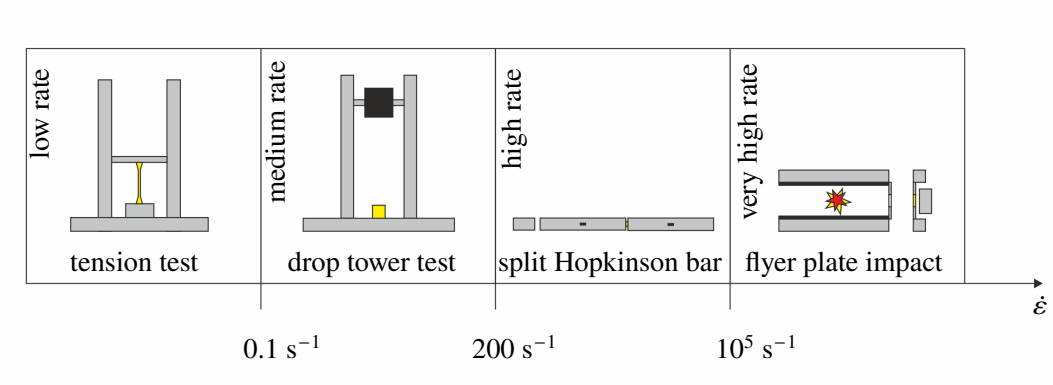

Fig. 4.1 – Strain rate regime and experimental techniques for characterization [Wong et al. 2008].

4.1.1 Historical review of the split Hopkinson pressure bar

The SHPB in its present form goes back to Herbert Kolsky, who established the experiment in 1949, see Fig. 4.2. He was professor of physics at the Brown University. For this reason, the SHPB is also known as Kolsky bar. The pulse generator unit from that time differs from the one used in today's experiments, but the basic setup remains the same. The first experiments in which velocity plays a substantial role in characterizing materials were conducted by the engineer John Hopkinson. His experiments examined the fracture behavior of an iron wire as a function of tensile speed. His son Bertram Hopkinson further developed his father's invention. He was Professor of at the Campbridge University. For more detailed information on the historical background of SHPB, please refer to [Chen and Song 2010; Othman 2018; Xia and Yao 2015].

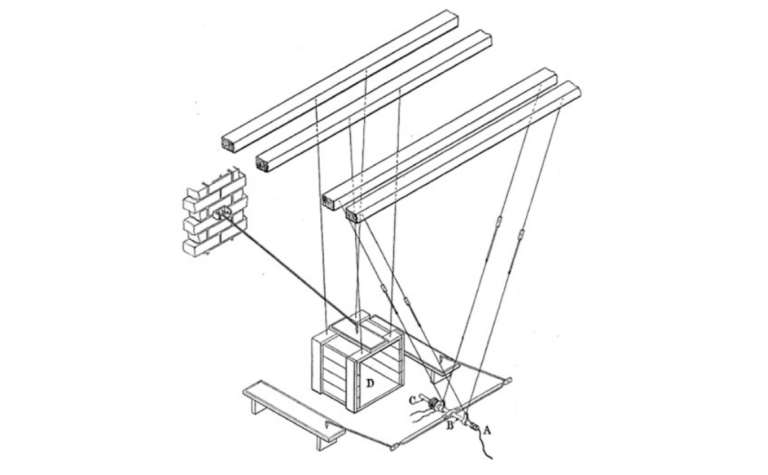

Fig. 4.2 – Original apparatus of Bertram Hopkinson, from [Hopkinson 1914].

4.1.2 Principle of the split Hopkinson pressure bar

Since the SHPB experiment represents a significant part of this thesis, a general overview of the test principle is presented. The basic structure of a SHPB consists of six components, cf. Fig. 4.3:

- accelerator unit (pressure vessel and acceleration tube)
- pulse generator unit (striker)
- incident bar
- specimen
- transmission bar
- data acquisition system (strain gauge and measuring system)

In the SHPB test, two bars (incident and transmission bar) are arranged along an axis, which are held in position by corresponding bearings. Both bars have a circular cross-sectional area

and have usually the same length. The bars have the same diameter and made of the same material. The bar lengths and bar material were adapted to the specific requirements of each experiment. Here, the diameter of the bars always remained at a diameter of $d_b = 20$ mm due to the bearing support.

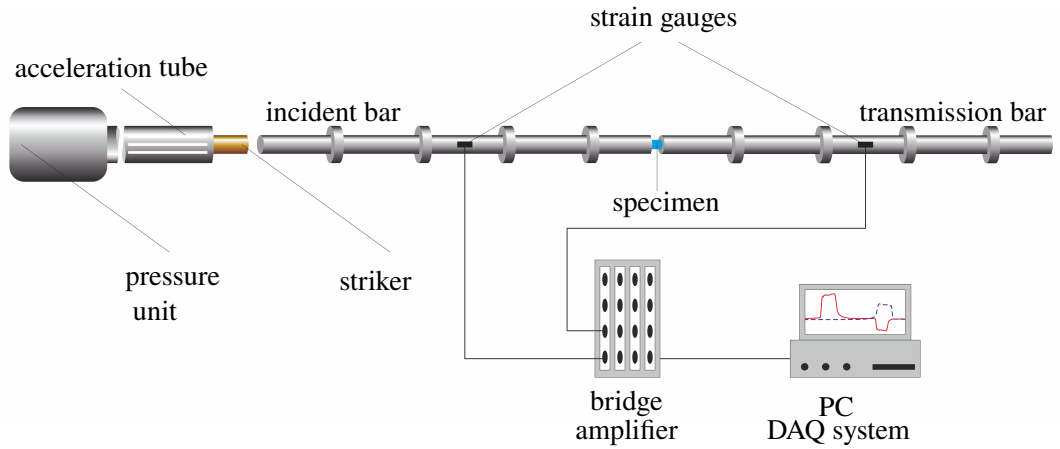

Fig. 4.3 – Schematic of the SHPB apparatus.

In the conventional SHPB test, the specimens are clamped between the two bars. This means that the bars and specimen are already in contact before the actual test has started. The specimen also has a cylindrical shape, but its thickness is many times smaller than that of the bars. The small thickness reduces axial inertial forces within the specimen and allows to treat the specimen like an interface. Furthermore, the diameter of the specimen should usually be chosen smaller than that of the two bars. Since the specimen material has a lower modulus of elasticity than the bar material, the diameter of the specimen increases during the test due to the transverse contraction. The striker is accelerated during the SHPB experiment by a pressure unit. The striker hits the front surface of the incident bar, when the air is released of the pressure unit. The projectile is made of the same material as the bars and has the same diameter. The length of the striker determines the impulse length, whereas the amplitude of the pulse is determined by the velocity of the striker. The specimen material and bar material should not have too high impedance mismatch, otherwise there will be no transfer of the incident pulse into the specimen. In general, the harder a material is, the higher its mechanical impedance. A suitable material pairing of bar and specimen material ensures that part of the incident pulse is reflected at the interface of the incident bar and specimen, whereas a part of the pulse is transmitted into the specimen and the transmission bar, see Section 4.4.1.

The direction of acceleration of the striker is determined by a corresponding acceleration tube, which serves to center the striker. The accerleration tube ensures that the front surface of the striker and the incident bar are parallel. Thus, the impulse can be completely transferred from the striker to the incident bar, cf. [Song et al. 2009]. The impact of the projectile on the incident bar induces an impulse (incident pulse) in the form of a longitudinal wave into

the incident bar. This one-dimensional longitudinal wave travels through the incident bar as an elastic mechanical compression wave. Part of the wave is reflected at the contact surface of the incident bar and specimen. The reflection results from the smaller diameter of the specimen and the impedance mismatch between the specimen and the incident bar materials. The reflected portion travels in the opposite direction through the incident bar. The transmitted wave component passes through the specimen and is partially reflected or transmitted again at its end (interface of specimen and transmission bar). Strain gauges are applied to the bars to record the wave. The incident pulse and the reflected pulse are measured by the strain gauge applicated to the incident bar and a strain gauge applied to the transmitted bar measures the transmitted pulse. These three pulses are important for the subsequent calculation. In the classic SHPB experiment, the strain gauges are attached to the center of both bars. Although the pulses at both surfaces of the specimen are of interest no strain gauges are applicated at the ends of the incident or transmission bar respectivly. This prevents the incident and reflected pulses from overlapping. For the calculations, the incident and reflected pulses must be recorded individually. However, a superposition of incident and reflected pulses is determined when measuring near at the end of the bars. By measuring near the bars ends the two pulses cannot be separated from each other. Therefore, the strain gauges must be placed at a certain distance, usually in the middle of the bars, to detect both pulses separately. Reflections of the mechanical wave also occur at the transitions between the specimen and the transmission bar as well as at the end of the transmission bar. However, this can be neglected during the evaluation, cf. [Korthäuer and El-Magd 2006].

Variants of the split Hopkinson bar

The significance of the SHPB test is largely attributed to the variety of its possible configurations. For this reason, several of these variations are presented in the following. The authors [Ganzenmüller et al. 2019; Miao et al. 2019] use a so-called split Hopkinson tension bar (SHTB) for the experiments. In the SHTB, a flange is attached to the incident bar, which serves as a stop for the striker, which in this setup is represented by a hollow cylinder. The specimen is pulled apart under high strain rates like a tensile machine. Another variant is the direct impact Hopkinson bar (DIHB). In this variant, the incident bar serves as a striker. Using the incident bar as impactor impacting the incident bar, it is possible to generate nearly identical stress waves in both bars, cf. [Jakkula et al. 2021]. [Fíla et al. 2021] goes into more detail about the sub-variants of the DIHB. The SHB is also suitable for dynamic torsion tests; split Hopkinson torsion bar (SHTB). The operation of this variant is described in [Yu et al. 2018]. The authors [Xue et al. 1995] conducted experiments on this concerning the localization and propagation of shear within hot-rolled steel.

4.2 Theoretical background

In this section, basic knowledge of wave propagation in long bars is introduced. The derivation of the one-dimensional wave equation is then presented due to its relevance in the SHPB experiment.

4.2.1 Wave propergation in long bars

First, an overview of wave propagation within the incident and transmission bars is given. Since both bars are manufactured from the same material and have identical dimensions, it is sufficient to derive the wave equation once. Because the bars used in the experimental setup are very long in relation to their cross-sectional area, the one-dimensional wave equation can be applied.

Wave types

The theory of elasticity is based on the reversible deformation of solids. Additionally, the stress and strain are proportional to each other. The speed of wave propagation depends on the material's density and elastic properties. Waves can be divided into several types. These wave types differ in their propagation behavior. First, waves are divided into waves moving in space and on surfaces, cf. [Ortlepp 2006]. Space waves propagate through the interior of solids, whereas surface waves propagate along the surface of objects or media (e.g., waves on the surface of water). Space waves are, in turn, divided into longitudinal waves (P-waves) and transverse waves (S-waves).

Longitudinal and transversal waves

In longitudinal waves, the oscillation amplitude oscillates in the direction of propagation. Primary waves, also known as P-waves, are the fastest type of waves that occur in solids. The principle of wave propagation is based on the compression and drifting apart of particles in the corresponding medium. This means that the wave propagates parallel to the direction of propagation; see Fig. 4.4 b). Transverse waves have an oscillation amplitude that oscillates perpendicular to the direction of propagation; see Fig. 4.4 c). These shear waves are slower than the P-waves. In contrast to longitudinal waves, which can also propagate in liquid media, transverse waves can only move in solid materials. A popular example of a transverse wave is the oscillation of a rope. Here, it becomes clear that the amplitude moves perpendicularly to the direction of propagation.

The longitudinal wave is important in the split Hopkinson pressure bar test. The wave propagates along the axes of the bars through local compression of material points. As the length of the bars is very large compared to the bar cross-section, a one-dimensional wave is assumed here.

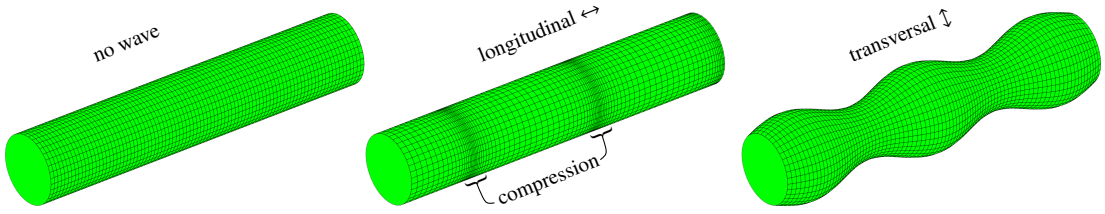

Fig. 4.4 – Illustration of a longitudinal and transversal wave.

Wave propagation speed

One-dimensional wave propagation in bars is fundamental in solid mechanics and wave physics. It describes how mechanical disturbances (such as stress or displacement waves) move along a slender bar, rod, or beam, typically in the longitudinal direction. The basic assumption for onedimensional wave propagation is that the bars are long, so wave propagation is considered along the axial direction. Furthermore, the transverse dimensions must be small compared to the wavelength, and the bars should made of homogeneous isotropic material that allows only small deformations.

4.2.2 Solution of the one-dimensional wave equation

The derivation of the generally one-dimensional wave equation is conveniently carried out using a differentially small element of a bar. Therefore, the second Newtonian law is considered in the formulation of Leonard Euler is used, see Eq. (4.1). The acceleration is represented by the double time derivative of displacement u, whereas m denotes the mass of the considered volume element. Since the approach here is based on one-dimensional theory of wave propagation, only the component in the x direction is needed. The longitudinal wave causes a shortening or lengthening of the bar due to the compression of material points. In a one-dimensional view, the displacement $u(x,t)$ cause force F along the axis.

$$F(x) = m \frac{\partial^2 u}{\partial t^2} \tag{4.1}$$

The mass m is composed of the density ρ multiplied by the volume V, whereby the volume is determined by the cross-sectional area A and the differential length dx.

$$F(x) = \rho\, A\, dx \frac{\partial^2 u}{\partial t^2} \qquad \text{with} \qquad V = A\, dx \tag{4.2}$$

In order to better understand the derivation of the one-dimensional wave equation, an infinitesimal piece is cut out of the bar and considered. The equilibrium of force on the infinitesimal volume element is given by Eq. (4.3). The one-dimensional wave equation can be derived using Newton's second law, cf. Eq. (4.2). Here σ_x represents the normal stress in

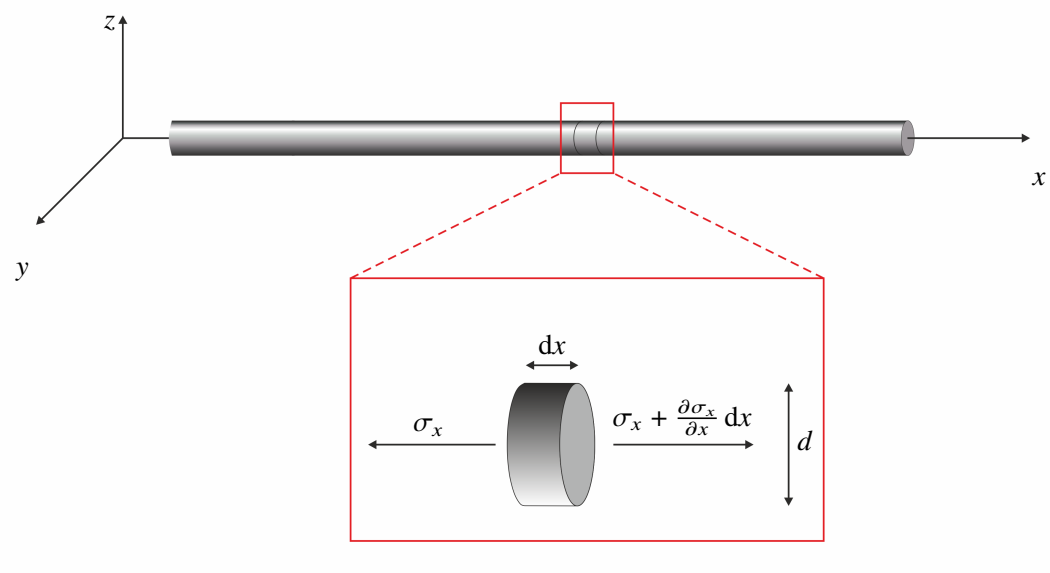

Fig. 4.5 – Stress at an infinitesimal small element of a long bar.

the cross-section and $u = u(x,t)$ the displacement of the cross-section and ρ the density of the bar material. Both the cross-section area A and the density ρ are constant. Stress acts in the positive and negative x-direction within the bar; see Fig. 4.5. Thus, Eq. (4.2) can be converted into the following form:

$$-\sigma_x A + \left(\sigma_x + \frac{\partial \sigma_x}{\partial x}\,dx\right) A = \rho\, A\, dx\, \frac{\partial^2 u}{\partial t^2} \tag{4.3}$$

By simplifying Eq. (4.3) we get:

$$\frac{\partial \sigma_x}{\partial x} = \rho\, \frac{\partial^2 u}{\partial t^2} \tag{4.4}$$

By applying Hooke's law $\sigma = E\,\varepsilon$ we get:

$$\frac{\partial (E\,\varepsilon)}{\partial x} = \rho\, \frac{\partial^2 u}{\partial t^2} \tag{4.5}$$

The relationship between displacement and strain $\varepsilon = \frac{\partial u}{\partial x}$ [Gross et al. 2013] it follows:

$$\frac{\partial}{\partial x}\left(E\, \frac{\partial u}{\partial x}\right) = \rho\, \frac{\partial^2 u}{\partial t^2} \tag{4.6}$$

Assuming that E is constant:

$$E\, \frac{\partial^2 u}{\partial x^2} = \rho\, \frac{\partial^2 u}{\partial t^2} \tag{4.7}$$

This gives the one-dimensional wave equation with the propagation velocity c:

$$c^2 \frac{\partial^2 u}{\partial x^2} = \frac{\partial^2 u}{\partial t^2} \qquad \text{with} \qquad c = \sqrt{\frac{E}{\rho}} \tag{4.8}$$

In Eq. (4.8) c, u, E and ρ are the wave propagation velocity, the displacement, the modulus of elasticity and the density of the material. The influence of temperature on the propagation velocity should initially be neglected, as this plays a subordinate role at room temperatures. A high modulus of elasticity increases the wave speed c of the material, whereas a high density ρ reduces the wave speed, as reflected in the denominator of Eq. (4.8). Table 4.1 shows the wave propagation velocities for different materials or media.

Table 4.1 – Wave propagation velocity in different media [Halliday et al. 2007].

medium	wave propergation velocity c [m/s]
air	331
helium	965
hydrogen	1284
water	1482
aluminum	5420
steel	5941
granit	6000

The solution of the one-dimensional wave equation goes back to D'Alembert, cf. [Hungerbühler 2011]. This equation consists of a so-called right-hand wave that travels in the positive direction ($f(x - c\,t)$) and a left-hand wave ($g(x + c\,t)$), which propagates in the opposite direction, cf. [Müller 2013].

$$u_1(x,t) = f(x - c\,t) + g(x + c\,t) \tag{4.9}$$

In both bars, the incoming wave is reflected at the bar end faces and passes through these until the final dissipation. However, for the experiments on the SHPB, only the incoming (incident) wave and the first reflected wave are important for the incident bar. For the transmission bar, only the transmitted wave, i.e., the wave that passes through the specimen, is important. The variables ξ_1 and ξ_2 in Eq. (4.10) denote the entire argument of f and g, respectively.

$$u_1(x,t) = f(\xi_1) + g(\xi_2) \tag{4.10}$$

Analogously, this simplification is performed for u_2. Only a right-running wave is required here. Accordingly, the following applies:

$$u_2(x,t) = h(x - c\,t) \tag{4.11}$$
$$u_2(x,t) = h(\xi_3) \tag{4.12}$$

The strain ε can be written as the derivative of the displacement u with respect to x, and the particle velocity $\dot{u}$ as the derivative of the displacement u with respect to time t:

$$\varepsilon = \frac{\partial u}{\partial x} \tag{4.13}$$
$$\dot{u} = \frac{\partial u}{\partial t} \tag{4.14}$$

Accordingly, the partial derivatives are as follows:

$$\frac{\partial u_1}{\partial x} = \frac{\partial f(x - c\,t)}{\partial x} + \frac{\partial g(x + c\,t)}{\partial x} \tag{4.15}$$
$$\frac{\partial u_2}{\partial x} = \frac{\partial h(x - c\,t)}{\partial x} \tag{4.16}$$

By the substitutions $\xi_1 = (x - c\,t)$, $\xi_2 = (x + c\,t)$ and $\xi_3 = (x - c\,t)$ we get the following representation:

$$\frac{\partial u_1}{\partial x} = \frac{\partial f}{\partial \xi_1}\frac{\partial \xi_1}{\partial x} + \frac{\partial g}{\partial \xi_2}\frac{\partial \xi_2}{\partial x} \tag{4.17}$$
$$\frac{\partial u_2}{\partial x} = \frac{\partial h}{\partial \xi_3}\frac{\partial \xi_3}{\partial x} \tag{4.18}$$

The derivatives with respect to ξ_1, ξ_2 and ξ_3 are denoted by f' and g' or h' in the following.

$$\frac{\partial u_1}{\partial x} = f'\frac{\partial \xi_1}{\partial x} + g'\frac{\partial \xi_2}{\partial x} \tag{4.19}$$
$$\frac{\partial u_2}{\partial x} = h'\frac{\partial \xi_3}{\partial x} \tag{4.20}$$

Since the derivative of $\frac{\partial \xi_i}{\partial x} = 1$ holds:

$$\frac{\partial u_1}{\partial x} = f' + g' \tag{4.21}$$
$$\frac{\partial u_2}{\partial x} = h' \tag{4.22}$$

Differentiating Eq. (4.9) and Eq. (4.11) with respect to time t it gives:

$$\frac{\partial u_1}{\partial t} = \frac{\partial f}{\partial \xi_1}\frac{\partial \xi_1}{\partial t} + \frac{\partial g}{\partial \xi_2}\frac{\partial \xi_2}{\partial t} \tag{4.23}$$
$$\frac{\partial u_2}{\partial t} = \frac{\partial h}{\partial \xi_3}\frac{\partial \xi_3}{\partial t} \tag{4.24}$$

Based on the chain rule, this results in:

$$\frac{\partial u_1}{\partial t} = -c\, f' + c\, g' \tag{4.25}$$
$$\frac{\partial u_2}{\partial t} = -c\, h' \tag{4.26}$$

With $f' = \varepsilon_i$, $g' = \varepsilon_r$ und $h' = \varepsilon_t$ the following relationship applies:

$$\frac{\partial u_1}{\partial t} = -c\, \varepsilon_i + c\, \varepsilon_r \tag{4.27}$$
$$\frac{\partial u_2}{\partial t} = -c\, \varepsilon_t\,. \tag{4.28}$$

4.2.3 Stresses and strains within the specimen

The strain rate in the specimen is calculated by:

$$\dot{\varepsilon_s} = \frac{\dot{u_1} - \dot{u_2}}{l_s} \tag{4.29}$$

Inserting Eq. (4.27) and Eq. (4.28) in Eq. (4.29) gives:

$$\dot{\varepsilon_s} = \frac{c}{l_s}\,(-\varepsilon_i + \varepsilon_r + \varepsilon_t) \tag{4.30}$$

We obtain the specimen's strain by integrating Eq. (4.30).

$$\varepsilon_s = \frac{c}{l_s}\int_{t_0}^{t} (-\varepsilon_i + \varepsilon_r + \varepsilon_t)\,\mathrm{d}t \tag{4.31}$$

The stress is directly related to the particle velocity $\dot{u}$ via Hooke's law $\sigma = E\,\varepsilon$. By substituting the relationships in Eq. (4.27) and Eq. (4.28) we get:

$$\sigma_i = E\,\varepsilon_i = -E\,\frac{\dot{u_i}}{c} \tag{4.32}$$
$$\sigma_r = E\,\varepsilon_r = E\,\frac{\dot{u_r}}{c} \tag{4.33}$$
$$\sigma_t = E\,\varepsilon_t = -E\,\frac{\dot{u_t}}{c} \tag{4.34}$$

Replacing the wave propagation velocity $c = \sqrt{\frac{E}{\rho}}$ yields:

$$\sigma_i = -\dot{u_i}\,\sqrt{E\,\rho} \tag{4.35}$$
$$\sigma_r = \dot{u_r}\,\sqrt{E\,\rho} \tag{4.36}$$
$$\sigma_t = -\dot{u_t}\,\sqrt{E\,\rho} \tag{4.37}$$

The following forces act on the bars:

$$F_1 = A_\mathrm{b}\,\sigma_1 = A_\mathrm{b}\,(\sigma_i + \sigma_r) \tag{4.38}$$

$$F_2 = A_\mathrm{b}\,\sigma_2 = A_\mathrm{b}\,\sigma_t \tag{4.39}$$

The forces at the respective end faces of the specimen can be calculated as follows. Here, F_1 represents the force at the specimen and incident bar interface, whereas F_2 represents the force acting on the surface orientated to the transmission bar.

$$\sigma_s = \frac{F_1 + F_2}{2\,A_\mathrm{s}} = \frac{A_\mathrm{b}\,(\sigma_i + \sigma_r) + A_\mathrm{b}\,\sigma_t}{2\,A_\mathrm{s}} \tag{4.40}$$

By inserting Eqs. (4.32) to (4.34), we obtain:

$$\sigma_s = \frac{E\,A_\mathrm{b}}{2\,A_\mathrm{s}}\,(\varepsilon_i + \varepsilon_r + \varepsilon_t) \tag{4.41}$$

Assuming that $\varepsilon_i + \varepsilon_r = \varepsilon_t$ holds, we obtain for Eq. (4.42), (4.43) and (4.44) an alternative form. These three equations are essential for evaluating the SHPB test and are used in many publications as basic equations for investigating dynamic material behavior, cf. [Frew et al. 2002], [Van Sligtenhorst et al. 2006], [Lu and Li 2011] and [Sasso et al. 2008]:

$$\dot{\varepsilon_s} = -2\,\frac{c}{l_s}\,\varepsilon_r \tag{4.42}$$

$$\varepsilon_s = -2\,\frac{c}{l_s}\int_{t_0}^{t} \varepsilon_r\,dt \tag{4.43}$$

$$\sigma_s = \frac{E_b\,A_b}{A_s}\,\varepsilon_t \tag{4.44}$$

4.2.4 Transmission of longitudinal waves between different media

Discontinuities occur at the interfaces between the incident bar and the specimen and between the specimen and the transmission bar due to the different materials and geometries. For better differentiation, indices are assigned to the incident bar as „1“, the specimen as „2“, and the transmission bar as „3“. The discontinuities will be examined in more detail at this point. Fig. 4.6 shows the stress amplitudes with their directions of propagation. It should be noted that the specimen is illustrated with an exaggerated thickness relative to the incident and transmission bars. This representation is intended solely to highlight the two interfaces.

Mechanical impedance

Mechanical impedance Z is a key parameter in the theory of one-dimensional wave propagation. It describes the resistance of a medium to particle motion caused by a longitudinal wave. Mechanical impedance is determined by the material properties and can be defined as follows for homogeneous, isotropic bars.

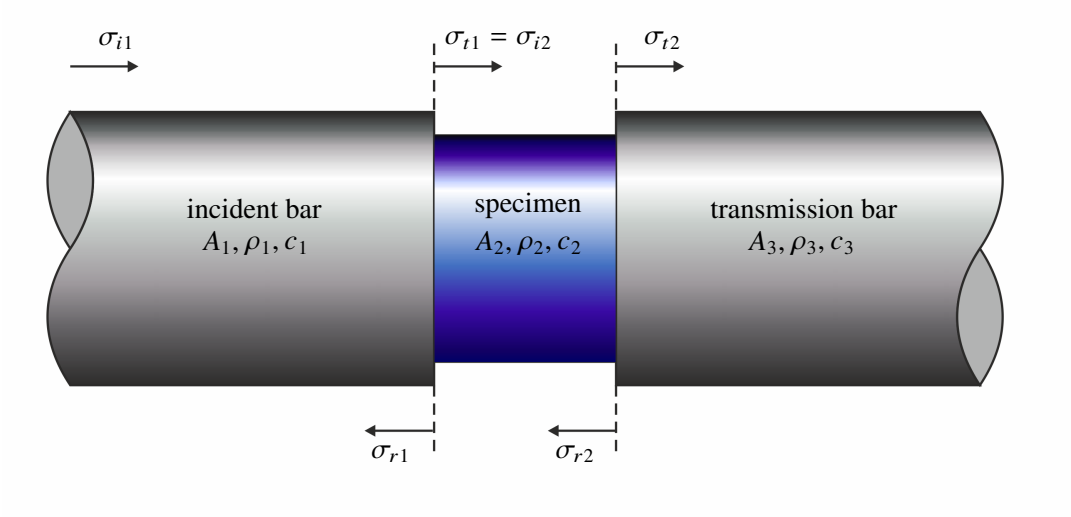

Fig. 4.6 – Wave reflection and transmission at interfaces of bars and specimen.

$$\bar{Z} = \rho\, c\, A \tag{4.45}$$

The impedance from Eq. (4.45) relates to the force F and the particle velocity $\dot{u}$:

$$F = \bar{Z}\, \dot{u} \tag{4.46}$$

Accordingly, the stress σ can be expressed as follows:

$$\sigma = \frac{F}{A} = \frac{\bar{Z}\, \dot{u}}{A} \tag{4.47}$$

If the impedance $\bar{Z}$ is related to the cross-sectional area A, the following relationship applies with reference to Eq. (4.45):

$$Z = \frac{\bar{Z}}{A} = \rho\, c. \tag{4.48}$$

By inserting Eq. (4.48) into Eq. (4.47), we obtain:

$$\sigma = \rho\, c\, \dot{u} = Z\, \dot{u} \qquad \text{or} \qquad \dot{u} = \frac{\sigma}{\rho\, c} = \frac{\sigma}{Z}. \tag{4.49}$$

The continuity of the velocity is considered at the interfaces. Since both the incident wave and the transmitted wave move forward (+) and the reflected wave moves in the opposite direction (-), the following applies:

$$\dot{u}_i + \dot{u}_r = \dot{u}_t \tag{4.50}$$

where the particle velocity of the reflected part $\dot{u}_r$ acts in the negative direction. The continuity

of stress at the interface from the incident bar to the specimen is given by:

$$\sigma_i + \sigma_r = \sigma_t \tag{4.51}$$

First, the interface between the incident bar and specimen from Fig. 4.6 is examined. Accordingly, the stress with the corresponding indices from this figure is considered. Inserting Eq. (4.49) into Eq. (4.50), keeping in mind the negative velocity of the reflected wave, gives:

$$\frac{\sigma_{i1}}{Z_1} - \frac{\sigma_{r1}}{Z_1} = \frac{\sigma_{t1}}{Z_2} \tag{4.52}$$

The reflection coefficient α represents the ratio of reflected stress to incident stress, whereas the transmission coefficient β represents the ratio of transmitted stress to incident stress. Dividing Eq. (4.52) by the incident stress yields:

$$\frac{1}{Z_1} - \frac{1}{Z_1} \underbrace{\frac{\sigma_{r1}}{\sigma_{i1}}}_{\alpha_{12}} = \underbrace{\frac{\sigma_{t1}}{\sigma_{i1}}}_{\beta_{12}} . \tag{4.53}$$

This results in a representation with the new coefficients:

$$\frac{1 - \alpha_{12}}{Z_1} = \frac{\beta_{12}}{Z_2}. \tag{4.54}$$

Analogously, we can write Eq. (4.51) in terms of the reflection coefficient α and transmission coefficient β by dividing both sides by the incident stress; this process isolates these coefficients and relates them directly to the ratios of reflected and transmitted stresses.

$$1 + \alpha_{12} = \beta_{12} \tag{4.55}$$

Inserting Eq. (4.54) into Eq. (4.55) and rearranging according to α and β yields:

$$\alpha_{12} = \frac{Z_2 - Z_1}{Z_2 + Z_1} \tag{4.56}$$

$$\beta_{12} = \frac{2\,Z_2}{Z_2 + Z_1} \tag{4.57}$$

Since transmission and reflection also occur at the interface between the specimen and the transmission bar, the coefficients α_{23} and β_{23} are obtained there, too. For the second interface, σ_{i2} becomes the incoming signal ($\sigma_{i2} = \sigma_{t1}$). Therefore, the incoming stress amplitude corresponds to the transmitted amplitude of the first interface; see Fig. 4.6. The following reflection coefficient and transmission coefficient apply to the interface between the specimen and the transmission bar:

$$\alpha_{23} = \frac{Z_3 - Z_2}{Z_2 + Z_3} \tag{4.58}$$

$$\beta_{23} = \frac{2\,Z_3}{Z_2 + Z_3} \tag{4.59}$$

4.3 Experimental setup and operation

This section provides a detailed description of the SHPB setup used in this work, which was further optimized during the course of the dissertation, along with the associated measurement system. Fig. 4.7 shows the SHPB which has been used for the experiments in this thesis.

Fig. 4.7 – Experimental setup of the custom-built split Hopkinson pressure bar at the laboratory of the chair for solid mechanics of the university Siegen.

4.3.1 Bearing system

Since the material pairing of the specimen and bars must be matched each other, a new system for the bearings of the bars was developed that enables a quick, safe, and uncomplicated exchange of bars. In the first setup of the SHPB system, it was very time-consuming to replace and align the bars. A large number of screws and snap rings had to be removed in order to prepare the system for a new bar setup. This complex system has been used successfully for numerous experiments and publications [Aghayan et al. 2018, 2019, 2022]. However, this work has improved the process of bar replacing, enabling faster, more effective operation across different experimental scenarios.

The new bearing system was designed as three different bar configurations are required for the investigated specimen materials in this work, see Fig. 4.8. The bars are fitted with bearing rings, which are inserted into the bearing mounts via corresponding guide rails and finally fastened by a screw. Plain bearing bushings are inserted in the bearing rings, which have a low

abrasion and friction coefficient. The bushings are pressed by pressure inside the bearing rings to ensure a firm hold between both components. The new bearing system ensures that the bars move smoothly, as this aspect is crucial for the experiments. The technical drawings for all components are shown in the Appendix A.2.

Furthermore, the acceleration tube has been optimized with air outlets that can be variably closed or fully closed for different striker lengths. A removable part of the acceleration tube allows the system to be fitted with different strikers more quickly. This new system allows even longer strikers of up to 300 mm to be exchanged in the SHPB system without significant effort. The corresponding technical drawings for the new design can be found in the Appendix A.2.

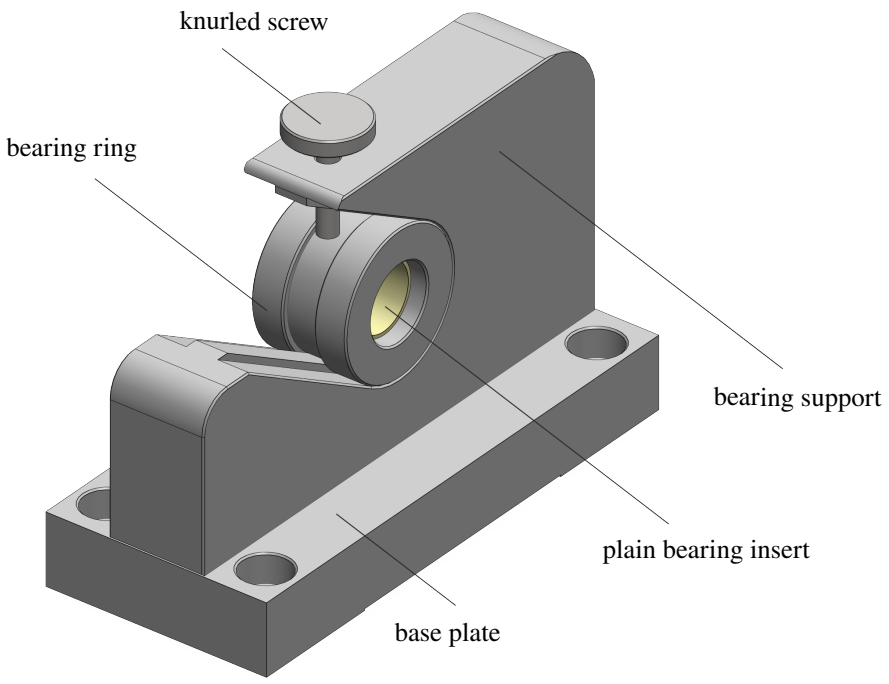

Fig. 4.8 – 3D CAD model of the newly developed bearing system.

4.3.2 Measuring system

For the data evaluation, strain gauges are used, which are applied to both the incident bar and the transmission bar. The operation of the strain gauges is based on the change in electrical stress due to changes in the cross-section of the electrical conductors as the wave travels through the bars. Since only very small strains occur in the SHPB test, appropriate measurement technology must amplify the low voltage values. Therefore, an amplifier is used to record the signal employing an oscilloscope. Both devices should have a sufficiently high-frequency response to record the signal's duration, which is usually shorter than one millisecond in the SHPB experiment. As a minimum frequency response, according to [Chen and Song 2010],

all measurement devices should be able to handle a frequency of 100 kHz. In our experiments, the waves are recorded at a sample rate of $10^6\ s^{-1}$ by the HBM GEN7t data acquisition system devloped by the company Hottinger Baldwin Messtechnik (HBM) equipped with two bridge cards, type GN411, see Fig. 4.9. Each bridge card is supplied by four channels, with each channel able to measure up to 1 MS/s. Wheatstone bridges in a full-bridge configuration are used (HBM 3/350 XY31), with a resistance of 350.0 Ω ± 0.30% and a gauge factor of 2.0 ± 1.0%. The laboratory has a constant temperature of 20° C.

Fig. 4.9 – GEN7t measuring system from HBM for evaluating strain gauges; equipped with 2 cards, each with 4 channels.

History and working principle of strain gauges

First a brief insight into the development and operation of strain gauges is given. The origin of strain gauges and their invention can be found in the USA. At the same time, the technique was used for the first time in different places. The first person who established the technique of strain gauges was the electrical engineer E. E. Simmons. He worked in California at the California Institute of Technology (Caltech) and was concerned with metal specimens subjected to impact stress. Prof. A. C. Ruge worked at the Massachusetts Institute of Technology (MIT). His application of strain gauges was to perform materials testing on water tanks. He was interested in recording the stresses that act on such tanks in the event of an earthquake, cf. [Hoffmann 1987]. Modern strain gauges employ conductive grids consisting of numerous loops, enabling more accurate strain measurements. This improvement has been made possible by advances in manufacturing technology, which, among other things, allow the production of finer conductive grids with smaller cross-sectional dimensions.

Strain gauges are used to determine stresses or strains in various components experimentally. They are exact measuring instruments with which minor strains in components can be registered.

Strain gauges consist of a carrier medium, the measuring grid, a cover layer, and the connections for the required measuring devices.

The resistance wire of a strain gauge is applied to the carrier in a meandering pattern. Due to the many loops, a relatively long resistance wire can be placed on a relatively small area. The principle of the strain gauge is based on an electrical conductor's resistance change. The resistance values R can be calculated using Eq. (4.60) as a function of the resistivity ρ and the cross-sectional area A and length l of the measuring grid. The resistivity is a temperature-dependent material constant. For example, if the strain gauge is stretched in length, l will increase. However, the cross-sectional area A will decrease at the same time. Both will cause an increase in electrical resistance. By compression of the strain gauge A increases, which in turn causes a reduction of R from Eq. (4.60).

The meandering shape of the resistive path increases the effective conductor length by a factor of n, where n corresponds to the number of loops in the strain gauge. If, for example, a strain gauge consists of 20 loops with an active length l^*, the effective conductor length, and thus the electrical resistance, increases by a factor of 20. This arrangement improves the sensitivity of the measurement, as even very small strains produce measurable changes in electrical resistance. Owing to the factor n, the resulting resistance changes are proportionally larger and can therefore be measured more accurately. The electrical resistance of a strain gauge is calculated according to Eq. (4.60)

$$R = \frac{\rho\, l}{A} = \rho \frac{4\, l}{D^2\, \pi} \qquad \text{with} \qquad l = n \cdot l^* \tag{4.60}$$

The total length of the strain gauge wire can be determined by the number of loop on the strain gauge. Another significant quantity is the sensitivity of the strain gauge. This proportionality factor, known as k-factor, represents the ratio of relative resistance change to the causing strain. The k-factor from Eq. (4.61) can be obtained from the datasheet for the corresponding strain gauge. A widely used material for the strain gauges is constantan (copper (Cu), nickel (Ni), manganese (Mn)), which has a very low-temperature dependence and a k-factor of 2.0, cf. [Blumenthal et al. 2007] and [Linse and Fischer 2005]. The k-factor is calculated as follows:

$$k = \frac{\Delta R / R_0}{\varepsilon} \qquad \text{with} \qquad \varepsilon = \frac{\Delta l}{l_0}. \tag{4.61}$$

Resolved according to the strain results in:

$$\varepsilon = \frac{1}{k} \frac{\Delta R}{R_0}. \tag{4.62}$$

Wheatston bridge

The Wheatstone bridge circuit finds great application in engineering with strain gauges. The structure of this measuring bridge is shown in Fig. 4.10 a). Wheatston's bridge has two series circuits (R_1 with R_2 and R_3 with R_4) connected in parallel, which is fed with voltage U_{ges}. The total current I_{ges} splits into the partial currents I_1 and I_2. Current I_1 passes through resistors R_1 and R_2, current I_2 passes through resistors R_3 and R_4. The total current of Wheatston's measuring bridge is formed by the sum of the two partial currents I_1 and I_2.

$$I_{\text{ges}} = I_1 + I_2 \tag{4.63}$$

The voltage U_{ges} can be calculated by the sum of the voltages of U_1 and U_2 or by the sum of the voltages U_3 and U_4.

$$U_{\text{ges}} = U_1 + U_2 = U_3 + U_4 \tag{4.64}$$

The voltage U_{AB} between points A and B from Fig. 4.10 is the difference of the voltages U_1 and U_4.

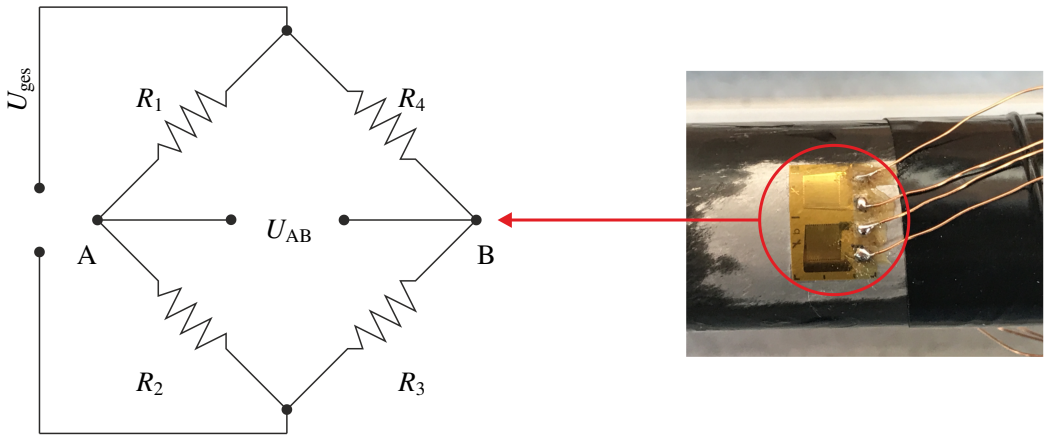

Fig. 4.10 – Wheatstone bridge: (a) basic structure and (b) applied strain gauge to the SHPB system equipped with aluminum bars.

By Ohm's law these voltages can be transformed into the product of current and resistance, cf. [Frohne et al. 2011].

$$\frac{U_1}{U_{\text{ges}}} = \frac{I_1 R_1}{I_1 (R_1 + R_2)} = \frac{R_1}{R_1 + R_2} \tag{4.65}$$

Solved for the voltage U_1 and analogously for U_4 we get:

$$U_1 = U_{\text{ges}} \frac{R_1}{R_1 + R_2} \qquad U_4 = U_{\text{ges}} \frac{R_4}{R_3 + R_4} \tag{4.66}$$

The voltage U_{AB} is calculated by:

$$U_{\text{AB}} = U_{\text{ges}} \left[\frac{R_1}{R_1 + R_2} - \frac{R_4}{R_3 + R_4} \right] \tag{4.67}$$

An elongation (ε = positive) increases the resistance. In the case of compression, the ΔR decreases the resistance. For Wheatston's bridge in connection with strain gauges, the requirement must hold that $R_1 = R_2 = R_3 = R_4$, cf. [Keil 2016]. The change in resistance of the individual resistors under load is denoted by ΔR_i.

$$\frac{U_{\text{AB}}}{U_{\text{ges}}} = \left[\frac{R_1 + \Delta R_1}{R_1 + \Delta R_1 + R_2 + \Delta R_2} - \frac{R_4 + \Delta R_4}{R_3 + \Delta R_3 + R_4 + \Delta R_4} \right] \tag{4.68}$$

Since all resistors are of the same type, $R_i = R_0$ applies to all resistors. Rearranging Eq. (4.68) yield many $\Delta R_i \Delta R_j$ terms. These terms are very small in relation to the resistances themselves. For this reason, these terms can be neglected and Eq. (4.68) can be simplified.

$$\frac{U_{\text{AB}}}{U_{\text{ges}}} = \frac{(\Delta R_1 - \Delta R_2 + \Delta R_3 - \Delta R_4)}{2\,(2\,R_0 + \Delta R_1 + \Delta R_2 + \Delta R_3 + \Delta R_4)} \tag{4.69}$$

Eq. (4.69) shows nonlinearity due to the sum in the denominator. However, this equation is often linearized in practice since $\Delta R_i \ll R_i$ usually holds. The linearized form is given in Eq. (4.70) and is a so-called full bridge.

$$\frac{U_{\text{AB}}}{U_{\text{ges}}} = \frac{1}{4} \left[\frac{\Delta R_1 - \Delta R_2 + \Delta R_3 - \Delta R_4}{R_0} \right] \tag{4.70}$$

In this full-bridge, all four resistors of Wheatston's bridge are used as strain gauges. Fig. 4.10 b) shows the applied strain gauges of the SHPB system. It can be seen that the coating on the bars has been removed for better adhesion of the strain gauges.In each case, two measuring grids oriented at 90° to each other are arranged on the carrier foil of a strain gauge. A second strain gauge is attached to the opposite side of the bar. Both strain gauges are interconnected to form a Wheatstone full bridge.

The strain gauges are usually applied to the measured object's surface, employing a carrier film or special adhesives. The carrier foil or the adhesive should transfer elastic and plastic changes to the strain gauge as unaltered as possible. The surface to which the strain gauge is applied should be neither too rough nor too smooth in order to ensure good adhesion. Different types of adhesives are used to apply the strain gauges. Depending on the experiment, the appropriate adhesive is more suitable. Examples of adhesives frequently used in strain gauge technology are cyanoacrylates, methyl acrylate, epoxy resin adhesives, and ceramic putty. For more detailed information, please refer to [Keil 2016]. There are some requirements for using

strain gauges in the SHPB-experiments like a good adhesion between adhesive and substrate material, thin adhesive layer (without entrapment of air) or curing as fast as possible after processing.

4.3.3 Stress equilibrium

In order to conduct valid experiments with the SHPB, there are a number of requirements that the system and the experiment must fulfill. There are three basic requirements that must hold for experiment at the classic SHPB test. cf. [Yang et al. 2015; Song et al. 2016]:

- one-dimensional wave propagation in bars and specimen
- achieving stress equilibrium
- constant strain rate $\dot{\varepsilon}$ during the experiment

The derivation of the one-dimensional wave equation in long bars has been discussed in the precending sections. In addition, a stress equilibrium within the specimen is necessary to approximately meet the assupmptions made for the specimen in section 4.2. The stress equilibrium in the SHPB experiment refers to the fact that the applied stress is evenly distributed in the material, allowing accurate measurements of material deformation and strength. This is important for obtaining precise data on the behavior of materials under dynamic loading.

Stress equilibrium means that the specimen undergoes uniform deformation. Suppose the deformation of a specimen is filmed with a high-speed camera. In that case, it can be seen in the individual images that an approximately uniform deformation occurs after a specific period of time. As shown in Fig. 4.11, the part of the specimen which is in contact with the incident bar deforms. Then the wave travels through the specimen and reaches the contact interface with the transmission bar. A reflection of the wave takes place at this second contact surface. Due to the „back-and-forth propagation“ of the wave in the specimen, a uniform deformation or stress equilibrium is established in the specimen, cf. [Chen and Song 2009] and [Chen and Song 2010]. The recordings were made using the Photron Nova S16 camera system, which allows high-speed capture up to 1,100,000 fps. However, higher recording rates result in lower quality. For this system, a frame rate at 16,000 fps gives a resolution of 1024×1024 pixels, while a recording at 1,100,000 fps gives a resolution of 128×16 pixels. For the recordings made here, a recording rate of 300,000 fps and a resolution of 128×128 pixels were used.

Soft materials exhibit lower stiffness and mechanical impedance than metals. Consequently, achieving stress equilibrium in these materials is generally more challenging than in stiffer materials with significantly higher impedance. However, stress equilibrium is a prerequisite for obtaining valid experimental results in split Hopkinson pressure Bar tests.

A critical parameter is the time t_s, which the wave needs to travel from the beginning to the end of the specimen. Assuming that the specimen consists of homogeneous material, t_s can be calculated by Eq. (4.71). By decreasing the specimens length l_s, the time required for the wave to traverse the specimen decreases. An advantage of a relatively short specimen

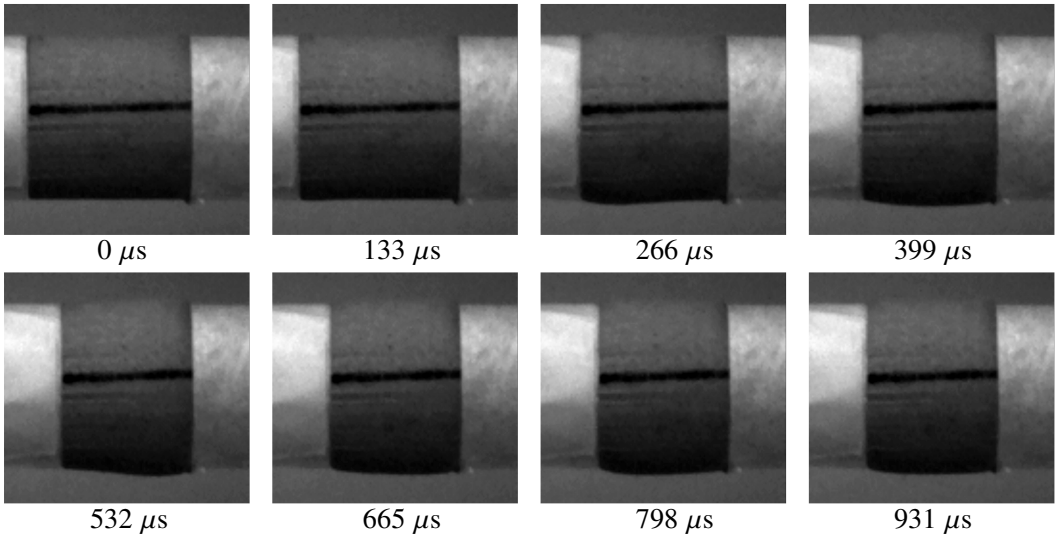

Fig. 4.11 – Deformation of foam recorded by a high-speed camera Photron Nova S16.

length is the reduction of axial inertial forces. However, with a very short specimen, there is a risk that the loading on the specimen will no longer be under uniaxial load. It is, therefore, essential to optimize the specimen in a way that both the time t_s and the inertia effect, as well as the uniaxial loading condition, are taken into account. This means that a compromise must be made between different conditions for the specimen geometry, particularly the initial length l_s.

$$t_s = \frac{l_\mathrm{s}}{c_\mathrm{s}} \tag{4.71}$$

According to [Ravichandran and Subhash 1994], Eqs. (4.76) and (4.77) represent a sufficient criterion for a stress equilibrium. Here $\Delta\sigma(t)$ denotes the stress difference between the leading and trailing ends of the specimen, and σ_m denotes the average stress value in the specimen body. This is called the stress equilibrium ratio $R(t)$. The stress amplitude at the contact area between the incident bar and the specimen is shown in Eq. (4.72).

$$\sigma_1 = \frac{A_\mathrm{b}}{A_\mathrm{s}} E_\mathrm{b} \left(\varepsilon_\mathrm{i} + \varepsilon_\mathrm{r}\right) \tag{4.72}$$

At the rear end of the specimen, where the specimen and the transmission bar are in contact, the stress is described by Eq. (4.73).

$$\sigma_2 = \frac{A_\mathrm{b}}{A_\mathrm{s}} E_\mathrm{b}\, \varepsilon_\mathrm{t} \tag{4.73}$$

Stress equilibrium is given by satisfying Eq. (4.74).

$$\varepsilon_\mathrm{i} + \varepsilon_\mathrm{r} = \varepsilon_\mathrm{t} \tag{4.74}$$

Inserting Eq. (4.74) in Eq. (4.72) results in:

$$\sigma_1 = \sigma_2 = \frac{A_\mathrm{b}}{A_\mathrm{s}} E_\mathrm{b}\, \varepsilon_\mathrm{t} \tag{4.75}$$

A perfect stress equilibrium is hard to realize. For this reason, the stress equilibrium ratio $R(t)$ is used to check whether a sufficient stress equilibrium exists. The stress equilibrium ratio should be at most a value of 10% to obtain valid results.

$$R(t) = \left|\frac{\Delta\sigma(t)}{\sigma_\mathrm{m}}\right| = 2\left|\frac{\sigma_1 - \sigma_2}{\sigma_1 + \sigma_2}\right| \leq 0.1 \tag{4.76}$$

Since the cross-section areas of both bars are identical throughout this work, stress equilibrium is achieved through force equilibrium.

$$R(t) = \left|\frac{\Delta F(t)}{F_\mathrm{m}}\right| = 2\left|\frac{F_1 - F_2}{F_1 + F_2}\right| \leq 0.1 \tag{4.77}$$

4.4 Hard 3D-printed polymere under high strain rates

The acrylic-like resin Anycubic Tough 2.0 is examined in this section under impact load using the SHPB test. The SHPB is equipped with bars made of aluminum for experiments. The aluminum bars are a suitable choise for hard polymers. The bars have a black powder coating, which allows the bars to slide easily through the bearing rings. The coating is removed at the strain gauges' positions to achieve better adhesion of the strain gauges, see Fig. 4.10 b). Table 4.2 shows the SHPB setup used for the tests with Anycubic Tough 2.0.

Table 4.2 – Dimensions of the conventional SHPB setup equipped with aluminium bars.

	incident bar	transmission bar	striker	Anycubic Tough 2.0
material	aluminum	aluminum	aluminum	acrylic-like
d [mm]	20.00	20.00	20.00	17.00
l [mm]	2000.00	2000.00	300.00	10.00
ρ [kg/m^3]	2700.00	2700.00	2700.00	1200.00
E_stat [GPa]	72.00	72.00	72.00	1.00
c [m/s]	5070.00	5070.00	5070.00	937.50
Z [kg/m$^2\mu$s]	13.69	13.69	13.69	1.13

If the values of the modulus of elasticity E and the density of the material ρ are known, the wave propagation speed can be calculated using $c = \sqrt{E/\rho}$. Since the modulus of elasticity E

is often not specified by the manufacturer for plastics (especially in the 3D printing sector) or E is challenging to measure -particularly for very soft materials- the wave propagation velocity of the specimen material can be determined using the SHPB setup. Furthermore, the actual wave propagation speed of such materials is highly dependent on the manufacturing process (light intensity of the printer, curing times, etc.). For this reason, it is generally recommended to evaluate the wave propagation speed directly on the material to be examined by performing tests.

4.4.1 Wave propagation velocity and impedance mismatch of polymers

For determination of the wave propagation velocity of the tested material Anycubic Tough 2.0, a reference measurement is necessary. For this reference measurement the incident and transmission bars are in direct contact without any specimen. In a first measurement the time of the pulse needed to propagate from the strain gauge mounted centrally on the incident bar to the strain gauge applied at the center of the transmission bar is recorded. In the second measurement, a specimen with a defined length is clamped between the incident bar and transmission bar. Because of the specimen between the bars, the wave induced by the striker, requires more time to propagate from the strain gauge of the incident bar to the strain gauge of the transmission bar; see Fig. 4.12. Based on the recorded values the propagation speed of the longitudinal wave of the specimen material is calculated.

$$c_\mathrm{s} = \frac{l_s}{\Delta t_\mathrm{s}} \qquad \text{where} \qquad \Delta t_\mathrm{s} = \Delta t_2 - \Delta t_1 \tag{4.78}$$

Here l_s and Δt_s are the length of the specimen and the additional time required for the wave to pass through the specimen. The values Δt_1 and Δt_2 indicate the time intervals between the signals measured by strain gauges at the incident bar and the transmission bar, with and without the specimen clamped between the bars. The method results in a wave propagation velocity of $c_\mathrm{s} = 937.5\,\mathrm{m/s}$ for Anycubic Tough 2.0. Since the propagation velocity is constant, the shape of the measured signals is not important at this point.

The impedances Z were calculated based on Eqs. (4.56),(4.57) and Table 4.2 for the aluminum bars and the specimen material Anycubic Tough 2.0. This results in the following reflection coefficient and transmission coefficient:

$$\alpha_\mathrm{Tough2.0} = -0.85$$
$$\beta_\mathrm{Tough2.0} = 0.15$$

Materials cannot generally be categorized into „static“ and „dynamic“ material behavior. As outlined at the beginning of Chapter 4, the density of the material only plays a subordinate role under quasi-static conditions. In dynamic tests under higher strain rates the material density -and consequently the mass inertia- becomes significant. This means that the material response

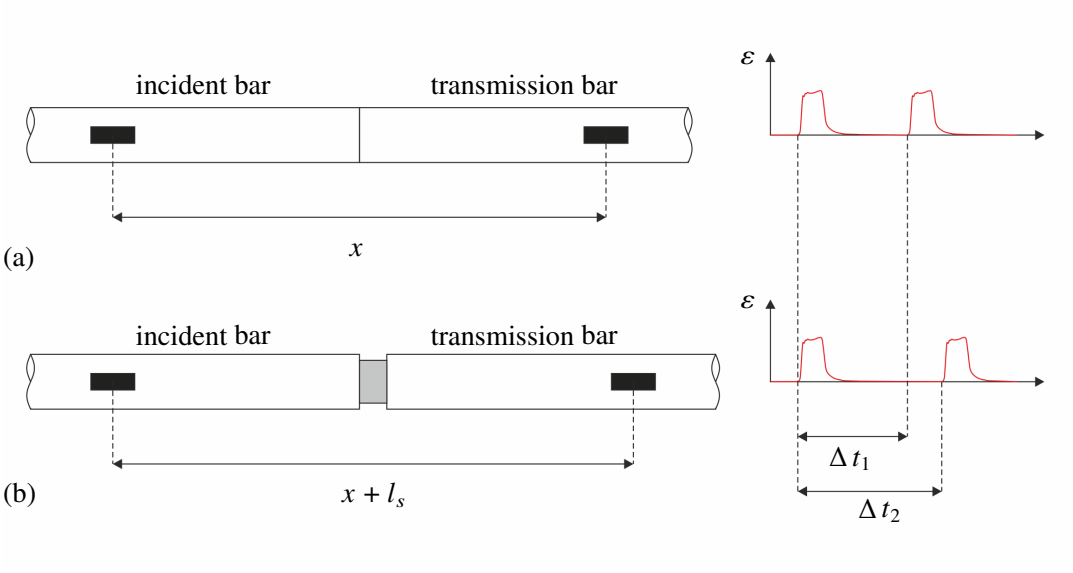

Fig. 4.12 – Wave propagation velocity: a) measurement without specimen and b) with specimen between the bars.

is sensitive to the strain rate, which shows that the SHPB test can be used to determine material responses for specific strain rates. Within this thesis, the tested materials are examined for different strain rates. The experimental setup must therefore be adjusted to maintain the desired constant strain rate under stress equilibrium.

4.4.2 Experimental results at different strain rates

The impact velocity of the striker specifies the amplitude of the pulse induced by the striker into the system. The length l_s of the striker, in turn, determines the length of the impulse [Janiszewski et al. 2016]. The strain rate in Eq. (4.42) depends on the propagation velocity of the bar material c_b, the specimen thickness l_s and the amplitude and shape of the reflected pulse. The wave propagation speed of the bar materials is constant and can no longer be influenced once the bar materials have been selected. Thus, the desired strain rate is approximated with the parameters of specimen thickness and the reflected pulse ε_r.

Moreover, it must be ensured that stress equilibrium has bee achieved in the specimen. The stress equilibrium depends on the incident pulse which is induced in the system by the striker. The striker length l_{st} and the velocity v_{st} influence the incident pulse. The SHPB system is designed to use strikers of different lengths and materials. Additionally, so-called pulse shapers can be used to change the shape, the duration and the rise time of the pulse. Pulse shapers are plastically deformable thin discs, which are attached to the front surface of the incident bar to „shape“ the pulse induced by the striker and thus adjust the shape in the pulse, [Ninan et al. 2001].

A specimen thickness of l_s = 10 mm was selected for the specimens made of Anycubic

Tough 2.0 investigated in this section. Stress equilibrium was achieved by using a striker length of l_{st} = 300 mm. Cylindrical discs with a thickness of 0.2 to 0.3 mm and a diameter of 5 mm made of polyethylene (PE) were used for pulse shaping. The main reason for using the pulse shaper in these measurements was to filter out oscillations, which makes subsequent evaluation more difficult [Song et al. 2008]. Additionally the rise time of the incident pulse was manipulated to achieve stress equilibrium. Due to the very thin pulse shaper, the rise of the incident pulse is only slightly influenced. The experiments were carried out for three strain rates:

- $\dot{\varepsilon} \approx 300\ \mathrm{s}^{-1}$
- $\dot{\varepsilon} \approx 500\ \mathrm{s}^{-1}$
- $\dot{\varepsilon} \approx 700\ \mathrm{s}^{-1}$

Fig. 4.13 a) to 4.15 a) show the corresponding signals of the strain gauges from the experiments. To evaluate the signals, the corresponding pulses (incident, reflected, and transmitted pulse) were cut out from the signal and shifted to time zero, see Fig. 4.13 b) to 4.15 b). By comparing the sum of the incident and reflected pulse with the transmitted pulse, it is possible to check whether a stress equilibrium has been achieved. Stress equilibrium was achieved in all specimens, see Fig. 4.13 c) to 4.15 c). The mean value of the plateau of the reflected pulse was used to determine the experiment's strain rate.

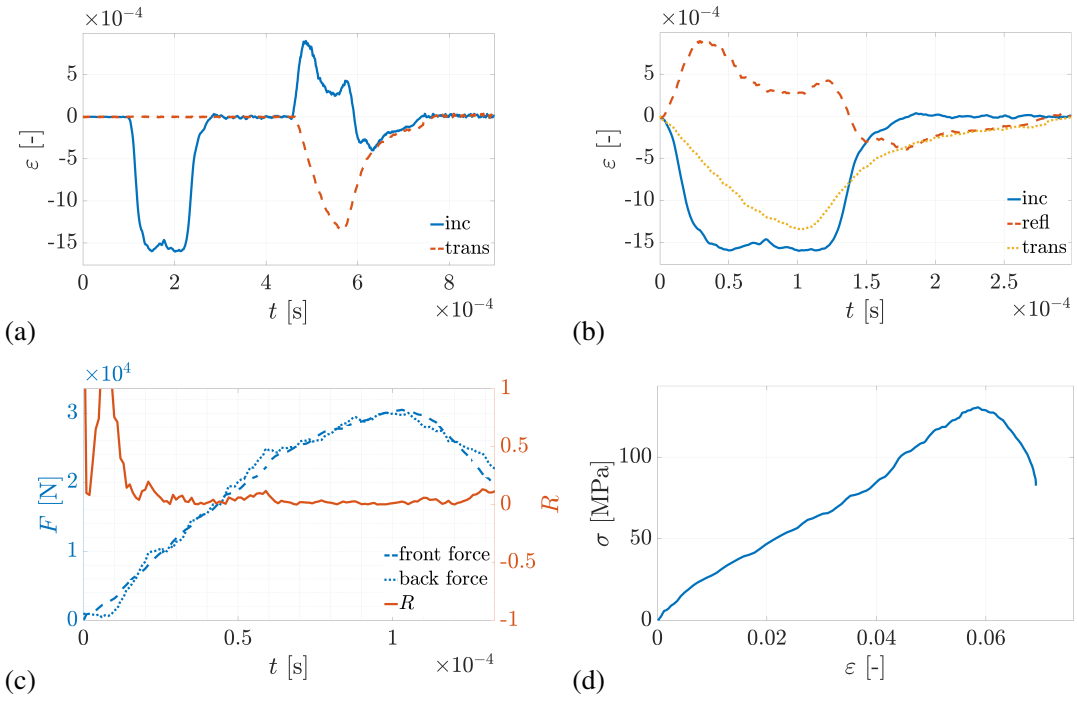

Fig. 4.13 – a) Recorded signals of the strain gauges, b) time-shifted pulses, c) front and back forces at the specimen surfaces and the resulting stress equilibrium ratio R and d) the calculated stress-strain curve for Anycubic Tough 2.0 at a strain rate of $\dot{\varepsilon} = 300\mathrm{s}^{-1}$.

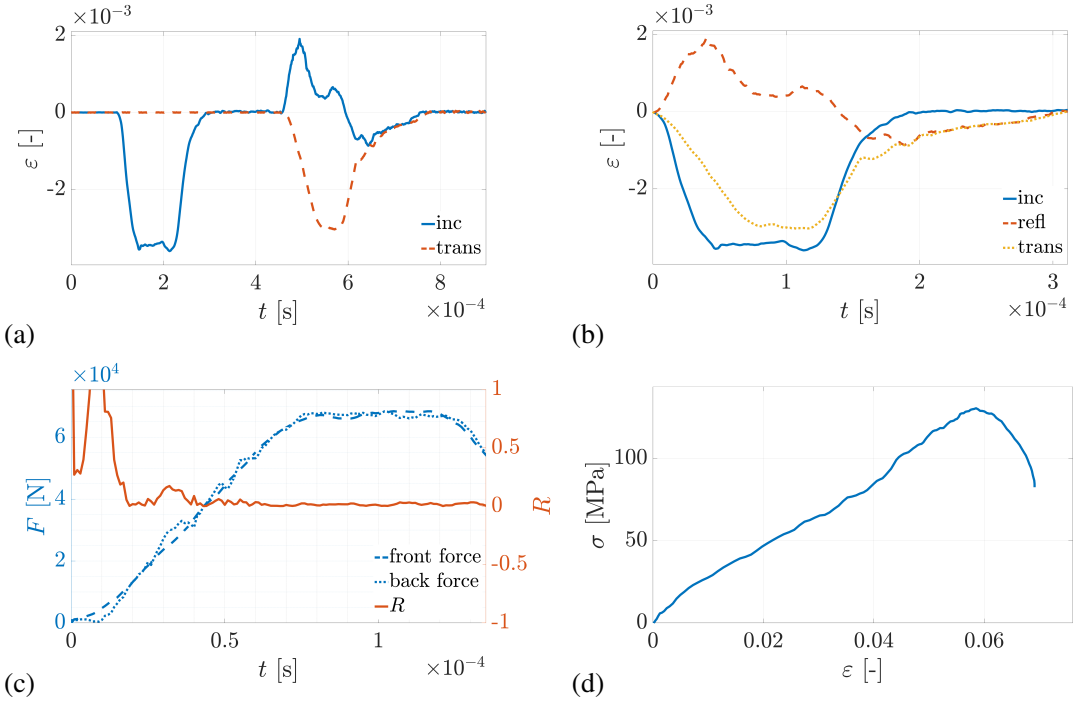

Fig. 4.14 – a) Recorded signals of the strain gauges, b) time-shifted pulses, c) front and back forces at the specimen surfaces and the resulting stress equilibrium ratio R and d) the calculated stress-strain curve for Anycubic Tough 2.0 at a strain rate of $\dot{\varepsilon} = 500\text{s}^{-1}$.

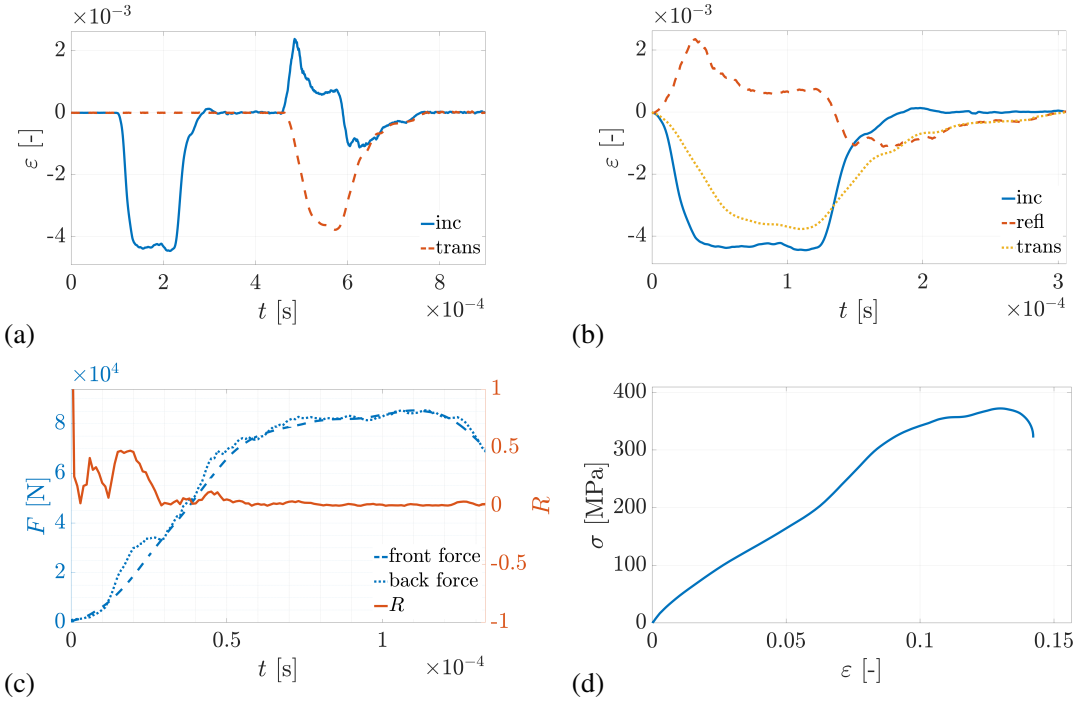

Fig. 4.15 – a) Recorded signals of the strain gauges, b) time-shifted pulses, c) front and back forces at the specimen surfaces and the resulting stress equilibrium ratio R and d) the calculated stress-strain curve for Anycubic Tough 2.0 at a strain rate of $\dot{\varepsilon} = 700\text{s}^{-1}$.

The evaluation of stress-strain curves calculated based on SHPB tests is usually only comparable to other publications to a limited extent. Even when using a similar experimental setup and the same material, the printing parameters and the age of the specimens must be similar to enable a reliable comparison of the results.

Although the SHPB test is a common used instrument to determine material properties under impact loading, the experimental setups can differ. Furthermore, there is no existing standard that describes the evaluation method or specifies the geometries of test specimens. The SHPB's more remarkable complexity makes it much more difficult to standardize than a quasi-static tensile test. For this reason, the characteristic values determined in this work are based on methods that result from our previously published publications and our own considerations. For the printed specimens within this work, the modulus of elasticity is determined by a linear regression line between the strains of $\varepsilon = 0.025$ and $\varepsilon = 0.05$ of the stress-strain diagram.

Five experiments were carried out for each strain rate. Although none of the specimens showed any visible crack or damage, it was decided to use the specimens only once. Using the specimens just once ruled out any measurement errors caused by micro-structural changes or cracks. The SHPB test exhibits a higher degree of measurement scatter. However, the result for the individual strain rates were reproducible within this variability. For the sake of clarify, only one representative measurement per strain rate is presented here. The fluctuations in the average strain rate across individual measurements were acceptable within the SHPB test's measurement accuracy, cf. Table 4.3.

The experiments show that the modulus of elasticity increases with increasing strain rate $\dot{\varepsilon}$, cf. Fig. 4.16. Especially with polymers or soft viscous materials, the modulus of elasticity can increase by several orders of magnitude (highly strain rate sensitive), cf. [Siviour and Jordan 2016]. Due to the high strain rate $\dot{\varepsilon}$, the viscous parts of the material do not have time to relax, which results in stiffer material behavior. In the investigation of the material Anycubic Tough 2.0, dynamic moduli of elasticity increases of up to 330% (for $\dot{\varepsilon} \approx 700\text{s}^{-1}$).

4.4.3 Comparison of mechanical response at different strain rates in hard polymers

To realize the different strain rates, the striker speed was varied, and the thickness of the pulse shaper was adjusted. The corresponding values are listed in Table 4.3. The static modulus of elasticity specified here refers to the maximum modulus of elasticity determined in the quasi-static experiments. This maximum modulus of elasticity occurs at a printing orientation of 45° and corresponds to the manufacturer's specifications. Other tested printing orientations show a lower static modulus of elasticity, see Fig. 3.10 in Chapter 3.

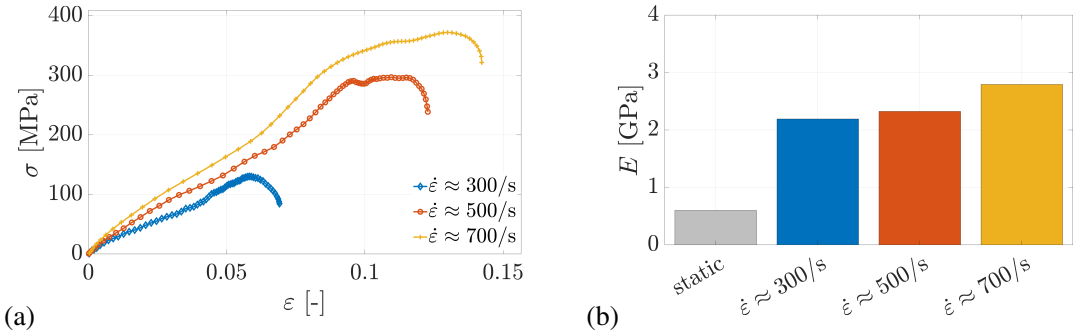

Fig. 4.16 – a) Comparison of the stress-strain curves of Anycubic Tough 2.0 at different strain rates and b) the elastic modulus calculated by the slope of the elastic region of the stress-strain diagram.

Table 4.3 – Static modulus of elasticity and dynamic moduli of elasticity of Anycubic Tough 2.0 for different strain rates, the corresponding striker velocity v_{st} and the geometry of the puls shaper.

E [GPa]	$\dot{\varepsilon}$ [s^{-1}]	v_{st} [m/s]	pulse shaper
1.0	quasi-static	-	-
2.1	314.40 ± 15.65	3.5	PE (5 mm × 0.2 mm)
2.3	503.80 ± 13.97	5.5	PE (5 mm × 0.3 mm)
2.7	723.00 ± 15.25	7.2	PE (5 mm × 0.3 mm)

4.5 Soft 3D-printed polymere under high strain rates

When testing soft materials with a conventional steel or aluminum SHPB setup, problems of mechanical impedance mismatch occur. Because of the high impedance mismatch the wave is almost completely reflected at the interface of specimen and incident bar. Consequently only a weak or no signal can be measured at the strain gauge applied to the transmission bar. There are several ways to deal with this problem. The impedance mitmatch can be controlled by two parameters: the material pairing and the specimen cross-section area, as shown in Eq. (4.45). The cross-sectional area of the test specimen can only be adjusted to a limited extent, as it is constrained by the dimensions of the SHPB bars.

One option is to decrease the transmitted bar's cross-section area. The authors of [Chen et al. 1999, 2002] use a hollow transmission bar to reduce the impedance mismatch between the bar and specimen. Another approach pursued by [Chen et al. 2000] is to increase the sensitivity of the strain gauges, especially on the transmission bar. An additional concept which is also use in this work is the substitution of the metal bars by viscoelastic bars, which have a much lower mechanical impedance. This way, the impedance mismatch between bars and specimen is effectly reduced. Therefore PMMA was chosen for the bar material. However, in such polymeric materials, wave attenuation and dispersion effects have a significant influence

on the measured signals. Because of the low attenuation and dispersion in metal bars, the signal measured at the center of the bars represents nearly the wave at every point of the bar. Unfortunately, these assumptions do not hold for the viscoelastic nature of PMMA, [Szabo and Wu 2000]. In this case, it cannot be assumed that the measured pulses at the center of the bars correspond to the pulses at the transition surfaces between bars and specimen, cf. Fig. 4.17. Instead the measured signal has to be corrected in some way.

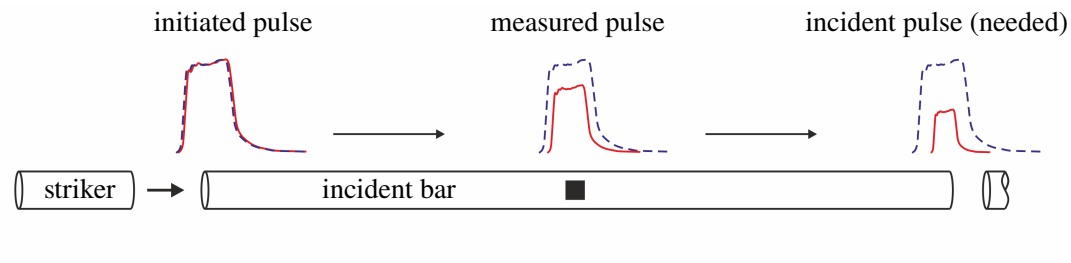

Fig. 4.17 – Illustration of wave attenuation and dispersion in PMMA bars (solid line) and metal bars (dashed line) [Bieler and Weinberg 2025d].

4.5.1 Signal correction by exponential fitting

An initial approach is based on carrying out preparatory experiments by using only the incident PMMA bar. In this preceding experiment a single strain gauge is attached to the center of the bar. The pulses generated in the subsequent actual experiments must be generated in the same way as in the preceding experiment. This means that the striker speed, striker dimensioning and pulse shaping, if applicable, correspond exactly to the later experiments. After the impact is generated by the striker, the wave is measured via the centrally mounted strain gauge. As the bar has a free end, the wave is completely reflected at the end of the bar. Accordingly, a „back and forth travel“ of the pulse is measured at the strain gauge, see Fig. 4.18.

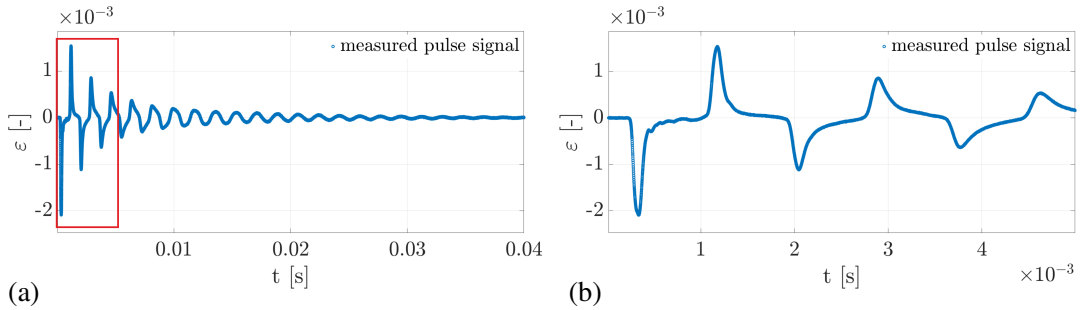

Fig. 4.18 – a) Signal measurement to generate a curve fit for the amplitude reduction and b) a zoomed segment of the measurement of the first 7 ms [Aghayan et al. 2022].

An exponential decrease in amplitude can be observed due to dispersion. The change in sign of the amplitudes results from the change in direction of the wave, which passes through

the bar several times in this preliminary test. Only the amplitude magnitudes are required to determine the correction factors, see Fig. 4.19 a). Using the data points of the peaks, an exponential curve fit $A(x)$ is performed with the software MATLAB.

$$A(x) = a_0\, e^{a_1 x} + a_2\, e^{a_3 x} \tag{4.79}$$

Here x is the distance between the strain gauge and the point of interest. The coefficients a_0, a_1, a_2 and a_3 in Eq. (4.79) are constants determined in the curve fitting algorithm. Since the strain gauges are applied to the center of the bars, the distance between two measurements is the length of the bar. The wave has to pass the half distance of the bar, is reflected and has to pass the same distance back to the strain gauge. By fitting a function, the correction factor can be obtained from the function, which is used for the relevant distance between the true measurement and the point of interest. Fig. 4.19 b) shows a measured and a corrected signal by using this method. Since in the actual experiment the measurement of the incident pulse is recorded before the pulse reach the incidentbar/specimen interface and accordingly the reflected pulse is detected after it this interface, the amplitudes must be corrected downwards for the incident pulse and upwards for the reflected pulse. Similarly to the reflected pulse, the transmitted pulse has to be corrected upwards.

It should be noted that these coefficients only refer to the current setup. This means that the exponential fit parameters can only be applied to subsequent corrections of measurements as long as the striker geometry and speed as well as the bar material and any applied pulse shapers correspond to the pre-experiment. Other setups and specifications require a new calibration of the coefficients. It should be mentioned that this method is only a very rough approximation of the attenuation of the signal. Moreover, this method only considers the amplitude of the signal, but not the change in the shape of the pulse. In Section 4.5.2 a more accurate and much better signal correction is discussed.

In [Aghayan et al. 2022] this signal correction was used to predict the pulse at certain points where measurements cannot be made, especially at the bar/specimen interface, see Fig. 4.19 b).

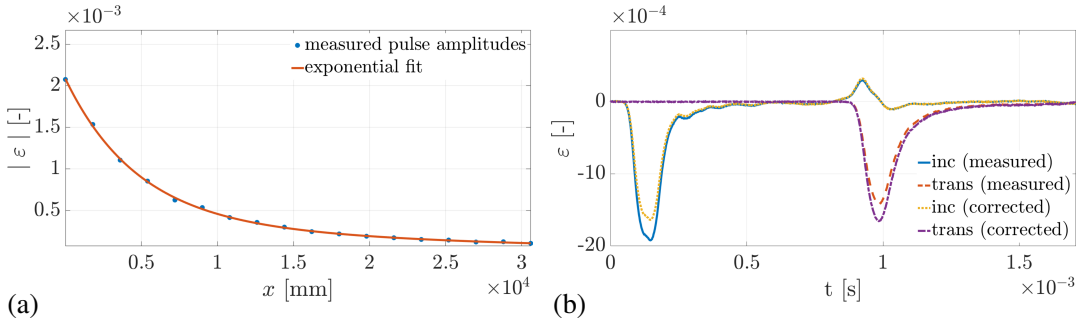

FIG. 4.19 – a) Curve fit of an exponential function through the amplitudes of the measured signal and b) application of the determined correction factors to the output signal in the center of the bars [Aghayan et al. 2022].

4.5.2 Signal correction by spectral analysis

A signal correction as in Section 4.5.1 does indeed reproduce the change in the amplitude response of the pulse caused by dispersion, but the actual shape of the pulse is retained. The pulse consists of a large number of individual waves with their own frequency, see Fig. 4.20. The measured pulses represent a wave packes include different frequencies and amplitudes. Since each frequency propagates at a different speed, the pulse changes its shape over time. In addition, the amplitudes of the individual frequencies are attenuated by the internal friction of the bar medium.

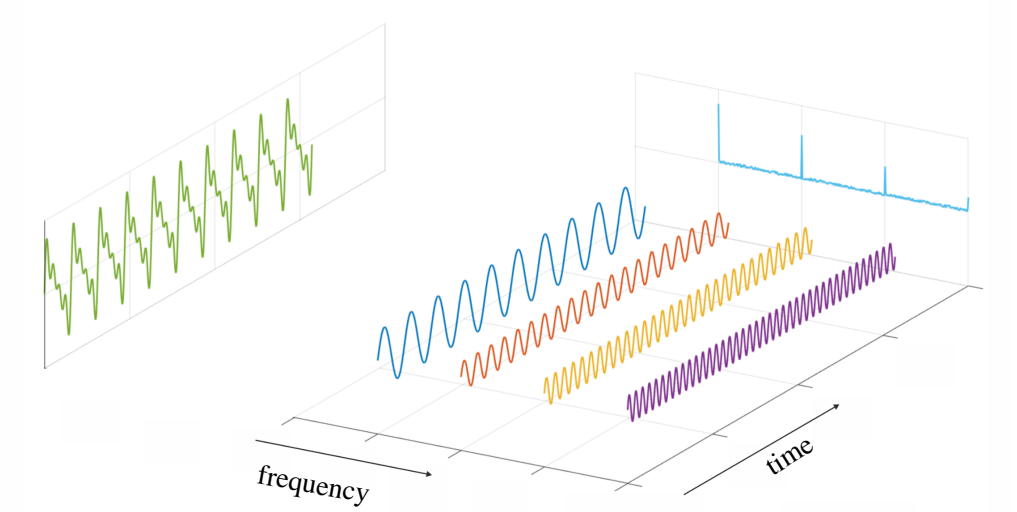

Fig. 4.20 – Illustration of a signal (green) with its individual frequency components with their corresponding amplitudes

Fast Fourier Transformation

This section provides an overview of the fundamental equations of the Fourier transform and the corresponding algorithms for discrete signals. Throughout this section, lowercase letters denote quantities in the time domain, whereas uppercase letters denote their corresponding representations in the frequency domain. With the Fourier transform method in Eq. (4.81), a signal can be converted from the time domain to the frequency domain:

$$x(t) \xrightarrow{\mathcal{F}} X(\omega). \tag{4.80}$$

Measured signals are usually available as digital and, therefore, discrete values. For this reason, the Discrete Fourier Transform (DFT) is used for discrete signals instead of the continuous Fourier transform.

$$X(\omega) = \int_{-\infty}^{\infty} x(t)\, e^{-i\omega t}\, \mathrm{d}t \tag{4.81}$$

The Fast Fourier Transformation (FFT) is an algorithm for the efficient calculation of the DFT in Eq. (4.82), a mathematical method for transforming a signal from the time domain into the frequency domain. The derivation of the FFT is based on various mathematical concepts such as the decomposition of complex numbers and the symmetry properties of the DFT. Essentially, the FFT is an algorithm that effeciently computes the DFT of a signal.

$$X(\omega_\mathrm{k}) = \sum_{n=0}^{N-1} x_\mathrm{n}\, e^{-i\frac{2\pi}{N}kn}, \qquad k = 0, 1, \ldots, N-1 \tag{4.82}$$

In the Cooley-Tukey form (Eq. (4.83)), the FFT decomposes a DFT of length N into smaller DFTs, which is especially efficient when N is a power of two, reducing the computational complexity from $O(N^2)$ to $O \log_2 N$. The time signal is decomposed into its frequency components. These components are individual sine waves at discrete frequencies whose amplitudes and phases are determined. So the FFT allows a signal to be viewed in the frequency range. This method makes it possible to predict the signal at certain positions where a direct measurement cannot be performed, cf. [Bacon 1998; Cheng et al. 1998; Zhao et al. 1997].

$$X(\omega_\mathrm{k}) = \sum_{n=0}^{N/2-1} x_{2n}\, e^{-i\frac{2\pi}{N}(2n)k} + \sum_{n=0}^{N/2-1} x_{2n+1}\, e^{-i\frac{2\pi}{N}(2n+1)k} \tag{4.83}$$

The SHPB setup was changed for the signal correction method using FFT. PMMA was again selected as the bar material with the same diameter of 20 mm, but longer bars were used here to avoid interfering with the measured pulses at the individual measuring points.

The wave propagation in structures based on an FFT-based algorithm was described in [Doyle 2012]. The analytical wave correction requires that the propagating wave is recorded at different positions of the PMMA bar. To reconstruct a signal at any point on the bar, two measuring points are required from which a prediction or correction for the signal at any position of the bar can be derived. However, the bars were equipped with three strain gauges for the reconstruction carried out in this work. For the signal correction the attenuation factor and the wave number for each frequency are needed. In this was the frequency spectrum at any position on the bar can be calculated.

Using the FFT in Eqs. (4.84) and (4.85), the signals are transformed from the time domain into the frequency domain. The pulses must be cut out by a suitable time window and provided with a corresponding sample rate. This allows the time signal $u(t)$ of the pulse to be converted into its frequency spectrum $U(\omega)$ using FFT:

$$U_1(\omega_n) = \mathrm{FFT}[u_1(t)] = \sum_n \mid U_1(\omega_n) \mid \mathrm{e}^{\mathrm{i}\phi_1(\omega_n)} \tag{4.84}$$

$$U_2(\omega_n) = \mathrm{FFT}[u_2(t)] = \sum_n \mid U_2(\omega_n) \mid \mathrm{e}^{\mathrm{i}\phi_2(\omega_n)} \tag{4.85}$$

For the prediction respectively correction, the attenuation factor $\hat{\alpha}_n$ and the wave number $\hat{k}_n$ are required for each frequency, see [Janiszewski et al. 2016; Zhao and Gary 1995]. These values are calculated based on the amplitudes $\mid U_{1n} \mid$ and $\mid U_{2n} \mid$ respectively the phases ϕ_{1n} and ϕ_{2n} of the spectral components as well as the distance between the measuring points x_1 and x_2. Since the signal of measuring point x_1 to measuring point x_2 is attenuated, the amplitude decreases exponentially:

$$U_2(x_2) = U_1(x_1)\mathrm{e}^{-\hat{\alpha}(x_2-x_1)} \tag{4.86}$$

Solve Eq. (4.86) for attenuation factor $\hat{\alpha}_n$:

$$\hat{\alpha}_n = \frac{\ln \mid U_{1n} \mid - \ln \mid U_{2n} \mid}{x_2 - x_1} \tag{4.87}$$

Eq. (4.88) shows the calculation of the wave number $\hat{k}_n$:

$$\hat{k}_n = \frac{\phi_{1n} - \phi_{2n}}{x_2 - x_1} \tag{4.88}$$

The attenuation coefficient $\hat{\alpha}_n$ from Eq. (4.87) depends on the amplitudes U_{1n} and U_{2n}. In contrast, the wavenumber $\hat{k}_n$ from Eq. (4.88) describes the dispersion and is expressed by the calculated phases ϕ_{1n} and ϕ_{2n}.

A spectral analysis is carried out for both signals $u_1(t)$ and $u_2(t)$ to predict the pulse spectrum at a specific position on the bar. Therefore, the distance Δx between the strain gauges that receive the pulses $(x_2 - x_1)$ is needed. To predict the signal at locations without strain gauges, Δx is calculated as follows:

$$\Delta x = x_m - x_{cp} \tag{4.89}$$

Here x_m is the position where the signal was measured and x_{cp} is the position of the corrected or predicted wave. This information can be used to predict an amplitude spectrum U_{cp} at any point:

$$U_{cp}(x, \omega) = U_{m,n}\mathrm{e}^{\mathrm{i}\phi_{mn}}\mathrm{e}^{(-\hat{\alpha}+\mathrm{i}\hat{k}_n)\Delta x} \tag{4.90}$$

The Inverse Fast Fourier transformation (IFFT) in Eq. (4.91) is used to transform the determined frequency spectrum at position x_{cp} back into the time domain.

$$u_{cp} = \text{IFFT}[U_{cp}(x, \omega)] \tag{4.91}$$

Validation of the method

To validate the presented method both bars of the SHPB were equipped with three strain gauges, see Fig. 4.21. For validation, the test is initially carried out without a clamped specimen. Since both bars are made of PMMA, there is no impedance mismatch at the interface, resulting in the absence of a reflected pulse in this setup. The three measurements for each bar are recorded and used to reconstruct/predict and to validate the wave signals. To enable better comparison, the pulses are isolated from the signal and shifted to time zero. We already published this method of signal reconstruction in [Bieler and Weinberg 2021] and [Bieler and Weinberg 2025d].

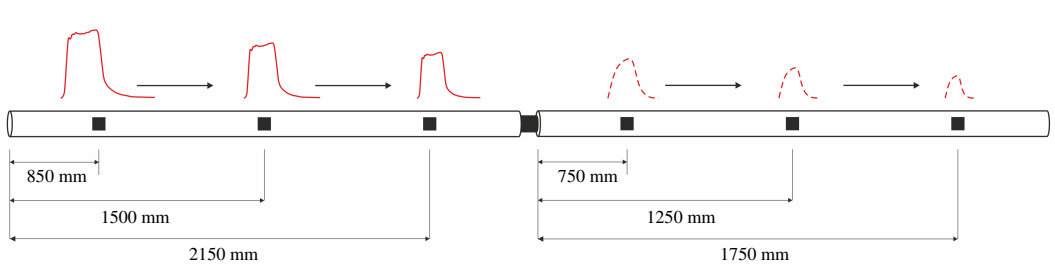

Fig. 4.21 – Location of the strain gauges with their corresponding signal placed on the incident bar (solid line) and transmission bar (dashed line) [Bieler and Weinberg 2025d].

The recorded signal at position $x_3 = 2150$ mm applied to the incident bar is used for validation. This signal is predicted using the method described above based on the measurements at positions $x_1 = 850$ mm and $x_2 = 1500$ mm. Then the predicted signal is compared to the actual measurement, see Fig. 4.22 a). Both signals are shifted back to time zero for a better comparability. In addition, in Fig. 4.22 b), the amplitude spectrum for the measured and reconstructed signal is plotted. Both figures show that the FFT method is well suited to predicting signals at different bar positions based on two measured signals. The existing signals at the interface of the incident bar and specimen are important for the subsequent calculation.

Analogous to validating the incident bar signal, the method is applied to the transmission bar. The measurement at position $x_4 = 750$ mm is reconstructed based on the measurements of $x_5 = 1250$ mm and $x_6 = 1750$ mm. Here, the transmitted pulse must be reconstructed from the signals that occur later in time. This type of pulse reconstruction is also used to determine the reflected pulse at the interface between the incident bar and the specimen, based on the reflected pulses measured at the strain gauge mounted to the incident bar. Fig. 4.22 c) and Fig. 4.22 d) show the validation of this backward reconstruction by comparison of the measured and reconstructed transmission pulse at the measuring point $x_4 = 750$ mm.

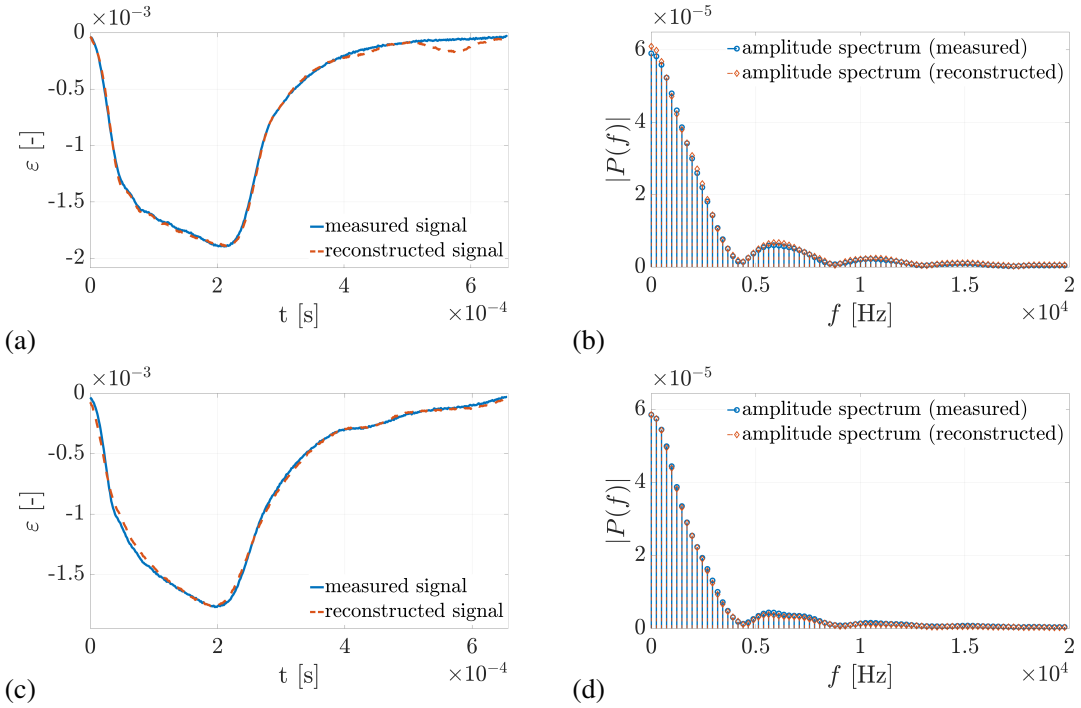

Fig. 4.22 – Comparison of measured predicted/corrected signals at position x_3: a) incident pulse, b) incident spectrum and position x_4: c) transmitted pulse and d) transmitted spectrum.

The validation demonstrates a good agreement between the measured and reconstructed signals. For the actual experiments, the pulses at the interfaces between the bars and the specimen are of particular relevance. Fig. 4.23 shows the three measured signals from the strain gauges and the reconstruction of the corresponding pulses at the interfaces between the specimen and the bars. Here, it can be seen, that the reconstructed amplitude of the incident pulse is smaller than the measured pulses; the reconstructed signal occurs later in time and therefore undergoes higher attenuation due to the distance it propagates. The situation is reversed for the transmission pulse. Due to the backward reconstruction, the calculated pulse exhibits a higher amplitude, since it corresponds to an earlier point in time than the signals measured on the transmission bar.

4.5.3 Experimental results at different strain rates

Testing soft materials is challenging not only in terms of signal correction. Specimen thickness is a crucial factor in SHPB experiments. In general, the specimen thickness for soft materials must be rather thin in order to maintain stress equilibrium. The thin geometry of the specimen allows the stress wave to pass through the specimen multiple times to ensure uniform stress distribution. Due to the low wave propagation speed in very soft materials, multiple passes require more time than with harder polymers. However, very thin specimens pose a problem in terms of surface precision. The thinner the specimen thickness, the more difficult it is to

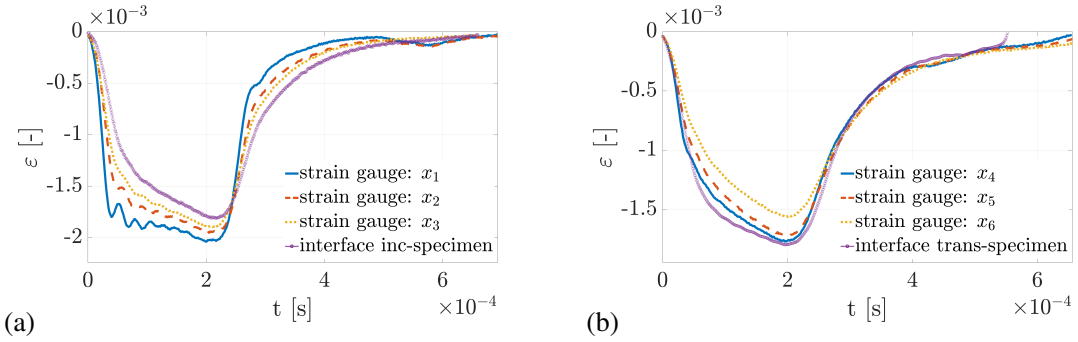

Fig. 4.23 – Measured signals from the three strain gauges applied to the incident bar a) and to the transmission bar b), as well as pulses determined at the interface between the bars and the specimen based on signal correction.

achieve a good surface finish or to process and optimize the contact surface. A suboptimal surface, in turn, causes increased friction between the bars and the specimen. A compromise must therefore be found between specimen thickness and surface quality. A ratio of thickness to diameter of $l_s/d_s = 0.2.....0.5$ has proven to be a good compromise. The specimen evaluated here have a diameter of $d_s = 17$ mm and a thickness of $l_s = 5$ mm, resulting in a ratio of $l_s/d_s = 0.3$.

Since the PMMA material of the bars already attenuates the pulse, no pulse shaper was used for the experiments with soft materials. The lower impedance and wave propagation velocity of the PMMA bars naturally result in a smoother rise time of the pulse. High frequencies are already attenuated by the internal damping of the material. Similar to the results for the tests in Section 4.4, the results in this section are based on five measurements per strain rate. The fluctuations in the respective strain rates for the material 3D-Materials SuperFlex can be found in Table 4.5.

To clarify the measured pulses, one representative measurement for each strain rate is shown in this section. All measurements fullfiled stress equilibrium, which is prerequisite for obtaining meaningful measurements. The wave propagation velocity c of the material 3D material SuperFlex in Table 4.4 was determined in the same way as in Section 4.4. The material pairing of bar material PMMA and the specimen material 3D material SuperFlex results in the following reflection coefficient and transmission coefficient:

$$\alpha_{\text{SuperFlex}} = -0.49$$
$$\beta_{\text{SuperFlex}} = 0.51.$$

Fig. 4.24 to Fig. 4.26 show the actual signals recorded by the six strain gauges applied for three different strain rates. The required impulses at the interfaces between the bars and the specimens were calculated from these signals using the described method of spectral analysis-based correction. Fig. 4.24 b) to Fig. 4.26 b) show the calculated time-shifted signals, whereas

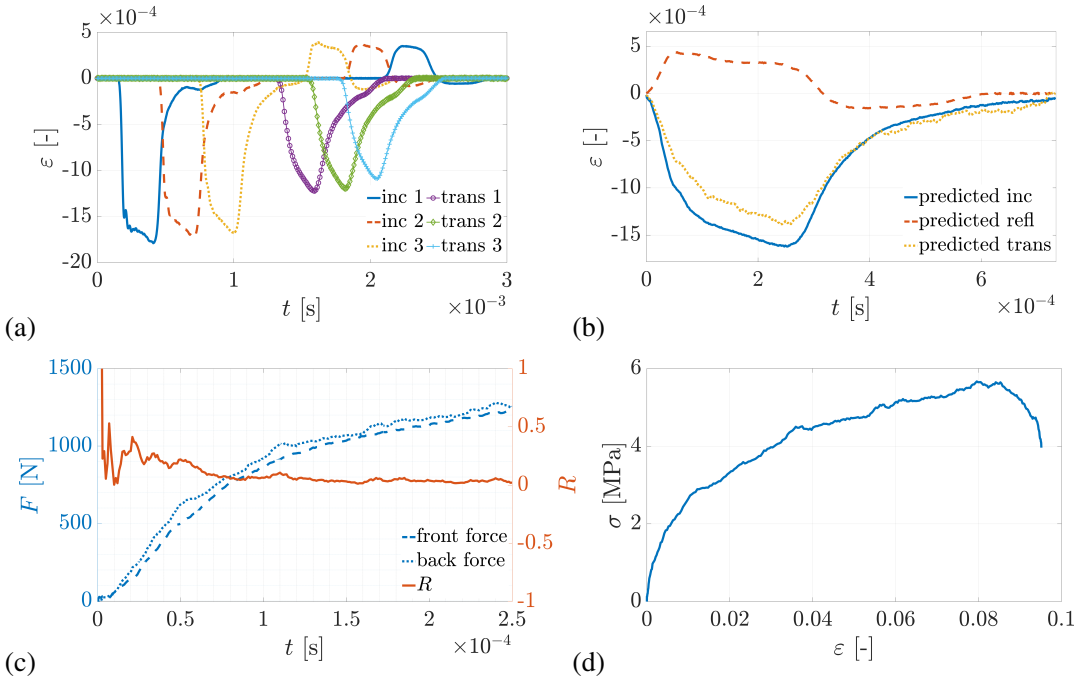

Fig. 4.24 – a) Recorded signals of six strain gauges, b) predicted time-shifted pulses at the interfaces of bar and specimen, c) front and back forces at the specimen surfaces and the resulting stress equilibrium ratio R and d) the calculated stress-strain curve of the predicted signals for 3D Materials SuperFlex at a strain rate of $\dot{\varepsilon} = 300\text{s}^{-1}$.

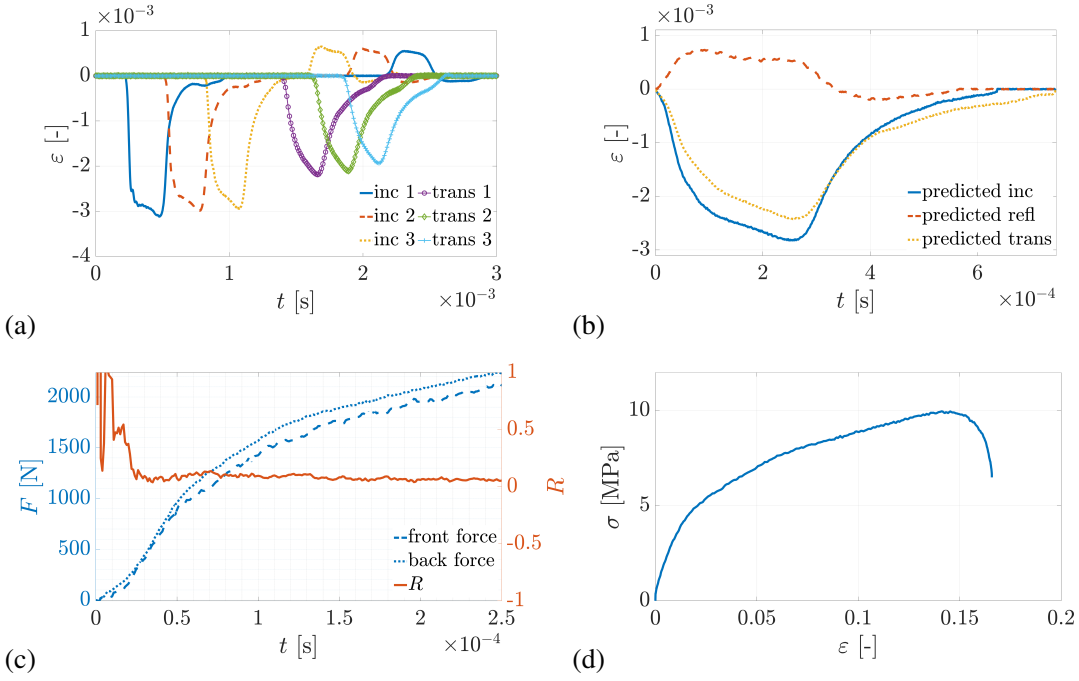

Fig. 4.25 – a) Recorded signals of six strain gauges, b) predicted time-shifted pulses at the interfaces of bar and specimen, c) front and back forces at the specimen surfaces and the resulting stress equilibrium ratio R and d) the calculated stress-strain curve of the predicted signals for 3D Materials SuperFlex at a strain rate of $\dot{\varepsilon} = 500\text{s}^{-1}$.

TABLE 4.4 – Dimensions of the SHPB setup for testing soft materials.

	incident bar	transmission bar	striker	SUPERFLEX
material	PMMA	PMMA	PMMA	TPU-like
d [mm]	20.00	20.00	20.00	17.00
l [mm]	3000.00	2000.00	300.00	5.00
ρ [kg/m^3]	1180.00	1180.00	1180.00	1150.00
E_{stat} [MPa]	3000.00	3000.00	3000.00	4.90
c [m/s]	2410.00	2410.00	2410.00	833.33
Z [kg/m$^2\mu$s]	2.84	2.84	2.84	0.96

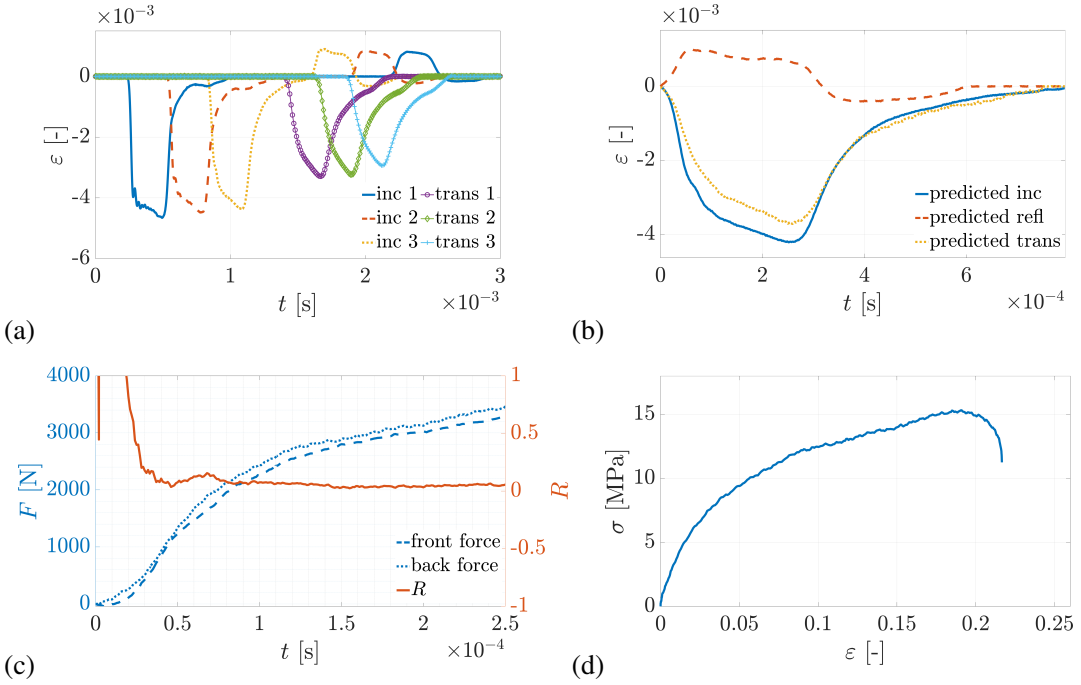

FIG. 4.26 – a) Recorded signals of six strain gauges, b) predicted time-shifted pulses at the interfaces of bar and specimen, c) front and back forces at the specimen surfaces and the resulting stress equilibrium ratio R and d) the calculated stress-strain curve of the predicted signals for 3D MATERIALS SUPERFLEX at a strain rate of $\dot{\varepsilon} = 700\text{s}^{-1}$.

Fig. 4.24 c) to Fig. 4.26 c) show the stress equilibrium ratio R. The strain rate $\dot{\varepsilon}$ is calculated in each case based on the reflected impulse, see Eq. (4.42). From the pulses determined by signal correction, a stress-strain curve can be generated for the specific strain rate $\dot{\varepsilon}$, cf. Eqs. (4.43) and (4.44).

The evaluation of the stress-strain relationship in the SHPB experiment - particularly the determination of the modulus of elasticity - is considerably more complex for soft materials than for metals or stiffer plastics, as described in Section 4.4. Since soft materials such as elastomers, rubber, or even TPU-like materials like the 3D MATERIAL SUPERFLEX investigated

in this work have only a very small and poorly defined linear-elastic initial region, even the determination of the quasi-static modulus of elasticity is difficult to examine, see Section 3.4.2. Standard methods for calculating the modulus of elasticity include the tangential modulus, typically evaluated at elongations of less than 1%, and the secant modulus, which is defined at spcific points of elongation. However, since neither approach is precisely defined, different experimenters may obtain varying results. The absence of standardized experimental procedures makes the evaluation of these material constants under dynamic loading conditions even more challenging. In this work, the modulus of elasticity is determined - analogous to the procedure used for the acrylic-like polymers - by linear regression of the stress-strain curve between $\varepsilon = 0.025$ and $\varepsilon = 0.05$.

The behavior of soft materials differs significantly when considering quasi-static and impact loading. Stiff polymers tend to fail at very high strain rates, as they exhibit pronounced hardening under those conditions. Soft polymers stiffen for the same reason; however, their modulus of elasticity of these materials is very low - even with a significant increase under impact loading, they are still less prone to damage. For this reason, such materials are well suited for absorbing impact energy, see Chapter 7.

4.5.4 Comparison of mechanical response at different strain rates in soft polymers

The approach used in this work to determine the modulus of elasticity reveals significant differences between the evaluated strain rates of $\dot{\varepsilon} \approx 300\text{s}^{-1}$, $\dot{\varepsilon} \approx 500\text{s}^{-1}$, and $\dot{\varepsilon} \approx 700\text{s}^{-1}$ and the quasi-static values. Fig. 4.24 d) to Fig. 4.26 d) show the stress-strain curves for the different strain rates of 3D-Materials SuperFlex.

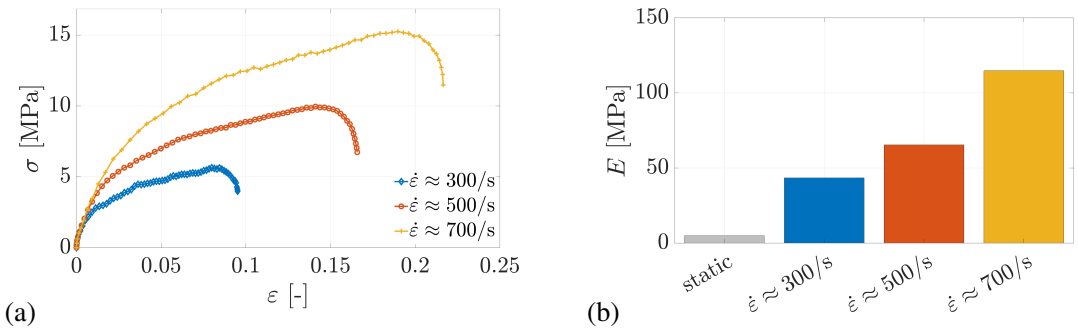

Fig. 4.27 – a) Comparison of the stress-strain curves of 3D-Materials SuperFlex at different strain rates and b) the elastic modulus calculated by the slope of the elastic region of the stress-strain diagram.

Table 4.5 is based on the mean value of the moduli of elasticity determined from quasi-static tests in Section 3.4 of this work. Refered to the averaged static modulus of elasticity, the material undergoes significant stiffening and thus a considerable increase in the modulus of elasticity for high strain rates. For a strain rate of $\varepsilon = 300\text{s}^{-1}$, the modulus of elasticity

increases by a factor of 88%. At a strain rate of $\varepsilon = 700\text{s}^{-1}$, the modulus of elasticity shows an increase of 2200% compared to the static one. Fig. 4.27 illustrates the pronounced differences in the stress-strain behavior at various strain rates investigated by showing all three stress-strain curves together with corresponding bars indicating the determined moduli of elasticity.

Table 4.5 – Static modulus of elasticity and dynamic moduli of elasticity of 3D-Materials Super-Flex for different strain rates, the corresponding striker velocity v_{st}.

E [MPa]	$\dot{\varepsilon}$ [s^{-1}]	v_{st} [m/s]	pulse shaper
4.9	quasi-static	-	-
43.4	314.60 ± 14.94	6.3	-
65.4	552.80 ± 10.62	11.1	-
114.8	727.60 ± 15.04	16.1	-

CHAPTER 5

DYNAMIC BEHAVIOR OF GLASS FIBER REINFORCED PLASTICS

We have already published parts of the chapter presented here in a similar form, and therefore, it contains illustrations and results identical to those in the publication [Bieler et al. 2023]. The co-authors S. Haller and R. Brandt provide the investigated material and the static reference results, whereas the dynamic investigation as well as the subsequent analysis were conducted at the Chair of Solid Mechanics.

Fiber-reinforced materials, particularly unidirectional glass fiber-reinforced plastic (GFRP), are used for highly advanced crash-absorbing structures, e.g., crash boxes in modern racing cars. In regular road traffic, guardrails and protective rails are made of steel; however, through changes in design and the choice of materials, the system can be designed in a way that both drivers and objects behind the protection rail are protected. Since most fatal accidents occur on country roads, it is reasonable to use high-quality GFRP materials. Furthermore, hybrid constructions are particularly desirable for cost reasons, i.e., constructions made of a of steel and GFRP combination. To design such structures against car impact, strain rate-dependent material data for GFRP are needed. Therefore, we investigate GFRP at high strain rates up to 700 s^{-1} in this work. For the impact experiments of our GFRP specimens, we use the split Hopkinson pressure bar.

Various authors have already studied the dynamic behavior of GFRP materials, e.g., [Amijima and Fujil 1980; Yuan and Takeda 2000; Takeda and Wan 1995; El-Habak 1993; Kumar et al. 1986; Kim et al. 2019; Shokrieh and Omidi 2009]. Most investigations focus on the failure modes and strengths at higher strain rates. While [Amijima and Fujil 1980] concentrated on the effect of different fiber orientations, the works [Yuan and Takeda 2000] and [Takeda and Wan 1995] only present experiments on a specimen with fiber orientation in the loading direction;

here an increase in Young's modulus was found. The work [Yuan and Takeda 2000] also dealt with different fiber volume fractions in their specimens. An increasing stress-strain curve is observed by [El-Habak 1993] by raise of strain rates for different fiber volume fractions during the tests. In the publication of [Kumar et al. 1986] test specimens similar to ours in terms of fiber volume fraction f_F. They noticed an increase in Young's modulus with an increasing strain rate for both parallel and orthogonal fiber orientation. The paper of [Shokrieh and Omidi 2009] deals with the investigation of the compressive impact properties of GFRP utilizing a servo-hydraulic apparatus (HSCT). This method allows to perform experiments in medium strain rates (up to approx. $\dot{\varepsilon} = 100\ s^{-1}$). The authors specify a dynamic Young's moduls (E_{dyn}) carefully in their work.

Since all investigated GFRP materials differ concerning the matrix material and the fiber material and its fiber volume fraction f_F, comparability of experimental data is possible to a limited extent.

5.1 Specimen preperation and properties

To manufacture UD-GFRP plates, the raw material of the unidirectional GFRP was available as tape. It consisted of an epoxy resin matrix and glass fibers with diameters of $20\,\mu m$, while the fiber volume fraction f_V reached 58%. The tape material has been provided by the company Mubea Attendorn. A specific amount of tapes with a thickness of each $600\,\mu m$ were pressed inside a hot pressing tool under a pressure of 4 bar and temperature up to 230°C. After the consolidation, cylindrical specimens were cut out using a water jet process. Since waterjet cutting produces the rough shape of the specimens, they are subsequently processed further. Computerized Numerical Control (CNC) machines turning ensures the roundness of the cylindrical specimen, and grinding processes guarantee a perfect surface of the specimen. Two types of cylindrical specimens have been prepared. The first type of specimen were cut in a way that the fibers were oriented parallel to the cylinder axis, see Fig. 5.1 (left). These specimens are refered to GFRP $\parallel$ in the following. The second type of specimen was prepared that the fibers oriented perpendicular to the cylinder axis, see Fig. 5.1 (right). These types of specimens are named GFRP $\perp$. Fig. 5.1 (bottom) show images of the prepared surfaces of the specimens under the Keyence VHX-900F digital microscope. The schematic illustration of the fiber orientation in Fig. 5.1 (top) can be clearly seen. The ratio of length l to diameter d is carefully chosen to achieve a constant strain rate as well as a stress equilibrium in the SHPB tests. A stress equilibrium in the specimen can be reached more quickly when using thin specimens [Dai et al. 2010; Gorham 1989].

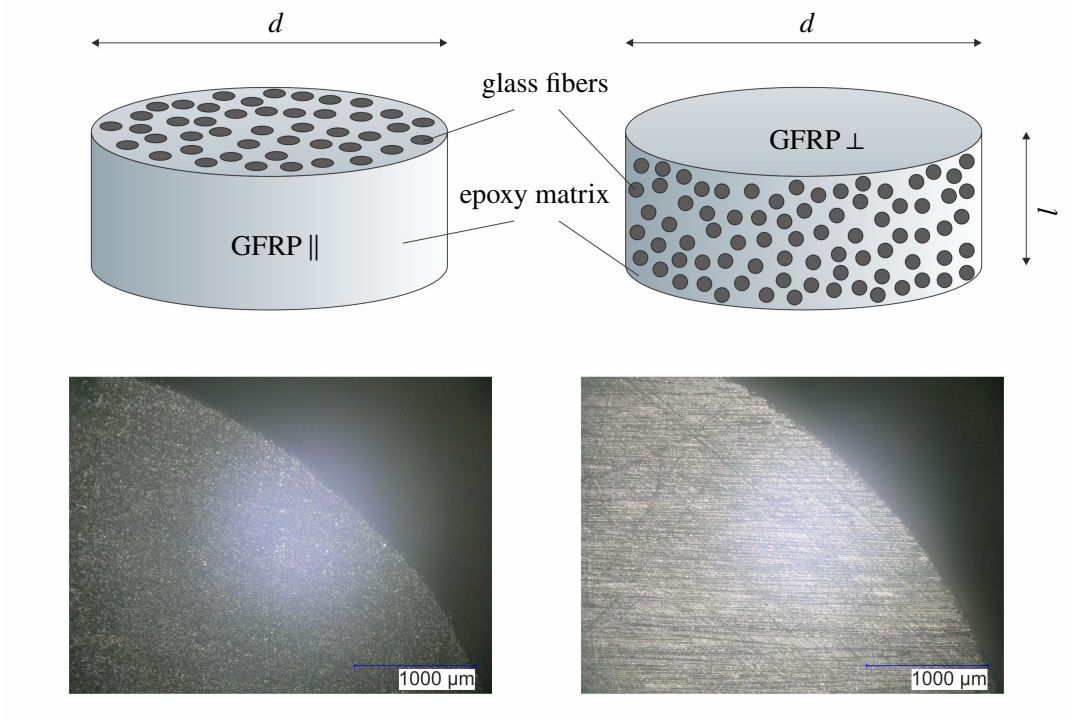

Fig. 5.1 – Two different types of GFRP specimens, with fibers aligned parallel (left) and perpendicular (right) to the force applied to the fiber matrix, which consists of epoxy resin. The images at the bottom show microscope images of the polished surfaces, revealing the differences in orientation.

5.2 Fiber volume fraction of the GFRP material

The Voigt-Reuss rule of mixture method is widely used in materials science to estimate the effective elastic properties of composite materials. By considering both the upper bound (Voigt model) and lower bound (Reuss model) of the elastic properties, the Voigt-Reuss-Hill method provides a more realistic prediction of the overall behavior of the composite material. This method is beneficial in predicting the mechanical response of heterogeneous materials, such as composites, where the individual phases have different elastic properties. Researchers and engineers often rely on the Voigt-Reuss rule of mixture method to design and optimize composite materials for specific applications. The lower and upper bound can be described using the following equations:

$$E_{\text{low}} = \left(\frac{f_{\text{M}}}{E_{\text{M}}} + \frac{f_{\text{F}}}{E_{\text{F}}} \right)^{-1} \tag{5.1}$$

$$E_{\text{up}} = f_{\text{F}} E_{\text{F}} + f_{\text{M}} E_{\text{M}} \tag{5.2}$$

Here f_{F} and f_{M} refer to the volume fraction of the fiber's and the matrix material, and E_{F} and E_{M} denote the corresponding moduli of both materials. The modulus of elasticity for glass is about

80 GPa. In comparison, epoxy resin has a modulus of elasticity of about 4.5 GPa. Inserting these values in Eqs. (5.1) and (5.2) and plotting the results, we obtain the curves shown in Fig. 5.2. The moduli of elasticity specified by the manufacturer for both fiber directions correspond approximately to the diagram in Fig. 5.2. The upper and lower static modulus of elasticity can be approximated from the digram for a given fiber content:

$$E_{\text{stat}} = 43.44\,\text{GPa} \quad \text{for} \quad \text{GFRP} \parallel$$
$$E_{\text{stat}} = 8.85\,\text{GPa} \quad \text{for} \quad \text{GFRP} \perp$$

The values determined correspond well with the values specified by the manufacturer. The material's strong orientation dependence (transversal isotrop) on its load is remarkable here. The influence of the fibers is significant when considering the elastic modulus. Under quasi-static loading, GFRP $\parallel$ exhibits an elastic modulus nearly five times higher than the GFRP $\perp$.

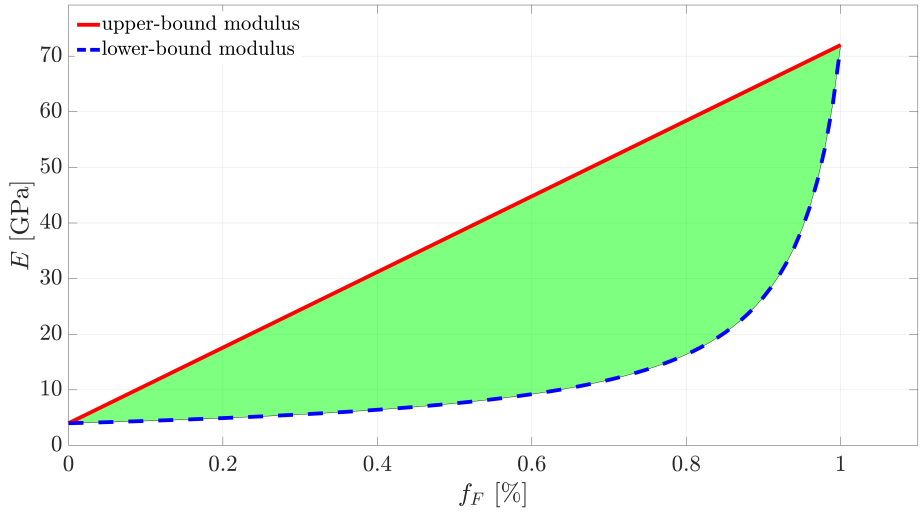

Fig. 5.2 – Voight-Reus rule of mixture for the investgated GFRP.

5.3 Experimental setup

The setup of the SHPB is similar to the setup for the dynamic characterization of homogeneous materials. However, bars and the striker made of steel, were selected for the GFRP material tests, see Fig. 5.3. The geometric dimensions of the SHPB setup and the corresponding material data are listed in Table 5.1. The reflection coefficient α and transmission coefficient β have the following values for the pairing of steel and the two GFRP specimens:

$$\alpha_{\text{GFRP}\parallel} = -0.6 \qquad \alpha_{\text{GFRP}\perp} = -0.77$$
$$\beta_{\text{GFRP}\parallel} = 0.4 \qquad \beta_{\text{GFRP}\perp} = 0.23$$

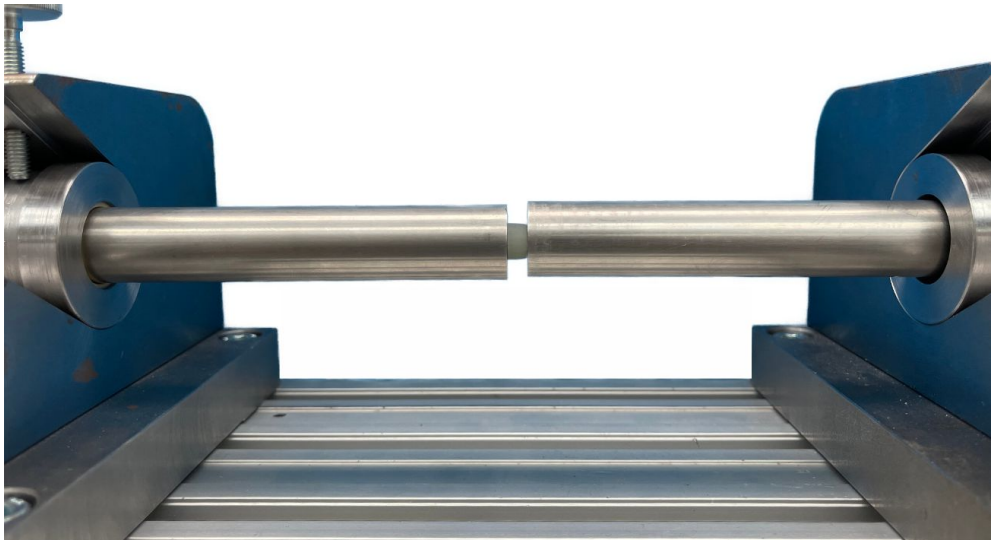

Fig. 5.3 – GRFP specimen clamped between steel bars.

Table 5.1 – Dimensions of the conventional SHPB setup equipped with steel bars.

	incident bar	transmission bar	striker	GFRP ∥	GFRP ⊥
material	steel	steel	steel	glass/ epoxy	glass/ epoxy
d [mm]	20.00	20.00	20.00	10.00	10.00
l [mm]	1800.00	1800.00	300.00	3.00 - 5.00	3.00 - 5.00
ρ [kg/m^3]	7850.00	7850.00	7850.00	2020.00	2020.00
E_{stat} [GPa]	210.00	210.00	210.00	43.40	8.80
c [m/s]	5100.00	5100.00	5100.00	4900.00	2600.00
Z [kg/m$^2\mu$s]	40.04	40.04	40.04	9.90	5.25

The striker velocities in the experiments vary between 4 m/s to 8.5 m/s. Different striker lengths were tested to determine a suitable pulse length, whereby the diameter always corresponded to 20 mm. For the GFRP specimens, a striker length of 300 mm was found to be sufficient for the speeds mentioned. To modify the pulse profile, pulse shapers were applied to the front surface of the incident bar, see Fig. 5.4 a). The circular pulse shapers were made of lead and had a thickness of 0.3 mm to 0.5 mm and a diameter of 8 mm. This allows high spectral frequencies to be filtered out of the signal (low-pass filter), resulting in a smoother pulse, cf. [Weinberg et al. 2018]. Furthermore, the pulse's rise time is increased by the plastic deformation of the pulse shaper. The effect of lead pulse shapers with different thicknesses on the shape of the pulse is shown in Fig. 5.4 b). With the described setup, results could be derived for three different strain rates of the material: 300 s^{-1}, 500 s^{-1}, and 700 s^{-1}.

In order to minimize friction and inertia effects, a uniform deformation of the specimen is necessary. A length-to-diameter ratio of about $l_s/d_s = 2/3$ was selected for the testet specimens.

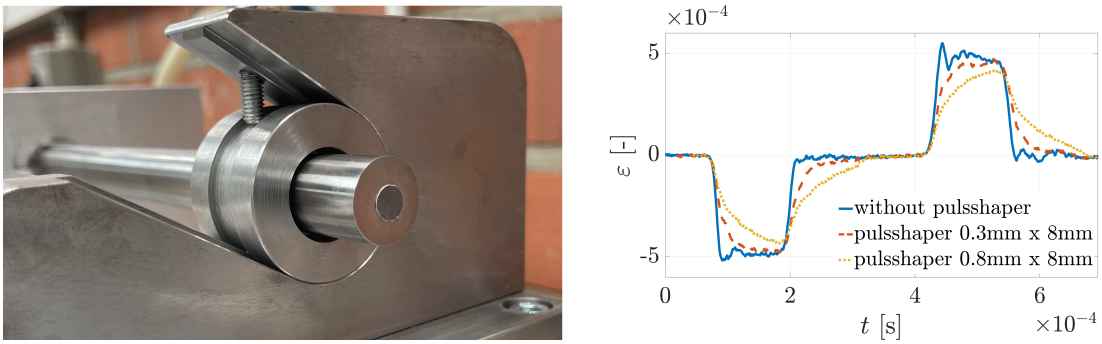

(a) (b)

Fig. 5.4 – a) Pulse shaper mounted to the surface of the incident bar and b) shapes of the signal by different applied pulse shapers.

Lubricant was applied to reduce friction effects between the specimen's body and the bar surfaces, cf. [Al-Mousawi et al. 1997]. Stress equilibrium according to Eqs. (4.76) and (4.77) was achieved in the tests, see Fig. 5.5.

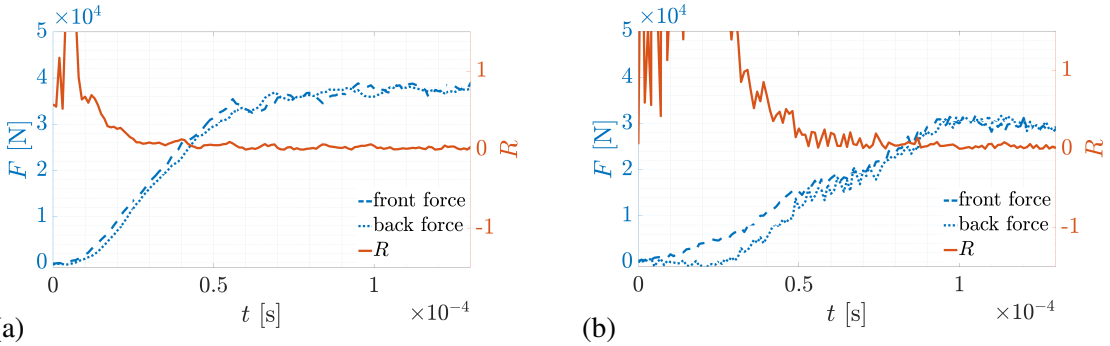

(a) (b)

Fig. 5.5 – Forces on the front side (dashed line) and back side (dotted line) of the specimen as well as the stress equilibrium factor R (solid line); a) GFRP $\parallel$ and b) GFRP $\perp$.

5.4 Experimental results

Each specimen was tested once for the experiments. Although the specimens showed no recognizable damage or cracks after the experiment, internal structural fractures cannot be ruled out. Five specimens were tested under the same test conditions for each configuration. In this way, erroneous measurements due to possible changes inside the material structure can be ruled out as far as possible. The GFRP material was tested both in the fiber direction and orthogonal to the fiber direction and at three different strain rates ($\approx 300\text{s}^{-1}$, 500s^{-1}, 700s^{-1}), resulting in a test setup of 30 measurements.

The stress-strain diagrams in Fig. 5.6 were generated from the raw data of the measurement program Perception and postprocessed with Matlab. For the calculations of strain ε, strain

rate $\dot{\varepsilon}$ and stress σ, Eqs. (4.42), (4.43) and (4.44) from Section 4.2.3 were used.

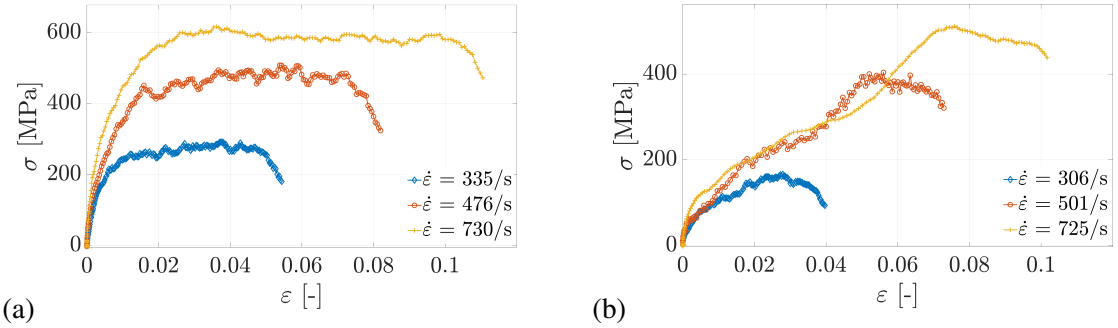

Fig. 5.6 – Stress-strain diagramms for GFRP ∥ (a) and GFRP ⊥ (b) at different strain rates.

As expected, the stresses in the specimens with parallel fiber orientation to the load direction are higher than those with perpendicular orientation. This higher stiffness results from the fibers being loaded in their axial orientation. The surrounding matrix material additionally holds the fibers in position and prevents them from buckling. For the GFRP ⊥ specimens, the fibers can move more easily due to the less stiff matrix material, allowing for higher strain at lower stresses.

Evaluating the determined stress-strain data allows an estimation of the dynamic modulus of elasticity for the tested material at the investigated strain rates. A regression in the linear increase of the curves up to a strain of 0.5% was selected for this reason. It should be mentioned that the dynamic modulus of elasticity must be determined individually for each strain rate. In this respect, this work shows that a material's dynamic modulus of elasticity increases with an increase in the strain rate. The calculated data are listed in Table 5.2 and 5.3 for the different specimens and strain rates.

Table 5.2 – Static modulus of elasticity and dynamic moduli of unidirectional GFRP ∥ with a fiber volume of 58% for different strain rates.

E [GPa]	$\dot{\varepsilon}$ [s^{-1}]	v_{st} [m/s]	pulse shaper
43.4	static	-	-
46.6	335.60 ± 13.09	4.8	lead (8 mm × 0.3 mm)
50.8	476.80 ± 18.75	7.2	lead (8 mm × 0.3 mm)
53.5	729.80 ± 15.39	8.5	lead (8 mm × 0.3 mm)

5.5 Comparison of results with previous studies

Materials with high stiffness and sufficient ductility are capable of absorbing significant amounts of energy before they fail. In this context, strain rate sensitivity describes the phenomenon

Table 5.3 – Static modulus of elasticity and dynamic moduli of unidirectional GFRP ⊥ with a fiber volume of 58% for different strain rates.

E [GPa]	$\dot{\varepsilon}$ [s^{-1}]	v_{st} [m/s]	pulse shaper
8.8	static	-	-
13.4	306.60 ± 14.12	4.0	lead (8 mm × 0.4 mm)
17.3	501.40 ± 6.88	4.9	lead (8 mm × 0.4 mm)
21.1	725.60 ± 12.40	6.1	lead (8 mm × 0.5 mm)

whereby the mechanical properties of a material - in particular its stiffness and strength - can increase under dynamic loading. This behavior is crucial for use in safety-relevant components, such as vehicle structures, protective systems, or housings for machine components that are potentially exposed to dynamic impact loads.

Modern manufacturing processes, such as customized forming processes or the integration of energy-absorbing interlayers and geometric inlets, can be used to optimize materials specifically for this type of load behavior. As shown in [Raj et al. 2020], fiber-reinforced composites based on Rubcrete exhibit significantly higher energy absorption compared to conventional materials like pure concrete. Such materials are mainly suitable for applications such as guardrail systems or protective barriers, where high impact energy must be dissipated in a targeted manner. The dynamic compression tests on the GFRP specimens show a significant increase in the stress-strain curves with increasing strain rate. This behavior is consistent with the results of previous studies, cf. [El-Habak 1993; Kumar et al. 1986; Takeda and Wan 1995; Tarfaoui et al. 2009].

However, a direct comparison of the strain rate-dependent stress-strain behavior between different studies is difficult because there is currently no standardized method for performing split Hopkinson pressure bar tests. In addition, material-specific parameters significantly influence the measurement results. The key influencing factors are listet in the following:

- strain rate
- selected test method
- fiber volume fraction f_F
- orientation of the fiber material
- matrix and fiber material

The orientation of the fibers within the specimens is highly relevant, as it significantly influences the mechanical response behavior under dynamic loading. Table 5.4 provides an overview of various polymer matrices investigated in the literature, along with corresponding fiber volume fraction in the range of $0.46 < f_F < 0.60$, as provided by the respective authors. The increase in the modulus of elasticity with increasing strain rate observed in our experiments is in good agreement with the trends reported in the literature. It confirms the strain rate-sensitive increase in stiffness of GFRP materials under dynamic loading.

Table 5.4 – Comparison of static and dynamic elastic moduli experimental results determined by SHPB tests [El-Habak 1993; Kumar et al. 1986; Tarfaoui et al. 2009; Yuan and Takeda 2000] and servohydraulic testing [Shokrieh and Omidi 2009]; the values are not explicitly given but are derived from the data in the publications.

source	f_F	matrix material	fiber orientation	E_{stat} [GPa]	E_{dyn} [GPa]	$\dot{\varepsilon}$ [s^{-1}]
here	0.58	epoxy resin	$\parallel$	43.44	46.60	≈ 300
here	0.58	epoxy resin	$\parallel$	43.44	50.80	≈ 500
here	0.58	epoxy resin	$\parallel$	43.44	53.50	≈ 700
[El-Habak 1993]	0.61	epoxy resin	$\parallel$	-	36.50	620
[Kumar et al. 1986]	0.46	epoxy resin	$\parallel$	32.00	33.50	265
[Shokrieh and Omidi 2009]	0.50	epoxy resin	$\parallel$	24.79	38.25	85
[Tarfaoui et al. 2009]	0.54	epoxy resin	$\parallel$	-	35.50	429
[Tarfaoui et al. 2009]	0.54	epoxy resin	$\parallel$	-	37.25	702
[Tarfaoui et al. 2009]	0.54	epoxy resin	$\parallel$	-	60.00	1031
[Yuan and Takeda 2000]	0.60	vinyl ester	$\parallel$	37.50	48.50	1020
here	0.58	epoxy resin	$\perp$	8.85	13.40	≈ 300
here	0.58	epoxy resin	$\perp$	8.85	17.30	≈ 500
here	0.58	epoxy resin	$\perp$	8.85	21.10	≈ 700
[Kumar et al. 1986]	0.46	epoxy resin	$\perp$	7.50	9.50	725
[Tarfaoui et al. 2009]	0.54	epoxy resin	$\perp$	-	25.25	265

Chapter 6

Energy absorption of open-cell structures under static loading conditions

Some parts of this chapter can already be found in publications [Bieler and Weinberg 2025a,b]. The results from the published results were extended for this work.

In nature, numerous examples of cellular structures can be found. Some of these exhibits an ordered architecture but are more commonly encountered as stochastically distributed cell structures. Medical scientists, for example, are familiar with cellular materials in the form of internal bone structures. Bakers observe cell-like structures in bread, and biologists study structural forms such as corals or wood grain, see Fig. 6.1, [Ashby 2006].

Cellular structures, particularly lattice structures, are used in various fields due to their lightweight yet efficient properties [Pan et al. 2020; Yan et al. 2015]. In architecture, lattice structures are employed in building facades, roofs, and interior framework to create aesthetically pleasing designs while minimizing materials usage. In civil engineering, such structures are encountered in many aspects of everyday life, for example in the construction of bridges and buildings. The Eiffel Tower is a famous building and a classic example of a truss structure in civil engineering. Another prominent building of shell structures is the Sydney Opera House in australia.

Lattice structures are widely used in medical implants, particularly in bone scaffolds and prostheses [Al-Jassir et al. 2013; Tao and Leu 2016], where they mimic the structure of natural bone to improve better integration and functionality. Similarly, stents rely on lattice structures and are designed to supports vessels and maintain patency during surgical procedures [Jiang et al. 2022].

In engineering fields, these structures are particularly important, as they offer multiple advantages for different applications. In aerospace engineering, lattice structures are part of the construction of wing components [Moon et al. 2014], fuselages [Niemann et al. 2013], and partsatellite modules [Kim et al. 2018]. Their ability to maintain strength while minimizing weight is crucial for flight efficiency. Lattice structures have long played a key role in the automotive industry: weight reduction combined with high strength plays an important role, e.g., in chassis, bumpers, and structural components. Other areas of application are the heat transfer design [Alqahtani et al. 2023], the development of heat exchangers, or the utilization of the filtration properties of lattice structures [Hasib et al. 2015]. In power generation, lattice structures are employed in the design of gas turbines fan blades due to their good weight-stiffness properties [Magerramova et al. 2018]. However, lattice structures are also used in military applications, e.g., for lightweight armor, radar components, and other structural elements.

Furthermore, due to their good deformability, lattices have excellent energy-absorbing properties, which are essential in many areas of technology. This energy absorption is the main focus of this chapter, which deals with energy absorption under static loading conditions.

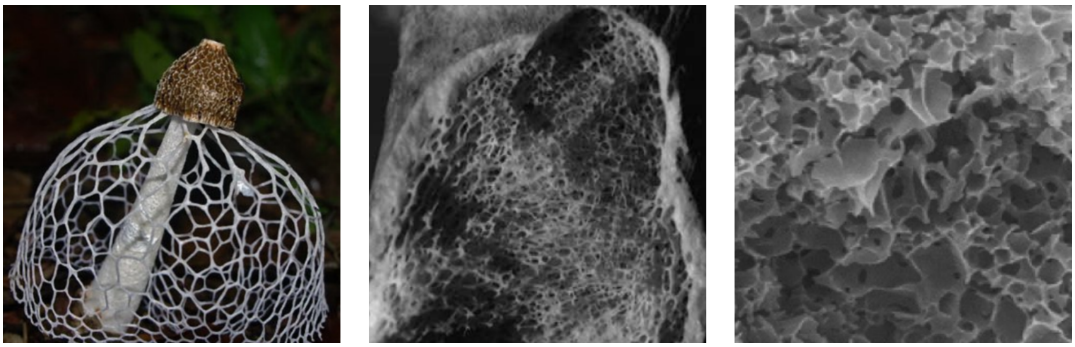

(a) (b) (c)

Fig. 6.1 – Various cellular structures from nature and technology: a) lattice structure of the fungus Phallus indusiatus [Winkler et al. 2014], b) inner bone structure [Olszta et al. 2007], c) SEM images of activated carbon [Sun et al. 2020].

6.1 Classification

As a superordinate class of structures, cellular materials are classified into the following categories, see Fig 6.2. At the primary level, cellular structures are divided into regularly periodic and irregular structures. Irregular structures usually refer to foams. These irregular structures can be further subdivided into open- and closed-cell pore structures [Bieler and Weinberg 2023; Park et al. 2022]. Due to the stochastic distribution of the pore number and size of foams, the material response is always subject to inevitable fluctuations. This is less the case with lattice structures, as their regular architecture ensures similar loading conditions across specimens. Honeycomb structures represents a widely used and well-known category of ordered,

closed-cell structures. Research on these structures is ongoing, and they are utilized to achieve high stiffness with minimal weight. The authors [Thomas and Tiwari 2019] investigate these structures and their behavior under loads from different directions both experimentally and numerically (in-plane, out-of-plan, bending). The work of [Ambur and Cruz 1995; Hazizan and Cantwell 2003; Nemes and Simmonds 1992] deals with modeling dynamic loads on sandwich structures. Sandwich structures are already regularly used in many areas, such as the aerospace industry or in boat building [Palomba et al. 2022]. These structures are the subject of research in terms of their thermo-mechanical behavior for buildings [Hossain et al. 2023].

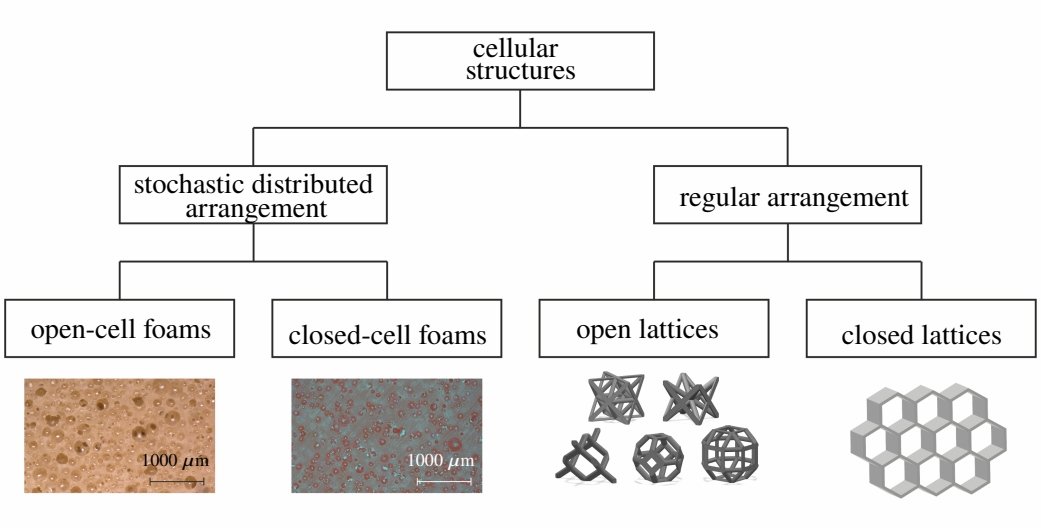

Fig. 6.2 – Cellular structure classification, [Park et al. 2022].

The present work focuses on the energy absorption behavior of three-dimensional open-celled structures. Such structures can be roughly divided into four categories; see Fig. 6.3.

The first group represents lattice structures consisting of classic beam elements. A wide variety of types of these structures differ in the number and arrangement or orientation of the struts. Due to the possibilities of additive manufacturing, such structures are the subject of numerous current publications and research. Given the vast number of variants, only a selection of the well-established structures are mentioned here: face-centered cubic FCC [Leary et al. 2018]; body-centered cubic BCC [Egan et al. 2019; Tancogne-Dejean and Mohr 2018]; OCTAHEDRON and CUBOCTAHEDRON [Hedayati et al. 2017] and RHOMBICUBOCTAHEDRON [Ahmadi et al. 2015]; OCTET, consisting of TETRA- and OCTAHEDRONS [Arabnejad et al. 2016; Tancogne-Dejean et al. 2016]; RE-ENTRANT CUBE [Li et al. 2018]; FCCZ [Lozanovski et al. 2021] and BCCZ [Zhao et al. 2022]. In the DIAMOND structure, four cheval-de-frise-like trusses are combined, resulting in a deformation-inhibiting structure [Ozdemir et al. 2016]. The structures FCCZ and BCCZ are variations of the well-known FCC and BCC structures, each with additional struts in the Z direction. This additional bar element makes the structure stiffer [Bieler and Weinberg 2023].

Plate-based structures represent a distinct class of configurations, [Tancogne-Dejean et al. 2018]. Similar to the beam-based lattice structures they also include simple cubic SC, face-centered FCC, or body-centered BCC structures. Combinations of different standard structures can be employed to enhance specific material properties, demonstrated by [Andrew et al. 2021] through the composition of SC-FCC and SC-BCC.

The third group is represented by shell-based structures. These so-called TPMS structures (triply periodic minimal surface) are defined by a series of trigonometric functions, which by definition have the properties of zero curvature with a significantly larger surface-to-volume ratio [Schoen 1970] compared to conventional foams. This group of structures is discussed in more detail in Section 6.2.2.

The fouth group consists of hierarchical-based structures. In hierarchical-based structures, the overall structures, or their individual beam elements, are themselves composed of small, constituent structures. Consequently, these configurations extend across multiple length scales. This special class of lattice structures has been investigated in [Meza et al. 2015], but is not the focus of the present thesis.

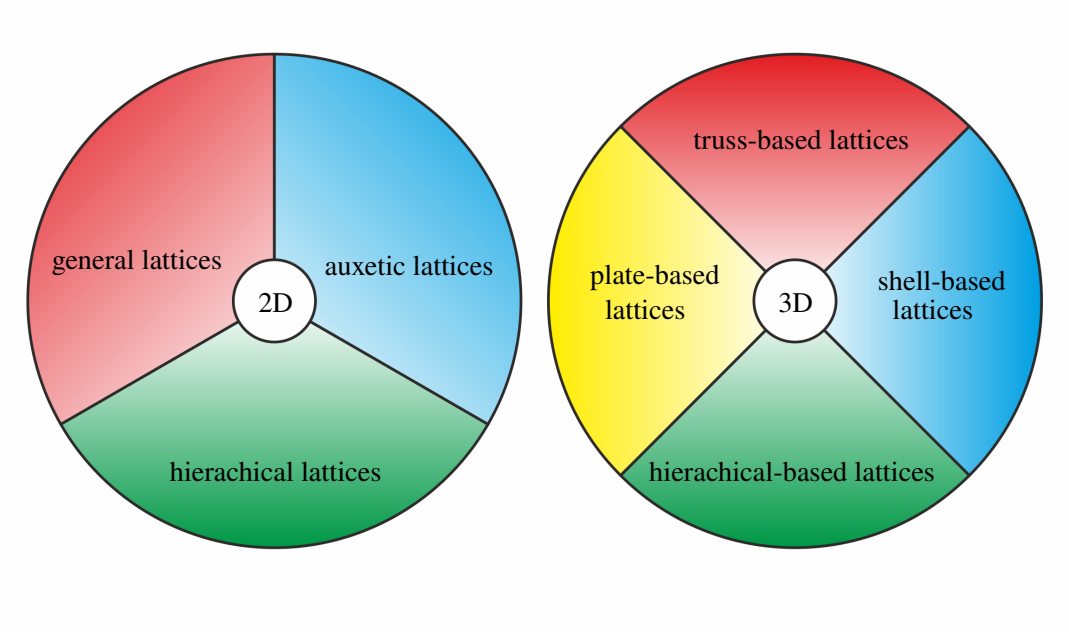

Fig. 6.3 – Different types of lattice structures in 2D and 3D, inspired by [Yin et al. 2023].

6.2 Investigated structures

This section presents the investigated lattice structures and their properties. This thesis investigates four different beam-based and four shell-based structures.

First of all, the concept of the unit cell should be explained. Here a unit cell is like a cube with a given edge length l_u, which has a reference volume V_{ref}. This volume represents the

design space for the smallest unit of the structure, [Park et al. 2022]. The final specimen for the experiments consists of a series of these unit cells. As a result, the relative density $\bar{\rho}$ of the later specimen is equal to the relative density $\bar{\rho}$ of the created unit cell, cf. Fig. 6.4. The relative density $\bar{\rho}$ within the unit cell depends on two parameters:

- edge length of the unit cell l_u
- radius of trusses r_u (for beam-based structures)
- wall thickness t_w (for shell-based structures)

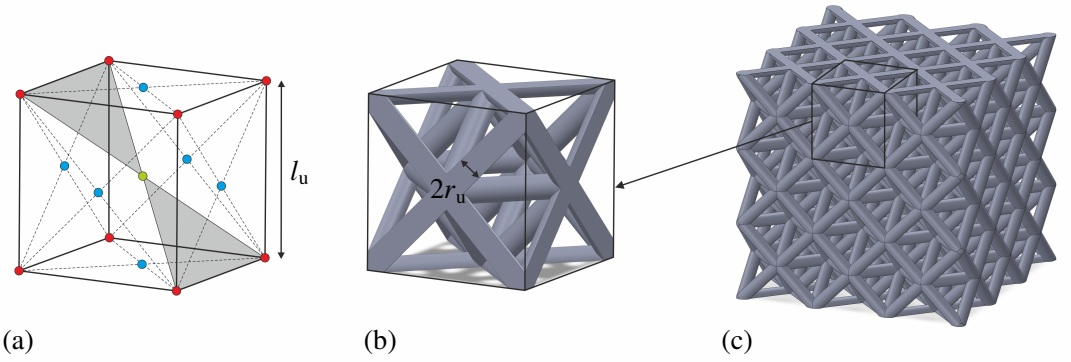

Fig. 6.4 – a) Node positions in a unit cell, b) Octet structure and c) final specimen design ($3 \times 3 \times 3$ unit cells).

For convenience, the edge length is set to a constant value for all specimens (l_u = const.). Due to the boundary conditions of the dynamic investigation using the SHPB in Chapter 7, the edge length of the unit cell is set to $l_u = 4.5$ mm. Therefore, the relative density $\bar{\rho}$ of the respective lattice structure only depends on the strut radius r_u or the wall thickness t_w. The larger these values are, the higher the structure's relative density $\bar{\rho}$. The relative density $\bar{\rho}$ corresponds to the ratio between the reference volume V_{ref} of the cube with the edge length l_u and the actual volume V of the lattice structure, cf. Eq. (6.1).

$$\bar{\rho} = \frac{V}{V_{ref}} \qquad \text{with} \qquad V_{ref} = l_u^3 \tag{6.1}$$

6.2.1 Beam based lattice structures

The following four beam-based lattice structures were investigated:

- the conventional octet truss lattice composed of tetrahedra and octahedra: Octet
- the face-centered cubic lattice with an additional body-centered node: BFCC
- the convex truncated rhombic dodecahedron truss or rhombicuboctahedron: RhomOcta
- the convex polyhedra truss arising from a octahedron by cutting of the vertices, called truncated octahedron: TrunOcta

The corresponding unit cells are shown in Fig. 6.5. The Octet structure is an established and well-studied lattice. It can, therefore, be regarded as a reference structure in some respects. The BFCC structure is a combination of the common crystal-like lattices BCC and FCC. The TrunOcta and RhomOcta lattices are similar to a pore-like structure, as there are only struts on the outer shell. Due to this structure, large deformations and failures are expected due to buckling.

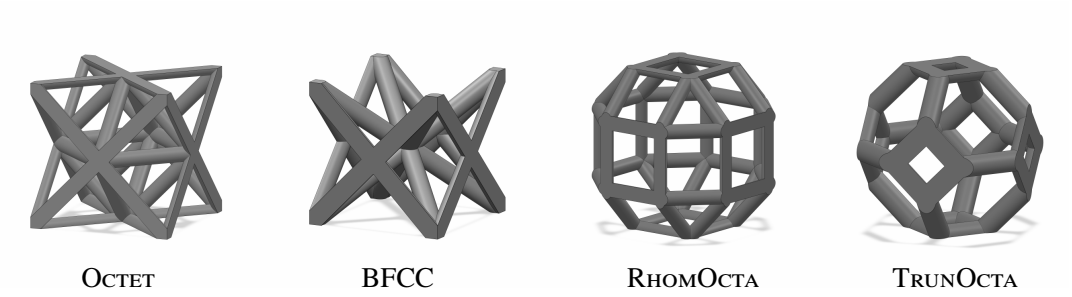

Fig. 6.5 – Unit cells of the investigated lattice types.

For quantification of the beam-based lattice characteristics, the lattice's topological properties are described by the Maxwell number M, [Maxwell 1864]. The Maxwell number is calculated from the n nodes and the s struts connected to the nodes and classifies the dominant loading regime, cf. [Deshpande et al. 2001],

$$M = s - 3\,n + 6. \tag{6.2}$$

A stretch-dominated behavior is given for $M \geq 0$, whereas a bending-dominated behavior corresponds to structures with $M < 0$. Table 6.1 shows some data for the lattices investigated in this work. Here, it can be found that only the popular Octet structure ($M = 0$) has a stretch-dominated behavior. The other investigated structures have a bending-dominated behavior: BFCC ($M = -9$), RhomOcta ($M = -18$) and the TrunOcta ($M = -30$).

Table 6.1 – Number of struts and nodes at different positions of the lattice unit cells.

	struts	nodes (corner)	nodes (center)	nodes (surface)	M
Octet	36	8	-	6	0
BFCC	24	8	1	4	-9
RhomOcta	48	-	-	24	-18
TrunOcta	36	-	-	24	-30

The Maxwell number M is a simple characteristic derived from classical trusses; large deformations of the lattices, including buckling and folding of layers, are not weighted. It should be emphasized that accurate material characterization of an irregular, stochastic microstructure requires either a sufficiently large number of specimen variations and multiple experiments.

Ordered structures consist of periodically repeating unit cells whose material response can be determined on small specimens that fluctuate solely due to manufacturing inaccuracy.

Due to the different structure types, the strut radius is different for different beam-based structures with the same relative density $\bar{\rho}$. This means that elementary structures (with few struts) have very thick strut radii r_u for higher relative densities $\bar{\rho}$. With increasing thickness, however, the characteristic of a lattice structure is lost; therefore, the lattice structure is no actual lattice structure anymore. As a result, a comparison of simple lattice structures with correspondingly thick strut radii r_u cannot be compared with more complex structures, as a very high stiffness is achieved, but the deformation is severely restricted. The known structures BCC and FCC are relatively simple lattices. The investigated BFCC lattice structure represents a fusion of these two structures; see Fig. 6.6. This more complex structure allows a comparison with the other investigated structures.

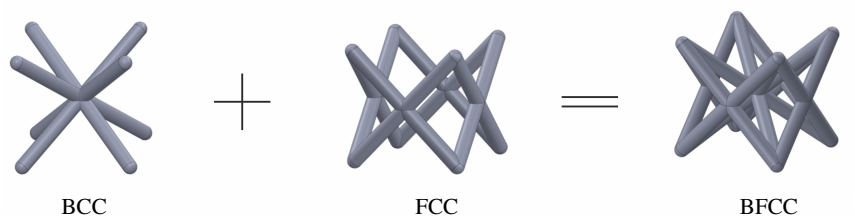

Fig. 6.6 – Composition of the BCC and FCC structure.

All beam-based structures were created using the CAD software SolidWorks in such a way that the parameters edge length l_u and strut radius r_u can be varied. This makes it possible to adapt the parameters of the lattice structures to a modified setup in later experiments.

The analytical calculation for the volume and surface area of the lattice structures is very complex due to the complex structure, especially at the nodes. The authors [Deshpande et al. 2001] calculate the density of the Octet structure approximately based on given strut radii r_u and the edge length l_u. Since the same relative density $\bar{\rho}$ is to be achieved for all structures within this work, the relative density $\bar{\rho}$ is specified, and then the necessary strut radius r_u is calculated for the respective structure.

First, numerical calculation within the CAD software determines the volumes and surface values for the structures for given radii. The strut radii are varied in 0.05 mm steps from 0 mm to 0.95 mm. The edge length $l_u = 4.5$ mm is always kept constant for all specimens; see Fig. 6.7. The required strut radius r_u concerning the required relative density $\bar{\rho}$ is thus determined by linear interpolation between the corresponding values.

Three different relative densities $\bar{\rho}$ are investigated in this work:

- $\bar{\rho} = 0.2$
- $\bar{\rho} = 0.3$
- $\bar{\rho} = 0.4$

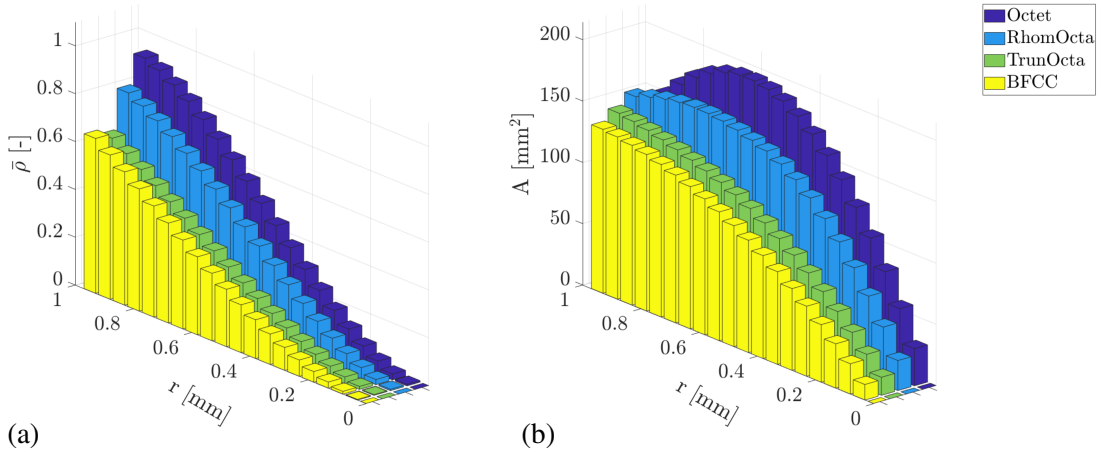

Fig. 6.7 – Relative density $\bar{\rho}$ a) and surface area A b) for different strut radii and a constant edge length of $l_u = 4.5$ mm per unit cell.

Table 6.2 shows the corresponding radii of the investigated beam-based lattice structures required for the investigated relative densities $\bar{\rho}$. The surface values for the relative densities $\bar{\rho}$ are also listed there.

Table 6.2 – Required strut radius r for a given relative density $\bar{\rho}$ as well as the resulting surface area A of the unit cells ($l = 4.5$ mm).

	$\bar{\rho}$	r [mm]	A [mm^2]
BFCC	0.2	0.359	122.49
Octet	0.2	0.308	145.98
RhomOcta	0.2	0.335	124.28
TrunOcta	0.2	0.442	100.46
BFCC	0.3	0.456	141.36
Octet	0.3	0.390	168.65
RhomOcta	0.3	0.428	142.45
TrunOcta	0.3	0.564	116.43
BFCC	0.4	0.546	153.41
Octet	0.4	0.466	183.37
RhomOcta	0.4	0.518	153.08
TrunOcta	0.4	0.679	127.05

6.2.2 Shell based structures

Triply Periodic Minimal surfaces (TPMS) are widespread in material science, architectural design, biomimetics, and 3D printing. Their high surface-area-to-volume ratio makes them mechanically robust and multifunctional in many applications. Some geometric properties characterize TPMS:

- periodic in all three spatial dimensions, enabling them to tile space uniformly without overlapping
- based on minimal surfaces with a zero mean curvature at every point, resulting in high mechanical performance and a good resistance to localized fatigue or failure
- no intersections, which serves to ensure high functionality of the structure.

TPMS structures are surfaces that can be translated in three independent directions to fill three-dimensional space without overlapping or leaving voids altogether. These structures are characterized by zero mean curvature and locally minimize their surface area under the imposed boundary conditions. Accordingly TPMS have no sharp edges.

A minimal surface is defined as a surface with vanishing mean curvature ($H = 0$) at every point, implying that it locally minimizes its surface area. For an implicitly defined surface described by the function $f(x, y, z) = 0$, the mean curvature can be expressed as follows, cf. [Goldman 2023]:

$$H = \frac{1}{2}\nabla \cdot \left(\frac{\nabla f}{|\nabla f|} \right) \tag{6.3}$$

Applying the product rule to the divergence operator and expressing the derivatives of the normalized gradient in terms of the Hessian matrix H_f and the trace operator, one obtains the equivalent expression:

$$H = \frac{|\nabla f|^2 \operatorname{tr}(H_\mathrm{f}) - \nabla f^\top H_\mathrm{f} \nabla f}{2|\nabla f|^3} \tag{6.4}$$

In this context, ∇f represent the gradient of the function f, and $\operatorname{tr}(H_\mathrm{f})$ represents the trace of the corresponding Hessian matrix of f. For $H = 0$, this yields a nonlinear partial differential equation. This minimal surface equation has to statify the function f, cf. [Bieler et al. 2025e].

TPMS structures can also be found in nature. For example, the wing structure of the Callophrys rubi butterfly has a structure similar to gyroid [Michielsen and Stavenga 2008] while the skeletal plate of sea urchins has a Schwarz P structure [Lai et al. 2007]. TPMS structures are the subject of current research and researchers study these surfaces to understand their unique properties and explore their potential uses in various fields. One well-known structure is the Schwarz P structure. This structure is based on the work of Hermann Schwarz in 1865, who deals with solving the plateau problem for a polygon [Schwarz and Schwarz 1890]. Other TPMS structures that go back to Hermann Schwarz and physicist Alan Hugh Schoen are the Schwarz D also known as Diamond and the Schwarz H („Hexagonal“) structure.

Schoen is known for discovering the also extensively studied Gyroid structure [Schoen 1970]. In addition, there are many other TPMS structures such as the Split P structure or the Lidinoid structure. Further information on different structures can be found in the works of [Lehder et al. 2021; Novak et al. 2021; Yan et al. 2021]. Implicit trigonometric functions describe the four TPMS structures investigated in this thesis:

Schwarz P:

$$\cos(x) + \cos(y) + \cos(z) = 0 \tag{6.5}$$

Gyroid:

$$\cos(x)\,\sin(y) + \cos(y)\,\sin(z) + \cos(z)\,\sin(x) = 0 \tag{6.6}$$

Schwarz D:

$$\begin{aligned}&\sin(x)\,\sin(y)\,\sin(z) + \sin(x)\,\cos(y)\,\cos(z) + \cos(x)\,\sin(y)\,\cos(z)\\&+ \cos(x)\,\cos(y)\,\sin(z) = 0\end{aligned} \tag{6.7}$$

Split P:

$$\begin{aligned}&1.1\,(\sin(2\,x)\,\sin(z)\,\cos(y) + \sin(2\,y)\,\sin(x)\,\cos(z)\\&+ \sin(2\,z)\,\sin(y)\,\cos(x)) - 0.2\,(\cos(2\,x)\,\cos(2\,y)\\&+ \cos(2\,y)\,\cos(2\,z) + \cos(2\,z)\,\cos(2\,x)) - 0.4\,(\cos(2\,x)\\&+ \cos(2\,y) + \cos(2\,z)) = 0\end{aligned} \tag{6.8}$$

The TPMS structures are created in the software environment Matlab. The mathematical description of the structures is done using the functions Eqs. (6.5) to (6.8) above that define an isosurface Φ [Al-Ketan et al. 2018; Novak et al. 2021]. With the command fimplicit3 an implicit function is plotted in Matlab. Since it is only a surface element, the surfaces must still be provided by a wall thickness t_w in order to generate a solid. Using the Isosurface function in Matlab, the mathematically described surface can be generated into a three-dimensional object with adjustable wall thickness t_w. Fig. 6.8 shows the creation of the 2D surface into the final three-dimensional specimen geometry consisting of several unit cells in Matlab. The created solid can be exported as a .stl file and then prepared for the printer in the existing 3D printer software.

The dimensioning of the TPMS structures for a given relative density $\bar{\rho}$ is carried out in the same way as for beam-based lattice structures with the difference that here the parameter of the wall thickness t_w must be adjusted instead of the radii of the struts r_u. The edge length of the unit cell is set to $l_u = 4.5$ mm, as with the beam-based lattice structures. The relative densities $\bar{\rho}$ for the TPMS, although defined by different geometric parameters (t_w), are determined in the same manner as for beam-based structures. To this end, the .stl files generated in Mabtlab are imported into the CAD software SolidWorks, where the corresponding volume and surface

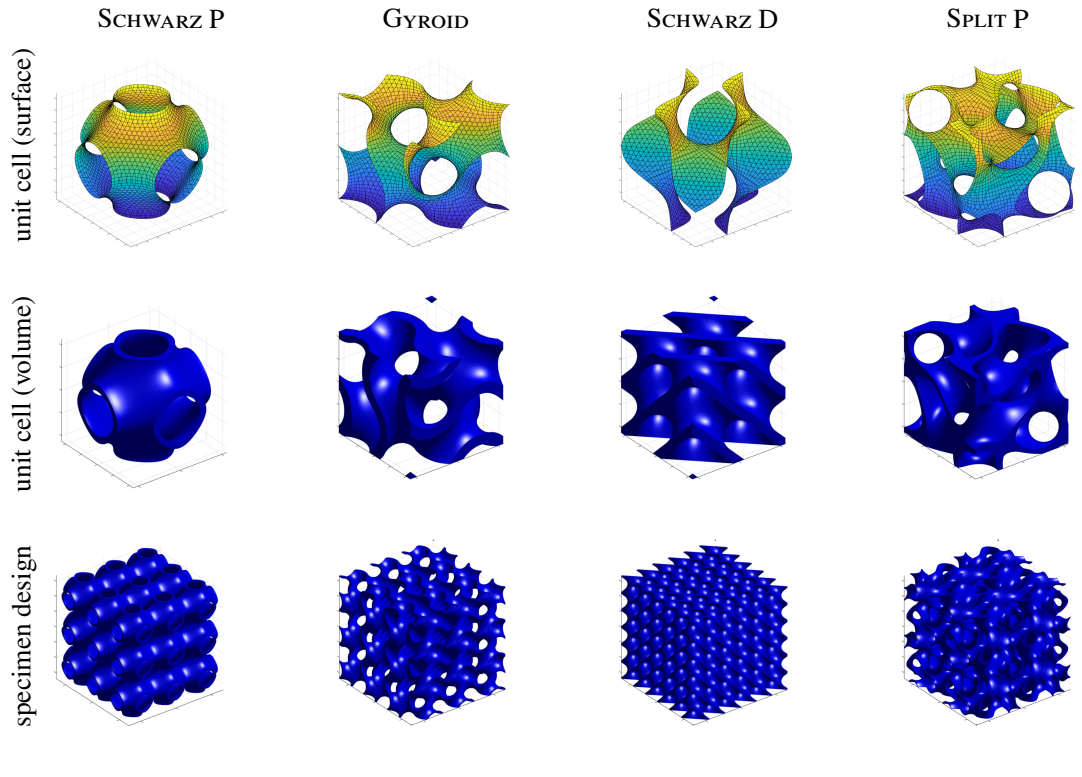

Fig. 6.8 – TPMS design with Matlab: the two-dimensional surface of the unit cell is provided with a wall thickness.

area are calculated numerically. The value for the wall thickness t_w is determined by linear interpolation of the corresponding neighboring values. Measured wall thicknesses between 0.05 mm and 0.95 mm are the basis for the linear interpolation; see Fig. 6.9 a). In contrast to the beam-based lattice structures, it is immediately noticeable that very high surface values of the TPMS structures result even at low wall thicknesses, see Fig. 6.9 b).

Table 6.3 shows the wall thickness t_w required for the relative densities examined from $\bar{\rho} = 0.2$ to $\bar{\rho} = 0.4$ for the investigated TPMS structures.

6.2.3 Printing process

Due to the more complex structure, the printing process is significantly more challenging than simple cylinder specimens or dog-bone specimens. Support structures are undesirable inside the specimen structure as they are difficult to remove. The DLP printing process has proven to be advantageous for printing lattice structures. As the lattice structures, or their unit cells, are very small and therefore only have a low weight, they are stable enough to be printed without support structures. This has the advantage that no mechanical post-processing is required, which means that very uniform and clean surfaces characterize the examined structures. The specimens must only be freed from liquid resin residues using a bath of isopropanol before

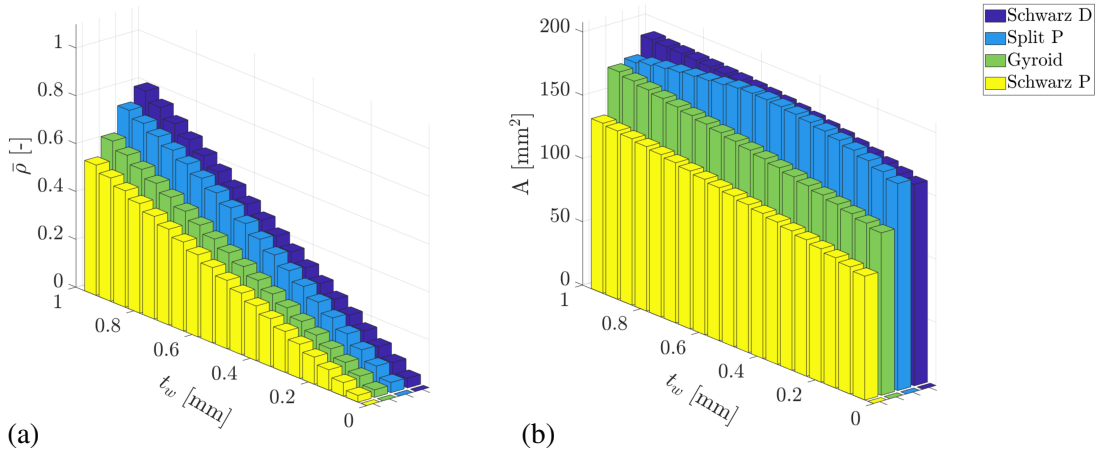

Fig. 6.9 – Relative density $\bar{\rho}$ a) and surface area A b) for different wall thicknesses and a constant edge length of l_u = 4.5 mm per unit cell.

Table 6.3 – Required wall thickness t_w for a given relative density $\bar{\rho}$ as well as the resulting surface area A of the unit cells (l_u = 4.5 mm).

	$\bar{\rho}$	t_w [mm]	A [mm^2]
Schwarz P	0.2	0.350	112.44
Gyroid	0.2	0.310	142.54
Schwarz D	0.2	0.244	170.65
Split P	0.2	0.234	178.00
Schwarz P	0.3	0.525	119.86
Gyroid	0.3	0.464	149.88
Schwarz D	0.3	0.366	176.22
Split P	0.3	0.356	183.91
Schwarz P	0.4	0.699	126.51
Gyroid	0.4	0.616	156.56
Schwarz D	0.4	0.486	180.67
Split P	0.4	0.478	187.21

they are cured under the material-specific parameters (temperature and UV light). Fig. 6.10 and 6.11 illustrate the examined structures made of the materials Anycubic Tough 2.0 and 3D Materials SuperFlex.

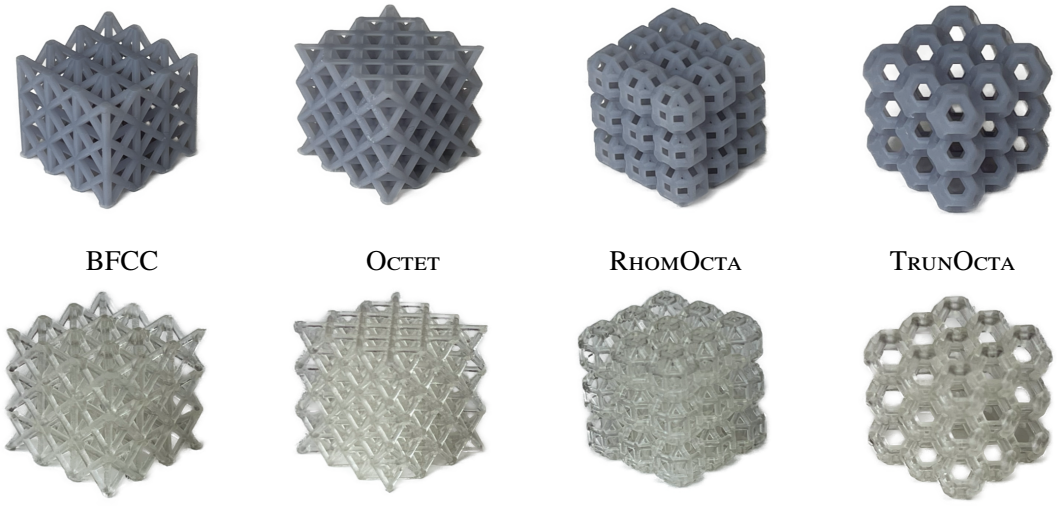

FIG. 6.10 – Printed lattice structure specimens consisting of $3 \times 3 \times 3$ unit cells (top: ANYCUBIC TOUGH 2.0, bottom: 3D-MATERIALS SUPERFLEX).

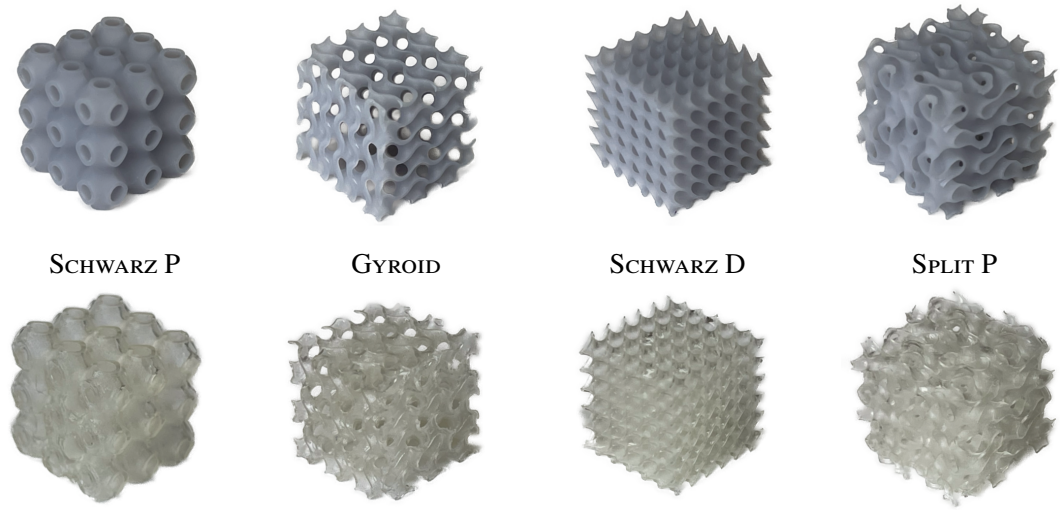

FIG. 6.11 – Printed TPMS structure specimens consisting of $3 \times 3 \times 3$ unit cells (top: ANYCUBIC TOUGH 2.0, bottom: 3D-MATERIALS SUPERFLEX).

6.3 Experimental investigation of hard polymer structures under static loading

In this section, different lattice structures are examined with regard to their energy absorption properties under static loading. By compressing lattice structures, they behave schematically as shown in Fig. 6.12.

Initially, the deformation of the individual cells is linear-elastic, resulting in relatively stiff behavior (phase I). In the event of buckling and failure of the individual struts, the struc-

ture's load-bearing capacity no longer increases and a plateau is formed (phase II). Further compression results in all cells being closed. Consequently, the solid material determines the deformation resistance and is correspondingly high (Phase III).

A characteristic feature is the nonlinear stress-strain curve, which can be divided into three phases. In the initial range, i.e., phase I, the structures react elastically. During this phase, the struts and walls (in the case of TPMS structures) deform reversibly. Here, the stress increases almost linearly with the strain, similar to the linear part in a classic tensile test. It should be noted that this slope is significantly lower than in the elasticity modulus measurement with solid material. The slope increases accordingly with higher relative densities $\bar{\rho}$. When a critical stress is exceeded, the unit cells begin to collapse. This stress σ_{pl} (plateau) marks the start of phase II, the plateau phase. The plateau is decisive for the high energy absorption capacity of foams and lattice structures. In phase III, most of the cells have collapsed, resulting in intense densification. Accordingly, the behavior here approaches that of a solid. As a result, the stress increases very sharply with further compression. Therefore, this strain is referred as ε_{D} (desification strain).

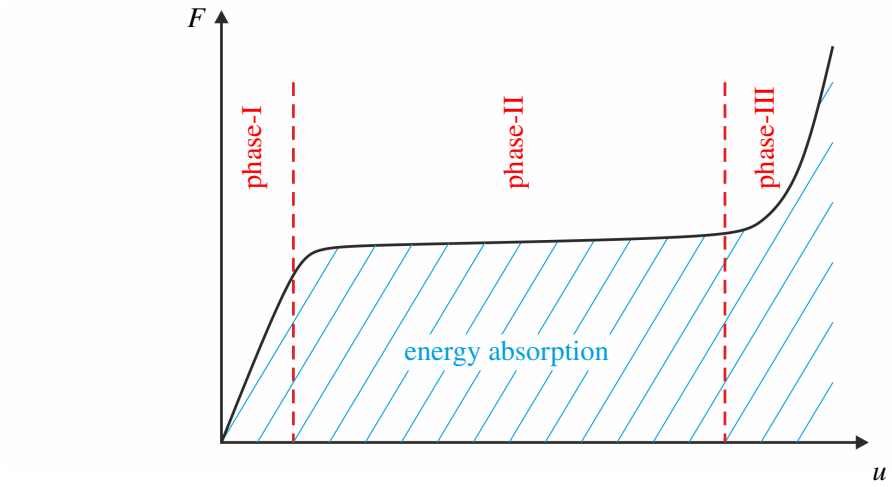

Fig. 6.12 – Typical force-displacement diagram for cellular structures under quasi-static compression.

All tested specimens consist of $3 \times 3 \times 3$ unit cells of the respective structure types. The edge length of the unit cells is $l_{\mathrm{u}} = 4.5$ mm. This results in a total edge length of the specimens of 13.5 mm and a total number of unit cells per specimen of $N = 27$, see Fig. 6.10 and Fig. 6.11.

In the experiments, the structures are compressed by up to 50%. The focus is on the reversibility of the deformation, which requires the right choice of material. This means that the structures should completely relax after the force is removed. The selection of an appropriate specimen material plays a crucial role in this context. On the one hand, the structures should exhibit sufficiently high strength; on the other hand, they must remain sufficiently elastic to return to their original configuration once the load is removed.

For brittle plastics, high deformation often results in fractures in individual struts, which excludes multiple loading of such materials. Soft elastomers or silicone-like materials provide pronounced deformability and relaxation capability but they exhibit relatively low stiffness. A compromise must be made between these different properties.

This section examines the reversible and thus sustainable energy absorption of four beam-based lattice structures and four shell-based structures under quasi-static loading conditions. The acrylic-like polymer material Anycubic Tough 2.0 domonstrates viscoelastically behavior under quasi-static deformation, similar to polymer foams. Consequently, the structures are capable of withstanding repeated loading and can return almost to their original configuration after a defined recovery period.

6.3.1 Experimental setup

The test setup enables uniaxial compression tests to be conducted on a universal tensile machine from Hegewald & Peschke. The machine is equipped with a load cell rated forces up to 2 kN. It features specialized aluminum compression plates supplied by the manufacturer, between which the test specimens are positioned and compressed, see Fig. 6.13. The lower compression plate is fixed, while the upper plate is connected to the movable crosshead.

The crosshead speed for compressing the specimens is set to a constant velocity of 0.5 mm/min in all tests. By selecting a relatively small load cell, forces in the lower measurement range can be determined with high precision.

In the implemented LabMaster software of the tensile machine, the compression test sequence was generated using corresponding program blocks. To ensure that all specimens are subject to the same test parameters, the program first establishes contact between the specimens and the upper crosshead with a preset force. Therefore, the specimen is placed between the lower and upper pressure plates. When the program is starts, the upper crosshead moves downwards at a preset velocity of 5 mm/min. The crosshead stops when the preset force of 0.05 N is reached. This is followed by a ten seconds dwell period, during which the crosshead remains stationary. After this idle time, all machine readings are reset to zero. The actual compression test is then carried out at a crosshead speed of 0.5 mm/min. The specimen is compressed to 50% of its initial height during the experiment. The force, displacement, time, and strain data are recorded at a sample rate of 50 Hz, which is sufficiently accurate for quasi-static tests. Due to the three layers of unit cell of the tested specimens, a compression of 50% corresponds to a movement of the upper crosshead by 6.75 mm, see Eq. (6.9).

$$\varepsilon = \frac{u}{3\,l_{\mathrm{u}}} \tag{6.9}$$

After compressing the specimen, the load is released at the same crosshead velocity of 0.5 mm/s as during compression. The specimens initially follow this slow release, i.e., they show a relatively fast relaxation behavior. During unloading, the structures relax more and

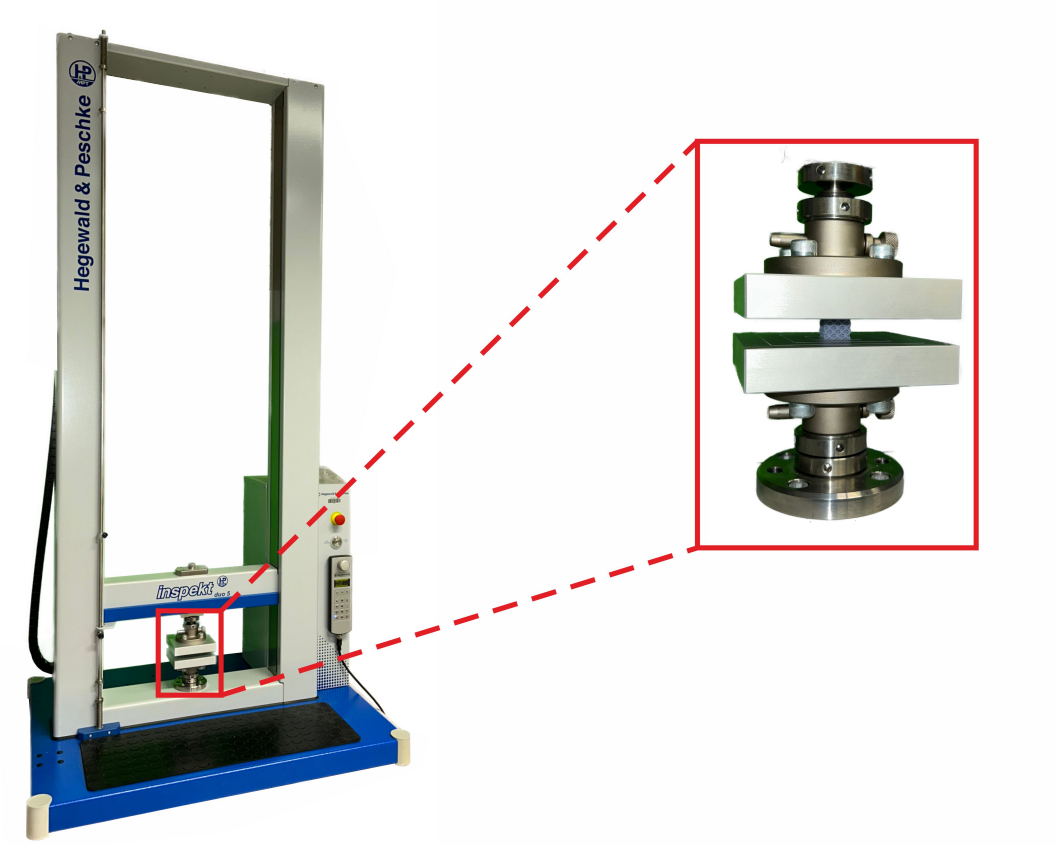

Fig. 6.13 – Tension machine from the companyHegewald & Peschke equipped with compression plates.

more slowly with increasing time. Accordingly the crosshead loses contact with the specimen after a travel distance of around 2 mm during displacement-controlled unloading. However, subsequent measurements show that the structures relax almost completely after 48 hours. The test sequence implemented in LabMaster is shown below, where F, u and P represent the current force, displacement and position:

- travel until: $F = 0.05$ N at $v = 5$ mm/min
- hold for: $t = 10$ s
- tara: F, u, P
- travel distance: $u = 6.75$ mm at 0.5 mm/min (compression)
- hold for: $t = 10$ s
- travel until: $F = 0$ (unloaded specimen)

In order to statistically validate the experiments shown, six specimens of each lattice geometry were tested. For the three relative densities $\bar{\rho}$, this results in a specimen size of 144 specimens for the four lattice structures and four TPMS structures. The statistical evaluation is done analogously to the procedure described in Section 3.4.2.

6.3.2 Results of static compression of lattice structures

Fig. 6.14 to 6.16 show different beam-based lattice structures at compressions of $\varepsilon = 0$, $\varepsilon = 0.25$ and $\varepsilon = 0.5$. Since the compression of the specimen takes 810 seconds due to the slow, quasi-static traverse movement, the experiment was recorded with a time-lapse camera, which only takes two images per second. Therefore, the deformation process of the specimen can be analyzed in the recorded video later.

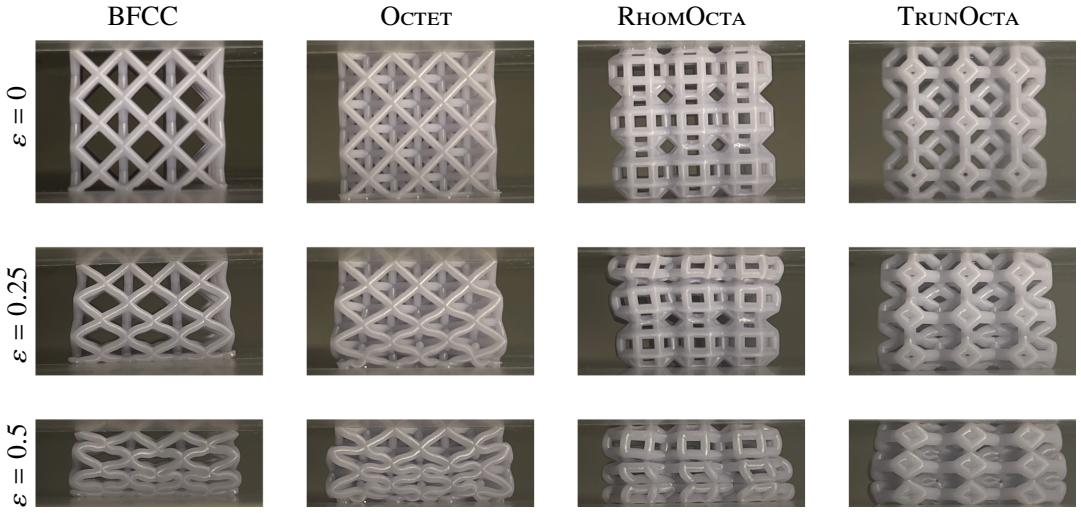

Fig. 6.14 – Investigated lattice structures with a relative density of $\bar{\rho} = 0.2$ under 0 %, 25 % and 50 % of compression.

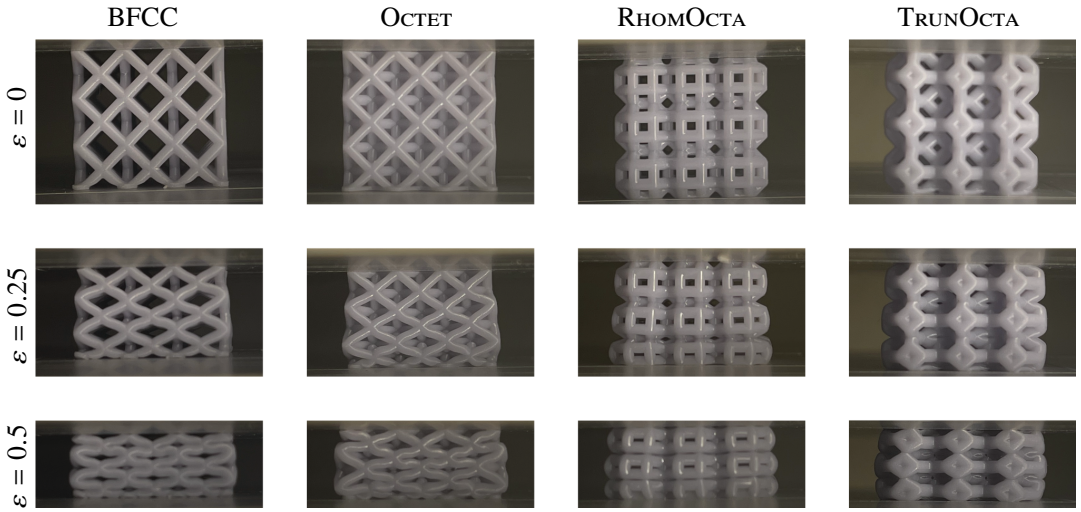

Fig. 6.15 – Investigated lattice structures with a relative density of $\bar{\rho} = 0.3$ under 0 %, 25 % and 50 % of compression.

The deformation is quite uniform at the beginning of the compression before buckling of individual struts in the structures occurs. The force-displacement curves in Fig. 6.17 illustrate

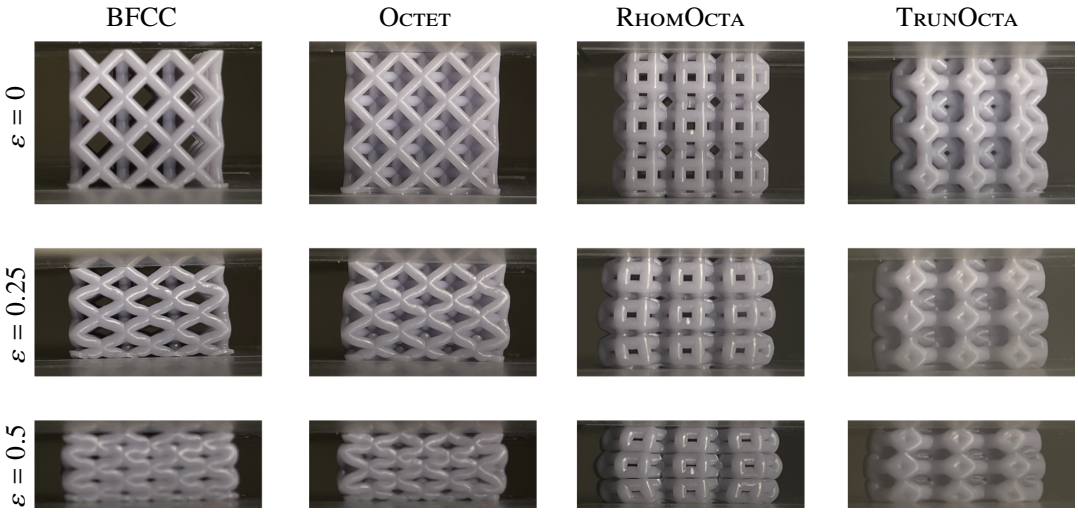

Fig. 6.16 – Investigated lattice structures with a relative density of $\bar{\rho} = 0.4$ under 0 %, 25 % and 50 % of compression.

the different reactions of the different lattice types. The TrunOcta structure turns out to be significantly stiffer than the other lattices with the same relative density. The narrow error bands observed within each structure set confirm the high manufacturing accuracy achieved during the printing process.

The typical three phases of the force-displacement curve can be recognized more or less well for all lattice structures. The strong increase at the beginning of the compression corresponds to phase I. This increase is followed by a pronounced force plateau (phase II). When the individual layers are pressed together, the layers finally come into contact with each other. This material densification causes the structure to lose its open-cell character, resulting in a rapid phase III force increase. Both the RhomOcta and the TrunOcta structure show a less pronounced plateau (phase II) due to their higher stiffness. Although not all cells in the lattice of the BFCC and the Octet structure are closed at 50% compression, both structures show an increase in force after the plateau phase. The Octet structure also shows the temporal folding of the individual layers through its fluctuations.

The TrunOcta shows a much steeper phase I force increase for all the investigated relative densities $\bar{\rho}$ than the other structures. The RhomOcta structure also shows a stronger increase in phase I, but only at the higher relative densities $\bar{\rho} = 0.3...0.4$. Due to the folding of the individual layers of the specimens, this phase is not followed by a classically pronounced phase II force plateau.

The structure of the RhomOcta and the TrunOcta could be described as spherical. The struts of these structures are only present on spherical shells. In contrast to the BFCC and Octet structures, there is no internal bracing. Accordingly, the different layers rest entirely on each other at higher compressions of these pore-shaped structures. The result is a plateau that is not classically pronounced for these structure types.

However, a very pronounced plateau is observed for the BFCC and Octet. After phase II, the force curve rises again due to phase III of the collapsed layers. The beginning of phase III is well demonstrated in Fig. 6.17 for the structures BFCC and Octet. In contrast, the begin of phase III for the RhomOcta and TrunOcta structure cannot be precisely characterized.

In Fig. 6.14 to Fig. 6.16, it can seen that the BFCC and Octet structures deform symmetrically up to maximum compression of $\varepsilon = 0.5$. These two structures have in common that there are nodes in the corners and, in the case of the BFCC structure, a node in the center of the unit cell so that their structure reacts more stable to the orthogonal force. For the convex structures, asymmetric deformation occurs with greater compression. Since the TrunOcta structure has approximately 25 % thicker struts than the RhomOcta structure at the same relative density $\bar{\rho}$ the TrunOcta structure has a greater bending stiffness. In contrast to the RhomOcta structure, the surface area of the TrunOcta structure is 20% smaller for the same relative density $\bar{\rho}$. For the RhomOcta structure, an asymmetric deformation occurs at a relative density of $\bar{\rho} = 0.2$. However, this asymmetric deformation no longer occurs with larger relative densities $\bar{\rho} = 0.3$ and $\bar{\rho} = 0.4$ as the thicker struts prevent buckling. Despite the strong deformation, none of the tested specimens exhibit externally visible fractures.

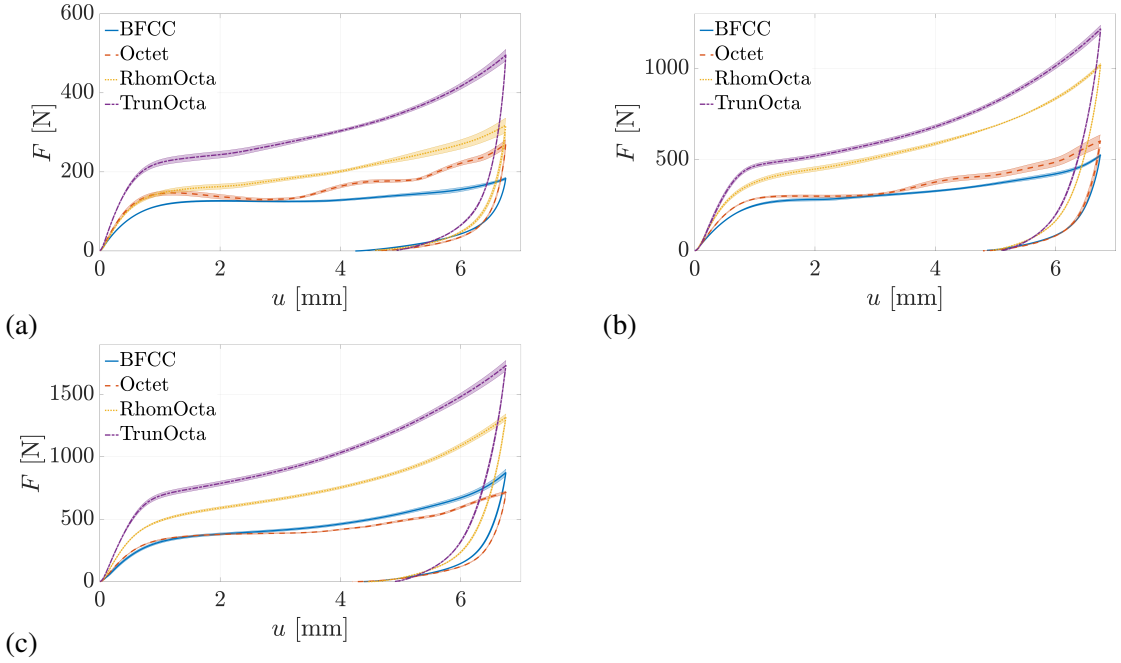

Fig. 6.17 – Recorded force-displacement curve for the lattice structures under quasi-static compression with a) $\bar{\rho} = 0.2$, b) $\bar{\rho} = 0.3$ and c) $\bar{\rho} = 0.4$

6.3.3 Results of static compression of TPMS structures

The test conditions for the TMPS structures are the same as those for the lattice structures. Fig. 6.18 to Fig. 6.20 show the deformation state of the structures at compression states $\varepsilon = 0 \ldots 0.5$

for the three relative densities $\bar{\rho}$ investigated. In general, the TPMS structures have a more pronounced and more recognizable plateau in phase II than the beam-based lattice structures. For the relative density of $\bar{\rho} = 0.2$, there is even a noticeable drop in force in the plateau phase after the first strong increase in force from phase I for the TPMS structures Schwarz P and Split P. As compression increases, the force rises again. This effect is no longer noticeable for the higher relative densities of $\bar{\rho}$, see Fig. 6.21. As observed for the beam-based structures, the narrow error bands here indicate a high degree of reproducibility for the TPMS structures.

The Schwarz D structure differs significantly from the other TPMS structures in terms of the force required for the same compression. The Schwarz D structure at a relative density of $\bar{\rho} = 0.2$ already exhibits nearly the same force required to compress the Gyroid structure at a relative density of $\bar{\rho} = 0.3$ by 50%. For a relative density of $\bar{\rho} = 0.4$, a force of approximately $F = 1700$ N is required to compress the Schwarz D structure at a compression of 50%. This force value is almost twice as high as the force required for the same compression of the Schwarz P at the same relative density $\bar{\rho} = 0.4$.

Due to the structural characteristics of TPMS structures, it is more difficult to determine whether deformation is symmetrical or asymmetrical than with beam-based lattice structures. The deformation of the Schwarz P structure can be described as symmetrical throughout the test. The Schwarz D structure shows uniform bulging of the structure. A clearly asymmetrical behavior as observed in beam-based lattice structures cannot be observed here.

No external damage was detected in any of the tested structures. The relaxation of the structures after the force is removed is initially rapid and then becomes increasingly slow. The measurements show that all structures relax almost completely back to their original state after 48 hours. Only very small deformations of up to >5% remains as plastic deformation.

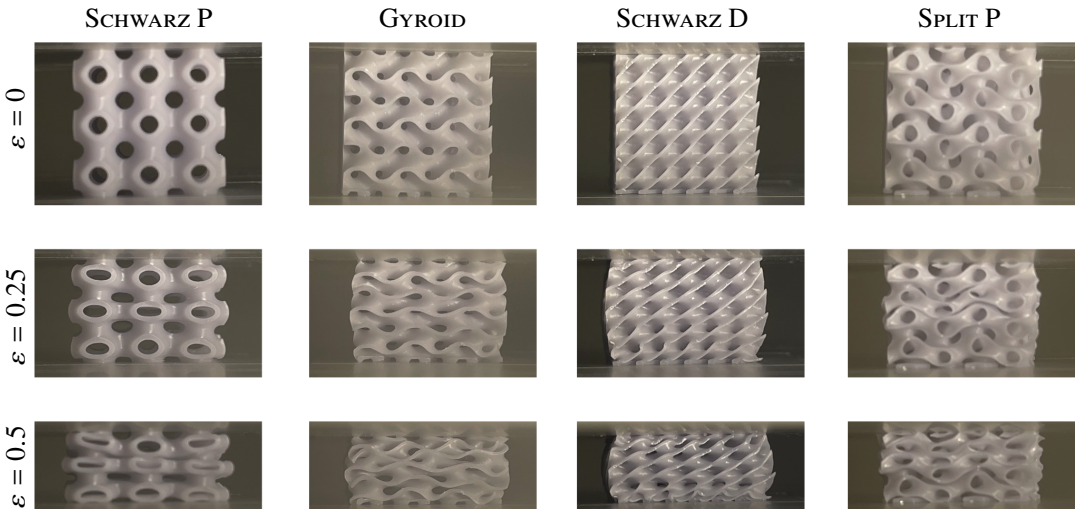

Fig. 6.18 – Investigated TPMS structures with a relative density of $\bar{\rho} = 0.2$ under 0 %, 25 % and 50 % of compression.

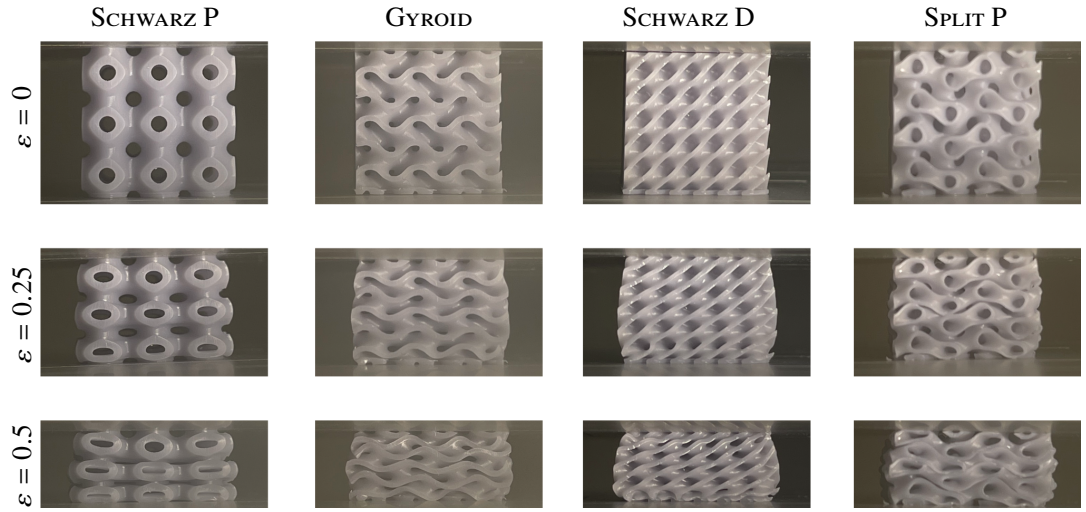

Fig. 6.19 – Investigated TPMS structures with a relative density of $\bar{\rho} = 0.3$ under 0 %, 25 % and 50 % of compression.

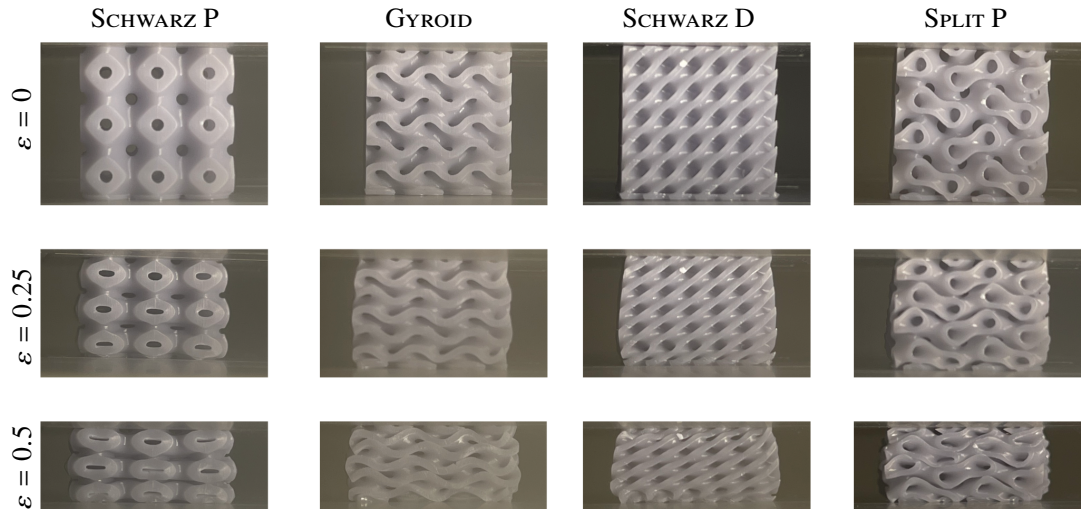

Fig. 6.20 – Investigated TPMS structures with a relative density of $\bar{\rho} = 0.4$ under 0 %, 25 % and 50 % of compression.

6.3.4 Energy absorption

The aim of the investigations is to determine the energy, which is absorbed by the (reversible) deformation of the specimen. The energy is stored in the lattice structure due to the strong deformation. The energy stored by the specimen is calculated - by neglecting friction and temperature - based on the measured force F and the displacement u of the upper crosshead of the tensile machine,

$$W = \int_0^u F(x)\,\mathrm{d}x\,. \tag{6.10}$$

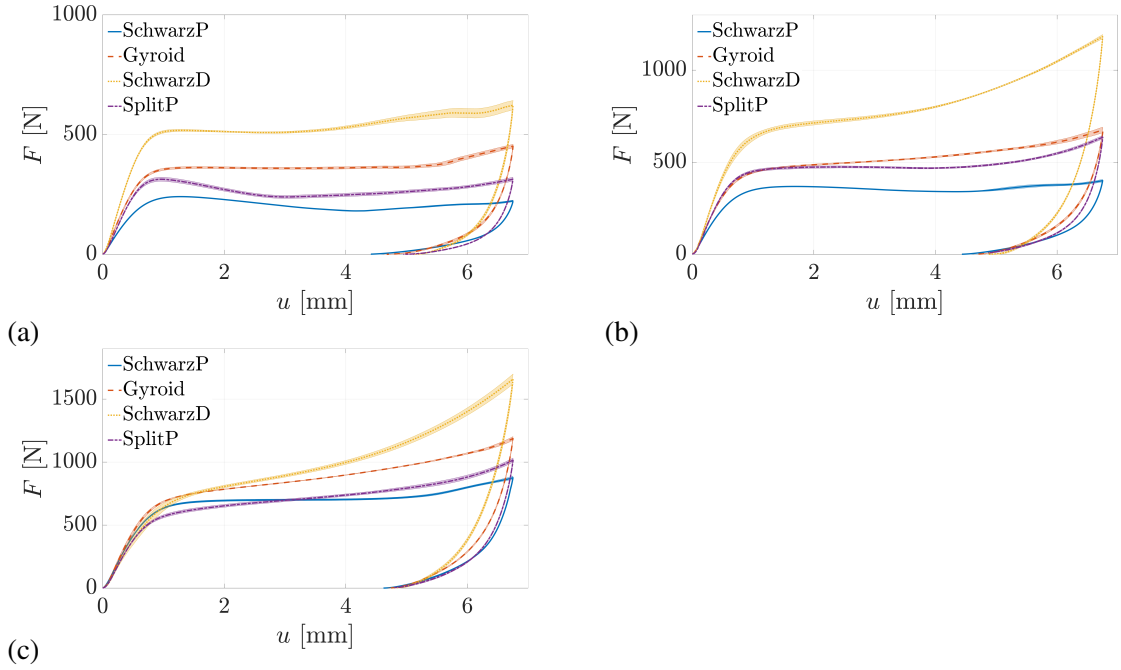

Fig. 6.21 – Recorded force-displacement curve for the TPMS structures under quasi-static compression with a) $\bar{\rho} = 0.2$, b) $\bar{\rho} = 0.3$ and c) $\bar{\rho} = 0.4$

Additionally, we define the (mass) specific energy absorption (SEA) as the quotient of the stored energy and the specimen's individual mass,

$$\mathrm{SEA} = \frac{W}{m} \tag{6.11}$$

The mass m of the specimen is calculated from the density of the fully cured resin ρ, the relative density $\bar{\rho}$ of the unit cells, the unit cell's length l_u and the number of unit cells (here: $N = 3 \times 3 \times 3$), see Eq. 6.12.

$$m = 27\,\rho\,\bar{\rho}\,l_u^3 \tag{6.12}$$

The energy absorption determined here obviously relates to the forces required to compress the specimens. Fig. 6.22 a) to 6.22 c) show the energy-strain curves for the beam-based lattice strucutures with different relative densities, whereas Fig. 6.22 d) show the (mass) specific energy absorption (SEA) at a full compression of 50%.

For a relative density of $\bar{\rho} = 0.2$, it can be seen that the BFCC has the lowest energy absorption. Even at this relative density, the TrunOcta structure already shows the highest energy absorption of the investigated structure. The energy absorption of the Octet and RhomOcta structures is above the value of the BFCC; for higher relative densities $\bar{\rho}$, the BFCC and Octet structures become very similar. They therefore show an almost similar energy absorption behavior for $\bar{\rho} \geq 0.3$.

The RhomOcta structure shows an energy absorption behavior that lies between the TrunOcta structure and the two structures BFCC and Octet. It is noticeable that the energy absorption of the RhomOcta structure at a relative density of $\bar{\rho} = 0.2$ is less separate from the energy absorption of the BFCC and Octet structures. As mentioned before, asymmetrical deformations occur in the RhomOcta structure at a relative density of $\bar{\rho} = 0.2$, see Fig. 6.14. The buckling of some struts is the reason for the lower forces required for compression. For higher relative densities $\bar{\rho}$ of the RhomOcta structure, the aforementioned asymmetric deformation no longer occurs due to stiffer struts, leading to significantly higher energy absorption.

The TrunOcta lattice stands out with the best specific energy absorption. Even though the RhomOcta structure has a similar structure, the total energy absorption of TrunOcta is about 36% higher for a compression of $\varepsilon = 0.5$ at a relative density of $\bar{\rho} = 0.4$. This finding has significant practical implications as it suggests that the TrunOcta lattice could be a favorable candidate for applications requiring high energy absorption in lattice structures.

For each investigated structure type, a comparison of $\bar{\rho} = 0.2$ to $\bar{\rho} = 0.3$ reveals a sharp increase in specific energy absorption for fully compressed structures (50%). The difference in specific energy absorption is much smaller for the comparison between $\bar{\rho} = 0.3$ and $\bar{\rho} = 0.4$, see Fig. 6.22 d). For the structures Octet and RhomOcta, the specimens with a relative density of $\bar{\rho} = 0.3$ even show the highest specific energy absorption on average. However, the difference between the relative densities $\bar{\rho} = 0.3$ and $\bar{\rho} = 0.4$ of these two structure types is minimal, so this can be attributed to imperfections in some of the specimens. It can be seen that the energy absorption flattens out more with increasing the relative density $\bar{\rho}$.

At a relative density of $\bar{\rho} = 0.2$, the Schwarz P structure exhibits the lowest energy absorption performance. In contrast, the Schwarz D structure achieves the highest energy absorption (EA), reaching 3.4, Nm at a compressive strain of $\varepsilon = 0.5$. This value is three times higher than that of the Schwarz P structure. The Split P and Gyroid structures lie between these two values. Fig. 6.23 a)-c) shows the energy-strain curves for the TPMS structures investigated.

For a relative density of $\bar{\rho} = 0.3$, the structures Gyroid and Split P show an almost similar curve. Furthermore, Schwarz P and Schwarz D mark the upper and lower limits concerning energy absorption properties.

The Gyroid structure shows a strong slope at a relative density of $\bar{\rho} = 0.4$. The energy-strain curve is almost identical to that of the Schwarz D curve up to a compression of approximately 30%. Only above this compression can the Schwarz D structure stand out again and achieve a better result. The structures Schwarz P and Split P show very similar behavior for the relative density of $\bar{\rho} = 0.4$.

Fig. 6.23 d) shows the (mass) specific energy absorption of the structures. It can be seen that both the Schwarz P and Split P structures have lower SEA values than the other two structures, but they show the strongest increase when considering the increase in relative density within a structure type. The Schwarz D structure exhibits the best properties in terms

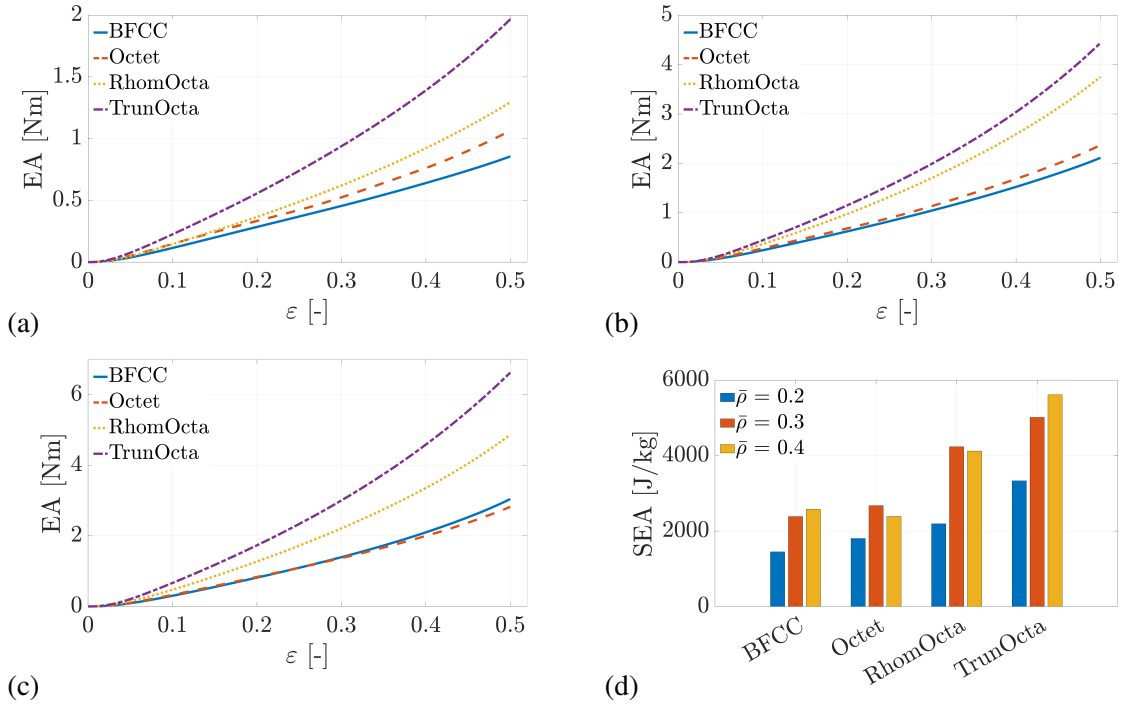

Fig. 6.22 – Energy absorption at different states of deformation during compression test for the investigated beam-based lattice structures with a) $\bar{\rho} = 0.2$, b) $\bar{\rho} = 0.3$, c) $\bar{\rho} = 0.4$ and d) the specific energy absorption by compression of $\varepsilon = 0.5$.

of total energy absorption and specific energy absorption. However, Fig. 6.23 d) shows that the difference between the SEA is small when comparing the three relative densities.

Upon consideration of the structures types, the increase in relative density $\bar{\rho}$ show that, on average, beam-based lattice structures exhibit a very strong increase in energy absorption when the relative density increases from $\bar{\rho} = 0.2$ to $\bar{\rho} = 0.3$. Here, the RhomOcta structure shows an increase in energy absorption of 191%. With a further increase in relative density from $\bar{\rho} = 0.3$ to $\bar{\rho} = 0.4$, the increase is smaller (< 50%).

For the TPMS structures, the increase in energy absorption is lower by comparing the relative densities $\bar{\rho} = 0.2$ and $\bar{\rho} = 0.3$. Here, the Schwarz P structure is the only TPMS topology that exhibits a 100% increase in energy absorption for both increments in relative density, i.e., from $\bar{\rho} = 0.2$ to $\bar{\rho} = 0.3$ and from $\bar{\rho} = 0.3$ to $\bar{\rho} = 0.4$. Table 6.4 shows the percentage increase of all structures with respect to the relative density $\bar{\rho}$.

One topic left out of this work is possible imperfections in the printed structures. The authors [Glaesener et al. 2023] deal with this topic by limiting the type of imperfection.

6.3.5 Energy absorption according to Gibson & Ashby

There are different approaches to compare the energy absorption of structures or materials. In Section 6.3.4, the energy absorption properties of the structures were compared to each other

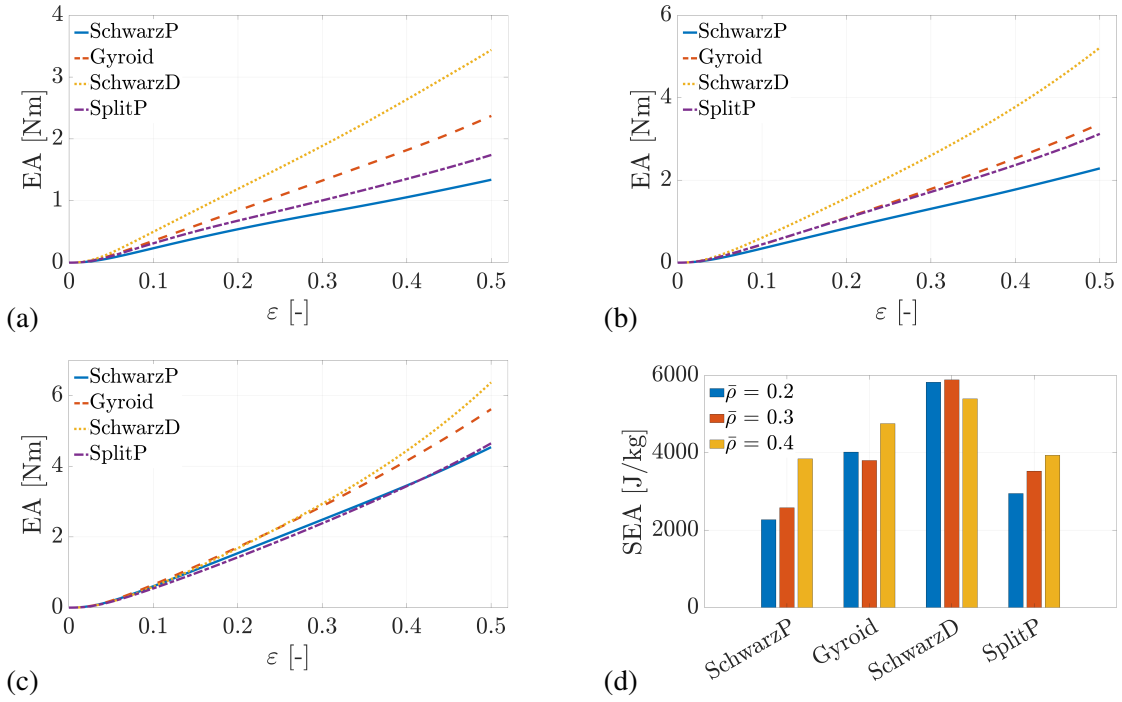

Fig. 6.23 – Energy absorption at different states of deformation during compression test for the investigated TPMS structures with a) $\bar{\rho} = 0.2$, b) $\bar{\rho} = 0.3$, c) $\bar{\rho} = 0.4$ and d) the specific energy absorption by compression of $\varepsilon = 0.5$.

Table 6.4 – Total energy absorption at $\varepsilon = 0.5$ and the percentage increase in energy absorption when the relative density $\bar{\rho}$ increases.

structure	$EA(\bar{\rho}_{0.2})$ [Nm]	$EA(\bar{\rho}_{0.3})$ [Nm]	$EA(\bar{\rho}_{0.4})$ [Nm]	$\bar{\rho}_{0.2} \rightarrow \bar{\rho}_{0.3}$ [%]	$\bar{\rho}_{0.3} \rightarrow \bar{\rho}_{0.4}$ [%]
BFCC	0.85	2.11	3.04	+148	+49
Octet	1.06	2.36	2.81	+122	+19
RhomOcta	1.29	3.75	4.86	+191	+30
TrunOcta	1.96	4.44	6.62	+127	+49
Schwarz P	1.34	2.28	4.54	+70	+100
Gyroid	2.37	3.35	5.60	+41	+67
Schwarz D	3.44	5.21	6.37	+51	+22
Split P	1.74	3.12	4.65	+79	+49

under the same compression. The work of [Gibson and Ashby 1997] compares different foams with completely collapsed structures. So the structures are compared at complete compression (i.e., the end of phase II). This approach means that structures with different relative densities $\bar{\rho}$ must be compressed to various levels to achieve the densification strain ε_{D}.

The question of when a structure has completely collapsed, i.e., when all cells have been compressed, cannot be answered in general, because it depends on the structure type and, to a large extent, on its density. In their work, Gibson & Ashby [Gibson and Ashby 1997] found that a complete compression of open-cell foams does not occur at a strain of $\varepsilon = 1 - \bar{\rho}$, as one might initially assume, but rather at a lower compression:

$$\varepsilon_{\mathrm{D}} = 1 - c_{\mathrm{D}}\,\bar{\rho} \qquad \text{with} \qquad c_{\mathrm{D}} = 1.4 \tag{6.13}$$

The factor $c_{\mathrm{D}} = 1.4$ in Eq. (6.13) may vary. However, this value provides a good indication of the strain when open-cell foams exhibit complete compression. Since the lattice structures and TPMS structures are considered open-cell materials, the authors' assumptions from Eq. (6.13) can be applied to the structures under investigation.

The comparison of this fully compressed state is justified by the fact that the largest proportion of energy absorption occurs during the plateau phase and thus represents a suitable measure for comparing the energy-absorption properties of the structures. Fig. 6.24 shows the densification strain ε_{D} for complete compression at different assumed factors c_{D}.

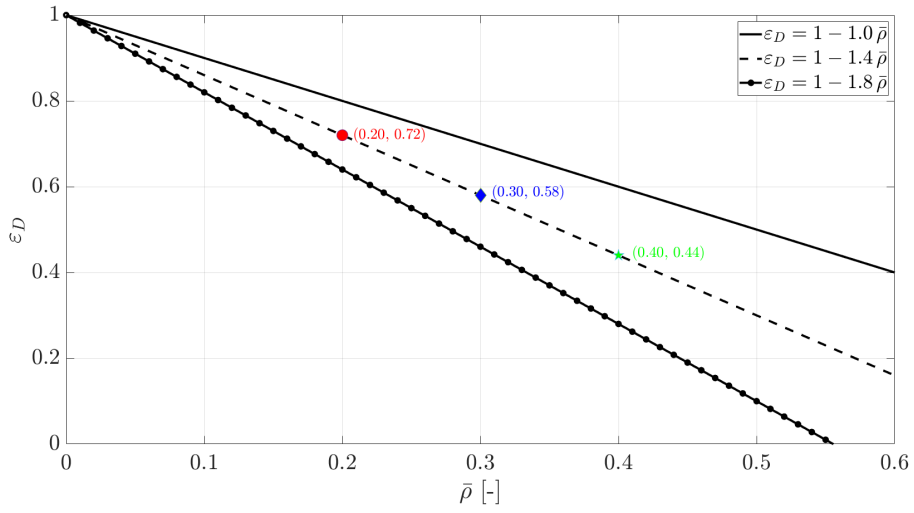

Fig. 6.24 – Densification strain ε_{D} for different factors c_{D}.

The compression experiments in this work were conducted only up to a strain of $\varepsilon = 0.5$. Assuming Eq. (6.13), a complete densification only occurs for the investigated structures with a relative density of $\bar{\rho} = 0.4$ within this work:

- $\varepsilon_{\mathrm{D}}(\bar{\rho} = 0.2) = 0.72$
- $\varepsilon_{\mathrm{D}}(\bar{\rho} = 0.3) = 0.58$
- $\varepsilon_{\mathrm{D}}(\bar{\rho} = 0.4) = 0.44$

Here, the energy absorption should be calculated based on the stress-strain curve rather than the force-displacement curve. The analysis should be based on the plateau phase. Since the force and displacement data are available from the experiment, the stresses must still be determined from this data. As shown previously, the strain can be calculated from the initial length and the crosshead displacement of the tensile testing machine. Classically, the stresses of the lattice structures are calculated based on the cross-sectional areas of the enclosing body. Since the unit cells are realized using a cubic building space (see Fig. 6.4), the cross-section area for a specimen with $n \times n \times n$ unit cells is the area above:

$$A_{\mathrm{ext}} = n^2 \, l_{\mathrm{u}}^2 \tag{6.14}$$

All specimens consist of 27 ($3 \times 3 \times 3$) unit cells, which results in an outer cross-sectional area of $A_{\mathrm{ext}} = 182.25\ \mathrm{mm}^2$.

Due to the complex structures, this cross-section area, A_{ext}, is only a supplemental variable for determining the stresses. Initial cross-sections are used in tensile tests to determine the engineering stress. In classical tensile tests, cross-sectional reduction, i.e., a change in the cross-section area, naturally occurs. However, such standardized tests use solid material and not, as in this case, an obviously more complex structure. Furthermore, the cross-sectional area of such structures is not constant, which makes it difficult to quantify an initial cross-section area A_0.

However, this does not pose a problem for determining the absorbed energy, since integrating the stress-strain curve delivers an energy per unit volume, which is then multiplied by the test specimen's volume. So the calculation of the absorbed energy by the stress-strain curve gives us the same result as integrating the force-displacement curve shown in Section 6.3.4.

The start of the plateau phase in the stress-strain diagram is the stress σ_p (plateau). Since polymers often do not exhibit an actual peak during the transition from elastic phase I to the plateau phase II, a criterion must be established for the onset of the plateau phase. A good measure in the absence of a peak is the slope, i.e., the derivative, of the stress-strain curve. The slope of the curve can be determined by numerically deriving the measurement data (force and displacement). The criterion used here for the start of the plateau is the slope at which only 10% of the maximum slope in the linear elastic range of phase I remains. The strain corresponds to the plateau strain ε_p, see Eq. (6.15) and Fig. 6.25.

$$\varepsilon_P = \min\left\{\varepsilon : \frac{\mathrm{d}\sigma}{\mathrm{d}\varepsilon} < 0.1\left(\frac{\mathrm{d}\sigma}{\mathrm{d}\varepsilon}\right)_{\mathrm{lin,max}}\right\} \tag{6.15}$$

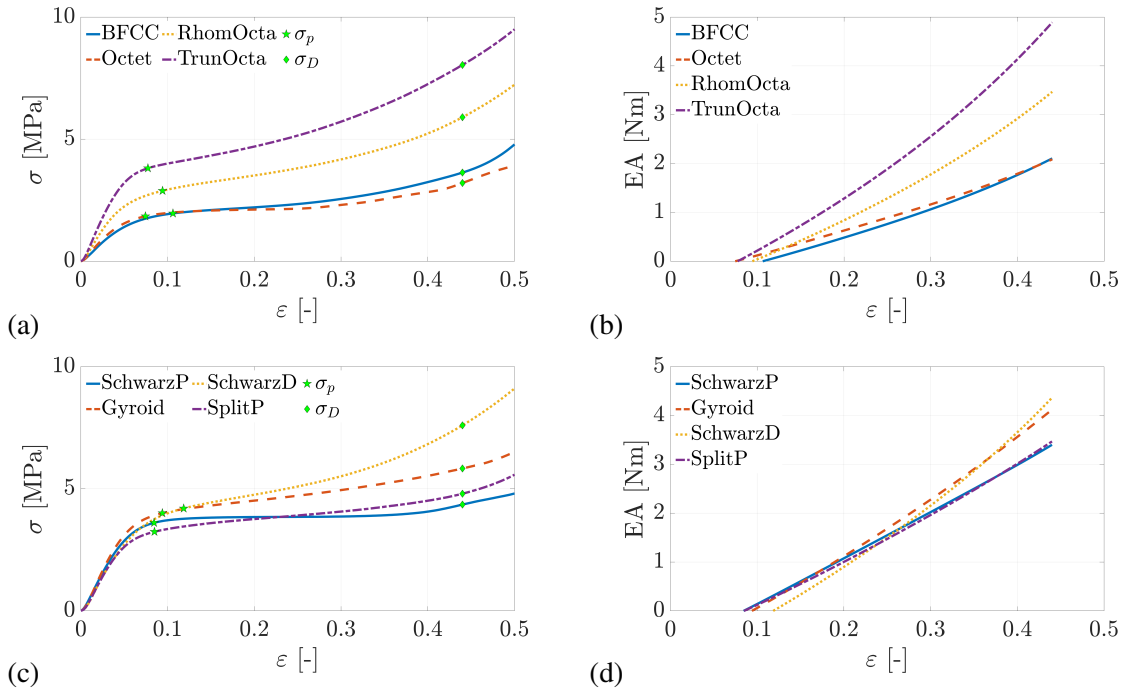

Fig. 6.25 – Stress-strain curves of the investigated structures with a relative density $\bar{\rho} = 0.4$: a) lattice structures and c) TPMS structures. The markers in the figures show the begin and the end of the plateaus. The corresponding energy absorption at differnt states of deformation within the plateau are shown: b) lattice structures and d) TPMS structures.

Since numerical differentiation is very sensitive to measurement noise, the data is first filtered in Matlab using the Savitzky–Golay filter. This filter is a so-called finite impulse response (FIR) filter. Using a specified window width, part of the signal is locally fitted with polynomials and then assembled. Using this filter means the signal is not smoothed to the point where the actual curve shape is lost. The smoothed curve is then differentiated, and the required slope is determined (10% of the maximum slope). The detailed derivation can be found in Appendix A.3.

Fig. 6.26 shows the specific energy absorption of the plateau region of the structures examined. The specific energy absorption is plotted in faded color. The figure shows that the most significant portion of energy absorption occurs during the plateau phase. Table 6.5 shows the total energy absorption divided into the three phases as a percentage. This table indicates that the compression in the linear elastic phase I and the compression during phase III are very small compared to the energy-absorption portion of the plateau phase II.

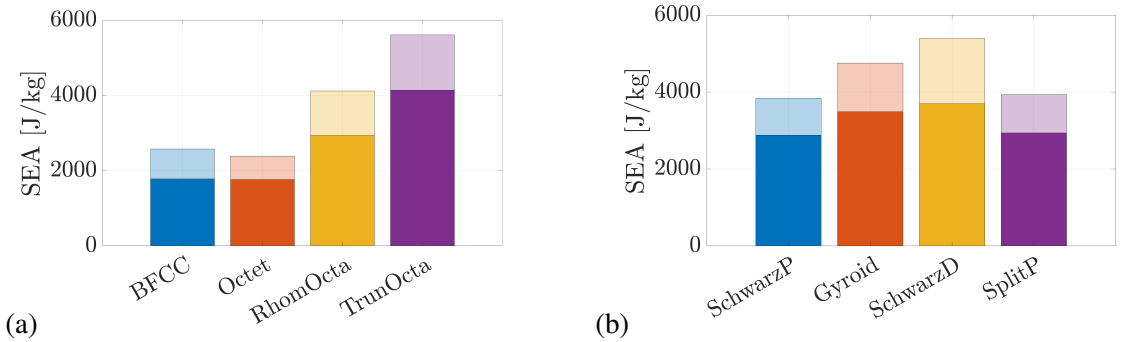

Fig. 6.26 – Specific energy absorption of the plateau part of the stress-strain curve; to illustrate the large proportion of energy absorption in the plateau region, the energy absorption across all three phases is plotted in a light color.

Table 6.5 – Percentage proportion of energy absorption in the three phases for a compression of 50% for the investigated structures with a relative density $\bar{\rho} = 0.4$.

structure	EA(phase I) [%]	EA(phase II) [%]	EA(phase III) [%]
BFCC	11	69	20
Octet	7	74	19
RhomOcta	9	71	20
TrunOcta	7	74	19
Schwarz P	10	75	15
Gyroid	10	74	16
Schwarz D	12	69	19
Split P	9	75	16

6.4 Numerical simulation

We reproduce the compression tests numerically to better understand the deformation process of the investigated structures and the associated mechanisms of energy absorption in the different lattice types. The numerical simulations were only performed for the beam-based lattice structures. All simulations were performed using the finite element software ABAQUS (Dassault Systmês), which is widely used in both academia and industry due to its versatility and robust analysis capabilities.

A non-linear static FEA is insufficient to model the buckling of the lattice struts and the subsequent collapse of the cell layers. Sveral studies have demonstrated that the symmetrical arrangement makes it too deterministic to find the points of instability. The numerical simulation of the beam-based lattice structures involves pronounced geometric nonlinearities, complex contact interaction between the struts, and large deformation up to 50%. For such problems, implicit solution shemes often suffer due to convergence difficulties. For this reason, a dynamic

FEA with ABAQUS/Explicit is used here to simulate the quasi-static tests.

The main difficulty when simulating quasi-static problems in ABAQUS/Explicit is the very small stable time increment. The critical time step Δt_{crit} in Eq. (6.16) depends on the characteristic element length L_{el}. In lattice models, the struts require a sufficiently fine discretization to accurately capture bending and local deformation effects. Consequently, the small element size significantly reduces the stable time step, leading to high computational costs.

$$\Delta t_{\text{crit}} = \frac{L_{\text{el}}}{c} \qquad \text{with} \qquad c = \sqrt{\frac{E}{\rho}} \tag{6.16}$$

The computational effort required to simulate the actual physical time would be excessively high. Therefore, the simulation time must be artificially reduced. This is achieved by slightly increasing the material density, which leads to an increase in the critical stable time steps.

$$\Delta t_{\text{crit}} = \frac{L_{\text{el}}\sqrt{\rho}}{\sqrt{E}} \tag{6.17}$$

This reduction lead to dynamic effects such as strong accelerations or vibrations. As a result, kinetic energy becomes significant, which is not accounted for in quasi-static tests. This issue can be mitigated through mass scaling. Mass scaling has to be calibrated, as excessive mass scaling increases structural interia and may introduce unwanted dynamic effects. The applied mass scaling was carefully controlled to ensure that quasi-static conditions were maintained troughout the simulations. We made sure that the kinetic energy E_{kin} was low compared to the internal energy E_{int} and did not compromise the quasi-static assumption:

$$\frac{E_{\text{kin}}}{E_{\text{int}}} \ll 1 \tag{6.18}$$

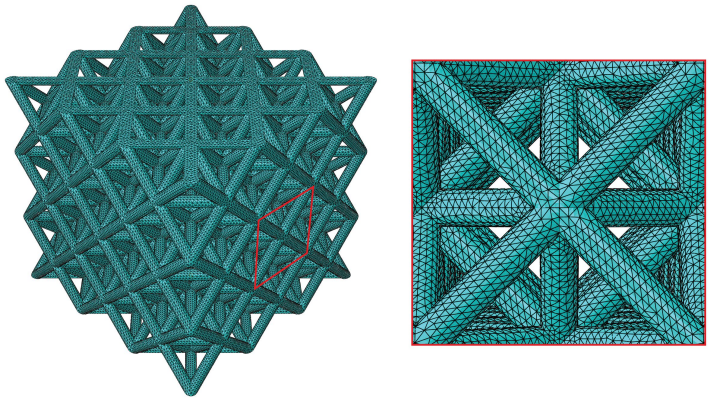

Fig. 6.27 – FEA mesh density for the Octet structure.

All structures were discretized using a sufficiently fine mesh. Mesh convergence was verified by systematically refining the element size. Fig. 6.27 shows details of the finite element mesh of the OCTET structure. The individual components of the simulation were designed as follows, see Fig. 6.28. The pressure plates were created as RIGID bodies that do not allow any deformation. The lower plate was fixed entirely and did not allow any movement in any spatial direction. The boundary conditions of the upper plate only allow movement in the z direction. A reference point created on the top surface of the upper plate was used to control the movement of the plate. The lattice structures are arranged centrally between the two plates. The contact conditions allow the structures to slide on the surface of the plates and thus expand in the $x - y$ plane. By compressing the structure, some trusses come into contact with other trusses. This contact interaction was implemented using the SELF CONTACT option within the GENERAL CONTACT formulation in ABAQUS.

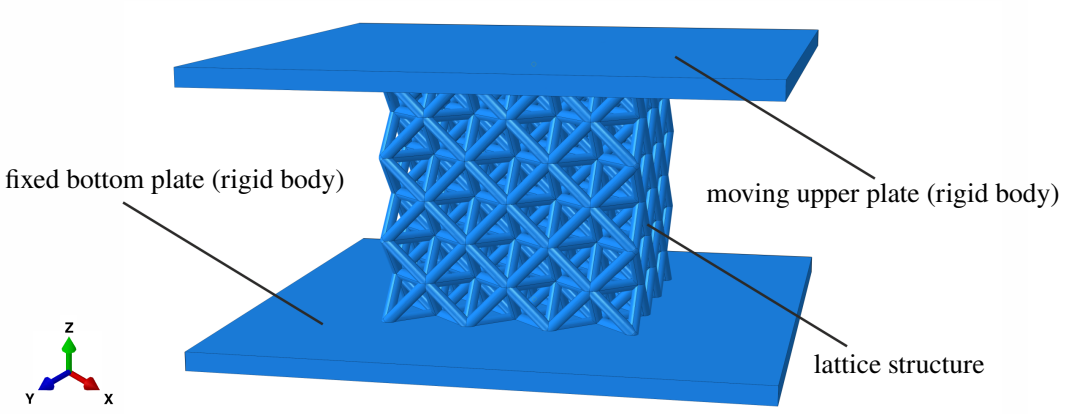

FIG. 6.28 – Assembly in ABAQUS of the quasi-static compression test with a OCTET structure.

Frictional behavior with a friction coefficient of 0.15 was assumed for all INTERACTION PROPERTIES. Due to their complex structure, the lattice structures were meshed with modified square tetrahedral elements with ten nodes (C3D10M). Since the compression analysis involves large deformations of up to 50%, significant geometric nonlinearities are expected. Therefore, C3D10M elements were employed, as they are more robust against severe element distortion than linear tetrahedral elements (C3D4). Moreover, the modified formulation improves the robustness of contact analyses and generally provides more stable convergence behavior than the standard C3D10 element formulation. The number of elements for the different lattice structures is listed in Table 6.6. As in the experiments, the specimens were compressed up to 50% by a reference point placed on the upper plate.

The Figs. 6.29 to 6.31 show the deformation of the lattice structures for the investigated relative densities $\bar{\rho}$. Similar to the experimental observations, the structures OCTET and BFCC deform uniformly in the simulation due to the high internal struts of the unit cells. The symmetric deformation of the TRUNOCTA structure is mapped by the simulation in the experiment for all

Table 6.6 – Number of elements for the FEA of the investigated specimen.

lattice structure	$\bar{\rho}$	number of elements
BFCC	0.2	1,307,384
BFCC	0.3	2,103,046
BFCC	0.4	2,201,775
Octet	0.2	1,757,082
Octet	0.3	2,417,654
Octet	0.4	3,542,680
RhomOcta	0.2	1,865,242
RhomOcta	0.3	1,948,503
RhomOcta	0.4	2,409,993
TrunOcta	0.2	870,350
TrunOcta	0.3	1,196,773
TrunOcta	0.4	1,536,409

relative densities $\bar{\rho}$. The non-symmetrical deformation of the RhomOcta for a relative density $\bar{\rho} = 0.2$ in the experiments is also mapped by the simulation, while for higher relative densities $\bar{\rho}$ the RhomOcta structure deforms symmetrically.

The quantitative agreement of simulation and experimental results is very good and demonstrates a realistic representation of the structural response, see Fig. 6.32. The FEAs show an apparent plateau for the BFCC and Octet structure. The fluctuations in the force values during phase-II of the Octet structure are reproduced in the simulations. The RhomOcta structure shows fluctuations in the curves for a relative density of $\bar{\rho} = 0.2$ in the simulation. These fluctuations are consistent with the non-uniform deformation occurring in the simulation, which was also observed in the experiments but not as strongly present.

The structures with a relative density $\bar{\rho} = 0.2$ are well represented by the simulation in the final behavior at a compression of $\varepsilon = 0.5$. Only the TrunOcta structure slightly underestimates the experiments. The initial slope of the Octet and RhomOcta structures is very steep in the simulation. Their initial behavior is similar to that of the TrunOcta structure. The experiments do not confirm this steep rise. Here, the slope of the two structures is more similar to that of the BFCC structure. The different behaviors could be due to imperfections during the printing process, which are weak points, especially at the beginning of the test. Compressing the structures during the test makes these possible imperfections less critical, which explains the similar final behavior of the structures of simulation and experiment. Such imperfections have a more substantial effect on the mechanical behavior the thinner the struts of the structure are. Since the TrunOcta structure has the thickest struts - with the same relative

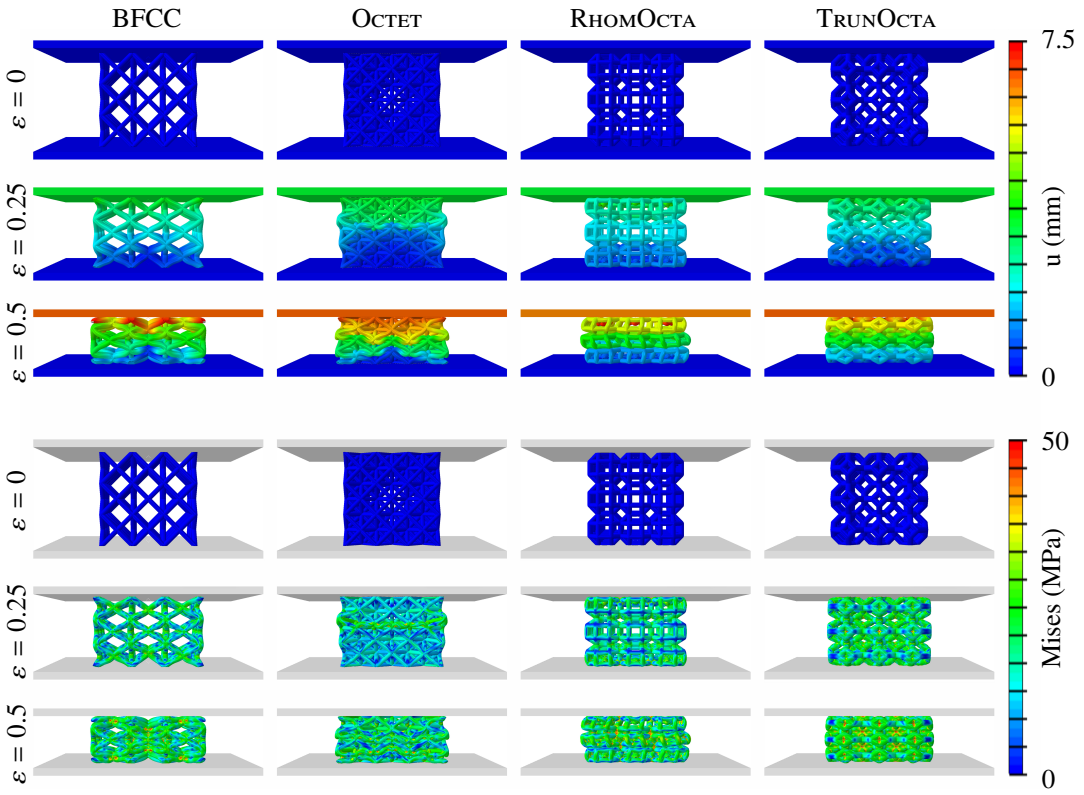

Fig. 6.29 – Simulation of the compression test of the investigated lattice structures with a relative density of $\bar{\rho} = 0.2$ at different stages of deformation (top: displacement, bottom: Mises stress).

density - the structure is more „tolerant“ of such imperfections than the other structures.

In particular for the relative density of $\bar{\rho} = 0.3$, the FEAs of RhomOcta and TrunOcta agree very well with the experiment. Only at the beginning of the slope does the simulation overestimate the force increase of the RhomOcta structure and underestimate the measured forces at a compression of 50%. The BFCC and Octet structures are well represented by the simulation. The slightly higher fluctuations of the Octet structure are represented by the simulation.

The structures with a relative density of $\bar{\rho} = 0.4$ agree with the force-displacement curves determined from the experiments. At this relative density, the FEA overestimates the forces at maximum compression. As with the simulations with the specimens of lower relative density, the simulation of the RhomOcta structure shows a stronger increase in force in the initial behavior, similar to the TrunOcta.

In general, the simulations reproduce the behavior of the structures well. For the relative densities $\bar{\rho} = 0.2$ and $\bar{\rho} = 0.3$, the simulations underestimate the experimental results, while the simulations overestimate them for a relative density of $\bar{\rho} = 0.4$. For example, the BFCC structure in the simulation shows only 95% of the force required in the experiment (at a relative densities $\bar{\rho} = 0.2$) to compress the structure up to 50%, whereas the same structure with a

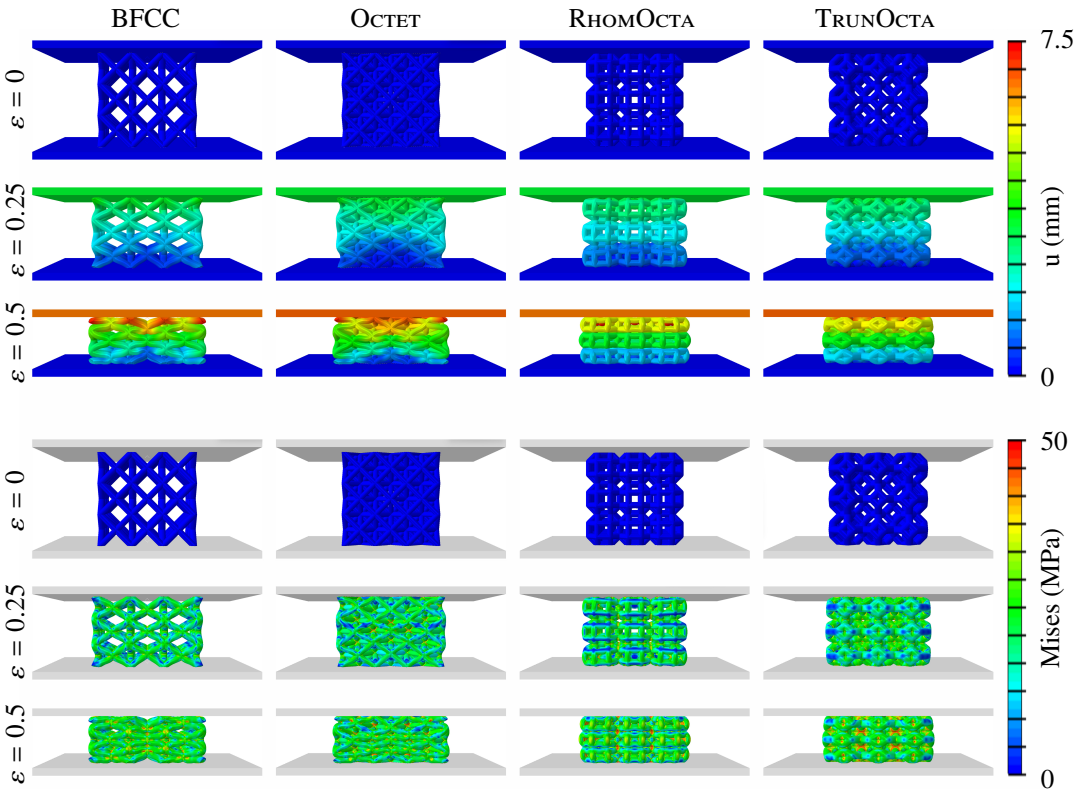

Fig. 6.30 – Simulation of the compression test of the investigated lattice structures with a relative density of $\bar{\rho} = 0.3$ at different stages of deformation (top: displacement, bottom: Mises stress).

relative density of $\bar{\rho} = 0.4$ needs 21% more force required in the experiment for a compression of 50%. Table 6.7 shows the differences between experiments and simulations of different structures and relative densities $\bar{\rho}$ at a compression of 50%.

The reason for the symmetrical deformation of Octet and BFCC is that the „inner structure“ has more connection nodes than the RhomOcta and TrunOcta structures, where no inner nodes are present. Since the structures Octet and BFCC include struts at the corners of the unit cell, and BFCC further incorparates a central node, the deformation tends to be more uniformly distributed. The spherical outer strut structure of the lattices RhomOcta and TrunOcta results in the higher stiffness that can be observed. However, these structures tend to buckle more easily in the event of strong deformations, such as a compression of 50%.

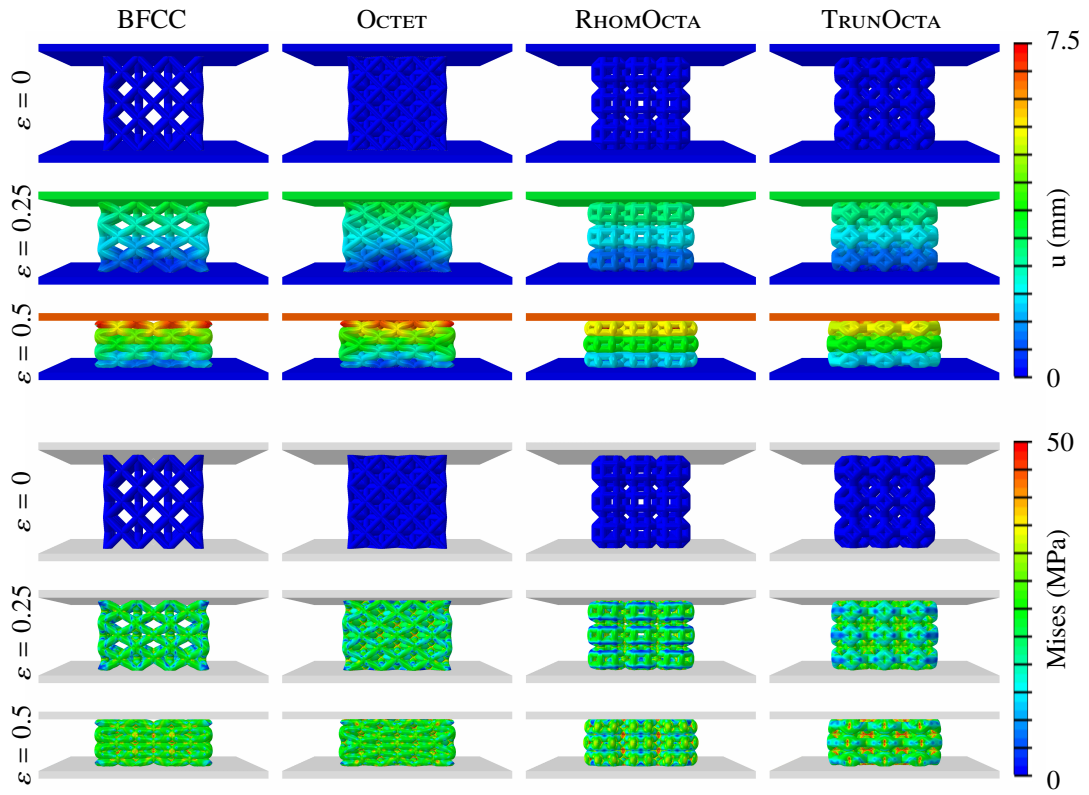

Fig. 6.31 – Simulation of the compression test of the investigated lattice structures with a relative density of $\bar{\rho} = 0.4$ at different stages of deformation (top: displacement, bottom: Mises stress).

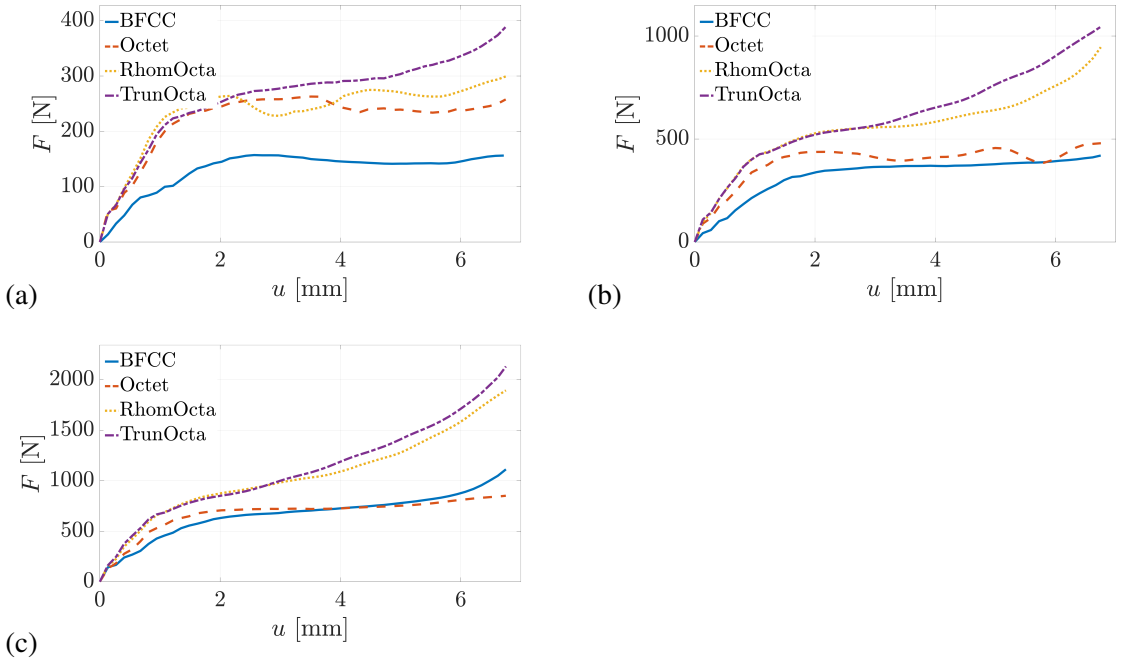

Fig. 6.32 – Numerical simulation of the force-displacement curve for the lattice structures under quasi-static compression with a) $\bar{\rho} = 0.2$, b) $\bar{\rho} = 0.3$ and c) $\bar{\rho} = 0.4$

Table 6.7 – Comparison of forces required for compression of 50%: experiments vs. simulation.

lattice structure	$\bar{\rho}$	F(exp.) [N]	F(sim.) [N]	$\frac{F(\text{exp})}{F(\text{sim})}$ [%]
BFCC	0.2	190	180	-5.5
BFCC	0.3	510	400	-27.5
BFCC	0.4	800	1100	+27.3
Octet	0.2	290	230	-26.1
Octet	0.3	600	500	-20.0
Octet	0.4	750	800	+0.6
RhomOcta	0.2	310	260	-19.2
RhomOcta	0.3	1000	900	-11.1
RhomOcta	0.4	1300	1850	+29.7
TrunOcta	0.2	490	400	-22.5
TrunOcta	0.3	1500	1100	-36.4
TrunOcta	0.4	1700	2150	+20.9

CHAPTER 7

ENERGY ABSORPTION OF OPEN-CELL STRUCTURES UNDER DYNAMIC LOADING CONDITIONS

As already mentioned in Chapter 1, the football helmet serves as a practical example of energy absorption under dynamic loadings to motivate the investigation. To absorb kinetic energy through collisions between players, buckling columns are integrated inside the shell of modern football helmets. These buckling columns allow the kinetic energy to be absorbed, thereby protecting the player's head inside the helmet from induced shock waves.

Within this chapter, the same structures with the same relative densities $\bar{\rho}$ as in Chapter 6 are examined, but under dynamic conditions. A classification of the structures and their geometric properties can be found in Sections 6.1 and 6.2.

Evolution of helmet structure

The evolution of the NFL helmet is shown in Fig. 7.1 with technological advantages such as full-head protection in 1925 (called Zuppke style helmet), fiber shell technology used from the 1930s to the early 1950s, and plastic helmets from the 50s. From the practical application, it was observed that the plastic helmets remained form-stable even when subjected to severe collisions. Henceforth, a plastic mask was attached to protect the entire head region. Nowadays, with the help of advanced technology, structures from almost any material can be assembled into any shape. It makes sense to optimize the helmet's shape to absorb the impact as much as possible.

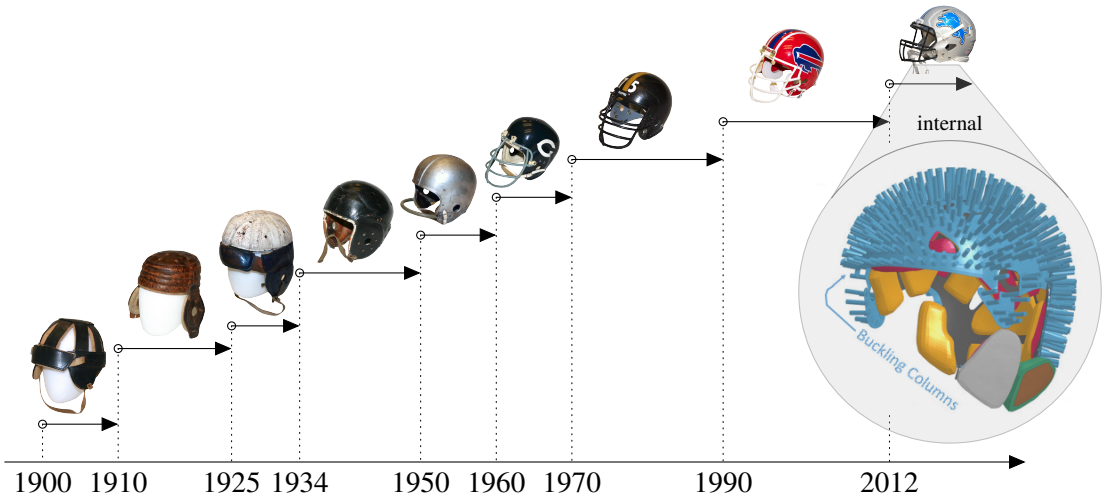

Fig. 7.1 – Evolution of football helmets according to [Miller 2023] and internal view of modern helmet [Giudice et al. 2020].

Equivalent model

As can be seen in Fig. 7.1, modern helmets already have an internal structure to cushion impacts to the player's head. A structure made of buckling bars is used for this purpose. The bending or buckling of the bars can absorb the impact energy. In this section of the thesis, more complex structures are tested for their energy absorption properties.

The first step in the study of any problem is to simplify the complex problem into an equivalent simpler model that is analytically or numerically solvable. To do so, in an abstract image, two player are modeled as cylinders. The printed structure represents the helmet's internal protection system. To investigate on the question about the drop impact on the brain, the striker is accelerated and collide with the structure. This abstraction is comparable to a modified SHPB test and is used to investigate wave propagation.

For the experiments in this section of the work, the eight structures that have already been examined in Section 6.3 under static load are tested under dynamic impact load. The classic SHPB setup has to be modified to match the impact problem, see Fig. 7.2.

7.1 Modified split Hopkinson pressure bar setup

The SHPB experiment in its conventional form has already been presented in Section 4. There, the focus was on characterizing materials under high strain rates. Lattice structures can be analyzed using classic SHPB tests, as demonstrated by the investigation of copper lattice structures at high strain rates in the publication [Kang et al. 2023] or in [Bieler et al. 2025e], where TPMS structures made of aluminum are examined regarding the energy absorption properties. In the publication [Khosravani et al. 2025], the mechanical fracture of SLS printed lattices made of Polyamide 12 is investigated. However, this chapter is dedicated to the energy

absorption properties of the presented structures under impact loading. To determine the energy absorbed by the specimen, a different, more energetic approach is used for experimental evaluation. An appropriately modified variant of the classic SHPB setup is used, where the striker directly impacts the specimen, as described in [Bieler and Weinberg 2025c] and [Bieler and Weinberg 2025a]. In this modification, the specimen is no longer clamped between the incident bar and transmission bar, but is attached to the front surface of the incident bar. This modified experiment is intended to show the effect on the measured impulse by applying the respective lattice structure to the front face of the incident bar. The impulse is temporally stretched due to the deformation of the structure, and its amplitude is attenuated. As only the induced first pulse is of interest for this experimental setup, the signal from the applied strain gauge on the transmission bar is irrelevant. Nevertheless, both bars are in contact during the experiment. Through the contact of the bars, the induced pulse can be transferred from the incident bar to the transmission bar without reflection. Consequently, no superposition of the induced and reflected impulses occur. A signal correction of the recorded signal is carried out in the same way as already explained in Section 4.5.2. The striker speed was set to v_{St} = 15 m/s for all structure types and all relative densities $\bar{\rho}$. PMMA was used as the bar material for the experiments due to a better impedance difference to the soft material SuperFlex and the small cross-sectional area of the structures. The dimensions of the individual components for the setup used here can be found in Table 7.1.

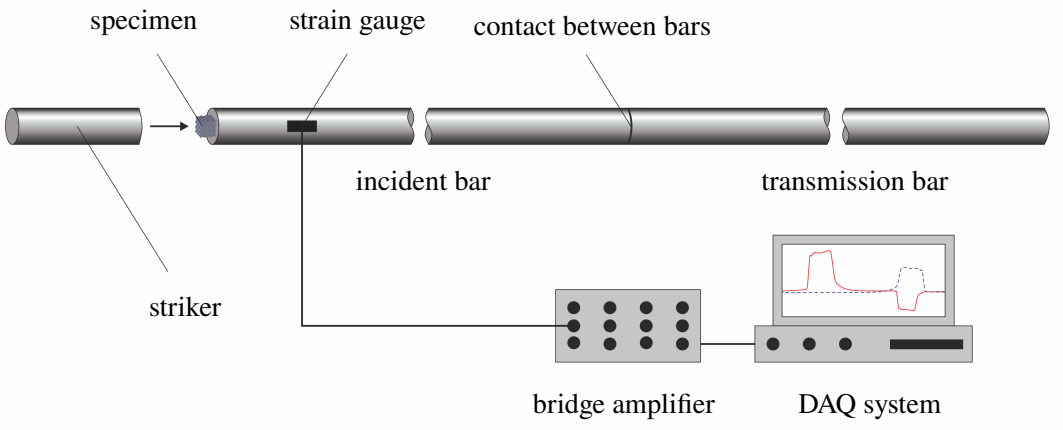

Fig. 7.2 – Modified SHPB setup.

The test procedure is as follows: The energy absorbed by the deformation of the applied structure is determined by evaluating the signal from the strain gauges. The measured signals are used to conclude the energy-absorbing properties of the respective structures. However, this means that a reference measurement is first carried out without any applied structure, so that it can then be compared with measurements made with the applied structure. Hard and brittle materials are only suitable to a limited extent for the multiple or sustainable use of

Table 7.1 – Dimensions of the SHPB-setup for lattice structure experiments.

	incident bar	transmission bar	striker
material	PMMA	PMMA	PMMA
d [mm]	20.00	20.00	20.00
l [mm]	3000.00	2000.00	300.00
ρ [kg/m^3]	1180.00	1180.00	1180.00
E_{stat} [GPa]	3.00	3.00	3.00

energy-absorbing structures under impact loads. Although some of the energy is absorbed here too, the structure is usually destroyed and lost. It should be noted that the material for the static tests from Section 6.3 (Anycubic Tough 2.0) are not suitable for impact loads. Due to the high strain rates, the viscous component in this material does not have sufficient time to evolve, and therefore, this material appears very brittle in dynamic tests. TPU-based polymers are more suitable for impact loads. Due to their good deformability, they can absorb energy well and return to their original state after a specific recovery time. The tests are recorded by a high-speed camera Photron SA3 with a frame rate of 30,000 fps to capture the deformation of the specimens. Fig. 7.3 (top) to Fig. 7.6 (top) show how lattice structures made of the acrylic-like material Tough 2.0 break under the influence of the striker.

As sustainability plays a key role in many areas of technology, the focus is set on the TPU-based resin. Structures made of this material dampen the impact and absorb energy through their deformation. The Octet structure is compressed by 80% at a relative density of $\bar{\rho} = 0.2$. Despite this strong compression, the structures return completely to their initial state within a few seconds without damage. Fig. 7.3 (bottom) to Fig. 7.6 (bottom) show the recorded compression of the four investigated beam-based lattices at different instances. Several experiments were conducted to evaluate the measured results statistically. Four specimens of each lattice and TPMS type and each relative density $\bar{\rho} = 0.2....0.4$ were produced for the impact experiments. Each specimen was subjected to several loads to prove further the structure's sustainability (three tests with a striker speed of $v_{\text{St}} = 15$ m/s). This results in a specimen set of 96 specimens for eight different structures with three different relative densities $\bar{\rho}$ and a test set of 288 experiments. As the specimens returned to their initial state within seconds, a three-minute time window was defined between the individual loads applied to a specimen.

7.2 Experimental investigation of soft polymer structures under dynamic loading

This section examines the properties in detail, including pulse attenuation of pulses and energy absorption.

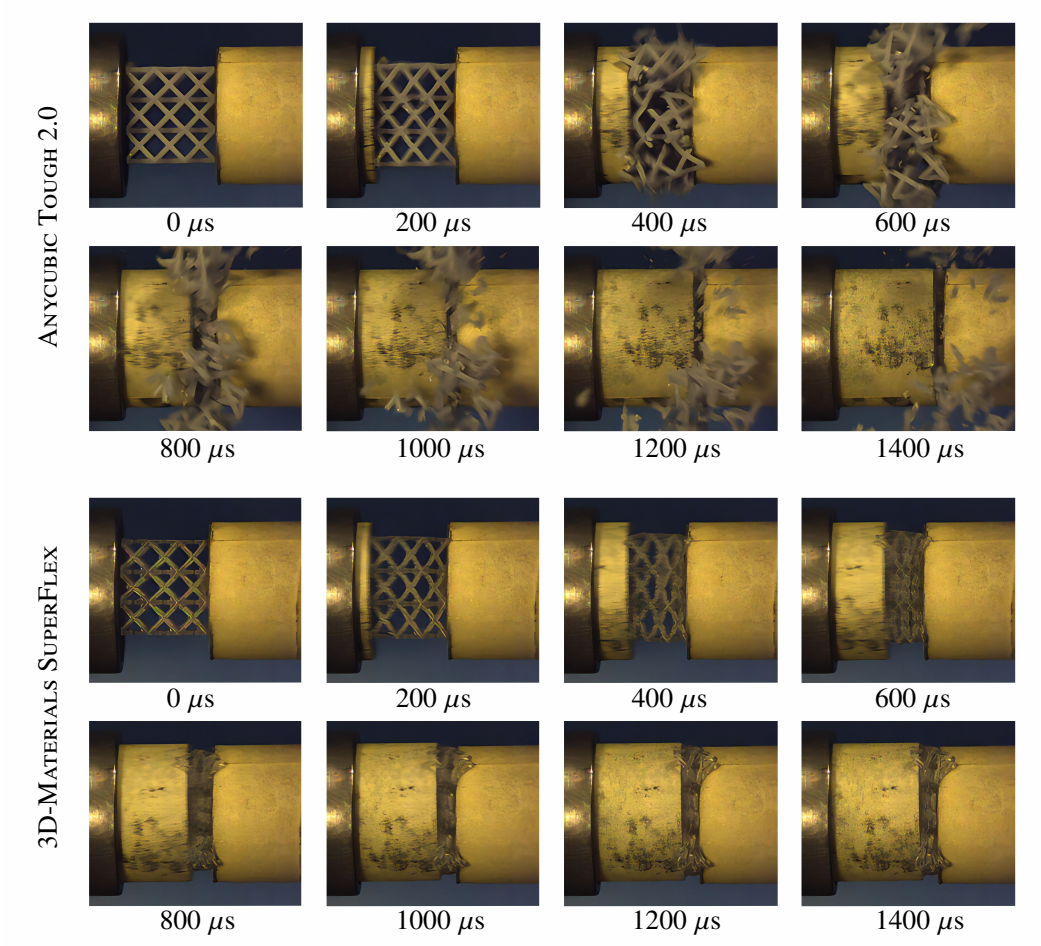

Fig. 7.3 – Different states of deformation during the experiment with the BFCC structure with a relative density of $\bar{\rho} = 0.2$. The specimen made of the acrylic-like material Anycubic Tough 2.0 fails completely, whereas the TPU-like material 3D-Materials SuperFlex deforms and returns to its initial state.

7.2.1 Attenuation of the pulses

The beam-based lattices and TPMS structures attenuate the pulses and stretch them out over time, i.e., the amplitudes of the individual structure types occur at different times. Due to the folding of the individual structure layers, the pulse shape differs depending on the lattice type or TPMS structure used. The higher the relative density $\bar{\rho}$ of the specimen, the flatter the amplitude for one type of structure. This flattening generally applies to all tested specimens, see Fig. 7.7 (left) and Fig. 7.8 (left). These curves display the mean values of the experiments for the respective lattice structures and relative densities, along with an error band and a 95% confidence interval. The curves include all three loads that were applied to the respective specimens. For better comparability of the impulses, they are all shifted to time zero with the first increase. By integrating the force over time, a pulse-time curve is obtained for each

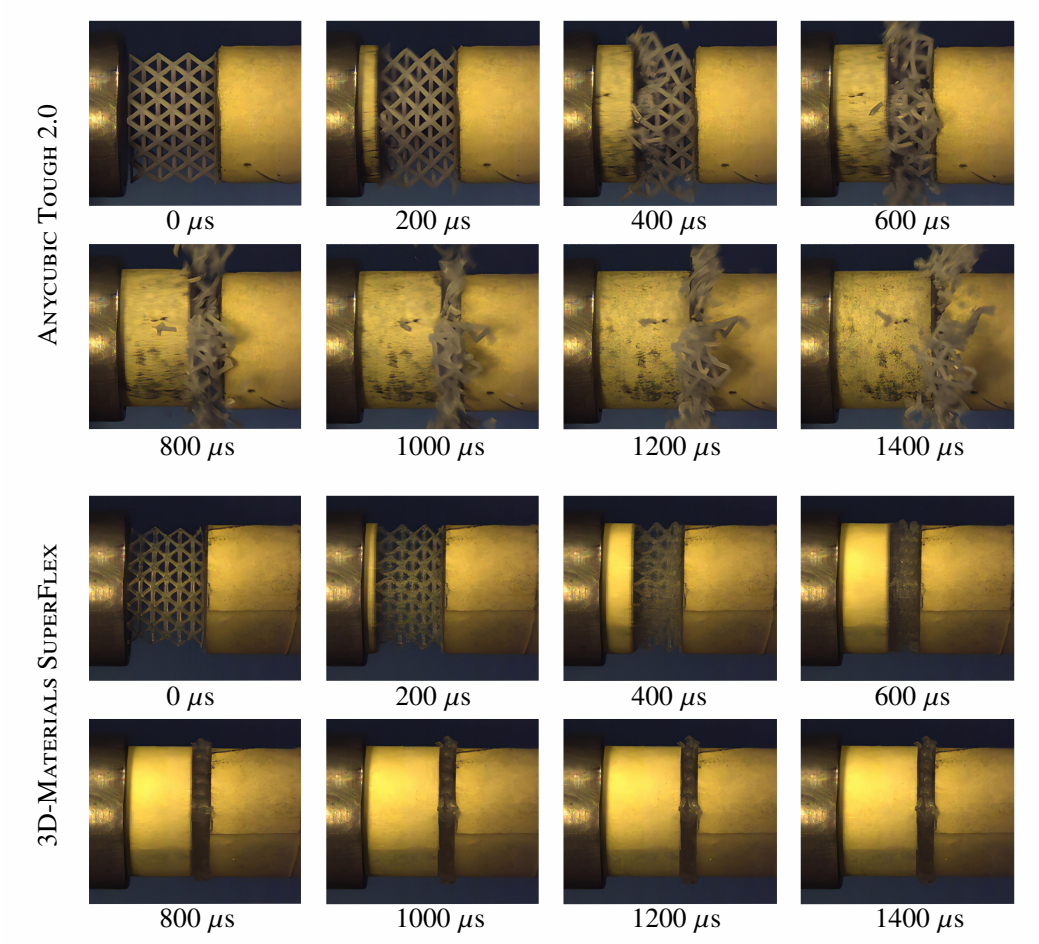

Fig. 7.4 – Different states of deformation during the experiment with the Octet structure with a relative density of $\bar{\rho} = 0.2$. The specimen made of the acrylic-like material Anycubic Tough 2.0 fails completely, whereas the TPU-like material 3D-Materials SuperFlex deforms and returns to its initial state.

measurement, see Eq. (7.1).

$$p(t) = E_b \frac{\pi d_b^2}{4} \int_{t_0}^{t_1} \varepsilon_I(t)\,\mathrm{d}t \tag{7.1}$$

Here d_b, E_b and ε_I denotes the diameter, Young's modulus of the bar and ε_I the measured signal from the strain gauge on the incident bar. The impulse-time curves show that the increase in the curves with decreasing relative density $\bar{\rho}$ is delayed in time when comparing the same lattice/ TMPS type. For the experiments with lower relative densities $\bar{\rho}$, however, the rise then follows very steeply in contrast to specimens with higher $\bar{\rho}$. Since the slope of the curve represents the load on the specimen over time, a higher relative density $\bar{\rho}$ can be considered a more uniform load on the specimen over time, see Fig. 7.7 (right).

The TPU-made structures attenuate the impulse and absorb energy through their deforma-

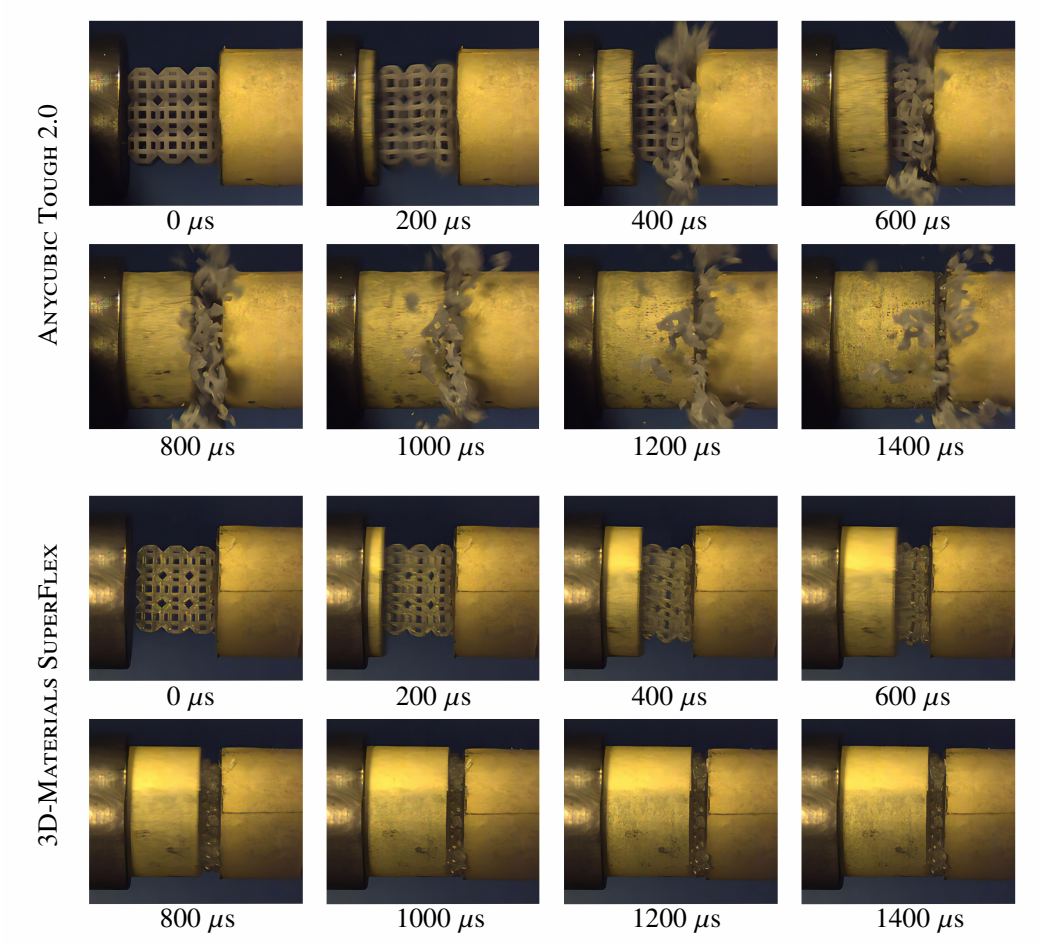

Fig. 7.5 – Different states of deformation during the experiment with the RhomOcta structure with a relative density of $\bar{\rho} = 0.2$. The specimen made of the acrylic-like material Anycubic Tough 2.0 fails completely, whereas the TPU-like material 3D-Materials SuperFlex deforms and returns to its initial state.

tion. After a specific recovery time, however, the structure returns to its original state. A strong compression of the specimens can be observed during the tests, see Fig. 7.3 (bottom) to Fig. 7.6 (bottom). The Octet structure is compressed by approximately 80% at a relative density of $\bar{\rho} = 0.2$ during the test. Despite this strong compression, the structure relaxes entirely to its initial state without fractures due to the deformation.

The TPU structures significantly reduce the pulse peaks compared to the reference shot without any specimen at the front surface of the incident bar. A reduction of 57% in the amplitude is achieved by applying a TrunOcta structure with a relative density of $\bar{\rho} = 0.4$. For all structures, the pulse lengths show a temporal elongation of the pulse between 113% (BFCC $\bar{\rho} = 0.4$) and 138% (TrunOcta $\bar{\rho} = 0.2$).

Despite the strong compression of the specimens, all lattices were able to return to their original shape without detection of any fractures or external cracks in the structure, even after

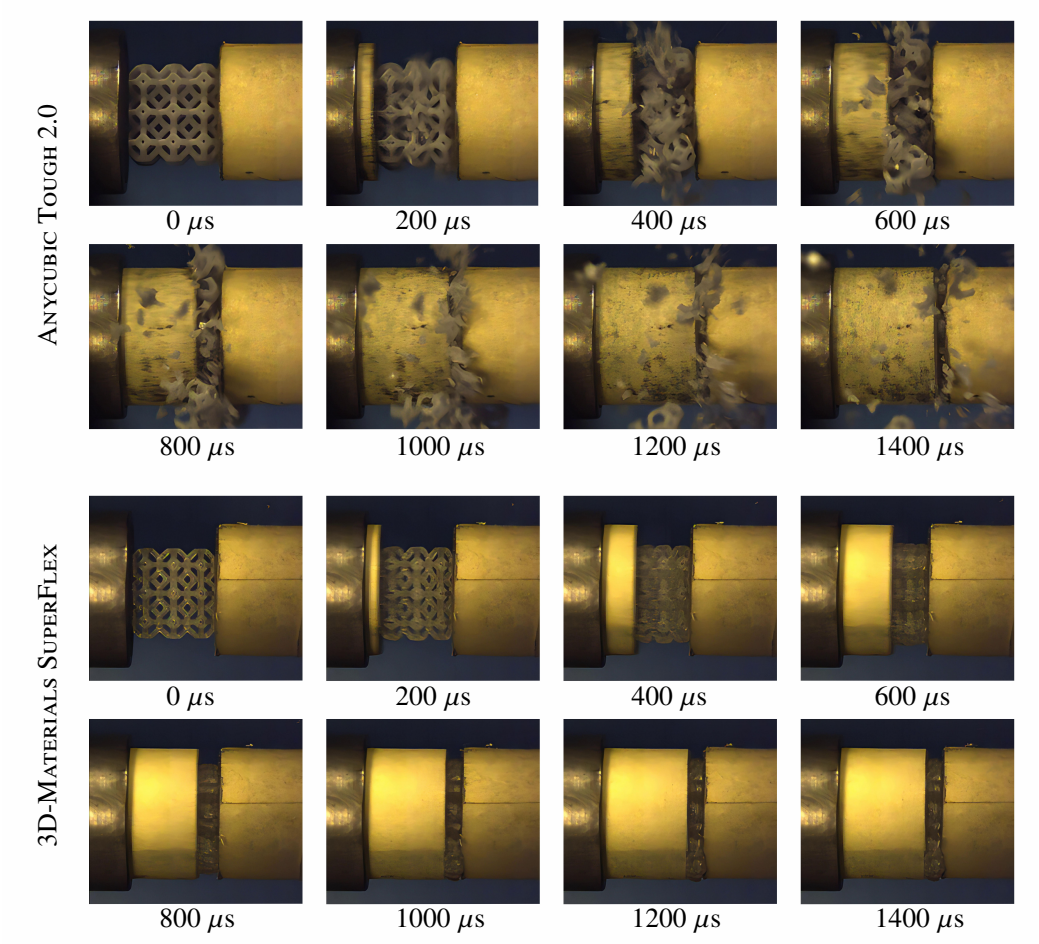

Fig. 7.6 – Different states of deformation during the experiment with the TrunOcta structure with a relative density of $\bar{\rho} = 0.2$. The specimen made of the acrylic-like material Anycubic Tough 2.0 fails completely, whereas the TPU-like material 3D-Materials SuperFlex deforms and returns to its initial state.

multiple loads.

To emphasize the sustainability of the structures concerning multiple loads, this is exemplified by the Octet structure in Fig. 7.9. The measured impulses under repeated loading exhibit a largely consistent shape. Fig. 7.9 shows three curves, each representing a set of four identical lattice types , subjected to a different number of loadings. The error bands (confidence interval to the level of 95%) within each set are very narrow, and a comparison across all three sets shows a similarly high consistency in impulse shape. This demonstrates that the Octet structure can reliablay withstand multiple loading cycles without experiencing structural changes, such as cracking or other damage, that might compromise their energy absorption performance.

Not every structure exhibits the same degree of reversibility. Depending on the structure, the response to the second and third loading cycles may vary slightly. At a relative density of $\bar{\rho} = 0.4$, most structures demonstrate excellent reversibility. The Octet and Split P structures

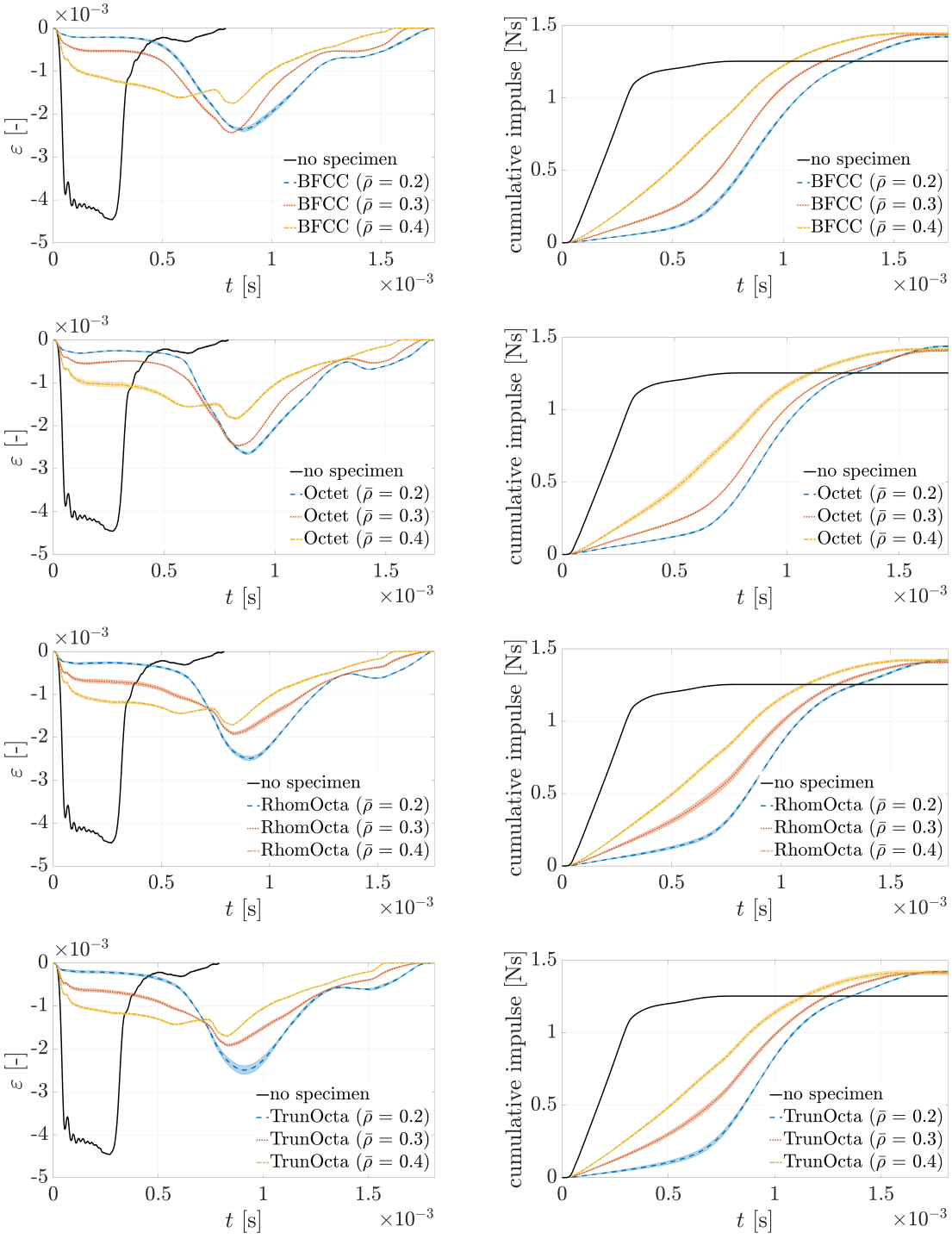

Fig. 7.7 – Measured pulses signals (left) and the cumulative impulse (right) of the different lattice types.

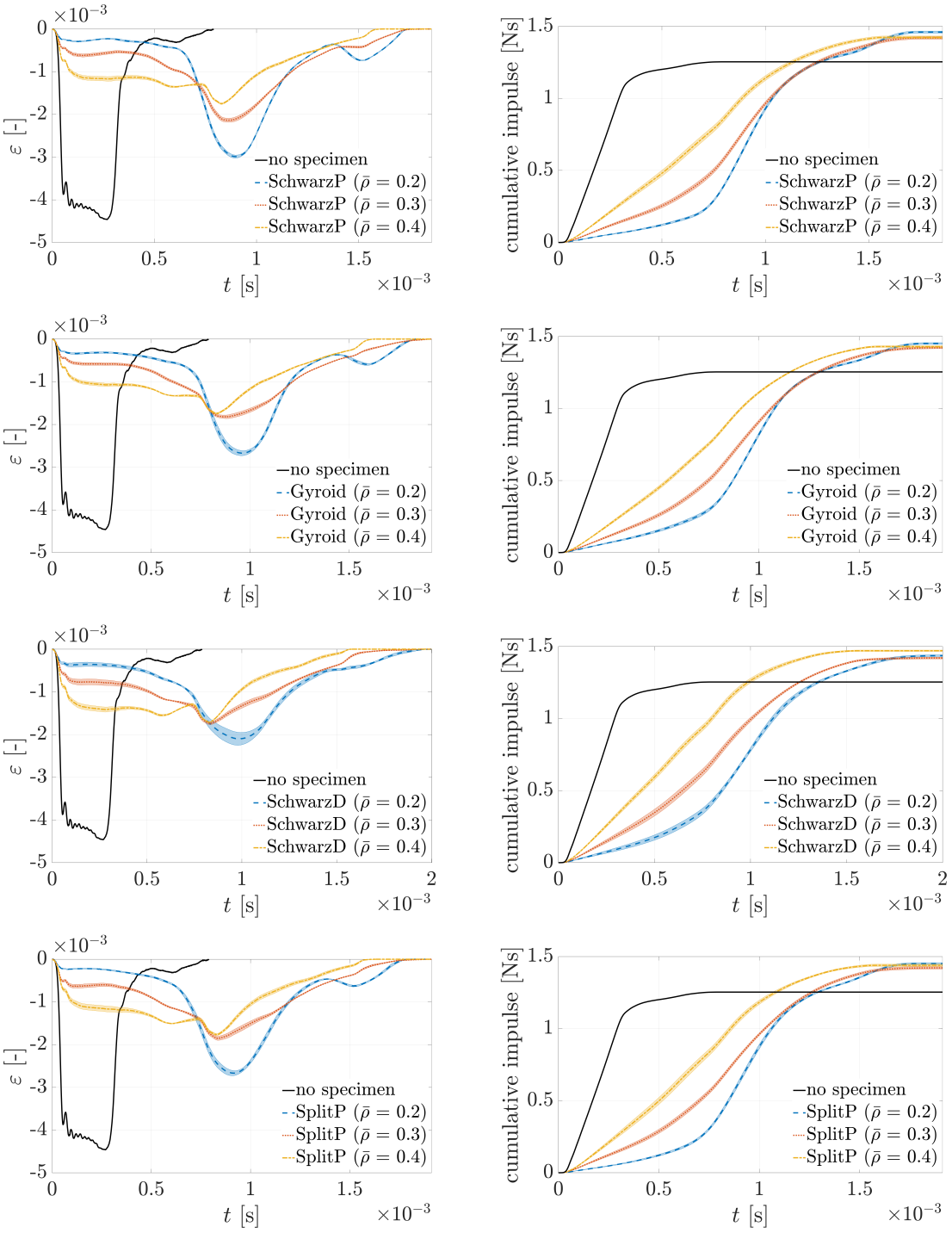

Fig. 7.8 – Measured pulses signals (left) and the cumulative impulse (right) of the different TPMS types.

also maintain good reversibility at lower relative densities $\bar{\rho}$. In contrast, the TrunOcta, Gyroid, and Schwarz D structures exhibit significant reductions in reversibility at a relative density of $\bar{\rho} = 0.2$. Accordingly, structural damage cannot be ruled out for all structures at every relative density. However, provided that the strain gauge signals exhibit consistent pulse waveforms across all loading cycles, it may be assumed that the applied loading has not caused any structural damage. For the multiple loading cases of all structures, the reader is referred to Section A.4.

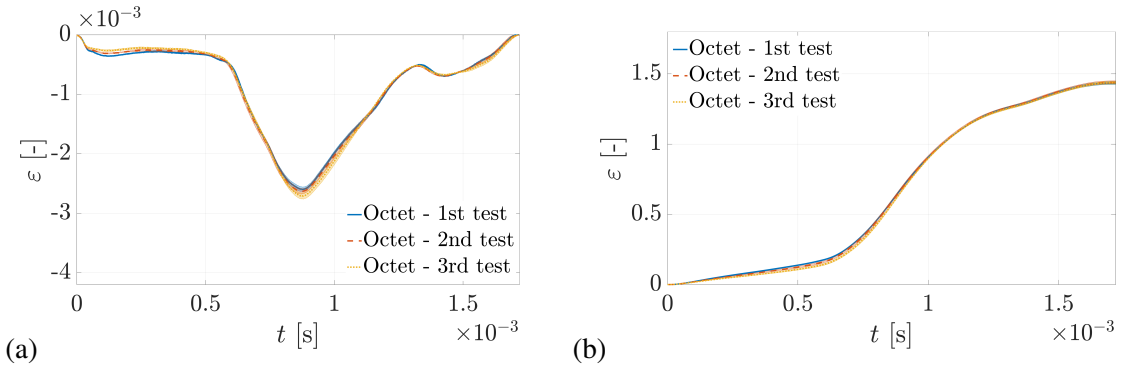

Fig. 7.9 – a) Octet $\bar{\rho} = 0.2$ pulses measured during repeated loading and b) the resulting cumulative pulses.

7.2.2 Energy absorption

In [Beccu and Lundberg 1987; Lundberg 1976] experiments on energy dissipation using a specimen on a conventional SHPB were already conducted in 1976. This was done by calculating the energies of the incident, reflected and transmitted pulses. It was found out the portion of dissipated energy by calculating the difference between the energy of the incident pulse and the sum of the reflected and transmitted pulses. In this way, the energy absorption of a specimen can be determined by Eq. (7.2):

$$\Delta W = W_\mathrm{I} - (W_\mathrm{R} + W_\mathrm{T}) \tag{7.2}$$

where ΔW is the absorbed energy and $W_\mathrm{I}, W_\mathrm{R}, W_\mathrm{T}$ are the energies of the incident, reflected and trasmitted pulse. The energy of the respective pulses is determined by Eq. (7.3):

$$W = \frac{A_\mathrm{b}\, c_\mathrm{b}}{E_\mathrm{b}} \int_0^t \sigma^2(\tilde{t})\, \mathrm{d}\tilde{t} = A_\mathrm{b}\, c_\mathrm{b}\, E_\mathrm{b} \int_0^t \varepsilon^2(\tilde{t})\, \mathrm{d}\tilde{t} \tag{7.3}$$

where A_b and c_b are the cross-section area of the bar and the wave propagation velocity of the bar material. This method for determining energy absorption has already been used in [Bieler et al. 2021] with copper lattice structures.

In the modified setup of the SHPB experiment, only the incident impulse is evaluated in the experiments discussed in this section. This means that for the procedure described here,

only the first incident impulse or its energy content is of interest. The difference between the induced energy of the reference measurement W_{ref} without applied lattice structures and the energy with applied structures W_{lattice} represents the absorbed energy of the specimen, see Eq. (7.4). For the reference impulse, the resulting energy measured through the induced pulse was 11.37 Nm at a striker velocity of 15 m/s.

$$\Delta W = W_{\text{ref}} - W_{\text{lattice}} \tag{7.4}$$

The total absorbed energy of the different lattice structures is shown in Fig. 7.10 a). The absorbed energy of the individual structures relative to the specimen mass of the structure gives the specific energy absorption, cf. Eq. (6.11). In Fig. 7.10 b) the SEA of the different beam-based lattices and TPMS structures with the investigated relative densities $\bar{\rho}$ are shown.

For the beam-based structures BFCC and Octet, as well as the TPMS structure Schwarz P, there is an apparent increase in energy absorption (EA) with increasing relative density $\bar{\rho}$.

For the structures RhomOcta, TrunOcta, and Gyroid, an almost similar energy absorption behavior can be observed at a relative density of $\bar{\rho} = 0.3$ and $\bar{\rho} = 0.4$. Both structures are characterized by a high negative Maxwell number M (RhomOcta: M = -18 and TrunOcta: M = -30). Furthermore, neither structure has nodes in the center or corners of the unit cell.

The structures Schwarz D and Split P initially show, an increase in energy absorption properties when the relative density increases from $\bar{\rho} = 0.2$ to $\bar{\rho} = 0.3$. However, when comparing the relative densities of $\bar{\rho} = 0.3$ to $\bar{\rho} = 0.4$, a decrease in energy absorption is observed. Due to the higher wall thickness t_{W}, the structure is less deformed, which in turn is reflected in lower energy absorption. Consequently, those structures are more suitable for high-load scenarios in which the structures undergoes larger deformations. At higher loads, the energy absorption of structures with lower relative density will be lower, as the stronger and faster compression allows a large part of the impact energy to be transferred to the incident bar through the fully collapsed structure.

The quality of the energy absorption properties is therefore highly dependent on the load acting on the structure. High relative densities $\bar{\rho}$ have a correspondingly disadvantageous effect at lower loads.

It can be seen that all structures exhibit a decrease in specific energy absorption as the relative density $\bar{\rho}$ increases. The Schwarz D structure with a relative density of $\bar{\rho} = 0.2$ exhibits the best specific energy absorption with a SEA = 11,150 J/kg.

7.2.3 Comparison of frequency spectrum

Observing the frequency spectrum of the induced pulses provides additional insight into the filtering characteristics of the lattice specimens by revealing which frequency components are attenuated or preserved during wave propagation. The spectra of the recorded signals were

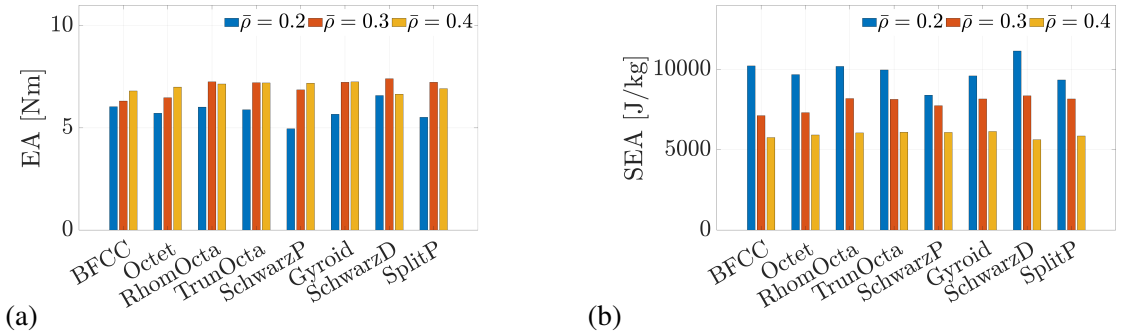

Fig. 7.10 – a) Absolute energy absorption and b) specific energy absoption for each lattice typ at different $\bar{\rho}$.

obtained using a Fast Fourier Transform (FFT). Figure 7.11 compares the frequency spectra measured with and without the presence of lattice structures at a relative density of $\bar{\rho} = 0.3$.

The data clearly show that all investigated lattice topologies reduce spectral amplitudes at higher frequencies, demonstrating that these structures function as low-pass filters. Lower-frequency components are transmitted with minimal attenuation, while higher-frequency components are suppressed. Notably, almost all frequencies above approximately 7 kHz are attenuated regardless of lattice topology. These findings indicate that the periodic cellular architecture efficiently limits high-frequency energy transmission by dissipating and scattering short-wavelength waves.

The spectra for the other lattice topologies and relative densities show similar reductions in higher-frequency amplitudes, as detailed in the Appendix A.5. This consistently demonstrates that all investigated lattice structures selectively attenuate higher frequencies across the entire parameter space of this study.

7.3 Numerical Simulation

To better understand the deformation during the SHPB test, numerical simulations using FEA were carried out. The whole experimental setup was built in Abaqus/ Explicit. Fig. 7.12 shows a detailed FE model. The full FEA is very time-consuming and computationally intensive and was run on the OMNI cluster at the University of Siegen, utilizing three nodes with 64 cores each and 240 GB of RAM, over a total period of 1.5 ms. Because of the high computational effort required for the simulation, the FEA was only carried out with the Octet structure with the relative density of $\bar{\rho} = 0.2$.

For the simulation, the transmission bar was omitted because it is not required, as explained in the experimental part before. The incident bar and the striker were meshed with hexagonal elements (C3D8R). The complexity of the lattice structures' geometry makes it difficult to mesh them using hexagonal elements (C3D8R). Therefore, the lattices were meshed by ten-node modified quadratic tetrahedron elements (C3D10M). The Octet structure has a high mesh

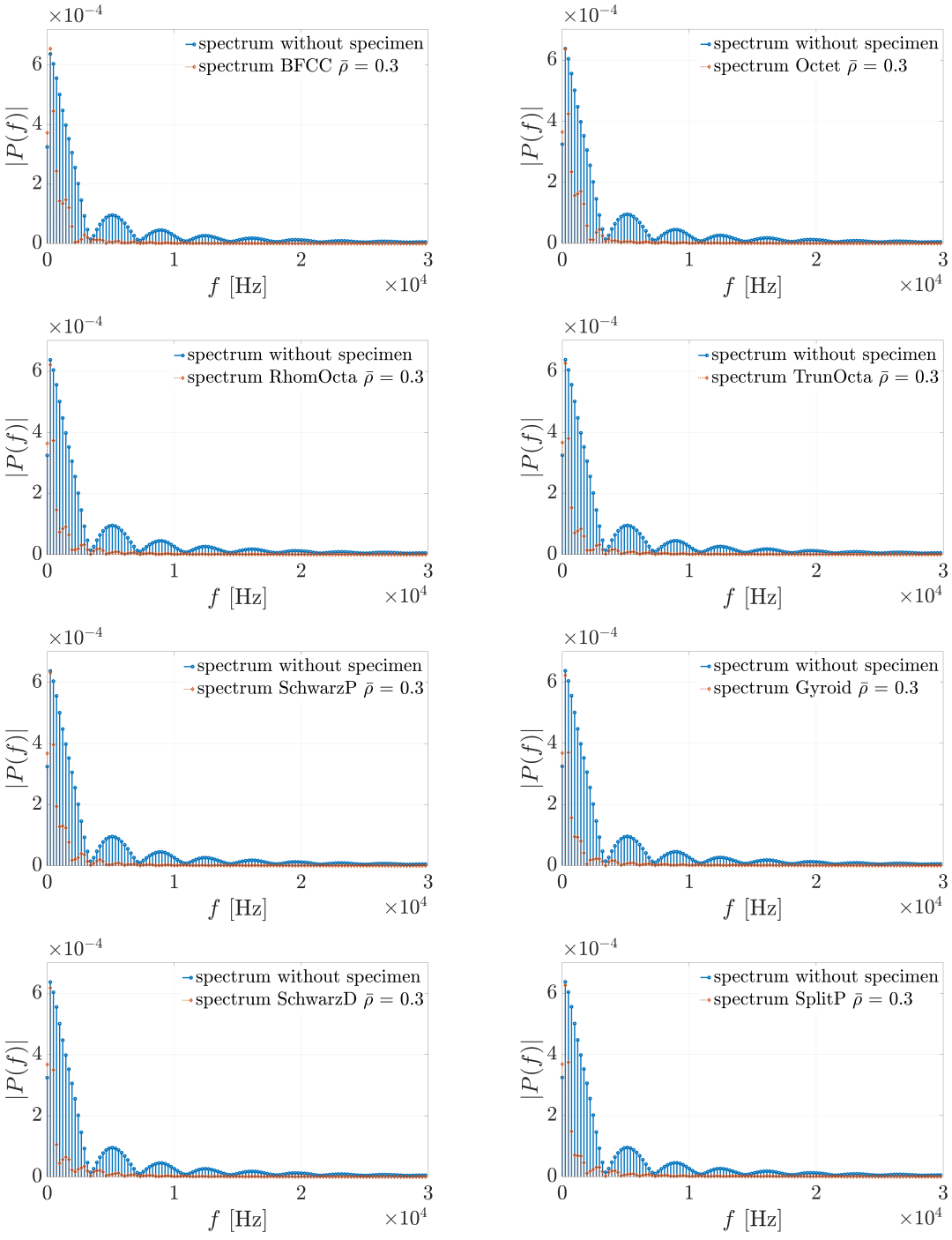

Fig. 7.11 – Spectra of the investigated lattices and TPMS structures at a relative density of $\bar{\rho} = 0.3$.

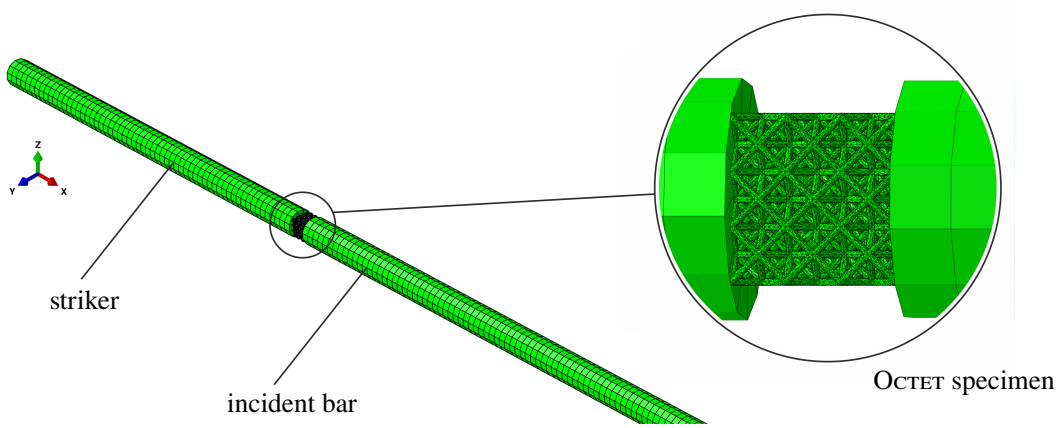

Fig. 7.12 – Finite element mesh for the simulation of the impact test.

density with a number of elements of 3,883,880. The authors [Huang et al. 2025] choose a similar approach in their work. This paper investigates the energy absorption of SLM printed Octet structures under static compression, with a subsequent comparison of the experimental results and a numerical simulation, implemented in Abaqus/Explicit.

The contact between the incident bar and the specimen and between the striker and the specimen was realized as surface-to-surface contact with a friction coefficient of 0.15. The striker and the incident bar were assigned with the material PMMA. For the PMMA, a modulus of elasticity of 3 GPa and a Poisson's ratio of $\nu = 0.37$ were chosen. For the specimen 3D Materials SuperFlex, a high modulus of elasticity $E = 120$ MPa was chosen because of the high strain rate during the impact. The Poisson's ratio was assigned as $\nu = 0.45$. For both bars, only movement in the axial direction is allowed. Due to the strong deformation in the simulation, parts of the structure come in contact. Therefore, Self Contact was added for the lattice structure. The striker velocity was set analogous to the experiments via a Predefined Field velocity of $v_{st} = 15$ m/s.

The simulation of the SHPB experiment shows a realistic mechanical deformation of the lattice structures under dynamic impact. Fig. 7.13 show the specimen compressed by about 80% within 1400 μs. The layers of the Octet structure are completely compressed at 800 μs. Therefore, the densified structure enables the impulse to be transferred more effectively to the incident bar. This interpretation fits very well to the measured impulses in Fig. 7.7, where we observe that the peak of the impulse is located at 800 μs. However, a systematic quantitative investigation of the corresponding energy absorption is not feasible. The complex calculations require very small time steps and partial mass scaling. In addition, the simulation depicts a perfect structure without any imperfections, which is not possible in the real printing process.

Despite of these idealisations, FEA has its justification and is helpful because it enables the investigation of details of deformation that cannot be captured in an experiment. Fig. 7.14 shows an example of the deformation behavior and the stress distribution of the Octet structure

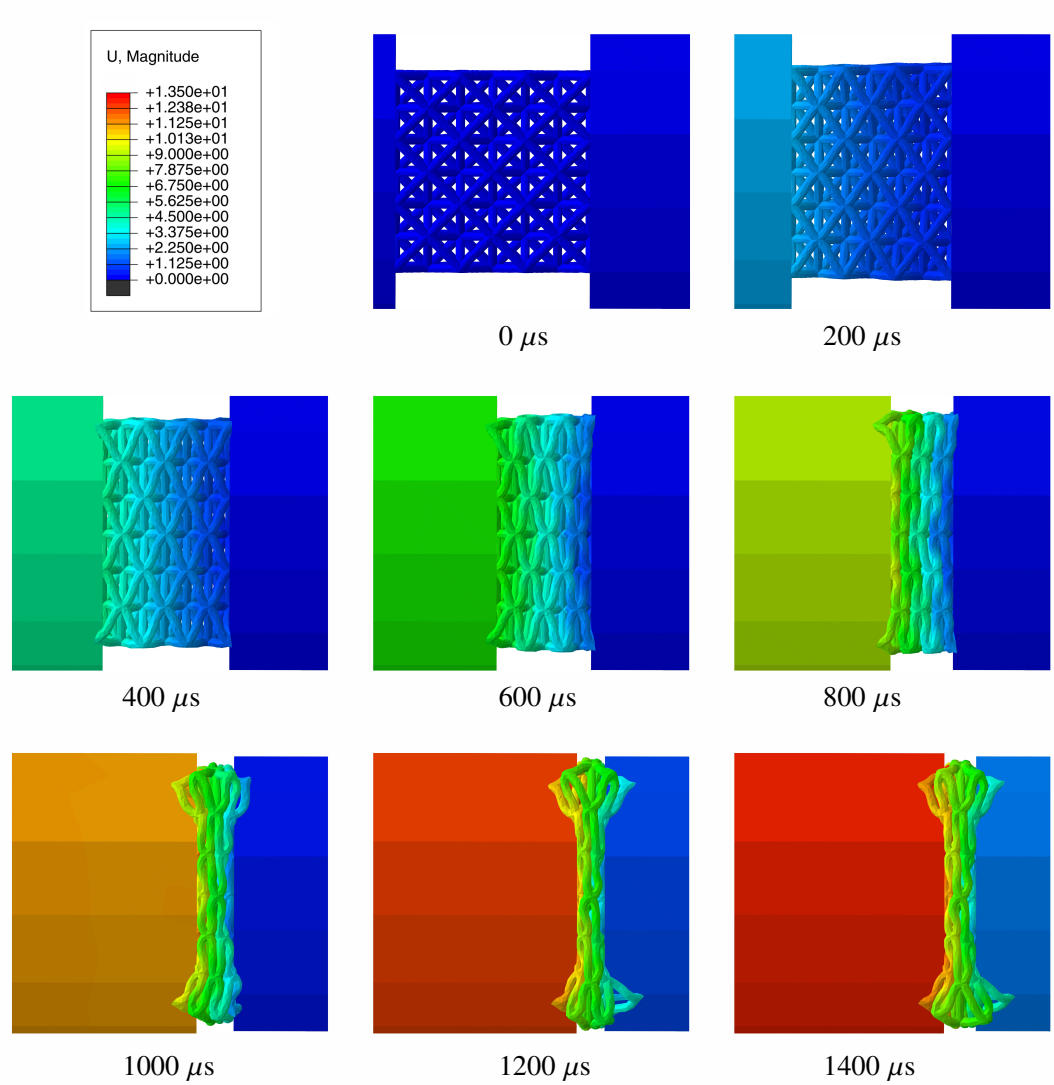

Fig. 7.13 – Snapshots of the FEA of the SHB experiment with an Octet-lattice structure ($\bar{\rho} = 0.2$); the striker impacts the lattice structure on the left side.

at different time steps. The structure deforms mainly due to twisting at the nodes. The nodes of the structure, especially at the contact points to the pressure plates, show the maximum stresses of the specimen. A simple estimation based on the Maxwell number of the corresponding structure does not allow any conclusions to be made about the stress distribution. It is not evident from the experiment itself. Thus, FEA supports the understanding of the deformation mechanism, but can only represent the process to a certain extent.

In Fig. 7.15, the signals from the strain gauges determined show a good agreement with the signals from the simulation. For comparison, the strains of the elements corresponding to the positions of the strain gauges from the experimental setup were evaluated in the simulation. Regarding the pulse amplitude, there is an excellent agreement between the simulation and the

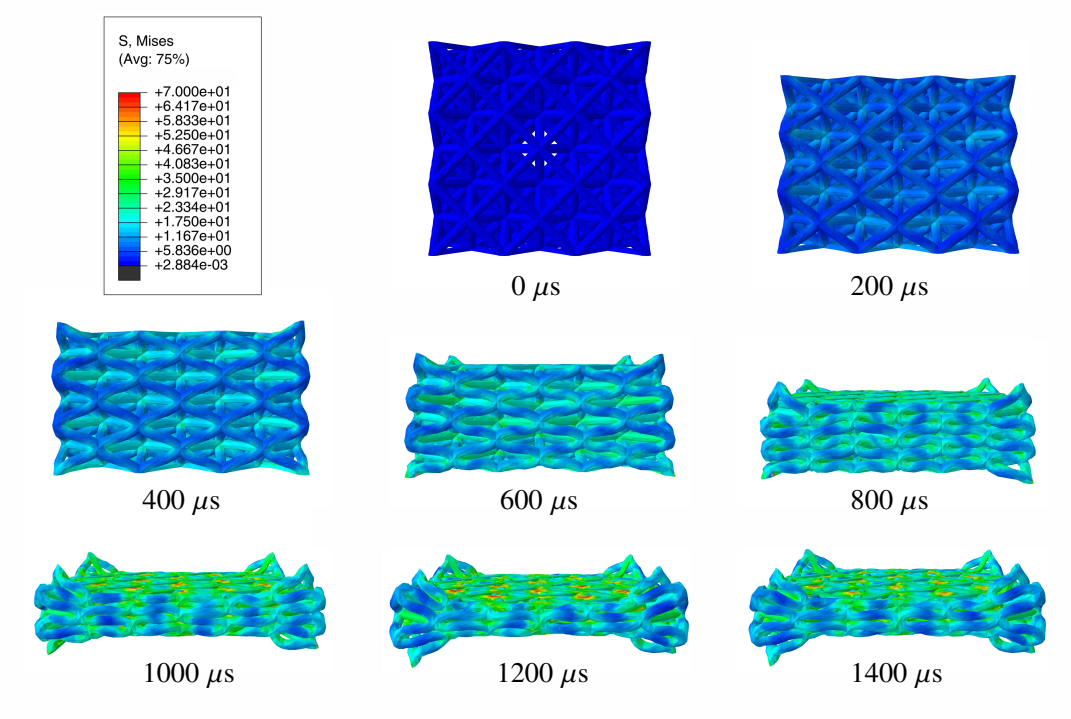

Fig. 7.14 – Stresses during dynamic deforamtion of the Octet structure ($\bar{\rho} = 0.2$) at different time steps.

experiment. Due to the high numerical effort involved, the simulation time was set to 1.5 ms. Because of the short simulation time, not the entire pulse was simulated. The last part of the falling pulse no longer fell within the specified simulation time. The high simulation effort is the reason why only a simulation of the Octet structure at a relative density of $\bar{\rho} = 0.2$ was performed in this case. The slope of the simulated pulse initially forms a longer plateau than in the experimental pulse. This longer plateau indicates a faster buckling of the structures upon the initial contact between the striker and the structure. However, the gradient during the rise of the measured and simulated pulse shows a very similar pattern. In Fig. 7.15, the pulses from the simulation and experiment were shifted in time in such a way that the peaks of the signals are plotted at the same time, thus allowing for better comparability.

The simulations help to understand the deformation process in detail. However, the simulation costs for those processes of lattices highly deformed under impact are correspondingly high. In future, simulations could be carried out with other structures types and/or relative densities.

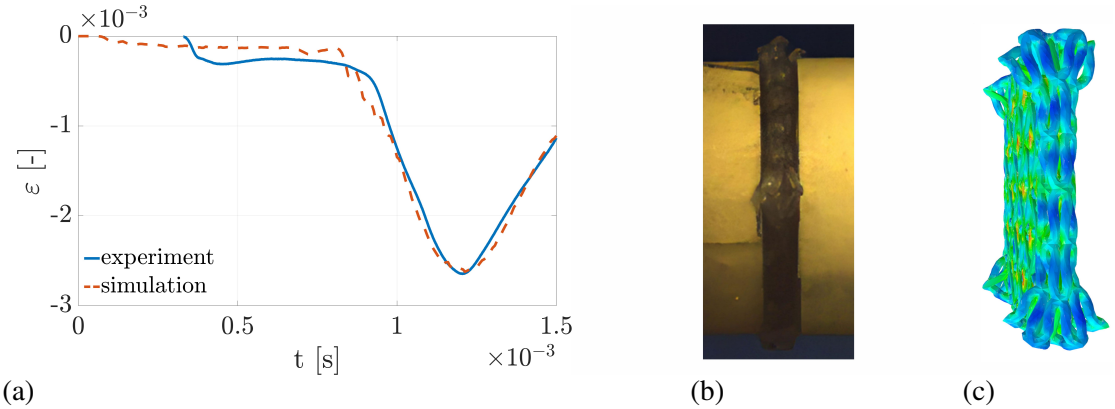

Fig. 7.15 – a) Comparison of pulse signals in the experiment and in the simulation for Octet $\bar{\rho} = 0.2$ and compressed specimen during the experiment b) and c) in the simulation.

Chapter 8

Summary of Achievements

The aim of this work was to investigate the properties of additively manufactured materials under static and dynamic loads. In particular, materials in different structural configurations were examined for their energy-absorption capabilities, as these properties are essestial for various applications, such as protective helmets for head safety.

Additive manufacturing offers numerous advantages over conventional production techniques or processes. With 3D printing, complex geometries can be realized with almost no design restrictions. Consequently, this technology is gaining increasing popularity in industry. It is not only used for the fabrication of prototypes, but is already being applied in series production components.

Materials properties under static and dynamic loading

In Chapter 3, the orientation dependence inherent to additive manufacturing was investigated. For this purpose, dog bone specimens were prepared in accordance with DIN ISO 527. Due to the high resolution of the SLA printer used (35 μm), all specimen geometries, particularly the tested structures, could be manufactured with high precision. The dog bone specimens were oriented at different angles for the printing process in order to assess the material for possible directional dependence.

The question of whether SLA-printed materials exhibit a dependence of their mechanical properties of printing direction, an issue widely discussed in the literature, was systematically analyzed. To this end, two materials were investigated using seven different printing orientations. The results indicate that any observed directional dependence is not inherent to the additive manufacturing process itself, but depends on the material system employed.

For the acrylic-like material Anycubic Tough 2.0, a strong dependence was observed in the overall stress-strain response. Tensile testing revealed a pronounced variation of the modulus

of elasticity with printing orientation. Across the seven examined printing orientations, the modulus of elasticity ranged from approximately 390 MPa to 1020 MPa, corresponding to an increase for about 160% between minimum and maximum.

The same experimental procedure was applied to the TPU-like material 3D-Materials SuperFlex. In contrast to the stiffer acrylic-like material, only minor variations in the stress-strain response were observed across the seven investigated printing orientations. The elastic modulus ranged from 4 MPa to 6.1 MPa. This corresponds to a relative difference of about 50%. However, due to the low absolute stress and force levels involved, differences between orientations are more difficult to resolve experimentally and are subject to increased measurement uncertainty.

Stress relaxation experiments revealed that, within each material, the relaxation curves obtained for the investigated printing orientations were highly similar. The slight deviations are visible not only in a direct comparison of the relaxation curves, but also in the calculated Prony coefficients. When comparing the two tested materials, distinct viscoelastic responses were observed, as reflected by clearly different Prony coefficients. The choice of material for the SLA printing process at high print resolution is a decisive factor in determining whether or not the material is dependent on its printing orientation.

The dynamic behavior of additively manufactured specimens was investigated using the split Hopkinson pressure bar experiment in Chapter 4. In addition to the 3D-printed specimens, glass fiber-reinforced composite materials were tested under high strain rates, which is discussed in Chapter 5. Due to the different materials, the experimental setup of the SHPB must be adapted to the specific material being tested. For this purpose, a new bearing system was developed for the SHPB to enable quick and sufficient replacement of the required test setup components. Within this work, three different materials were investigated under high-strain-rate loading conditions ranging from 300s^{-1} to 700s^{-1}. The evaluation of the SHPB test is based on the measured strain pulses obtained using strain gauges.

The SHPB experiment requires special modifications depending on the structure and properties of the specimen material. When using metal bars in the SHPB test, strain gauges attached at the center are sufficient to apply the established equations for evaluation, as wave dissipation along the length of the bars is minimal. For testing soft materials, PMMA was chosen as the bar material to reduce the impedance mismatch between the bars and the specimen. However, since wave dissipation in PMMA bars is no longer negligible, a signal correction method based on multiple measurement points along the bars was employed. The recorded time-discrete signals were decomposed into their frequency components using the Fast Fourier Transform (FFT). By comparing the amplitudes and phases of the individual signals with the known distances between measurement points, it was possible to reconstruct the signals at the relevant location for test evaluation. This method was validated by comparing the reconstructed signals with the actual measured signals.

For all materials, the required stress equilibrium was achieved across different strain rates

in the experiments. Stress equilibrium enables the determination of the stress-strain behavior of the tested materials and allows for the calculation of the dynamic modulus of elasticity E_{dyn}. For all materials, E_{dyn} is higher than the corresponding static modulus of elasticity E_{stat}. As the strain rate increases, the initial slope of the stress-strain curve becomes steeper, an effect that is particularly pronounced for soft materials with a low quasi-static modulus of elasticity. At higher strain rates, the viscoelastic component of the material becomes less significant, as strain is applied over a very short time. Consequently, softer materials exhibit a significantly higher effective modulus under high strain rates compared to quasi-static loading.

For the soft TPU-like material 3D-Materials SuperFlex, the effective modulus of elasticity increases by roughly one order of magnitude (factor ≈ 20) relative to the quasi-static tensile modulus. This increase reflects the suppression of viscoelastic relaxation at high strain rates. For the acrylic-like material Anycubic Tough 2.0, which exhibits orientation-dependent behavior under quasi-static loading, the apparent modulus increases by a factor of approximately 2–3 at high strain rates, depending on the print orientation. In both materials, these increases reflect strain-rate sensitivity rather than a fundamental change in the intrinsic elastic properties.

Minor differences between tensile and compressive measurements may occur for orientation-sensitive materials such as Anycubic Tough 2.0, but the overall trend of increasing stiffness with strain rate dominates the mechanical response. The elastic modulus in all tests was consistently determined by linear regression of the stress-strain response over the range $0.025 \leq \varepsilon \leq 0.05$, ensuring comparability across all loading regimes.

Overall, the results demonstrate that the modulus of elasticity increases with rising strain rates, but the extent of this increase is strongly dependent on the intrinsic properties of the base material. In particular, soft, compliant materials exhibit a substantially greater relative increase in elastic modulus under dynamic loading conditions compared to stiffer, harder materials. This behavior can be attributed to the reduced influence of viscoelastic relaxation at high strain rates, which allows the material to respond more elastically within the very short time scales of loading. Consequently, the mechanical response of soft materials becomes significantly stiffer under dynamic conditions, whereas the effect is less pronounced for harder materials that already possess a high quasi-static modulus.

Glass fiber reinforced materials under high strain rates

As part of this work, dynamic compression tests were carried out on glass fiber-reinforced plastic (GFRP) using the split Hopkinson pressure Bar (SHPB) technique. GFRP specimens with different fiber orientations (parallel and orthogonal to the direction of loading) were examined. The results showed a significant increase in the modulus of elasticity with increasing strain rate. At a strain rate of approximately 700 s^{-1}, an increase of up to 19% was observed for GFRP with parallel fiber orientation ($\parallel$) and up to 58% for GFRP with orthogonal orientation ($\perp$) compared to the static modulus.

The results were evaluated in the context of existing scientific work. Although a direct comparison is only possible to a limited extent due to differences in test methods and varying material compositions and properties of the GFRP materials examined, there are nevertheless plausible similarities with the trends reported in the literature.

Energy absorption of additiv manufactured structures

Various lattice structures were examined in terms of their energy absorption properties under both static and impact loading conditions. Four beam-based lattice structures (Octet, BFCC, Rhombicuboctahedron, Truncated Octahedron) and four shell-based structures (Schwarz P, Gyroid, Schwarz D, Split P) were investigated for their energy absorption properties. The CAD models were designed to enable the adjustment of relative densities for each structure type by varying the beam radius in beam-based structures or the wall thickness in shell-based structures. Comparisons between individual structures are meaningful only if they have the same relative density. Within this work, we focus on three different relative densities: $\bar{\rho} = 0.2, 0.3, 0.4$.

The static tests were conducted using the rigid 3D printing material Anycubic Tough 2.0. Due to the material's inherent viscosity, the structures could be compressed by up to 50% in the static tests without causing permanent damage. The absorbed energy was determined from the recorded force-displacement curves. Among the investigated structures, the TPMS structure Schwarz D achieved the highest specific energy absorption. After unloading, all tested structures returned approximately to their original shape, and no fractures were observed. In addition to the experimental investigations, finite element (FE) simulations were performed to gain a deeper understanding of the underlying deformation mechanisms. At this stage, however, the FE simulations cannot yet fully replace experimental evaluation.

A modified SHPB system was employed to investigate dynamic impact loading. The specimens were subjected to the direct impact of the striker. Stress equilibrium is not required in this setup, as the impulses recorded on the incident bar are compared with a reference measurement obtained without a specimen to determine the proportion of absorbed energy. Due to the high compressions of up to 80% occurring within a very short time window, the tests were conducted using the soft 3D printing material 3D-Materials SuperFlex, since harder materials with lower viscosity would fail under such impact conditions. Tests with 3D-Materials SuperFlex showed significant amplitude damping and a temporal elongation of the measured impulse. Even after multiple loadings, the structures exhibited no damage in the form of cracks or other external defects. The specimens returned to their initial shape within a few seconds after loading, demonstrating their suitability as damping materials for various applications. FE simulations of the high-strain-rate tests required substantially more computational effort than the quasi-static loading simulations. Consequently, only a single structure type was simulated as a representative example. Additional simulations of the remaining investigated structures

would further improve the understanding of the deformation mechanisms of lattice and TPMS structures under impact loading.

Due to the high mesh density and the complexity of the structures, the simulations performed for the static and dynamic investigations were computationally demanding and were therefore limited to beam-based structures. Despite the good agreement between experimental results and simulations, the simulations cannot fully replace experiments for these complex configurations. Nevertheless, they provide valuable insights into the underlying deformation mechanisms. Deviations between experimental and simulated results can be attributed to the simplified material model used in ABAQUS and to imperfections inherent to the additive manufacturing process. Errors occurring during printing may influence the resulting material behavior. While statistical evaluation of the experimental data helps to reduce this source of error, the presence of occasional defective prints cannot be entirely excluded.

8.1 Outlook

The classic SHPB experiments showed reasonable results for the determined strain rates. Extending the tests to higher strain rates would provide a solid ground for more accurately estimating the modulus of elasticity for various damage scenarios. Whether a sufficient number of measurements would allow for extrapolation remains questionable, as the material fails at very high strain rates and/or achieving stress equilibrium is difficult or impossible.

Investigations into energy absorption by lattice structures have shown optimistic results and should be expanded to include additional loads in the future. Furthermore, the results of this work could be expanded by additional relative densities of the investigated structures. Due to the variable design of the CAD files and the MATLAB script developed, the required radii of the beam-based structures and the wall thicknesses of the shell-based structures can be determined for any relative density. Therefore, further simulations are recommended. Extending the FE simulations for shell-based structures would also contribute to understanding the deformation mechanisms, as neither static nor dynamic simulations of TPMS structures were performed within this work.

References

3D-Materials (2025). Data sheet: Superflex. https://www.3dmaterials.com/sub/resins.php?ptype=view&page=1&&prdcode=2109150009. [Online; accessed 20-August-2025].

Aghayan, S., Bieler, S., Reppel, T., and Weinberg, K. (2019). Experiment on wave propagation in soft resins. *PAMM*, 19(1):e201900187.

Aghayan, S., Bieler, S., and Weinberg, K. (2022). Determination of the high-strain rate elastic modulus of printing resins using two different split hopkinson pressure bars. *Mechanics of Time-Dependent Materials*, 26(4):761–773.

Aghayan, S., Reppel, T., Bieler, S., and Weinberg, K. (2018). Experiments on wave propagation in soft materials. *PAMM*, 18(1):e201800346.

Ahmadi, S. M., Amin Yavari, S., Wauthle, R., Pouran, B., Schrooten, J., Weinans, H., and Zadpoor, A. A. (2015). Additively manufactured open-cell porous biomaterials made from six different space-filling unit cells: The mechanical and morphological properties. *Materials*, 8(4):1871–1896.

Aktaş, C., Acar, E., Güler, M. A., and Altın, M. (2023). An investigation of the crashworthiness performance and optimization of tetra-chiral and reentrant crash boxes. *Mechanics Based Design of Structures and Machines*, 51(12):6881–6904.

Al-Jassir, F. F., Fouad, H., and Alothman, O. Y. (2013). In vitro assessment of function graded (fg) artificial hip joint stem in terms of bone/cement stresses: 3d finite element (fe) study. *Biomedical engineering online*, 12:1–17.

Al-Ketan, O., Rowshan, R., and Al-Rub, R. K. A. (2018). Topology-mechanical property relationship of 3d printed strut, skeletal, and sheet based periodic metallic cellular materials. *Additive Manufacturing*, 19:167–183.

Al-Mousawi, M., Reid, S., and Deans, W. (1997). The use of the split hopkinson pressure bar techniques in high strain rate materials testing. *Proceedings of the Institution of Mechanical Engineers, Part C: Journal of Mechanical Engineering Science*, 211(4):273–292.

Al-Tamimi, A. A., Almeida, H., and Bartolo, P. (2020). Structural optimisation for medical implants through additive manufacturing. *Progress in Additive Manufacturing*, 5:95–110.

Alqahtani, S., Ali, H. M., Farukh, F., and Kandan, K. (2023). Experimental and computational analysis of polymeric lattice structure for efficient building materials. *Applied Thermal Engineering*, 218:119366.

Ambur, D. and Cruz, J. (1995). Low-speed impact response characteristics of composite

sandwich panels. In *36th Structures, Structural Dynamics and Materials Conference*, page 1460.

Amijima, S. and Fujil, T. (1980). Compressive strength and fracture characteristics of fiber composites under impact loading.

Andrew, J. J., Schneider, J., Ubaid, J., Velmurugan, R., Gupta, N., and Kumar, S. (2021). Energy absorption characteristics of additively manufactured plate-lattices under low-velocity impact loading. *International Journal of Impact Engineering*, 149:103768.

Anycubic (2025). Data sheet: Tough 2.0. https://de.anycubic.com/products/tough-resin-2. [Online; accessed 20-August-2025].

Arabnejad, S., Johnston, R. B., Pura, J. A., Singh, B., Tanzer, M., and Pasini, D. (2016). High-strength porous biomaterials for bone replacement: A strategy to assess the interplay between cell morphology, mechanical properties, bone ingrowth and manufacturing constraints. *Acta biomaterialia*, 30:345–356.

Ashby, M. F. (2006). The properties of foams and lattices. *Philosophical Transactions of the Royal Society A: Mathematical, Physical and Engineering Sciences*, 364(1838):15–30.

Bacon, C. (1998). An experimental method for considering dispersion and attenuation in a viscoelastic hopkinson bar. *Experimental mechanics*, 38(4):242–249.

Balaji, G. and Annamalai, K. (2019). Numerical investigation of honeycomb filled crash box for the effect of honeycomb's physical parameters on crashworthiness constants. *International Journal of Crashworthiness*, 24(2):184–198.

Bandyopadhyay, A. and Bose, S. (2019). *Additive manufacturing*. CRC press.

Beccu, R. and Lundberg, B. (1987). Transmission and dissipation of stress wave energy at a percussive drill rod joint. *International journal of impact engineering*, 6(3):157–173.

Bieler, S., Haller, S., Brandt, R., and Weinberg, K. (2023). Experimental investigation of unidirectional glass-fiber-reinforced plastics under high strain rates. *Applied Mechanics*, 4(4):1127–1139.

Bieler, S., Kang, S. G., Heußen, D., Ramachandramoorthy, R., Dehm, G., and Weinberg, K. (2021). Investigation of copper lattice structures using a split hopkinson pressure bar. *PAMM*, 21(1):e202100155.

Bieler, S. and Weinberg, K. (2021). Correction of wave signals for pmma split hopkinson pressure bar setups. *PAMM*, 20(1):e202000143.

Bieler, S. and Weinberg, K. (2023). Behavior of additively manufactured lattice structures unter compressive loading. *PAMM*, 22(1):e202200305.

Bieler, S. and Weinberg, K. (2025a). Energy absorption in lattice-structured materials under impact loading. *European Journal of Mechanics-A/Solids*, page 105734.

Bieler, S. and Weinberg, K. (2025b). Energy absorption of sustainable lattice structures under static compression. *Meccanica*, pages 1–15.

Bieler, S. and Weinberg, K. (2025c). Lattice structures as an energy-absorbing component

for impact loads. *PAMM*, 25(1):e202400071.

Bieler, S. and Weinberg, K. (2025d). Signal correction for the split-hopkinson bar testing of soft materials. *Dynamics (2673-8716)*, 5(1).

Bieler, S., Anders, D., Walkowiak, M., and Weinberg, K. (2025e). Experimental investigations on the energy absorption of aluminum TPMS structures under dynamic loading. *PAMM*, 26(2):e70125.

Blumenthal, G., Linke, D., and Vieth, S. (2007). *Chemie: Grundwissen für Ingenieure*. Springer-Verlag.

Bourell, D., Kruth, J. P., Leu, M., Levy, G., Rosen, D., Beese, A. M., and Clare, A. (2017). Materials for additive manufacturing. *CIRP annals*, 66(2):659–681.

Boursier Niutta, C., Ciardiello, R., and Tridello, A. (2022). Experimental and numerical investigation of a lattice structure for energy absorption: application to the design of an automotive crash absorber. *Polymers*, 14(6):1116.

Chen, W., Lu, F., Frew, D., and Forrestal, M. (2002). Dynamic compression testing of soft materials. *J. Appl. Mech.*, 69(3):214–223.

Chen, W., Lu, F., and Zhou, B. (2000). A quartz-crystal-embedded split hopkinson pressure bar for soft materials. *Experimental mechanics*, 40(1):1–6.

Chen, W., Zhang, B., and Forrestal, M. (1999). A split hopkinson bar technique for low-impedance materials. *Experimental mechanics*, 39(2):81–85.

Chen, W. W. and Song, B. (2009). Dynamic failure of materials and structures. *Dynamic Characterization of Soft Materials*.

Chen, W. W. and Song, B. (2010). *Split Hopkinson (Kolsky) bar: design, testing and applications*. Springer Science & Business Media.

Cheng, Z., Crandall, J., and Pilkey, W. (1998). Wave dispersion and attenuation in viscoelastic split hopkinson pressure bar. *Shock and Vibration*, 5(5-6):307–315.

Cournoyer, J., Post, A., Rousseau, P., and Hoshizaki, B. (2016). The ability of american football helmets to manage linear acceleration with repeated high-energy impacts. *Journal of athletic training*, 51(3):258.

Crisco, J. J., Fiore, R., Beckwith, J. G., Chu, J. J., Brolinson, P. G., Duma, S., McAllister, T. W., Duhaime, A.-C., and Greenwald, R. M. (2010). Frequency and location of head impact exposures in individual collegiate football players. *Journal of athletic training*, 45(6):549–559.

Dai, F., Huang, S., Xia, K., and Tan, Z. (2010). Some fundamental issues in dynamic compression and tension tests of rocks using split hopkinson pressure bar. *Rock mechanics and rock engineering*, 43:657–666.

de Mattos Nascimento, D. L., Mury Nepomuceno, R., Caiado, R. G. G., Maqueira, J. M., Moyano-Fuentes, J., and Garza-Reyes, J. A. (2022). A sustainable circular 3d printing model for recycling metal scrap in the automotive industry. *Journal of Manufacturing Technology*

Management, 33(5):876–892.

Deckard, C. R. (1988). *Selective laser sintering*. The University of Texas at Austin.

Deckers, J., Vleugels, J., and Kruth, J.-P. (2014). Additive manufacturing of ceramics: A review. *Journal of Ceramic Science and Technology*, 5(4):245–260.

Deshpande, V. S., Fleck, N. A., and Ashby, M. F. (2001). Effective properties of the octet-truss lattice material. *Journal of the Mechanics and Physics of Solids*, 49(8):1747–1769.

DIN, E. (1996). 527-2 kunststoffe-bestimmung der zugeigenschaften–teil 2: Prüfbedingungen für form-und extrusionsmassen (iso 527-2: 1993 einschließlich cor. 1: 1994). *Deutsche Fassung EN ISO*, pages 527–2.

Doyle, J. F. (2012). *Wave propagation in structures: an FFT-based spectral analysis methodology*. Springer Science & Business Media.

Egan, P., Wang, X., Greutert, H., Shea, K., Wuertz-Kozak, K., and Ferguson, S. (2019). Mechanical and biological characterization of 3d printed lattices. *3D Printing and Additive Manufacturing*, 6(2):73–81.

El-Gizawy, A. S., Ma, X., Arnone, J. C., and Melaibari, A. A. (2024). Customized lattice structures tailored to mimic patients' bone anisotropic properties and microarchitecture for joint reconstruction applications. *BioMed*, 4(2):171–184.

El-Habak, A. (1993). Compressive resistance of unidirectional gfrp under high rate of loading. *Composites Technology and Research*, 15(4):311–317.

Fíla, T., Koudelka, P., Falta, J., Zlámal, P., Rada, V., Adorna, M., Bronder, S., and Jiroušek, O. (2021). Dynamic impact testing of cellular solids and lattice structures: Application of two-sided direct impact hopkinson bar. *International Journal of Impact Engineering*, 148:103767.

Frew, D., Forrestal, M. J., and Chen, W. (2002). Pulse shaping techniques for testing brittle materials with a split hopkinson pressure bar. *Experimental mechanics*, 42(1):93–106.

Frohne, H., Löcherer, K.-H., Müller, H., and Moeller, F. (2011). *Moeller Grundlagen der Elektrotechnik*. Springer-Verlag.

Ganzenmüller, G., Plappert, D., Trippel, A., and Hiermaier, S. (2019). A split-hopkinson tension bar study on the dynamic strength of basalt-fibre composites. *Composites Part B: Engineering*, 171:310–319.

Gardan, J. (2016). Additive manufacturing technologies: state of the art and trends. *International Journal of Production Research*, 54(10):3118–3132.

Gerber, B. (2016). Eliminate Football Concussion with Shocking Simulation. https://www.ansys.com/de-de/blog/reducing-concussions-in-football-with-simulation. [Online; accessed 19-June-2023].

Gibson, I., Rosen, D. W., Stucker, B., Khorasani, M., Rosen, D., Stucker, B., and Khorasani, M. (2021). *Additive manufacturing technologies*, volume 17. Springer.

Gibson, L. J. and Ashby, M. F. (1997). Cellular solids: structure and properties. *Press Syndicate of the University of Cambridge, Cambridge, UK*, pages 175–231.

Giudice, J. S., Caudillo, A., Mukherjee, S., Kong, K., Park, G., Kent, R., and Panzer, M. B. (2020). Finite element model of a deformable american football helmet under impact. *Annals of Biomedical Engineering*, 48(5):1524–1539.

Glaesener, R. N., Kumar, S., Lestringant, C., Butruille, T., Portela, C. M., and Kochmann, D. M. (2023). Predicting the influence of geometric imperfections on the mechanical response of 2d and 3d periodic trusses. *Acta materialia*, 254:118918.

Goldman R. (2005). Curvature formulas for implicit curves and surfaces. *Computer Aided Geometric Design*, 22(7), 632-658.

Golewski, P., Rusinek, A., and Sadowski, T. (2020). Material characterization of pmc/tbc composite under high strain rates and elevated temperatures. *Materials*, 13(1):167.

Gorham, D. (1989). Specimen inertia in high strain-rate compression. *Journal of Physics D: Applied Physics*, 22(12):1888.

Gross, B. C., Erkal, J. L., Lockwood, S. Y., Chen, C., and Spence, D. M. (2014). Evaluation of 3d printing and its potential impact on biotechnology and the chemical sciences.

Gross, D., Hauger, W., Schnell, W., and Wriggers, P. (2013). *Technische Mechanik 2 - Elastostatik*, volume 2. Springer.

Gross, D., Hauger, W., and Wriggers, P. (2002). *Hydromechanik, Elemente der Höheren Mechanik, Numerische Methoden*. Springer.

Guedes, R., Vaz, M., Ferreira, F., and Morais, J. (2005). Response of cfrp laminates under high strain rate compression until failure. *Science and Engineering of Composite Materials*, 12(1-2):145–152.

Gurusideswar, S., Velmurugan, R., and Sarathi, R. (2022). High strain rate studies of polymer and hybrid nanocomposites for aerospace application. pages 55–92.

Habibi, M., Foroughi, S., Karamzadeh, V., and Packirisamy, M. (2022). Direct sound printing. *Nature Communications*, 13(1):1800.

Halliday, D., Resnick, R., Walker, J., and Koch, S. M. (2007). Halliday Physik–Bachelor Edition. Weinheim: Wiley.

Hashemi, S. M. H., Babic, U., Hadikhani, P., and Psaltis, D. (2020). The potentials of additive manufacturing for mass production of electrochemical energy systems. *Current Opinion in Electrochemistry*, 20:54–59.

Hasib, H., Rennie, A., Burns, N., and Geekie, L. (2015). Non-stochastic lattice structures for novel filter applications fabricated via additive manufacturing. *Filtration*, 15(3):174–180.

Hazizan, M. A. and Cantwell, W. (2003). The low velocity impact response of an aluminium honeycomb sandwich structure. *Composites Part B: Engineering*, 34(8):679–687.

Hedayati, R., Sadighi, M., Mohammadi-Aghdam, M., and Zadpoor, A. (2017). Analytical relationships for the mechanical properties of additively manufactured porous biomaterials

based on octahedral unit cells. *Applied Mathematical Modelling*, 46:408–422.

Hoerber, J., Glasschroeder, J., Pfeffer, M., Schilp, J., Zaeh, M., and Franke, J. (2014). Approaches for additive manufacturing of 3d electronic applications. *Procedia CIRP*, 17:806–811.

Hoffmann, K. (1987). *Eine Einführung in die Technik des Messens mit Dehnungsmeßstreifen: mit 20 Tafeln*. na.

Hopkinson, B. (1914). X. a method of measuring the pressure produced in the detonation of high, explosives or by the impact of bullets. *Philosophical Transactions of the Royal Society of London. Series A, Containing Papers of a Mathematical or Physical Character*, 213(497-508):437–456.

Hossain, F., Arifuzzaman, M., Islam, M. S., and Islam, M. M. (2023). Thermo-mechanical behavior of green sandwich structures for building and construction applications. *Processes*, 11(8):2456.

Hou, W., He, P., Yang, Y., and Sang, L. (2023). Crashworthiness optimization of crash box with 3d-printed lattice structures. *International Journal of Mechanical Sciences*, 247:108198.

Huang, Z., Antion, C., and Toussaint, F. (2025). Identification for elastoplastic constitutive parameters of 316l stainless steel lattice structures using finite element model updating and integrated digital image correlation. *Mechanics of Materials*, 202:105232.

Hull, C. W. (1984). Apparatus for production of three-dimensional objects by stereolithography. *United States Patent, Appl., No. 638905, Filed*.

Hüll, M. (2019). Möglicher zusammenhang mit frontalhirnfunktionen. *InFo Neurologie & Psychiatrie*, 21(2):11–11.

Hungerbühler, N. (2011). *Einführung in partielle Differentialgleichungen: für Ingenieure, Chemiker und Naturwissenschaftler*. vdf Hochschulverlag AG.

Jakkula, P., Ganzenmüller, G., Beisel, S., Rüthnick, P., and Hiermaier, S. (2021). The symmpact: A direct-impact hopkinson bar setup suitable for investigating dynamic equilibrium in low-impedance materials. *Experimental Mechanics*, pages 1–10.

Janiszewski, J., Bużantowicz, W., and Baranowski, P. (2016). Correction procedure of wave signals for a viscoelastic split hopkinson pressure bar. *Problems of Mechatronics. Armament, Aviation, Safety Engineering*, 7(1):17–30.

Javaid, M. and Haleem, A. (2018). Additive manufacturing applications in medical cases: A literature based review. *Alexandria Journal of Medicine*, 54(4):411–422.

Jiang, H., Ziegler, H., Zhang, Z., Zhang, H., Le Barbenchon, L., Atre, S., and Chen, Y. (2022). 3d printed tubular lattice metamaterials for mechanically robust stents. *Composites Part B: Engineering*, 236:109809.

Kang, S.-G., Gainov, R., Heußen, D., Bieler, S., Sun, Z., Weinberg, K., Dehm, G., and Ramachandramoorthy, R. (2023). Green laser powder bed fusion based fabrication and rate-dependent mechanical properties of copper lattices. *Materials & Design*,

231:112023.

Keil, S. (2016). *Dehnungsmessstreifen*. Springer.

Kerns, J. (2016). Replacing metal with plastic. *Machine design*, 88(9):34–42.

Keuerleber, M. (2006). *Bestimmung des Elastizitätsmoduls von Kunststoffen bei hohen Dehnraten am Beispiel von PP*. PhD thesis, Universität Stuttgart.

Khosravani, M. R., Bieler, S., Weinberg, K., and Reinicke, T. (2025). Mechanical fracture of lattice structures fabricated by selective laser sintering. *Archives of Civil and Mechanical Engineering*, 25(2):1–12.

Kim, D.-H., Kang, S.-Y., Kim, H.-J., and Kim, H.-S. (2019). Strain rate dependent mechanical behavior of glass fiber reinforced polypropylene composites and its effect on the performance of automotive bumper beam structure. *Composites Part B: Engineering*, 166:483–496.

Kim, Y., Kim, P., Kim, H., and Park, J. (2018). Optimal design of a composite lattice rectangular plate for solar panels of a high-agility satellite. *International Journal of Aeronautical and Space Sciences*, 19:762–775.

Korthäuer, M. and El-Magd, E. A. (2006). *Größeneinflüsse beim mechanischen Verhalten von Wolfram, Kupfer-Teilchenverbundwerkstoffen*. Number RWTH-CONV-123139. Fakultät für Maschinenwesen.

Kruth, J.-P. (1991). Material incress manufacturing by rapid prototyping techniques. *CIRP annals*, 40(2):603–614.

Kucera, K. L., Klossner, D., Colgate, B., and Cantu, R. C. (2014). Annual survey of football injury research. https://nccsir.unc.edu/files/2013/10/Annual-Football-2014-Fatalities-Final.pdf. [Online; accessed 21-June-2023].

Kumar, P., Garg, A., and Agarwal, B. (1986). Dynamic compressive behaviour of unidirectional gfrp for various fibre orientations. *Materials Letters*, 4(2):111–116.

Lachmayer, R. and Lippert, R. B. (2017). *Additive Manufacturing Quantifiziert: Visionäre Anwendungen und Stand der Technik*. Springer.

Lachmayer, R. and Lippert, R. B. (2020). *Entwicklungsmethodik für die additive Fertigung*. Springer.

Lai, M., Kulak, A. N., Law, D., Zhang, Z., Meldrum, F. C., and Riley, D. J. (2007). Profiting from nature: macroporous copper with superior mechanical properties. *Chemical communications*, (34):3547–3549.

Leary, M., Mazur, M., Williams, H., Yang, E., Alghamdi, A., Lozanovski, B., Zhang, X., Shidid, D., Farahbod-Sternahl, L., Witt, G., et al. (2018). Inconel 625 lattice structures manufactured by selective laser melting (slm): Mechanical properties, deformation and failure modes. *Materials & Design*, 157:179–199.

Lehder, E., Ashcroft, I., Wildman, R., Ruiz-Cantu, L., and Maskery, I. (2021). A multiscale optimisation method for bone growth scaffolds based on triply periodic minimal surfaces. *Biomechanics and modeling in mechanobiology*, 20:2085–2096.

Li, D., Yin, J., Dong, L., and Lakes, R. S. (2018). Strong re-entrant cellular structures with negative poisson's ratio. *Journal of materials science*, 53(5):3493–3499.

Lifshitz, J. and Leber, H. (1998). Response of fiber-reinforced polymers to high strain-rate loading in interlaminar tension and combined tension/shear. *Composites science and technology*, 58(6):987–996.

Linse, H. and Fischer, R. (2005). *Elektrotechnik für Maschinenbauer: Grundlagen und Anwendungen*. Springer-Verlag.

Liu, J., Xu, M., Zhang, R., Zhang, X., and Xi, W. (2022). Progress of porous/lattice structures applied in thermal management technology of aerospace applications. *Aerospace*, 9(12):827.

Lozanovski, B., Downing, D., Tino, R., Tran, P., Shidid, D., Emmelmann, C., Qian, M., Choong, P., Brandt, M., and Leary, M. (2021). Image-based geometrical characterization of nodes in additively manufactured lattice structures. *3D Printing and Additive Manufacturing*, 8(1):51–68.

Lu, Y. and Li, Q. (2011). Retracted: Dynamic behavior of polymers at high strain-rates based on split hopkinson pressure bar tests.

Lunawat, P. (2022). How are car crash tests carried out.

Lundberg, B. (1976). A split hopkinson bar study of energy absorption in dynamic rock fragmentation. In *International Journal of Rock Mechanics and Mining Sciences & Geomechanics Abstracts*, volume 13, pages 187–197. Elsevier.

Magerramova, L., Volkov, M., Afonin, A., Svinareva, M., and Kalinin, D. (2018). Application of light lattice structures for gas turbine engine fan blades. In *Proccedings of the 31st Congress of the International Council of the Aeronautical Sciences, ICAS*.

Maxwell, J. C. (1864). L. on the calculation of the equilibrium and stiffness of frames. *The London, Edinburgh, and Dublin Philosophical Magazine and Journal of Science*, 27(182):294–299.

Mckee, A. C., Abdolmohammadi, B., and Stein, T. D. (2018). Chapter 28 - the neuropathology of chronic traumatic encephalopathy. In Hainline, B. and Stern, R. A., editors, *Sports Neurology*, volume 158 of *Handbook of Clinical Neurology*, pages 297–307. Elsevier.

Meza, L. R., Zelhofer, A. J., Clarke, N., Mateos, A. J., Kochmann, D. M., and Greer, J. R. (2015). Resilient 3d hierarchical architected metamaterials. *Proceedings of the National Academy of Sciences*, 112(37):11502–11507.

Miao, Y., Du, B., Ma, C., Hu, H., and Deng, Q. (2019). Some fundamental problems concerning the measurement accuracy of the hopkinson tension bar technique. *Measurement Science and Technology*, 30(5):055009.

Michielsen, K. and Stavenga, D. G. (2008). Gyroid cuticular structures in butterfly wing scales: biological photonic crystals. *Journal of The Royal Society Interface*, 5(18):85–94.

Mihalik, J. P., Bell, D. R., Marshall, S. W., and Guskiewicz, K. M. (2007). Measurement of head impacts in collegiate football players: an investigation of positional and event-type

differences. *Neurosurgery*, 61(6):1229–1235.

Miller, S. A. (2023). The Evolution of the Helmet. https://www.nfl.com/photos/the-evolution-of-the-helmet-0ap1000000094622#b66c9f27-1341-4b48-919c-4d6fee54639f. [Online; accessed 19-June-2023].

Ming, S., Zhou, C., Li, T., Song, Z., and Wang, B. (2019). Energy absorption of thin-walled square tubes designed by kirigami approach. *International Journal of Mechanical Sciences*, 157:150–164.

Moon, S. K., Tan, Y. E., Hwang, J., and Yoon, Y.-J. (2014). Application of 3d printing technology for designing light-weight unmanned aerial vehicle wing structures. *International Journal of Precision Engineering and Manufacturing-Green Technology*, 1:223–228.

Müller, R. K. (2013). *Handbuch der Modellstatik*. Springer-Verlag.

Naik, D. L. and Kiran, R. (2018). On anisotropy, strain rate and size effects in vat photopolymerization based specimens. *Additive Manufacturing*, 23:181–196.

Nemes, J. and Simmonds, K. (1992). Low-velocity impact response of foam-core sandwich composites. *Journal of composite materials*, 26(4):500–519.

Niemann, S., Kolesnikov, B., Lohse-Busch, H., Hühne, C., Querin, O. M., Toropov, V. V., and Liu, D. (2013). The use of topology optimisation in the conceptual design of next generation lattice composite aircraft fuselage structures. *The Aeronautical Journal*, 117(1197):1139–1154.

Ninan, L., Tsai, J., and Sun, C. (2001). Use of split hopkinson pressure bar for testing off-axis composites. *International Journal of Impact Engineering*, 25(3):291–313.

Norm, D. (2022). 8580: 2003-09 din 8580: 2003-09. *Fertigungsverfahren-Begriffe, Einteilung*.

Novak, N., Al-Ketan, O., Krstulović-Opara, L., Rowshan, R., Al-Rub, R. K. A., Vesenjak, M., and Ren, Z. (2021). Quasi-static and dynamic compressive behaviour of sheet tpms cellular structures. *Composite Structures*, 266:113801.

Olszta, M. J., Cheng, X., Jee, S. S., Kumar, R., Kim, Y.-Y., Kaufman, M. J., Douglas, E. P., and Gower, L. B. (2007). Bone structure and formation: A new perspective. *Materials Science and Engineering: R: Reports*, 58(3-5):77–116.

Ortlepp, S. (2006). *Zur Beurteilung der Festigkeitssteigerung von hochfestem Beton unter hohen Dehngeschwindigkeiten*. PhD thesis, Dissertation, Universität Dresden.

Othman, R. (2018). *The Kolsky-Hopkinson bar machine: selected topics*. Springer.

Owens, A. and Tippur, H. (2009). A tensile split hopkinson bar for testing particulate polymer composites under elevated rates of loading. *Experimental mechanics*, 49:799–811.

Ozdemir, Z., Hernandez-Nava, E., Tyas, A., Warren, J. A., Fay, S. D., Goodall, R., Todd, I., and Askes, H. (2016). Energy absorption in lattice structures in dynamics: Experiments. *International Journal of Impact Engineering*, 89:49–61.

Palomba, G., Epasto, G., and Crupi, V. (2022). Lightweight sandwich structures for marine applications: a review. *Mechanics of Advanced Materials and Structures*, 29(26):4839–4864.

Pan, C., Han, Y., and Lu, J. (2020). Design and optimization of lattice structures: A review. *Applied Sciences*, 10(18):6374.

Park, K.-M., Min, K.-S., and Roh, Y.-S. (2022). Design optimization of lattice structures under compression: study of unit cell types and cell arrangements. *Materials*, 15(1):97.

Raj, A., Nagarajan, P., and Aikot Pallikkara, S. (2020). Application of fiber-reinforced rubcrete for crash barriers. *Journal of Materials in Civil Engineering*, 32(12):04020358.

Ravichandran, G. and Subhash, G. (1994). Critical appraisal of limiting strain rates for compression testing of ceramics in a split hopkinson pressure bar. *Journal of the American Ceramic Society*.

Reddy, B. V. S., Shaik, A. M., Sundeep, D., Chebiyyam, C. S., Krishnaiah, J., and Chandrasekhar, U. (2024). Performance evaluation of metallic honeycomb and gyroid microlattice structures for armoured fighting vehicles. *Transactions of the Indian Institute of Metals*, 77(3):615–626.

Richard, H. A., Schramm, B., and Zipsner, T. (2017). *Additive Fertigung von Bauteilen und Strukturen*. Springer-Verlag.

Roylance, D. (2001). Engineering viscoelasticity. *Department of Materials Science and Engineering–Massachusetts Institute of Technology, Cambridge MA*, 2139:1–37.

Saini, J., Dowling, L., Kennedy, J., and Trimble, D. (2020). Investigations of the mechanical properties on different print orientations in sla 3d printed resin. *Proceedings of the Institution of Mechanical Engineers, Part C: Journal of Mechanical Engineering Science*, 234(11):2279–2293.

Sasso, M., Newaz, G., and Amodio, D. (2008). Material characterization at high strain rate by hopkinson bar tests and finite element optimization. *Materials Science and Engineering: A*, 487(1-2):289–300.

Schnebel, B., Gwin, J. T., Anderson, S., and Gatlin, R. (2007). In vivo study of head impacts in football: a comparison of national collegiate athletic association division i versus high school impacts. *Neurosurgery*, 60(3):490–496.

Schoen, A. H. (1970). *Infinite periodic minimal surfaces without self-intersections*, volume 5541. National Aeronautics and Space Administration.

Schwarz, H. A. and Schwarz, H. (1890). *Ueber ein die Flächen kleinsten Flächeninhalts betreffendes Problem der Variationsrechnung: Festschrift zum siebzigsten Geburtstage des Herrn Karl Weierstrass*. Springer.

Shokrieh, M. M. and Omidi, M. J. (2009). Compressive response of glass–fiber reinforced polymeric composites to increasing compressive strain rates. *Composite structures*, 89(4):517–523.

Siviour, C. R. and Jordan, J. L. (2016). High strain rate mechanics of polymers: a review. *Journal of Dynamic Behavior of Materials*, 2:15–32.

Song, A. W. and Bruce, I. (2019). Human Structure & Function 2019-2020 | Labo-

ratory Guide. https://anatomy.oit.duke.edu/Lab28_2019/2020_Lab_Internal_Anatomy_of_the_Forebrain.pdf. [Online; accessed 21-June-2023].

Song, B., Connelly, K., Korellis, J., Lu, W.-Y., and Antoun, B. R. (2009). Improved kolsky-bar design for mechanical characterization of materials at high strain rates. *Measurement Science and Technology*, 20(11):115701.

Song, B., Syn, C., Grupido, C. L., Chen, W., and Lu, W.-Y. (2008). A long split hopkinson pressure bar (lshpb) for intermediate-rate characterization of soft materials. *Experimental mechanics*, 48:809–815.

Song, Z., Wang, Z., Kim, H., and Ma, H. (2016). Pulse shaper and dynamic compressive property investigation on ice using a large-sized modified split hopkinson pressure bar. *Latin American Journal of Solids and Structures*, 13(3):391–406.

Strain, J., Didehbani, N., Cullum, C. M., Mansinghani, S., Conover, H., Kraut, M. A., John Hart, J., and Womack, K. B. (2013). Depressive symptoms and white matter dysfunction in retired nfl players with concussion history. *Neurology*, 81(1):25–32.

Sun, L., Zhao, Z., Sun, Y., Wang, X., Liu, X., Yang, Y., and Qiu, J. (2020). Activated coal-based graphene with hierarchical porous structures for ultra-high energy density supercapacitors. *Diamond and Related Materials*, 106:107827.

Suva, A. I. and Rahman, K. A. (2025). Additive manufacturing and industry 4.0 integration: An approach for bangladesh's industrial advancement. In *AIP Conference Proceedings*, volume 3307, page 020021. AIP Publishing LLC.

Szabo, T. L. and Wu, J. (2000). A model for longitudinal and shear wave propagation in viscoelastic media. *The Journal of the Acoustical Society of America*, 107(5):2437–2446.

Takeda, N. and Wan, L. (1995). Impact compression damage evolution in unidirectional glass fiber reinforced polymer composites. *High strain rate effects on polymer, metal and ceramic matrix composites and other advanced materials*, pages 109–113.

Tancogne-Dejean, T., Diamantopoulou, M., Gorji, M. B., Bonatti, C., and Mohr, D. (2018). 3d plate-lattices: an emerging class of low-density metamaterial exhibiting optimal isotropic stiffness. *Advanced Materials*, 30(45):1803334.

Tancogne-Dejean, T. and Mohr, D. (2018). Stiffness and specific energy absorption of additively-manufactured metallic bcc metamaterials composed of tapered beams. *International Journal of Mechanical Sciences*, 141:101–116.

Tancogne-Dejean, T., Spierings, A. B., and Mohr, D. (2016). Additively-manufactured metallic micro-lattice materials for high specific energy absorption under static and dynamic loading. *Acta Materialia*, 116:14–28.

Tanner, R. I. and Walters, K. (1998). *Rheology: an historical perspective*, volume 7. Elsevier.

Tao, W. and Leu, M. C. (2016). Design of lattice structure for additive manufacturing. In *2016 International Symposium on Flexible Automation (ISFA)*, pages 325–332. IEEE.

Tarfaoui, M., Nême, A., and Choukri, S. (2009). Damage kinetics of glass/epoxy composite

materials under dynamic compression. *Journal of Composite Materials*, 43(10):1137–1154.

Thomas, T. and Tiwari, G. (2019). Crushing behavior of honeycomb structure: a review. *International journal of crashworthiness*.

Totaro, G. and Gürdal, Z. (2009). Optimal design of composite lattice shell structures for aerospace applications. *Aerospace Science and Technology*, 13(4-5):157–164.

Uenishi, A., Yoshida, H., Kuriyama, Y., and Takahashi, M. (2003). Material characterization at high strain rates for optimizing car body structures for crash events. *Nippon Steel Technical Report*, 88(7):22–26.

Van Sligtenhorst, C., Cronin, D. S., and Brodland, G. W. (2006). High strain rate compressive properties of bovine muscle tissue determined using a split hopkinson bar apparatus. *Journal of biomechanics*, 39(10):1852–1858.

Vasiliev, V. V., Barynin, V. A., and Razin, A. F. (2012). Anisogrid composite lattice structures–development and aerospace applications. *Composite structures*, 94(3):1117–1127.

VDI-3405 (2007). Vdi 3405 - additive fertigungsverfahren-grundlagen, begriffe, verfahrensbeschreibungen.

Velu, R., Calais, T., Jayakumar, A., and Raspall, F. (2019). A comprehensive review on bio-nanomaterials for medical implants and feasibility studies on fabrication of such implants by additive manufacturing technique. *Materials*, 13(1):92.

Wang, J., Wu, B., Liu, G., Bu, T., Guo, T., Pang, Y., Fu, X., Zhao, J., Xi, F., and Zhang, C. (2018). Flexure hinges based triboelectric nanogenerator by 3d printing. *Extreme Mechanics Letters*, 20:38–45.

Ward, J., Williams, J., and Manchester, S. (2017). 110 N.F.L. Brains. https://www.nytimes.com/interactive/2017/07/25/sports/football/nfl-cte.html. [Online; accessed 21-June-2023].

Weinberg, K., Khosravani, M. R., Thimm, B., Reppel, T., Bogunia, L., Aghayan, S., and Nötzel, R. (2018). Hopkinson bar experiments as a method to determine impact properties of brittle and ductile materials. *GAMM-Mitteilungen*, 41(2):e201800008.

West, J. (2018). The NFL's New Helmet-Lowering Rule, Explained. https://www.si.com/.image/t_share/MTY4MDI4Njc2OTI4NjQ0NDgw/new-nfl-helmet-lowering-rule-explainerjpg.jpg. [Online; accessed 19-June-2023].

Winkelmann, A., Flath, C. M., and Thiesse, F. (2021). *Sharing Economy in der Industrie*. Springer.

Winkler, D., Evans, L., et al. (2014). A field guide to tropical amazon mushrooms. *A Field Guide to Tropical Amazon Mushrooms*.

Wong, E., Selvanayagam, C., Seah, S., Van Driel, W., Caers, J., Zhao, X., Owens, N., Tan, L., Frear, D., Leoni, M., et al. (2008). Stress–strain characteristics of tin-based solder alloys for drop-impact modeling. *Journal of Electronic Materials*, 37:829–836.

Wong, K. V. and Hernandez, A. (2012). A review of additive manufacturing. *International scholarly research notices*, 2012.

Wrana, C. (2014). *Polymerphysik: Eine physikalische Beschreibung von Elastomeren und ihren anwendungsrelevanten Eigenschaften*. Springer-Verlag.

Xia, K. and Yao, W. (2015). Dynamic rock tests using split hopkinson (kolsky) bar system–a review. *Journal of Rock Mechanics and Geotechnical Engineering*.

Xue, Q., Shen, L., and Bai, Y. (1995). A modified split hopkinson torsional bar in studying shear localization. *Measurement Science and Technology*, 6(11):1557.

Yan, C., Hao, L., Hussein, A., Young, P., and Raymont, D. (2014). Advanced lightweight 316L stainless steel cellular lattice structures fabricated via selective laser melting. *Materials & Design*, 55:533-541.

Yan, C., Hao, L., Yang, L., Hussein, A. Y., Young, P. G., Li, Z., and Li, Y. (2021). *Triply periodic minimal surface lattices additively manufactured by selective laser melting*. Academic Press.

Yang, F., Ma, H., Jing, L., Zhao, L., and Wang, Z. (2015). Dynamic compressive and splitting tensile tests on mortar using split hopkinson pressure bar technique. *Latin American Journal of Solids and Structures*, 12(4):730–746.

Yin, H., Zhang, W., Zhu, L., Meng, F., Liu, J., and Wen, G. (2023). Review on lattice structures for energy absorption properties. *Composite Structures*, 304:116397.

Yin, S., Chen, H., Wu, Y., Li, Y., and Xu, J. (2018). Introducing composite lattice core sandwich structure as an alternative proposal for engine hood. *Composite Structures*, 201:131–140.

Yu, X., Chen, L., Fang, Q., Jiang, X., and Zhou, Y. (2018). A review of the torsional split hopkinson bar. *Advances in Civil Engineering*, 2018.

Yuan, J. and Takeda, N. (2000). Impact compressive failure of gfrp unidirectional composites. *Science and Engineering of Composite Materials*, 9(1):1–10.

Zhao, C., Zhong, J., Goh, K. L., and Liu, X. (2023). Mechanics of carbon fiber reinforced plastics negative poisson's ratio structures. *Materials Today: Proceedings*.

Zhao, C., Zhou, Z., Zhang, K., Zhu, H., Zhong, J., Sun, C., Ren, J., and Le, G. (2021). Experimental study on tensile mechanics of arrow combination structure with carbon fiber–epoxy resin composite. *Arabian Journal for Science and Engineering*, 46:2891–2900.

Zhao, H. and Gary, G. (1995). A three dimensional analytical solution of the longitudinal wave propagation in an infinite linear viscoelastic cylindrical bar. application to experimental techniques. *Journal of the Mechanics and Physics of Solids*, 43(8):1335–1348.

Zhao, H., Gary, G., and Klepaczko, J. R. (1997). On the use of a viscoelastic split hopkinson pressure bar. *International Journal of Impact Engineering*, 19(4):319–330.

Zhao, J., Knauss, W., and Ravichandran, G. (2007). Applicability of the time–temperature superposition principle in modeling dynamic response of a polyurea. *Mechanics of Time-Dependent Materials*, 11:289–308.

Zhao, S., Zong, X., and Wu, N. (2022). Design of load path-oriented bccz lattice sandwich

structures. In *Journal of Physics: Conference Series*, volume 2239, page 012014. IOP Publishing.

Zhong, J., Zhao, C., Ren, J., Liu, X., and Zhang, Z. (2021). A constitutive model for carbon fiber reinforced epoxy resin laminate under compression load: considering the initial non-linearity. *Applied Composite Materials*, pages 1–21.

Zhu, J.-H., Zhang, W.-H., and Xia, L. (2016). Topology optimization in aircraft and aerospace structures design. *Archives of Computational Methods in Engineering*, 23:595–622.

Appendices

In this Appendix, the remaining information is stored.

A.1 Technical drawings of the newly developed bearing system and acceleration tube of the Split-Hopkinson pressure bar

Below is the technical drawing for the newly designed split Hopkinson pressure bar. The bearing systems of the bars were completely redesigned, and the acceleration tube was modified to improve the handling of the striker and to enable faster and more efficient striker exchange.

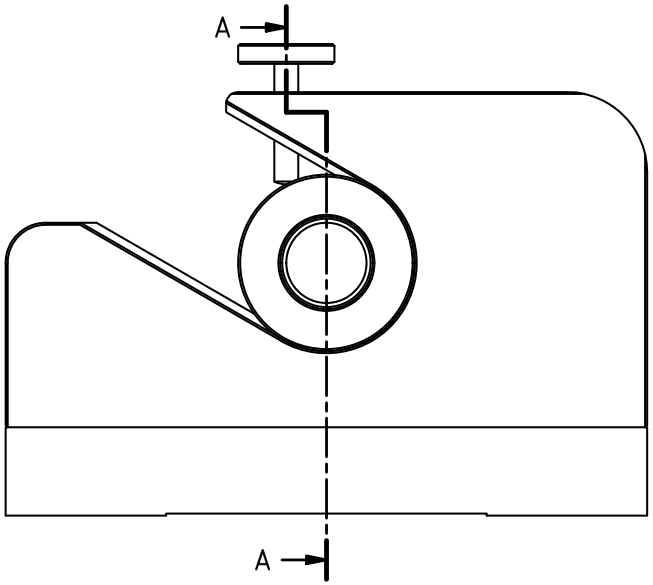

A-A (1 : 1)

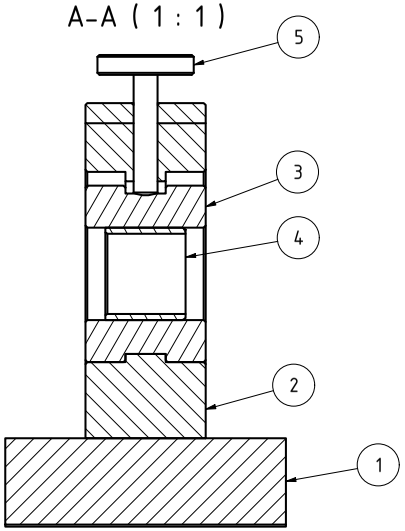

BAUTEILLISTE			
OBJEKT	ANZAHL	BAUTEILNUMMER	BESCHREIBUNG
1	1	Grundplatte Wechsellager	
2	1	SHPB_Wechsellager	
3	1	SHPB_Wechsellager_Aufnahme	
4	1	J260SM_2023_20_1	STEP AP214
5	1	DIN 653 - M6 x 30	Rändelschraube

	Datum	Name
Gezeichnet	01.10.2020	
Kontrolliert		
Norm		

Baugruppe Wechsellager

1

A3

Status	Änderungen	Datum	Name

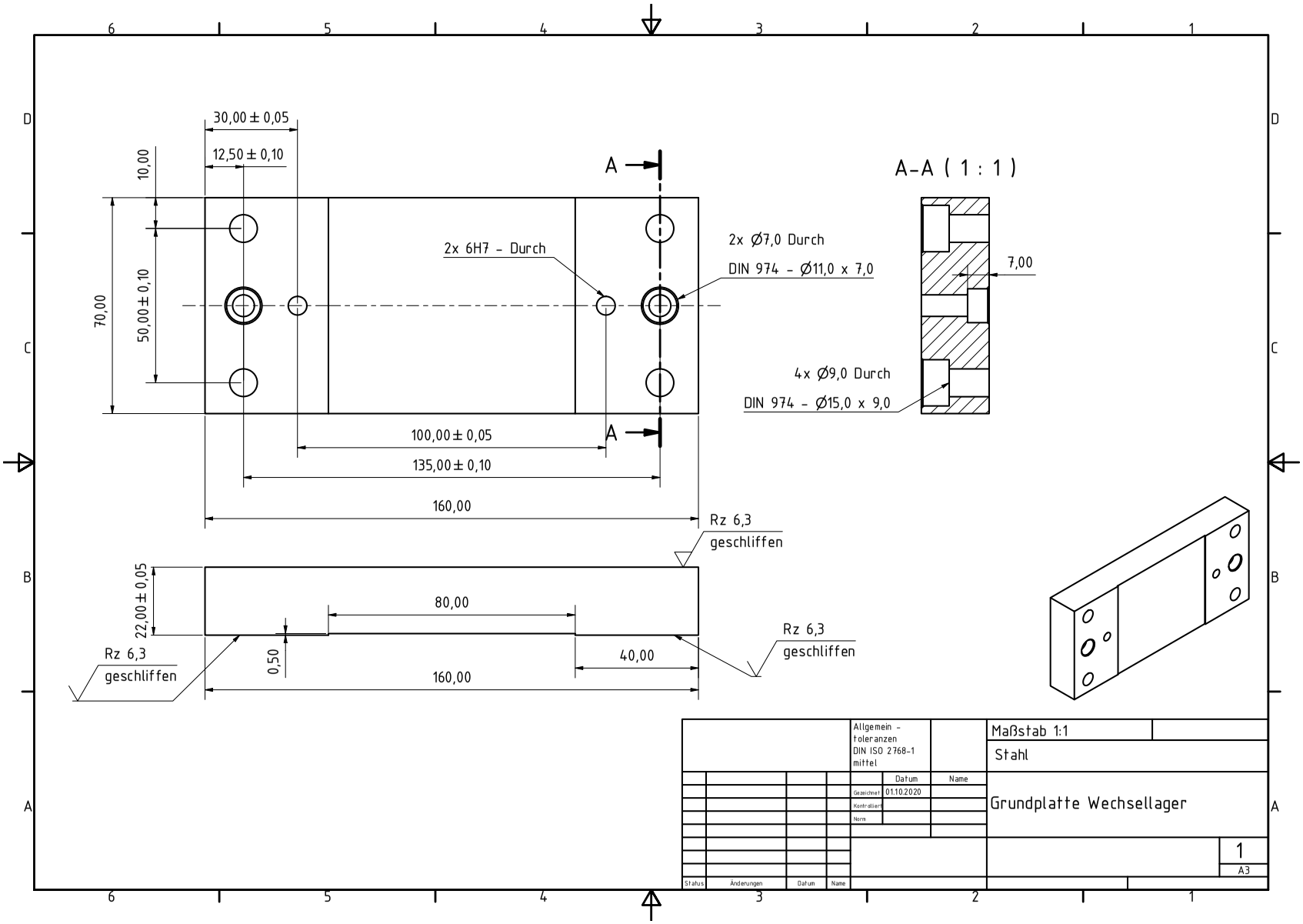
30,00 ± 0,05
12,50 ± 0,10
10,00
70,00
50,00 ± 0,10
A
2x 6H7 – Durch
2x Ø7,0 Durch
DIN 974 – Ø11,0 x 7,0
A-A (1 : 1)
7,00
4x Ø9,0 Durch
DIN 974 – Ø15,0 x 9,0
100,00 ± 0,05
135,00 ± 0,10
160,00
Rz 6,3
geschliffen
22,00 ± 0,05
80,00
Rz 6,3
geschliffen
0,50
40,00
160,00
Rz 6,3
geschliffen
Allgemein – toleranzen DIN ISO 2768-1 mittel
Datum
Name
Gezeichnet 01.10.2020
Kontrolliert
Norm
Maßstab 1:1
Stahl
Grundplatte Wechsellager
1
A3
Status
Änderungen
Datum
Name

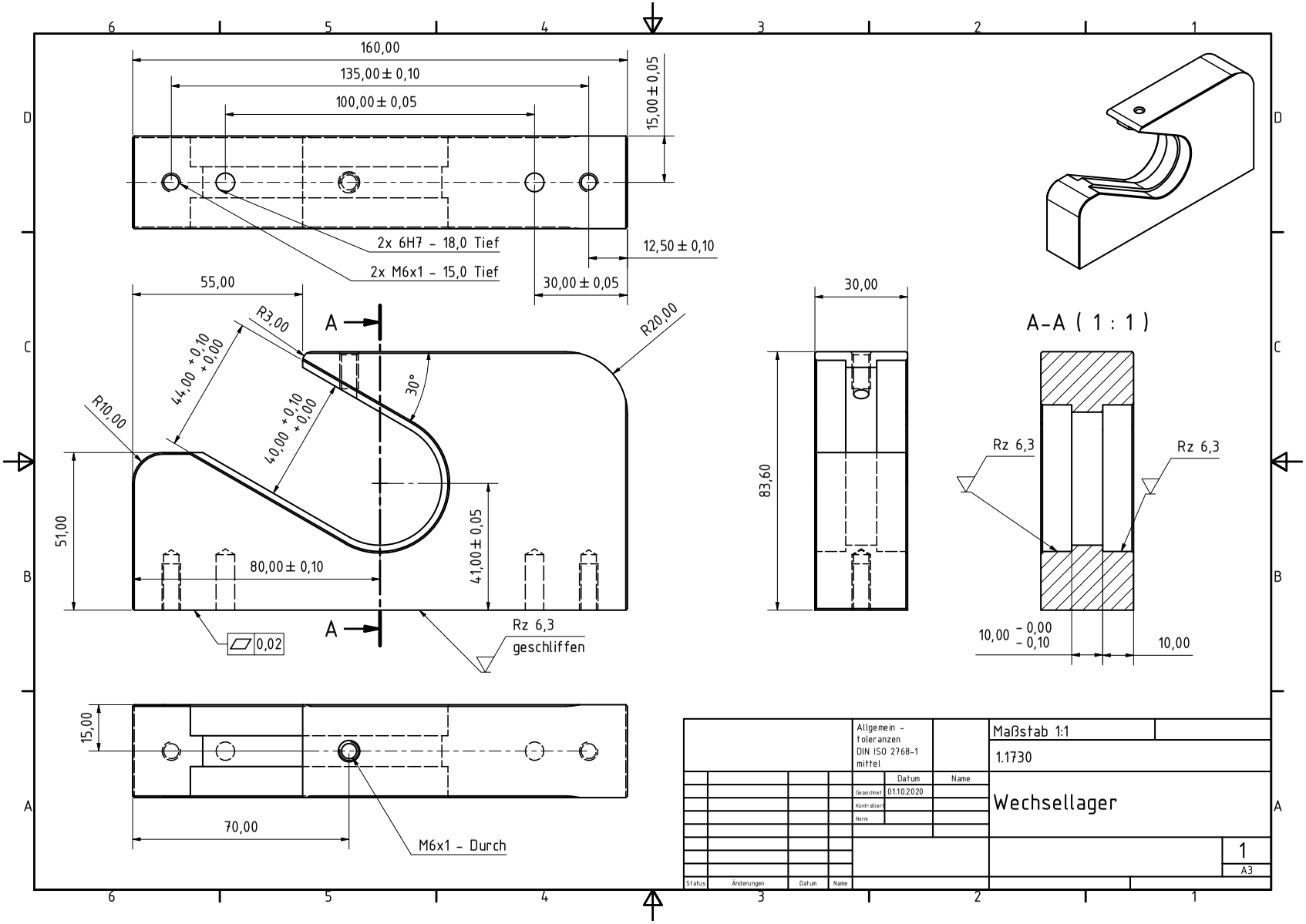
160,00
135,00 ± 0,10
100,00 ± 0,05
15,00 ± 0,05
2x 6H7 - 18,0 Tief
2x M6x1 - 15,0 Tief
12,50 ± 0,10
30,00 ± 0,05
55,00
R3,00
R20,00
R10,00
44,00 +0,10 +0,00
40,00 +0,10 +0,00
30°
A
51,00
80,00 ± 0,10
41,00 ± 0,05
0,02
Rz 6,3
geschliffen
30,00
83,60
A-A (1 : 1)
Rz 6,3
Rz 6,3
10,00 -0,00 -0,10
10,00
15,00
70,00
M6x1 - Durch
Allgemein - toleranzen DIN ISO 2768-1 mittel
Datum
Name
Gezeichnet 01.10.2020
Kontrolliert
Norm
Maßstab 1:1
1.1730
Wechsellager
1
A3
Status
Änderungen
Datum
Name

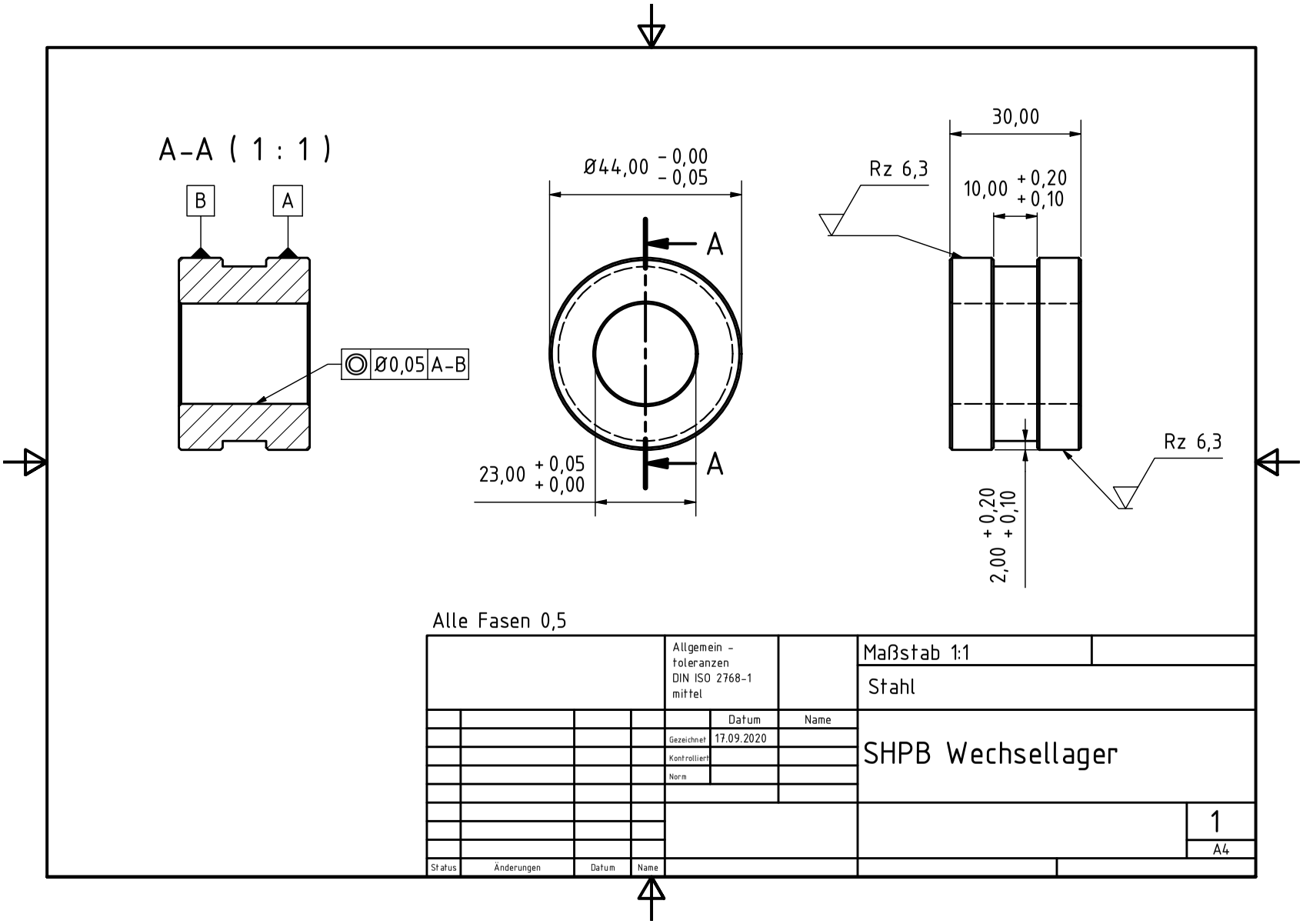
A-A (1 : 1)
B
A
Ø0,05 A-B
Ø44,00 - 0,00 - 0,05
A
A
23,00 + 0,05 + 0,00
30,00
Rz 6,3
10,00 + 0,20 + 0,10
Rz 6,3
2,00 + 0,20 + 0,10
Alle Fasen 0,5
Allgemein - toleranzen DIN ISO 2768-1 mittel
Maßstab 1:1
Stahl
Datum
Name
Gezeichnet
17.09.2020
Kontrolliert
Norm
SHPB Wechsellager
1
A4
Status
Änderungen
Datum
Name

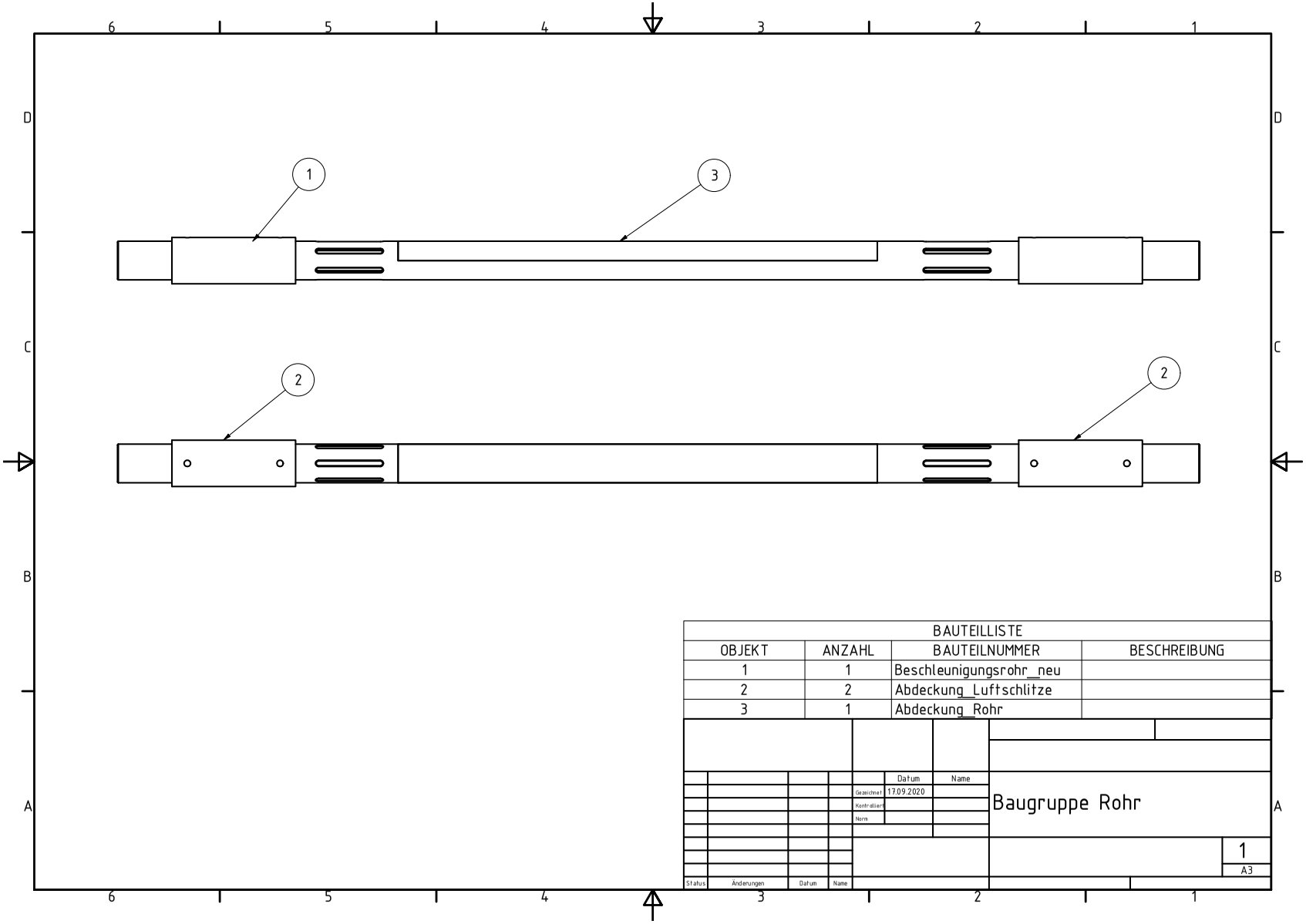

BAUTEILLISTE			
OBJEKT	ANZAHL	BAUTEILNUMMER	BESCHREIBUNG
1	1	Beschleunigungsrohr_neu	
2	2	Abdeckung_Luftschlitze	
3	1	Abdeckung_Rohr	

	Datum	Name
Gezeichnet	17.09.2020	
Kontrolliert		
Norm		

Baugruppe Rohr

1

A3

Status	Änderungen	Datum	Name

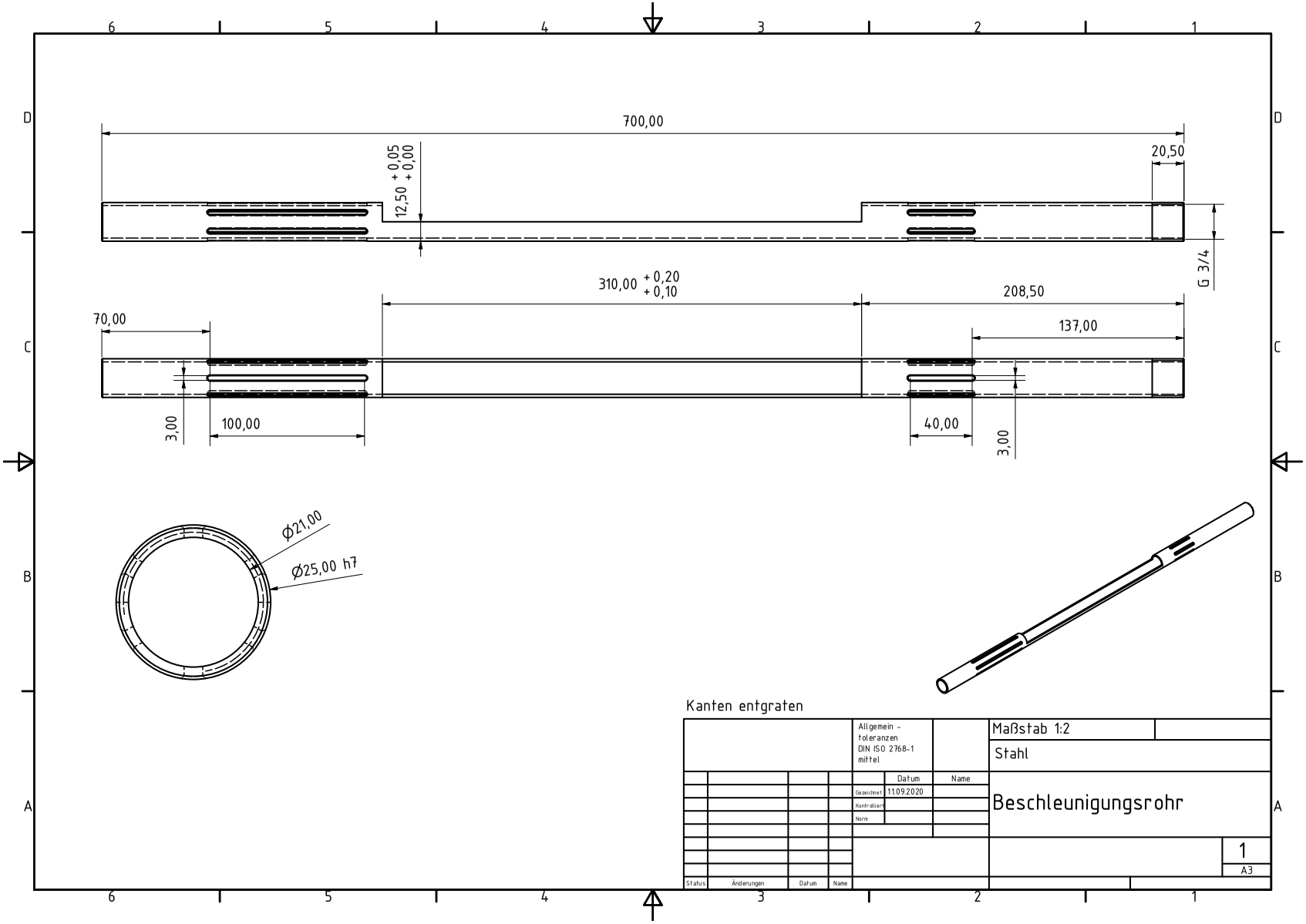
700,00
20,50
12,50 +0,05 +0,00
G 3/4
310,00 +0,20 +0,10
208,50
70,00
137,00
3,00
100,00
40,00
3,00
Ø21,00
Ø25,00 h7
Kanten entgraten
Allgemein – toleranzen DIN ISO 2768-1 mittel
Maßstab 1:2
Stahl
Beschleunigungsrohr
Datum
Name
Gezeichnet 11.09.2020
Kontrolliert
Norm
Status
Änderungen
Datum
Name
1
A3

177

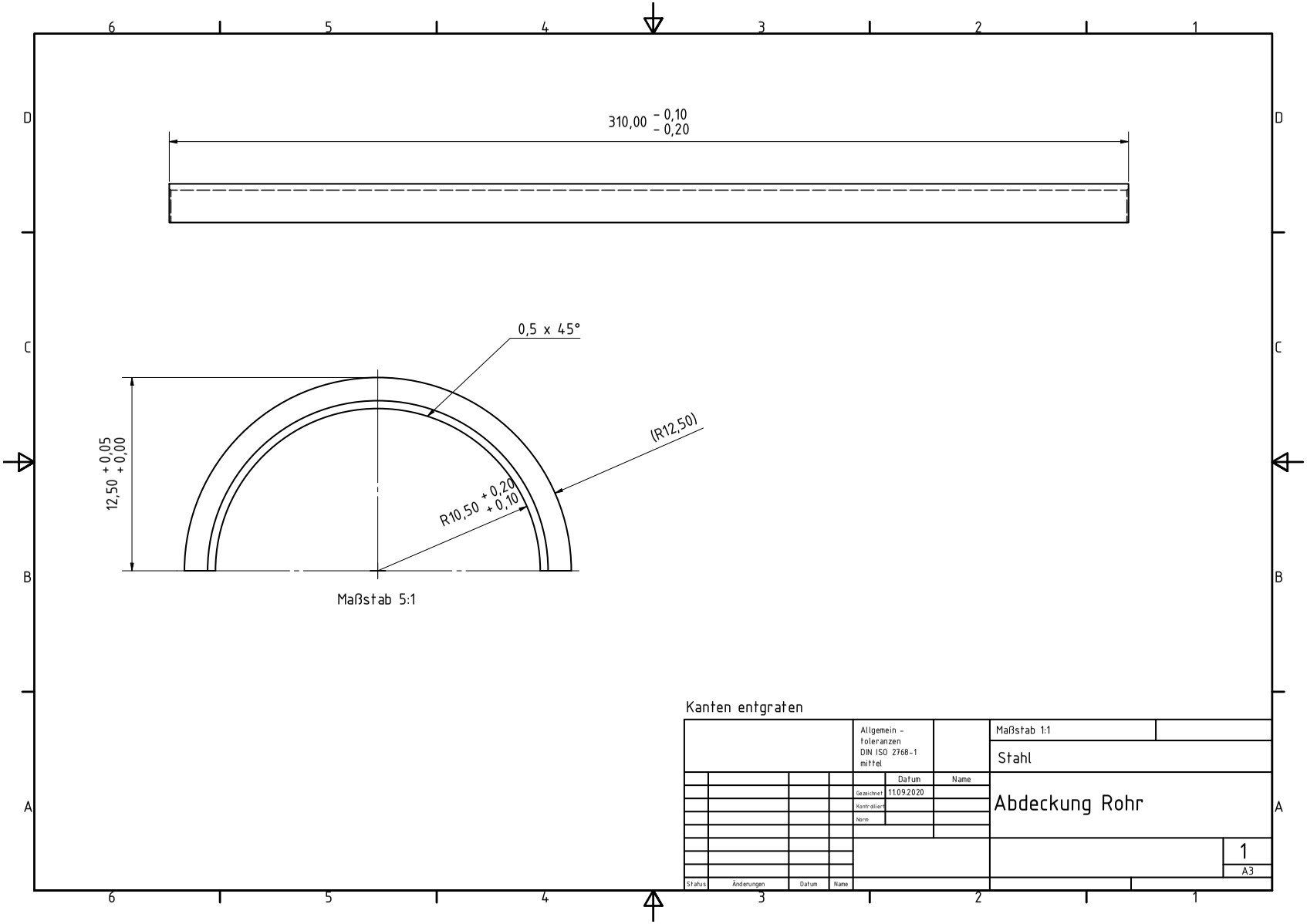

Kanten entgraten

				Allgemein - toleranzen DIN ISO 2768-1 mittel			Maßstab 1:1
					Datum	Name	Stahl
				Gezeichnet	11.09.2020		Abdeckung Rohr
				Kontrolliert			
				Norm			
							1
Status	Änderungen	Datum	Name				A3

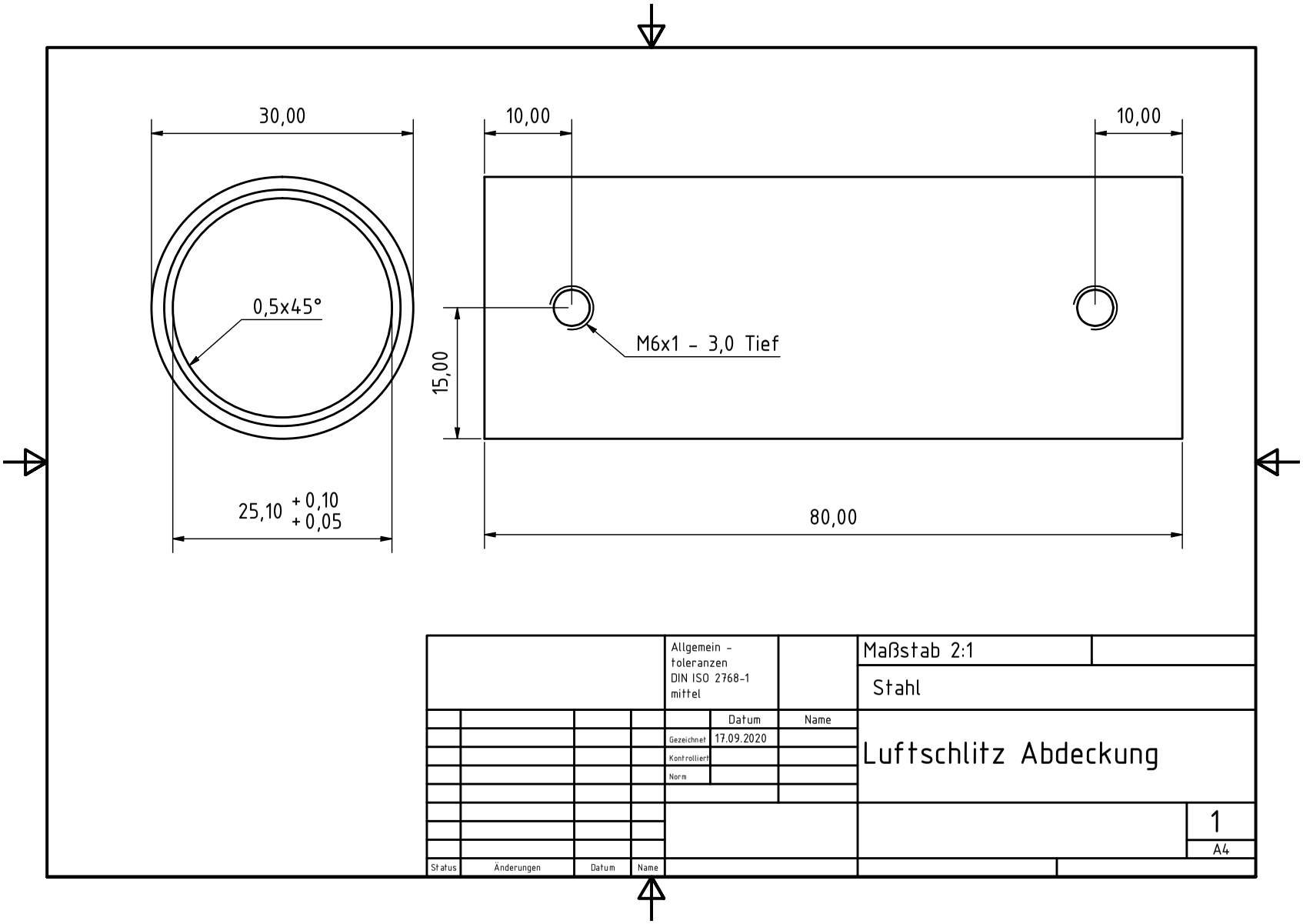

				Allgemein – toleranzen DIN ISO 2768-1 mittel		Maßstab 2:1
						Stahl
					Datum	Name
				Gezeichnet	17.09.2020	Luftschlitz Abdeckung
				Kontrolliert		
				Norm		
						1
						A4
Status	Änderungen	Datum	Name			

A.2 Derivations of the stress-strain curves for determining the starting point of the respective plateau

For the evaluation of the experimental data, a Savitzky–Golay filter was applied to smooth the measured signals and to compute their numerical derivatives.

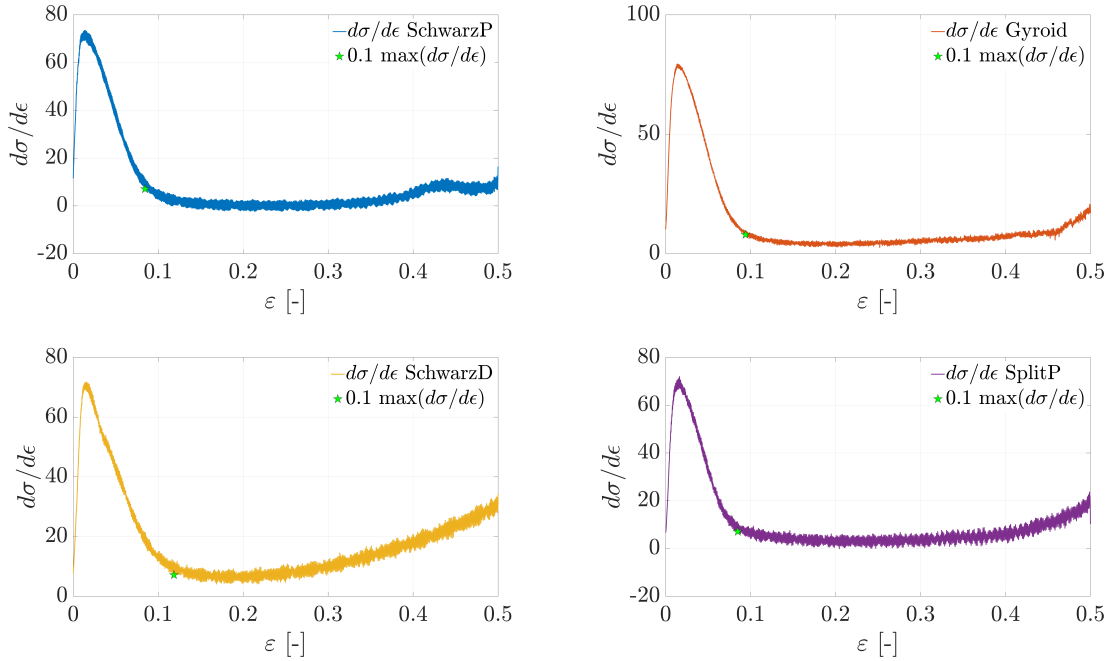

Fig. A.1 – Derivations of the stress-strain curves for the investigated lattice structures with a relative density $\bar{\rho} = 0.4$.

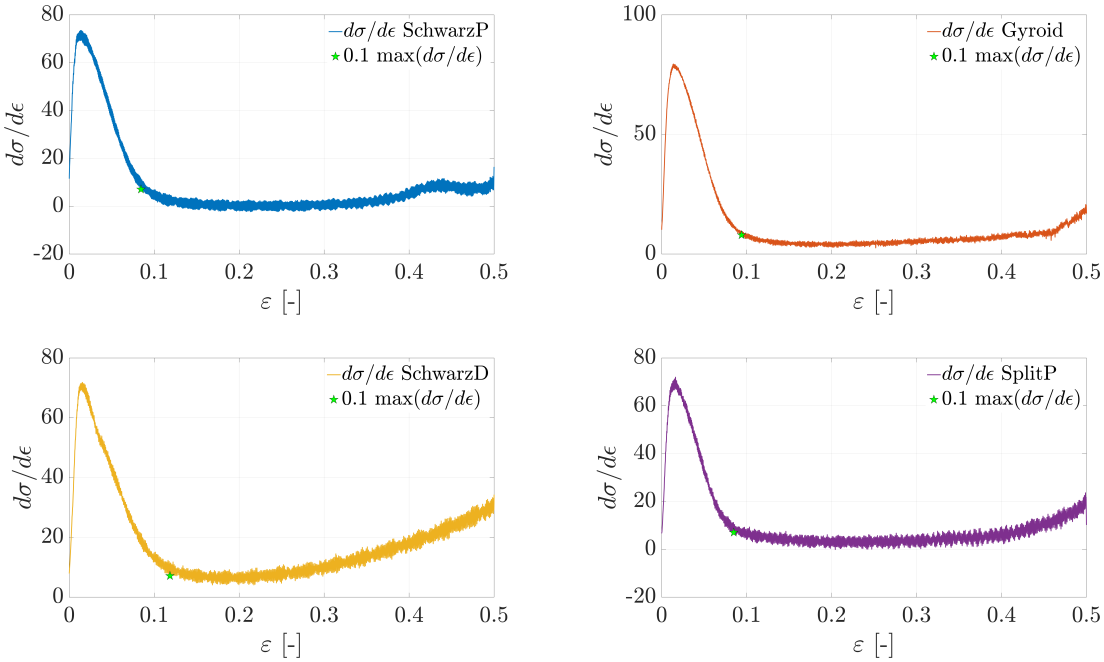

FIG. A.2 – Derivations of the stress-strain curves for the investigated TPMS structures with a relative density $\bar{\rho} = 0.4$.

A.3 Response signals of investigated structures under repeated loading

This appendix presents the response signals of the investigated structures under repeated loading. The structures were subjected to up to three consecutive tests to examine their structural sustainability. In addition, the resulting cumulative impulses are provided for comparison.

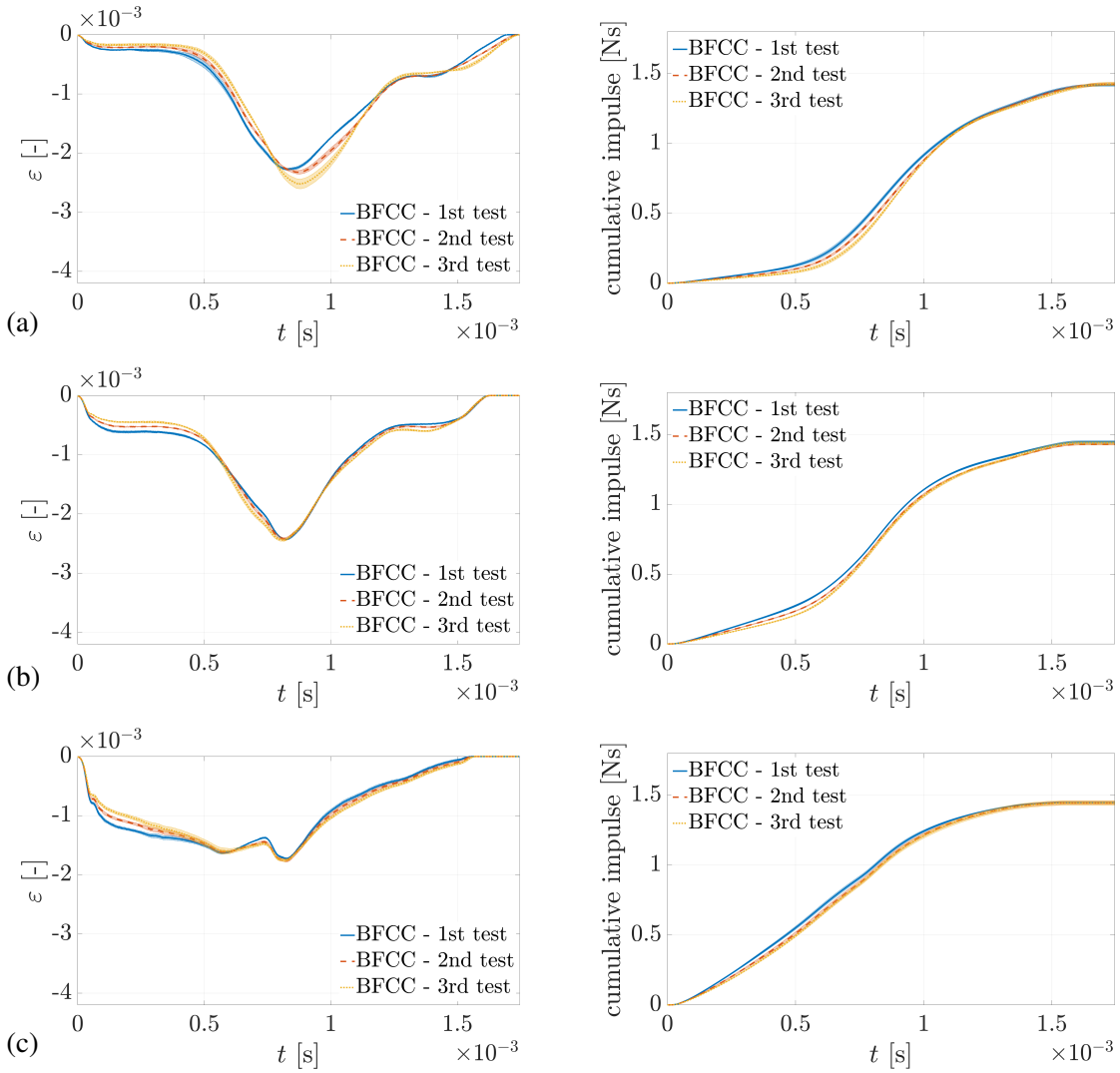

Fig. A.3 – Pulses (left) of BFCC for different relative densities: a) $\bar{\rho} = 0.2$, b) $\bar{\rho} = 0.3$, c) $\bar{\rho} = 0.4$, under repeated loading to examine the structural sustainability, together with the resulting cumulative impulse (right).

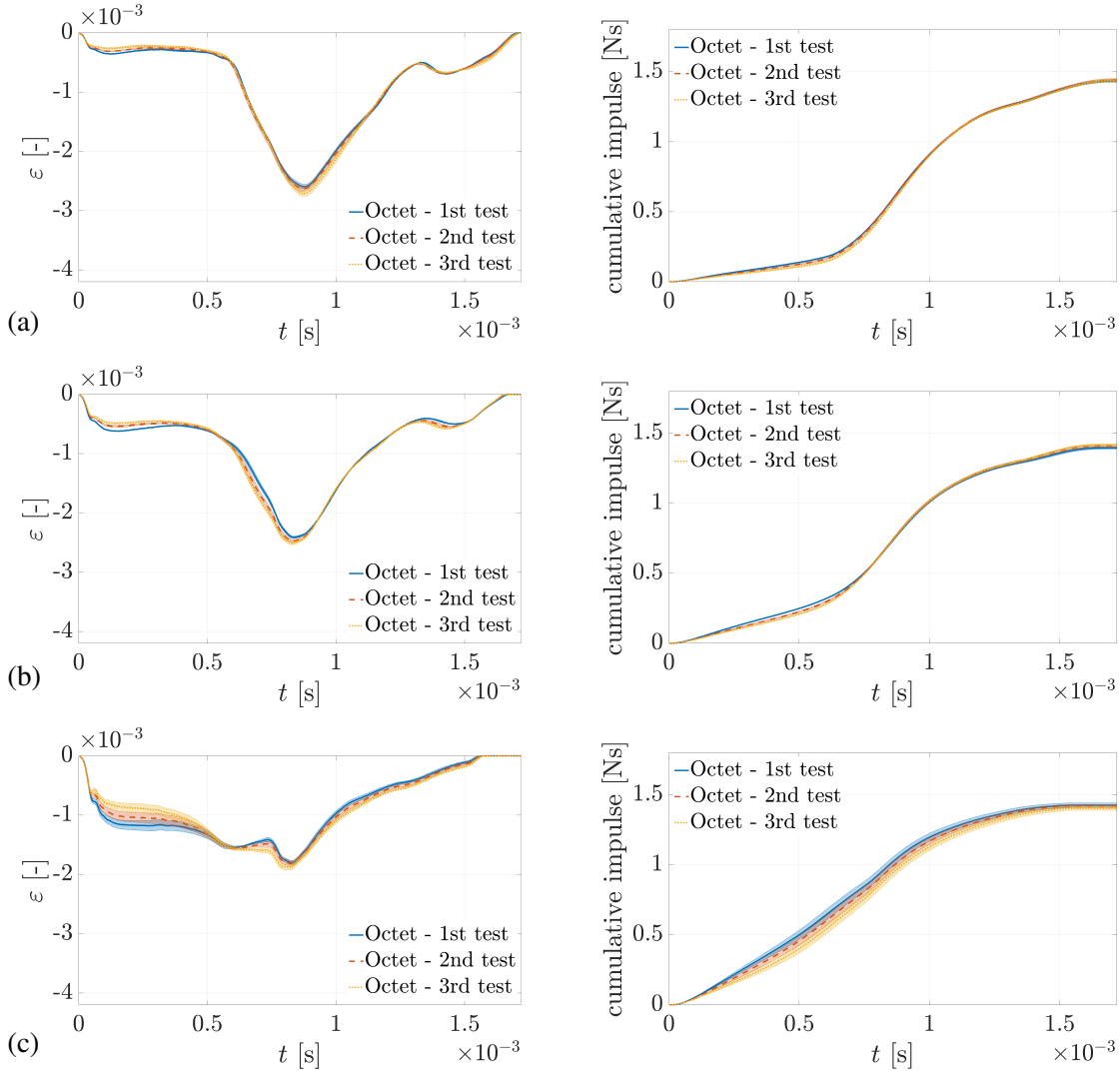

FIG. A.4 – Pulses (left) of OCTET for different relative densities: a) $\bar{\rho} = 0.2$, b) $\bar{\rho} = 0.3$, c) $\bar{\rho} = 0.4$, under repeated loading to examine the structural sustainability, together with the resulting cumulative impulse (right).

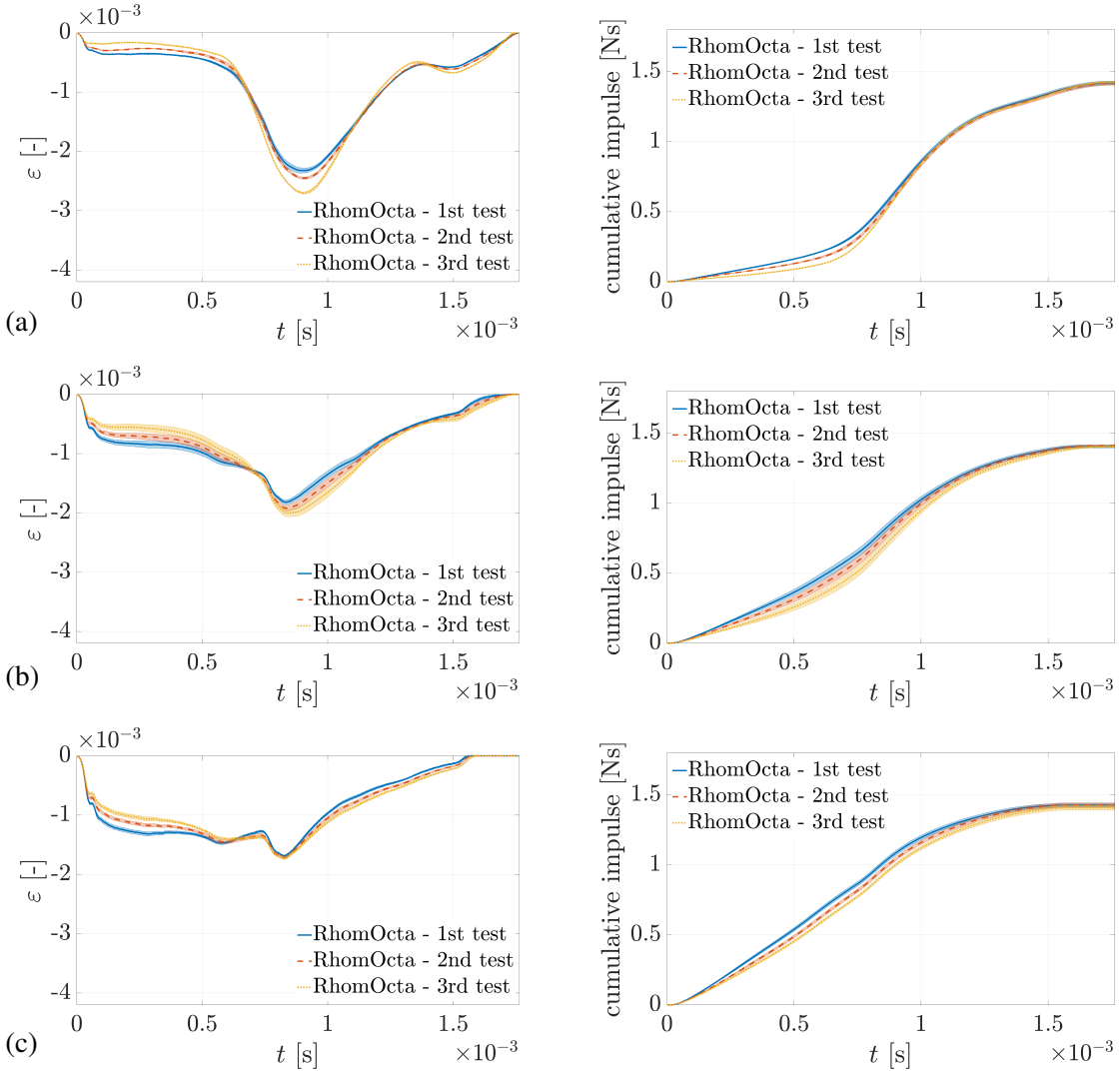

Fig. A.5 – Pulses (left) of RhomOcta for different relative densities: a) $\bar{\rho} = 0.2$, b) $\bar{\rho} = 0.3$, c) $\bar{\rho} = 0.4$, under repeated loading to examine the structural sustainability, together with the resulting cumulative impulse (right).

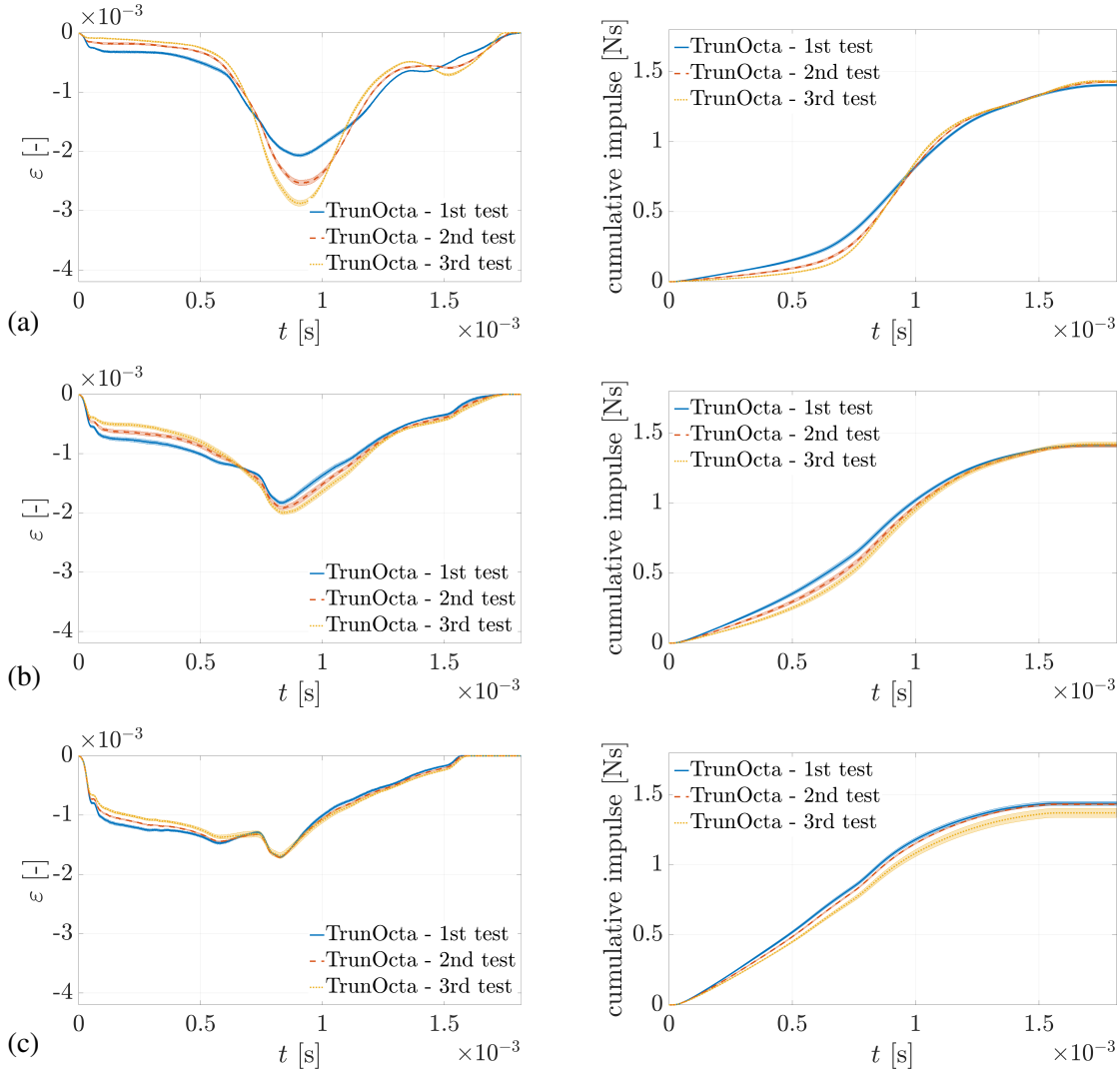

FIG. A.6 – Pulses (left) of TRUNOCTA for different relative densities: a) $\bar{\rho} = 0.2$, b) $\bar{\rho} = 0.3$, c) $\bar{\rho} = 0.4$, under repeated loading to examine the structural sustainability, together with the resulting cumulative impulse (right).

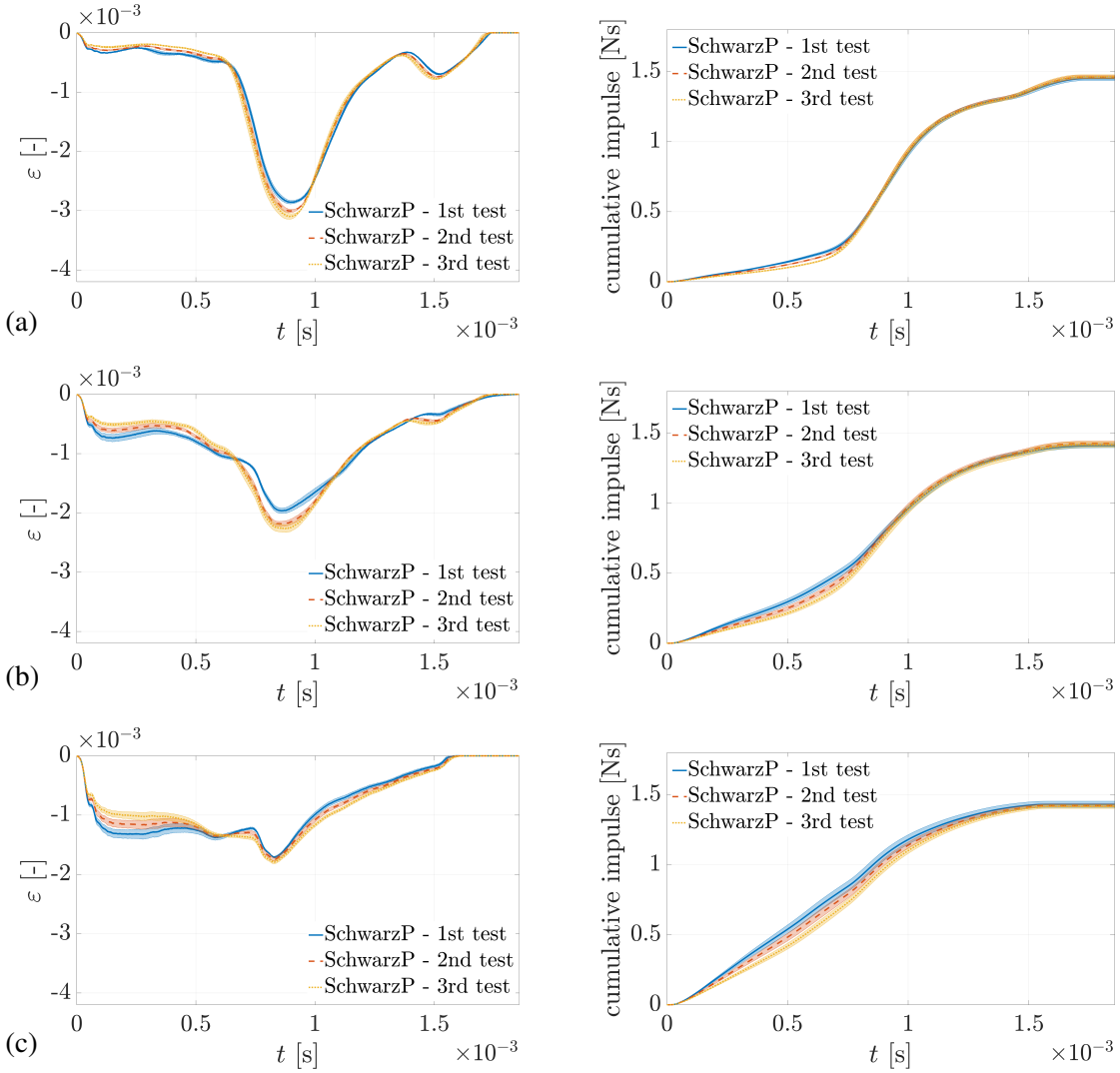

FIG. A.7 – Pulses (left) of SCHWARZP for different relative densities: a) $\bar{\rho} = 0.2$, b) $\bar{\rho} = 0.3$, c) $\bar{\rho} = 0.4$, under repeated loading to examine the structural sustainability, together with the resulting cumulative impulse (right).

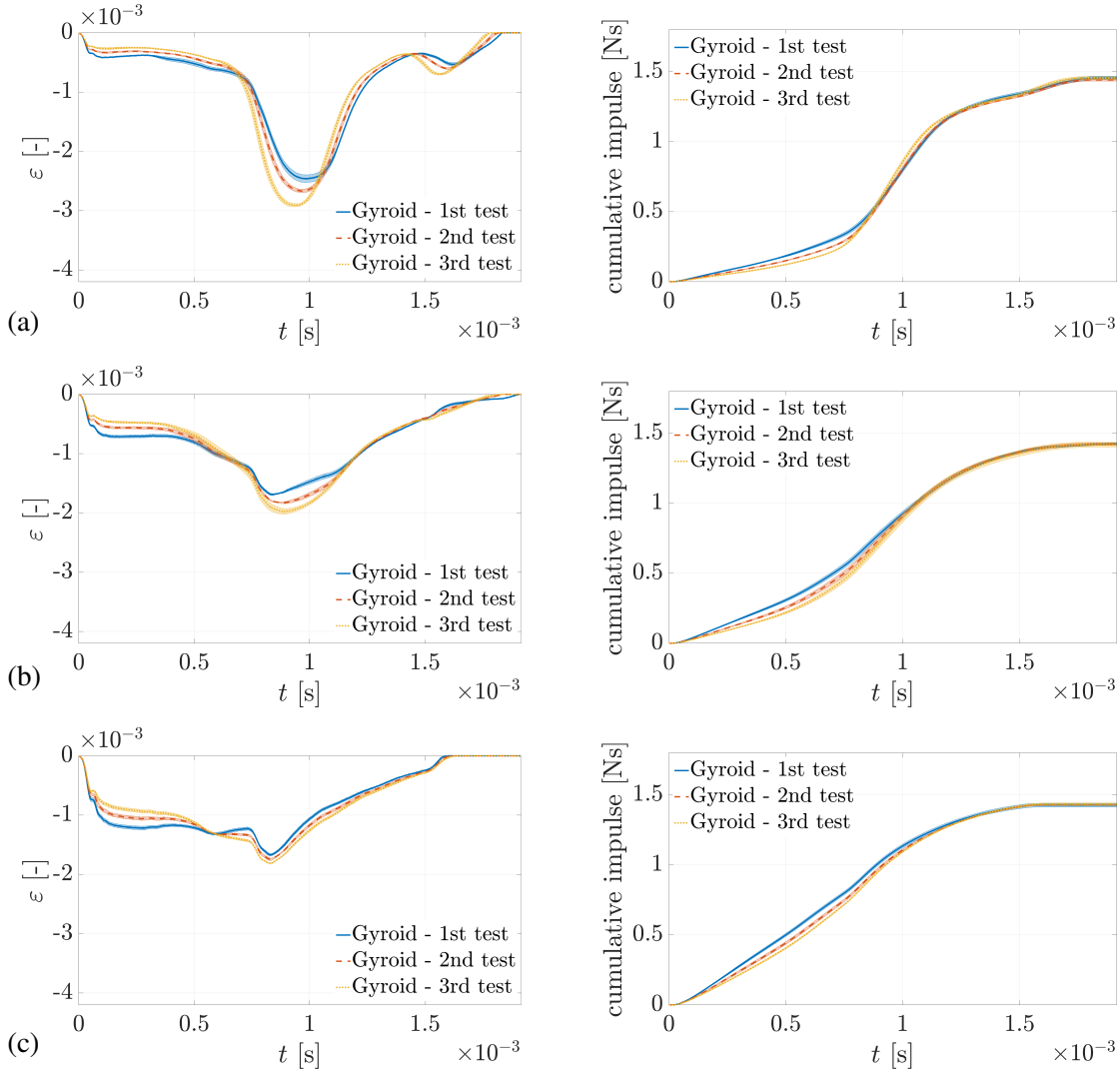

FIG. A.8 – Pulses (left) of GYROID for different relative densities: a) $\bar{\rho} = 0.2$, b) $\bar{\rho} = 0.3$, c) $\bar{\rho} = 0.4$, under repeated loading to examine the structural sustainability, together with the resulting cumulative impulse (right).

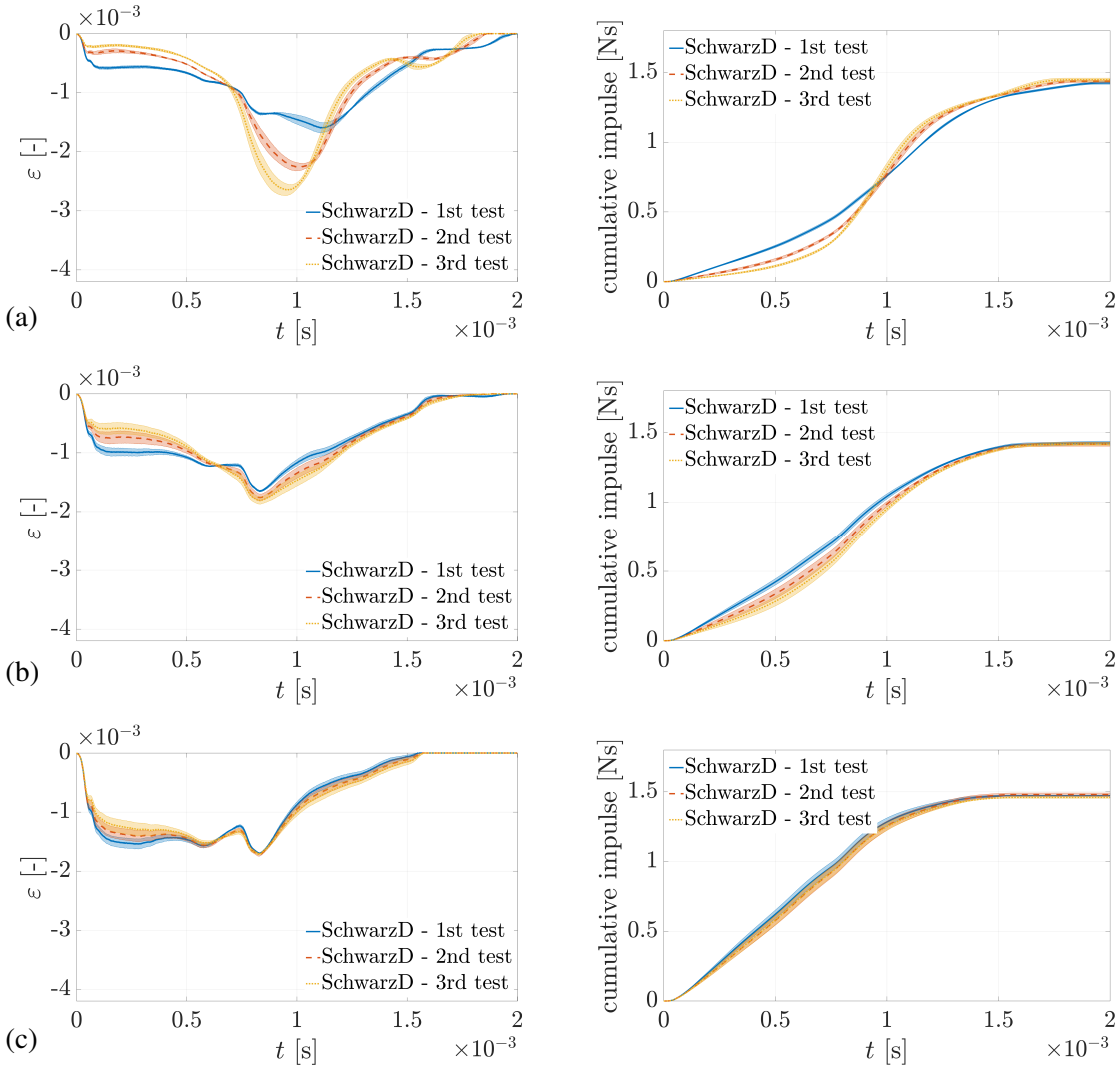

Fig. A.9 – Pulses (left) of SchwarzD for different relative densities: a) $\bar{\rho} = 0.2$, b) $\bar{\rho} = 0.3$, c) $\bar{\rho} = 0.4$, under repeated loading to examine the structural sustainability, together with the resulting cumulative impulse (right).

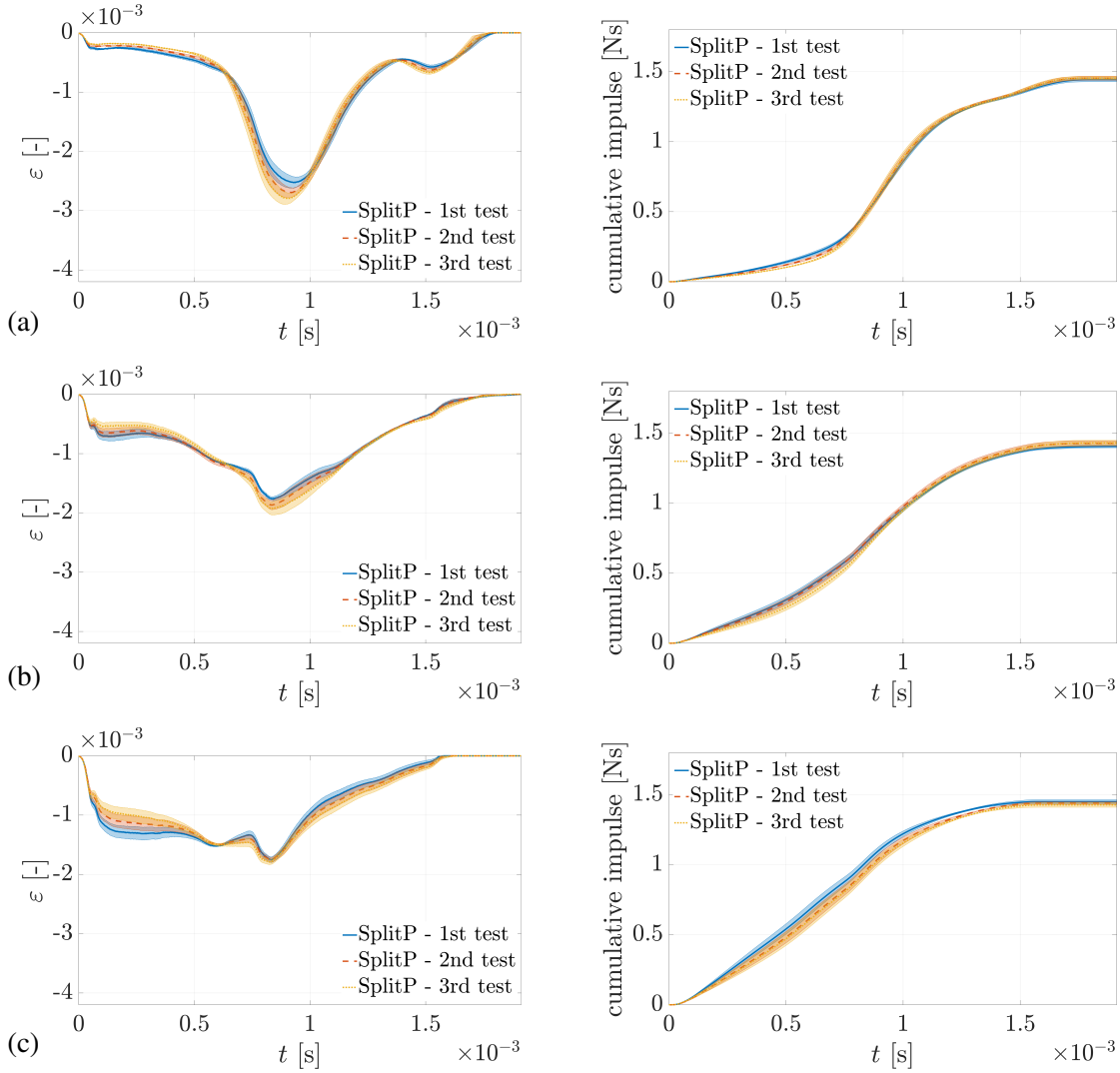

FIG. A.10 – Pulses (left) of SPLITP for different relative densities: a) $\bar{\rho} = 0.2$, b) $\bar{\rho} = 0.3$, c) $\bar{\rho} = 0.4$, under repeated loading to examine the structural sustainability, together with the resulting cumulative impulse (right).

A.4 Spectra of the pulses attenuated by investigated structures at different relative densities

This appendix presents the frequency spectra of the impulses attenuated by the investigated structures. The spectra were obtained by applying a Fast Fourier Transform to the measured time-domain signals.

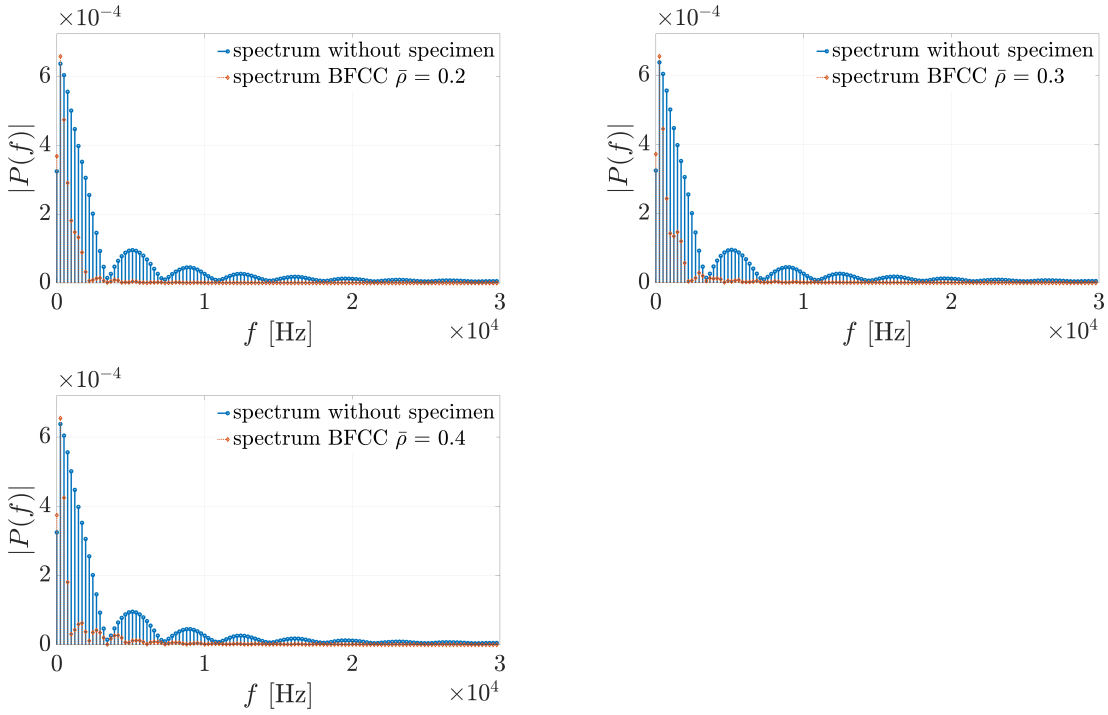

Fig. A.11 – Spectra for BFCC for different relative densities $\bar{\rho}$.

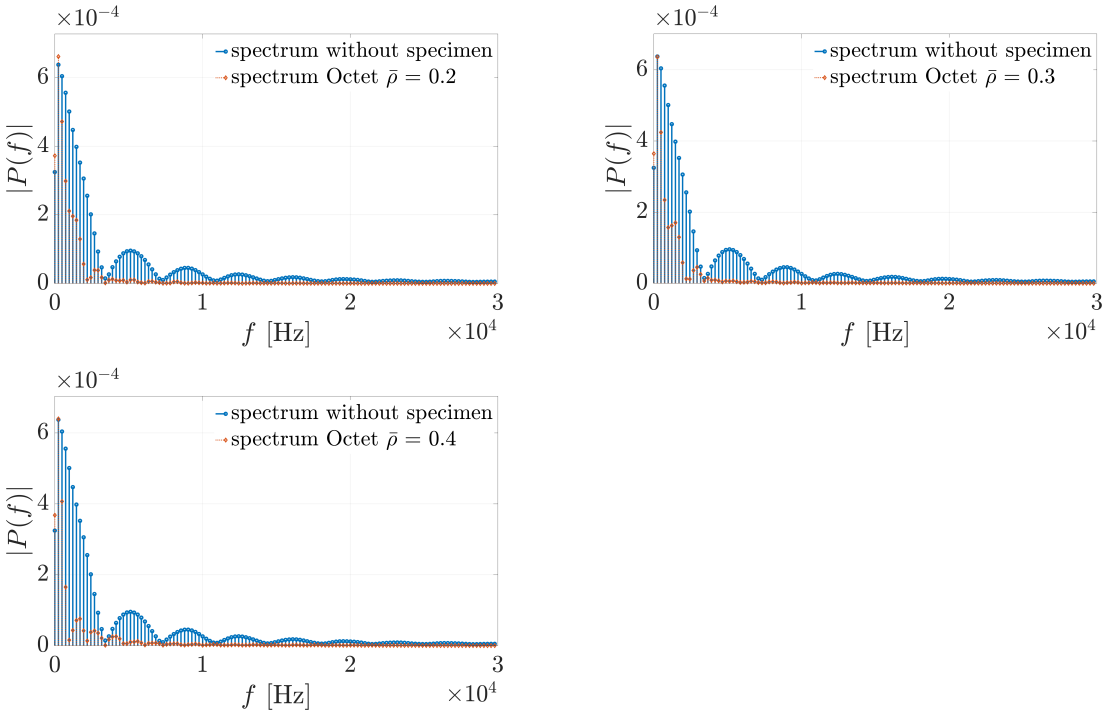

FIG. A.12 – Spectra for OCTET for different relative densities $\bar{\rho}$.

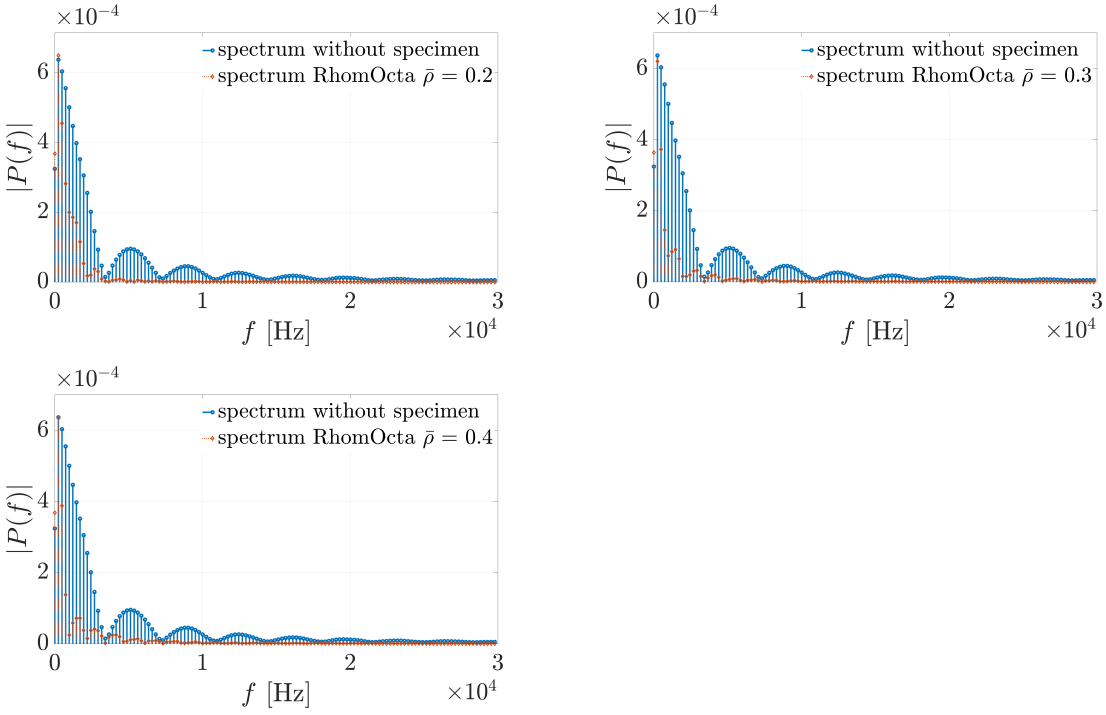

FIG. A.13 – Spectra for RHOMOCTA for different relative densities $\bar{\rho}$.

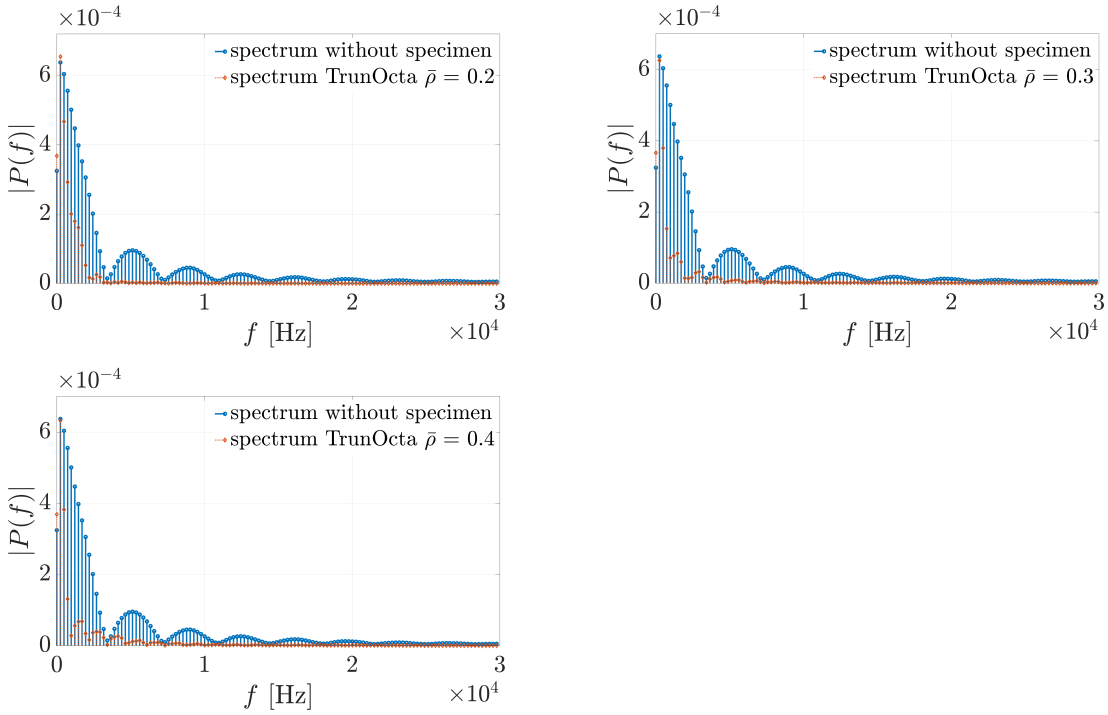

Fig. A.14 – Spectra for TrunOcta for different relative densities $\bar{\rho}$.

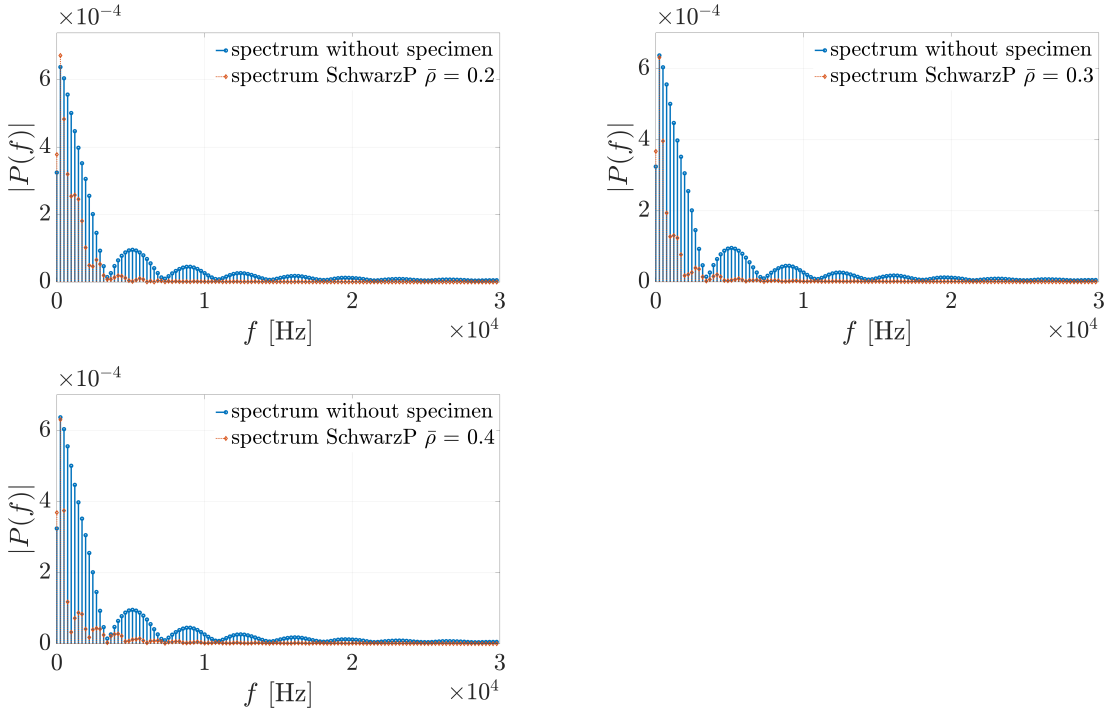

Fig. A.15 – Spectra for SchwarzP for different relative densities $\bar{\rho}$.

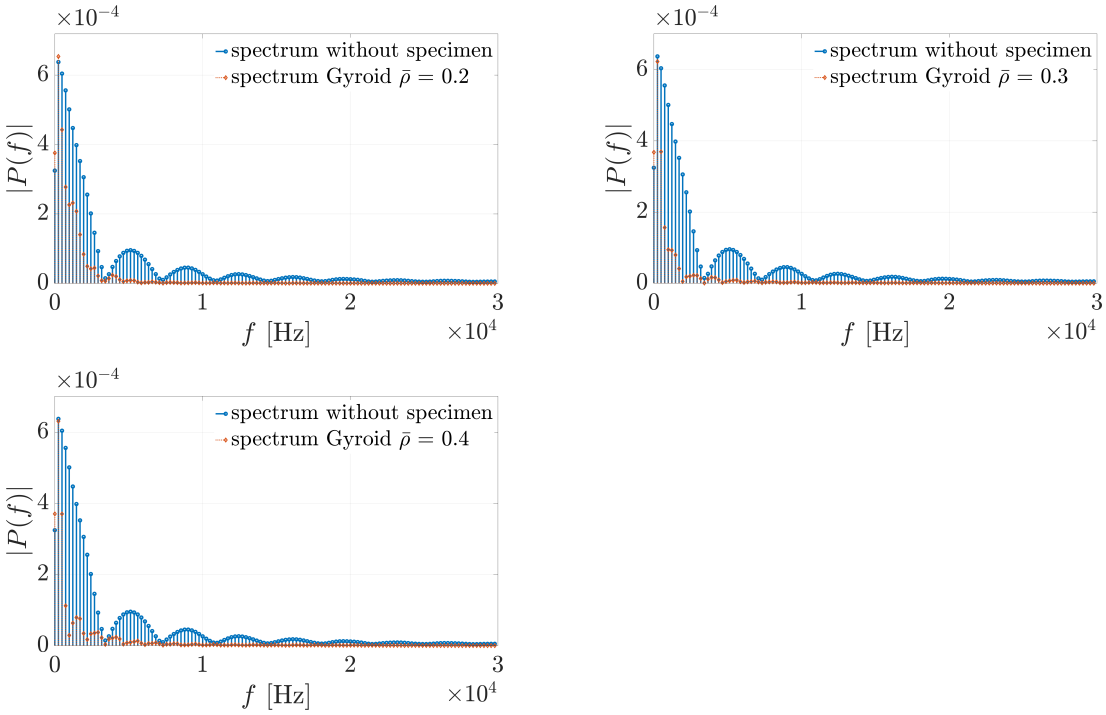

FIG. A.16 – Spectra for GYROID for different relative densities $\bar{\rho}$.

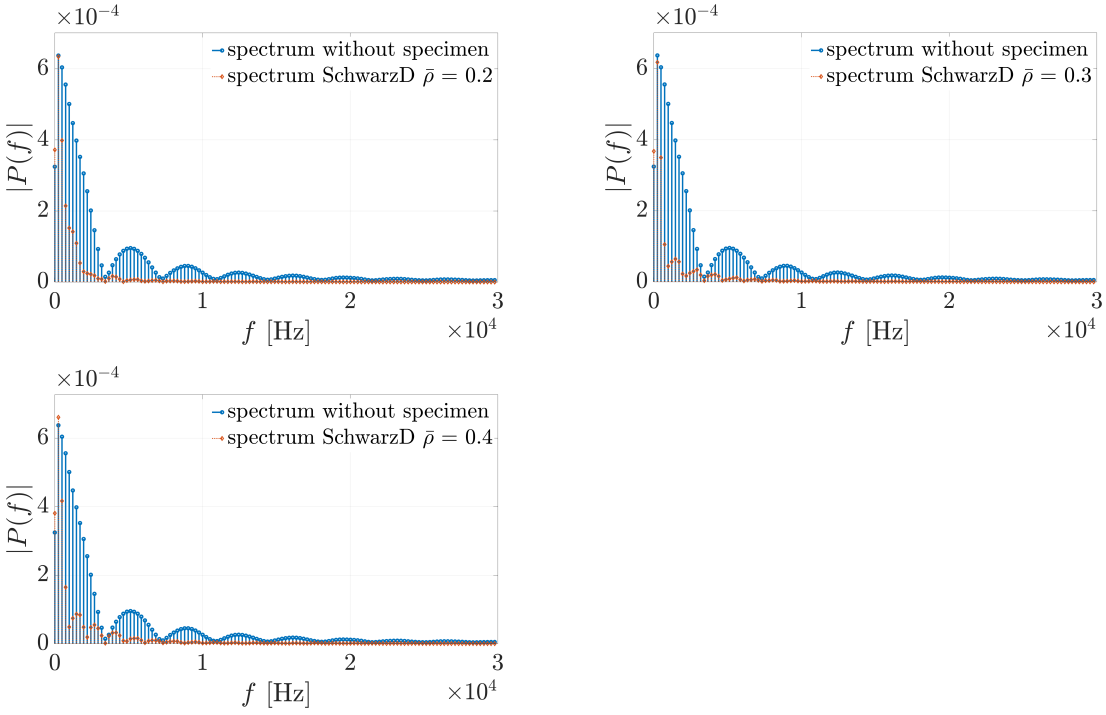

FIG. A.17 – Spectra for SCHWARZD for different relative densities $\bar{\rho}$.

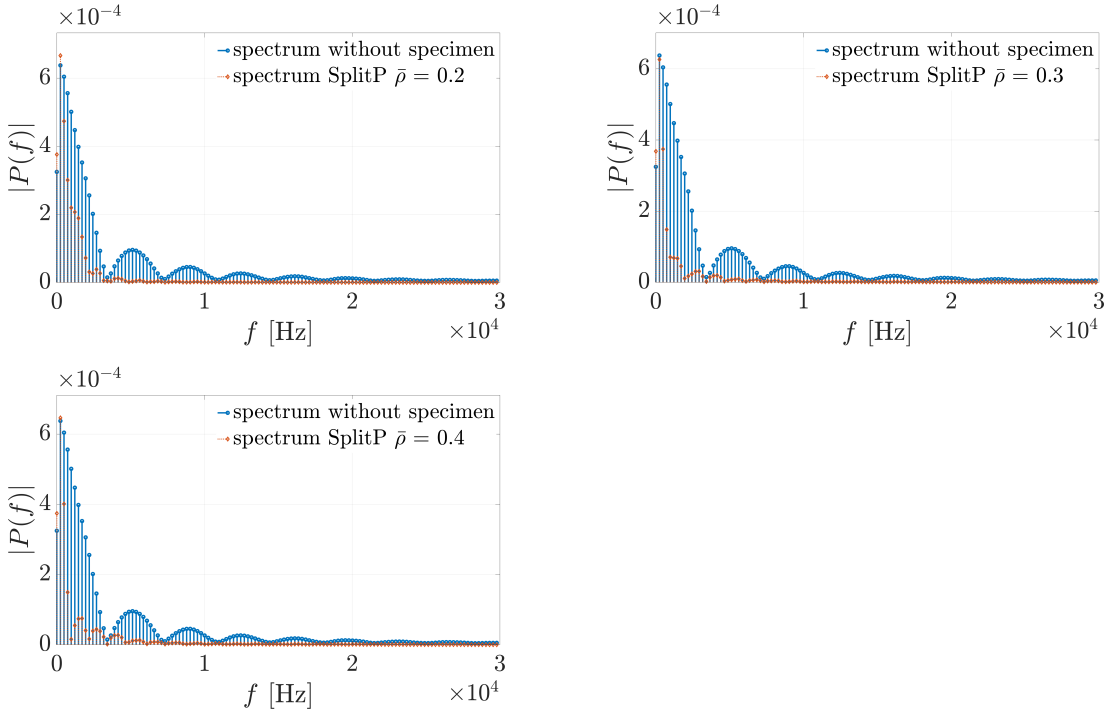

FIG. A.18 – Spectra for SPLITP for different relative densities $\bar{\rho}$.